INTEGRATED CONTROL OF WIND FARMS, FACTS DEVICES AND THE POWER NETWORK USING NEURAL NETWORKS AND ADAPTIVE CRITIC DESIGNS

A Dissertation
Presented to
The Academic Faculty

by

Wei Qiao

In Partial Fulfillment
of the Requirements for the Degree
Doctor of Philosophy in the
School of Electrical and Computer Engineering

Georgia Institute of Technology
August 2008

INTEGRATED CONTROL OF WIND FARMS, FACTS DEVICES AND THE POWER NETWORK USING NEURAL NETWORKS AND ADAPTIVE CRITIC DESIGNS

Approved by:

Dr. Ronald G. Harley, Advisor
School of Electrical and Computer Engineering
Georgia Institute of Technology

Dr. David G. Taylor
School of Electrical and Computer Engineering
Georgia Institute of Technology

Dr. Thomas G. Habetler
School of Electrical and Computer Engineering
Georgia Institute of Technology

Dr. Ganesh Kumar Venayagamoorthy
Department of Electrical and Computer Engineering
Missouri University of Science and Technology

Dr. Deepakraj M. Divan
School of Electrical and Computer Engineering
Georgia Institute of Technology

Date Approved: June 25, 2008

To my mother, Yuehua Yao, my father, Taisheng Qiao, my wife, Liyan Qu, and my brother, Yu Qiao, for their love and support.

ACKNOWLEDGEMENTS

A doctoral dissertation is usually considered to be a personal accomplishment. However, it would not have been possible for me to finish this work without the inspiration, encouragement, and support from many people.

Dr. Ronald G. Harley has been a wise and trusted advisor throughout the entire process. It is due to his constant inspiration and encouragement that I have gained a deeper understanding of engineering and made progress toward solving problems and improving my communication skills as a researcher. Had it not been for his vision, encouragement, and his confidence in my ability, much of this work would not have been completed. I am deeply grateful for his guidance.

I would also like to express my gratitude to Dr. Thomas Habetler and Dr. Deepak Divan, for their time and invaluable input into my research. I have benefited immensely from their knowledge and experience.

I am also indebted to Dr. Ganesh Kumar Venayagamoorthy for his help and assistance to my experimental work on RTDS in the Real-Time Power and Intelligent Systems Laboratory at the Missouri University of Science and Technology, Rolla, MO.

I would also like to thank Dr. Jose M. Aller for his help and assistance to my experimental work.

I was fortunate to work with many exceptional fellow colleagues in my research group. I would like to thank Dr. Xianghui Huang, Dr. Zhi Gao, Dr. Long Wu, Dr. Bin Lu, Dr. Wei Zhou, Dr. Young-Kook Lee, Dr. Joy Mazumdar, Dr. Salman Mohagheghi, Dr. Satish Rajagopalan, Dr. Afroz Imam, Yi Yang, Yi Du, Yao Duan, Pinjia Zhang, Jin Dai, Jiaqi Liang, Siwei Chen, Jung-Sik Yim, Yamille del Valle, Jean Carlos Hernandez Mejia, Harjeet Johal, Jyoti Sastry, Anish Prasai, Frank Karl Kreikebaum, Stefan Grubic, and Ari Zachas for their help on various aspects of this work, and other fellow graduate

students in the research group for their friendship and support over the past four years of my endeavor. There are numerous names of faculty, family, and friends that should be mentioned here, who have supported me directly or indirectly during my stay at Georgia Tech. I express my gratitude to all of the people I have known.

Most of all, I would like to thank my parents, my wife, and my brother for being a constant source of encouragement and motivation throughout my pursuit for the doctoral degree. I could never fully express my love and gratitude to them.

The financial supports from the following institutions/organizations are gratefully acknowledged:

- National Science Foundation, USA.
- Georgia Institute of Technology, USA.
- Duke Power Company, Charlotte, NC, USA.
- IEEE Computational Intelligence Society
- IEEE Power Engineering Society
- IEEE Power Electronics Society

TABLE OF CONTENTS

Page

LIST OF TABLES

Page

LIST OF FIGURES

Page

LIST OF SYMBOLS AND ABBREVIATIONS

ACD	Adaptive critic design
A/D	Analog-to-digital
ANN	Artificial neural network
AR	Autoregressive
ARX	Autoregressive with an exogenous variable
ARMA	Autoregressive moving average
ARMAX	Autoregressive moving average with an exogenous variable
AVR	Automatic voltage regulator
CONVC	Conventional controller
CONVEC	Conventional external linear controller
DCM	Dc machine
DFIG	Doubly fed induction generator
DHP	Dual heuristic programming
D/A	Digital-to-analog
DSP	Digital signal processor
FACTS	Flexible ac transmission system
FTC	Fault-tolerant control
FTIANC	Fault-tolernat indirect adaptive neurocontrol
FTONC	Fault-tolerant optimal neurocontrol scheme
GA	Genetic algorithm
GDHP	Globalized dual heuristic programming
GPS	Global positioning satellite
GRBFN	Gaussian radial basis function network
GSC	Grid side converter

GTO	Gate turn-off
HDP	Heuristic dynamic programming
IG	Induction generator
IGBT	Insulated gate bipolar transistor
IGCT	Integrated gate commutated thyristor
INC	Interface neurocontroller
INDAEC	Indirect adaptive external neurocontroller
LMS	Least mean square
MA	Moving average
MLP	Multilayer perceptron
MLPNN	Multilayer perceptron neural network
MPPT	Maximum power point tracking
MSE	Mean-square error
MSFTC	Missing-sensor-fault-tolerant control
MSR	Missing sensor restoration
NAR	Nonlinear autoregressive
NARMA	Nonlinear autoregressive moving average
NARX	Nonlinear autoregressive with exogenous inputs
NARMAX	Nonlinear autoregressive moving average with exogenous inputs
NONC	Nonlinear optimal neurocontroller
OWAM	Optimal wide-area monitor
PC	Personal computer
PCC	Point of common coupling
PI	Proportional integral
PID	Proportional integral derivative
PMU	Phasor measurements unit
PRBS	Pseudorandom binary signals

PSO	Particle swarm optimization
PSS	Power system stabilizer
PWM	Pulse-width modulation
RBF	Radial basis function
RBFNC	Radial basis function neurocontroller
RBFNI	Radial basis function neuroidentifier
RBFNN	Radial basis function neural network
RNN	Recurrent neural network
RSC	Rotor side converter
RTDS	Real Time Digital Simulator
SCIG	Squirrel-cage induction generator
SERS	Sensor evaluation and (missing sensor) restoration scheme
SMIB	Single machine infinite bus
SPSS	Supervisory level power system stabilizer
SRRFT	Synchronously rotating reference frame transformation
SSSC	Static synchronous series compensator
STATCOM	Static synchronous compensator
SVC	Static var compensator
SVD	Singular value decomposition
TCPAR	Thyristor controlled phase angle regulator
TCPS	Thyristor controlled phase shifter
TCSC	Thyristor controlled series capacitor
TDL	Time delay lock
UPFC	Unified power flow controller
VFC	Variable frequency converter
VSC	Voltage source converter
VSI	Voltage source inverter

WACC	Wide-area coordinating control
WACNC	Wide-area coordinating neurocontroller
WAM	Wide-area monitor
WTG	Wind turbine generator

SUMMARY

Worldwide concern about the environmental problems and a possible energy crisis has led to increasing interest in clean and renewable energy generation. Among various renewable energy sources, wind power is the most rapidly growing one. Therefore, how to provide efficient, reliable, and high-performance wind power generation and distribution has become an important and practical issue in the power industry.

In addition, because of the new constraints placed by the environmental and economical factors, the trend of power system planning and operation is toward maximum utilization of the existing infrastructure with tight system operating and stability margins. This trend, together with the increased penetration of renewable energy sources, will bring new challenges to power system operation, control, stability and reliability which require innovative solutions. Flexible ac transmission system (FACTS) devices, through their fast, flexible, and effective control capability, provide one possible solution to these challenges.

To fully utilize the capability of individual power system components, e.g., wind turbine generators (WTGs) and FACTS devices, their control systems must be suitably designed with high reliability. Moreover, in order to optimize local as well as system-wide performance and stability of the power system, real-time local and wide-area coordinated control is becoming an important issue.

Power systems containing conventional synchronous generators, WTGs, and FACTS devices are large-scale, nonlinear, nonstationary, stochastic and complex systems distributed over large geographic areas. Traditional mathematical tools and system control techniques have limitations to control such complex systems to achieve an optimal performance. Intelligent and bio-inspired techniques, such as swarm intelligence, neural

networks, and adaptive critic designs, are emerging as promising alternative technologies for power system control and performance optimization.

This work focuses on the development of advanced optimization and intelligent control algorithms to improve the stability, reliability and dynamic performance of WTGs, FACTS devices, and the associated power networks. The proposed optimization and control algorithms are validated by simulation studies in PSCAD/EMTDC, experimental studies, or real-time implementations using Real Time Digital Simulation (RTDS) and TMS320C6701 Digital Signal Processor (DSP) Platform. Results show that they significantly improve electrical energy security, reliability and sustainability.

CHAPTER 1

INTRODUCTION

Worldwide concern about the environmental pollution and a possible energy crisis has led to increasing interest in innovative technologies for generation of clean and renewable electrical energy. Among a variety of renewable energy sources, wind power is the most rapidly growing one in the power industry.

The traditional wind turbine generator (WTG) systems employ squirrel-cage induction generators (SCIGs) to generate wind power. These WTGs have no speed control capability and cannot provide voltage or frequency support when connected the power grid [1], [2]. During the past decade, the concept of a variable-speed wind turbine driving a doubly fed induction generator (DFIG) has received increasing attention because of its noticeable advantages over other WTG systems [2]-[5]. Most existing wind farms and those in planning employ this type of WTGs. Compared to the fixed-speed SCIG wind turbines, the DFIG wind turbines can provide decoupled active and reactive power control of the generator, more efficient energy production, improved power quality, improved dynamic performance and grid fault ride-through capability. However, compared to the conventional synchronous generators, the reactive power control capability of the DFIG wind turbines is limited.

Moreover, many WTGs are installed in remote, rural areas with good wind resources. These remote areas usually have electrically weak power grids, characterized by low short circuit ratios and under-voltage conditions. In such grid conditions and during a grid fault, the DFIGs may not be able to provide sufficient reactive power support. Without any external dynamic reactive compensation, there can be a risk of voltage instability in the power grid [2]. To prevent further contingencies, utilities typically require the immediate disconnection of the WTGs from the grid, and allow

reconnection when normal operation has been restored. This is possible, as long as wind power penetration remains low. However, in some power systems, the penetration of wind power is increasing rapidly and is starting to influence overall power system behavior. Moreover, due to growing demands and limited resources, the power industry is facing challenges on the electricity infrastructure. As a consequence, it will become necessary to maximize the use of all generating sources, including WTGs, to support the network voltage and frequency not only during steady-state conditions but also during disturbances.

In the era of a deregulated electricity industry, the policy of open access to transmission systems, which helped create competitive electricity markets, led to a huge increase in energy transactions over the grid and possible congestion in transmission systems. On the other hand, because of new constraints placed by economical and environmental factors, the trend in power system planning and operation is toward maximum utilization of existing electricity infrastructure with tight operating and stability margins. Under these conditions, power systems become more complex to operate and to control, and, thus, more vulnerable to a disturbance.

In a conventional power system, synchronous generators are the key components related to the system stability. The control of a synchronous generator is achieved by an automatic voltage regulator (AVR) to maintain constant terminal voltage and a speed governor to maintain constant power and constant speed at some set point. During large disturbances, the synchronous generators and their controllers are often unable to respond fast enough to keep the system stable. A power system stabilizer (PSS) can extend the stability limits of a power system by providing supplemental damping to the oscillation of a synchronous generator's rotor speed through the generator excitation. However, in the case of low-frequency oscillations between generators separated by high system reactance, the PSS may not be able to provide sufficient damping [6].

The controllability of a power system can be further enhanced by using power-electronics-based flexible ac transmission system (FACTS) devices [7]. By rapidly controlling the voltage, impedance, and phase angle of the ac transmission systems, FACTS controllers have shown powerful capability in voltage regulation, power flow control, power oscillation damping, and improving transient stability. Therefore, the use of FACTS devices allows more efficient utilization of existing electricity infrastructure.

Power systems are large-scale, nonlinear, nonstationary, stochastic and complex systems distributed over large geographic areas. The standard power system controllers are local noncoordinated linear controllers. Each of them controls some local quantity to achieve a local optimal performance, but has no information on the entire system performance. Consequently, the entire power system is normally operated at a nonoptimal operating condition. Further, the possible interactions among these local controllers might lead to adverse effects causing inappropriate control effort by different controllers. As a result, when severe system-wide disturbances or contingencies occur, these local controllers are not always able to guarantee stability. Therefore, wide-area coordinating control (WACC) is becoming an important issue in the power industry.

The control and operation of power systems rely on the availability and quality of sensor measurements. Measurements are inevitably subjected to faults caused by sensor failure, broken or bad connections, bad communication, or malfunction of some hardware or software. These faults may result in the failure of the power system controllers and consequently severe contingencies in the power system. To avoid such contingencies, fault-tolerance is an essential requirement for power system control and operation. In addition to the fault-tolerant design, the concept of sensorless control provides another approach to improve the system reliability, as well as to reduce the cost associated with using sensors, e.g., the anemometers used by most variable-speed WTGs.

This chapter discusses some issues and challenges related to the control and operation of voltage source converter (VSC)-based FACTS devices, WTGs, and the

associated power network. The main concerns relate to voltage regulation, power flow control, power oscillation damping, transient stability, fault tolerance and reliability of power systems with wind power generation and VSC-based FACTS devices.

1.1 Voltage Source Converter-Based FACTS Devices

Power-electronics-based FACTS devices have been widely recognized as powerful controllers to enhance the controllability of the ac transmission systems. Among various FACTS devices, those based on the VSC concept have some attractive features [8], such as rapid and continuous response characteristics for smooth dynamic control, allowing advanced control methodologies for high-performance operation, elimination or reduced requirements for harmonic filtering, ability to add energy storage devices, allowing simultaneous active and reactive power exchange with the ac system, etc. The VSC-based FACTS devices include the static synchronous compensator (STATCOM), the static synchronous series compensator (SSSC), and the unified power flow controller (UPFC).

A STATCOM [7], [9], [10] is a shunt FACTS device. The basic configuration of a STATCOM is shown in Figure 1.1. It consists of a gate turn-off (GTO), insulated gate bipolar transistor (IGBT), or integrated gated commutated thyristor (IGCT)-based VSC that uses charged capacitors as the dc source. The converter is connected in shunt to a bus through a coupling transformer. The STATCOM generates a set of balanced three-phase sinusoidal voltages in synchronism with the ac system, with rapidly controllable amplitude and phase angle. A typical application of the STATCOM is to provide smooth and rapid steady-state and transient voltage control at the point of common coupling (PCC) in the power network.

An SSSC is a series FACTS device, which uses a VSC to inject a controllable voltage in quadrature with the line current of the power network through a series-connected transformer, as shown in Figure 1.2. This is equivalent to providing a

controllable capacitive or inductive impedance compensation which is independent of the line current [11]-[13]. A typical application of the SSSC is for power flow control. In addition, with a suitably designed damping controller, the SSSC has an excellent performance in damping low-frequency power oscillations in a power network [14]. By coupling an additional energy storage system to the dc terminal, the SSSC can also provide simultaneous active power compensation, which further enhances its capability in power flow control, power oscillation damping, and improving transient stability [7], [11], [15].

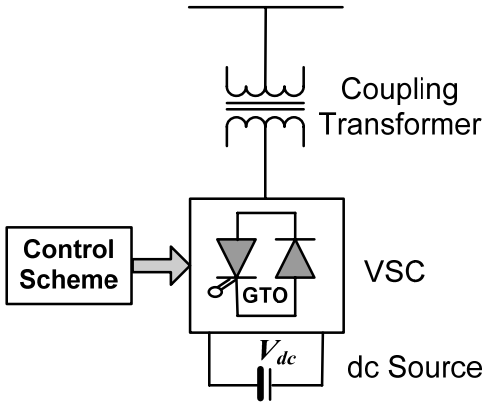

Figure 1.1: Single-line diagram of a STATCOM.

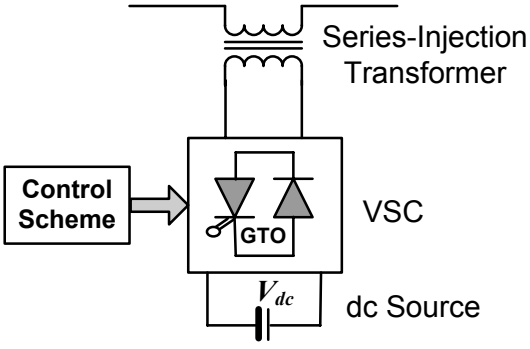

Figure 1.2: Single-line diagram of an SSSC.

Power systems containing generators and FACTS devices are large-scale, nonlinear, nonstationary, multivariable systems with dynamic characteristics over a wide operating range. Conventionally, linear control techniques are used to design the controllers of FACTS devices based on a linearized system model with fixed parameters around a specific operating point [9]-[15]. Final tuning of these controllers gains are typically made using field tests at one or two operating points. However, in practical applications, the FACTS devices and the associated power network cannot be accurately modeled as a linear system with fixed and known parameters. Therefore, at other operating points or in the event of a severe disturbance, these linear controllers may not able to provide an acceptable performance or stability.

1.2 Control, Operation, and Grid Integration of DFIG Wind Turbines

The basic configuration of a DFIG wind turbine is shown in Figure 1.3. The wind turbine is connected to the DFIG through a mechanical shaft system, which consists of a low-speed shaft and a high-speed shaft and a gearbox in between. The wound-rotor induction machine in this configuration is fed from both stator and rotor sides. The stator is directly connected to the grid while the rotor is fed through a variable frequency converter (VFC), which only needs to handle a fraction (25-30%) of the total power to achieve full control of the generator. In order to produce electrical power at constant voltage and frequency to the utility grid over a wide operating range from subsynchronous to supersynchronous speeds [16], the power flow between the rotor circuit and the grid must be controlled both in magnitude and in direction. Therefore, the VFC consists of two four-quadrant IGBT PWM converters, namely, a rotor side converter (RSC) and a grid side converter (GSC), connected back-to-back by a dc-link capacitor [17]. The crow-bar circuit is used to short-circuit the RSC to protect it from over-current in the rotor circuit during transient disturbances.

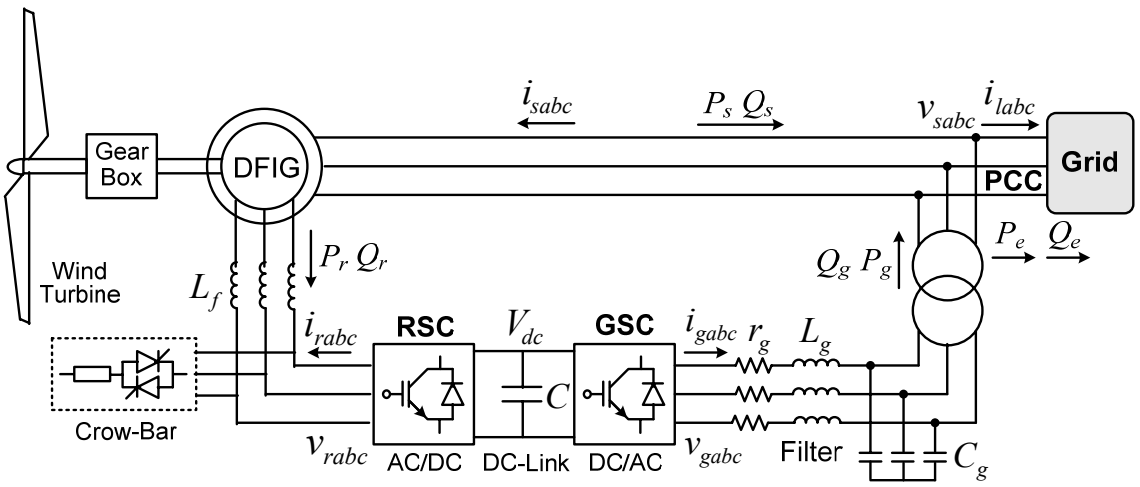

Figure 1.3: Configuration of a DFIG wind turbine.

By adjusting the shaft speed optimally, the variable-speed WTGs can achieve the maximum wind power generation at various wind speeds within the operating range. To implement maximum wind power extraction, most controller designs of the variable-speed WTGs employ anemometers to measure wind speed in order to derive the desired optimal shaft speed for adjusting the generator speed. In most cases, a number of anemometers are placed surrounding the wind turbine at some distance to provide adequate wind speed information. The anemometers are mechanical sensors. There are several problems of using anemometers. First, the use of anemometers increases the cost (e.g., equipment and maintenance costs) of the WTG system. Second, the anemometers are inevitably subjected to failure during lightning strokes, storms, and strong winds. This reduces the reliability of the WTG system. A mechanical sensorless control removes the need of using the anemometers, and therefore, reduces the cost and improves the reliability of the WTG system.

Another key issue related to the operation of the DFIG wind turbines is the grid fault or low voltage ride-through capability. When connected to the grid and during a grid fault, the voltage sags at the PCC of the WTGs can cause a high current in the stator windings of the DFIG. Because of the magnetic coupling between stator and rotor, this

current will also flow in the rotor circuit and the VFC. Since the power rating of the VFC is only 25-30% of the DFIG power rating, this over-current can lead to the destruction of the converter. In order to protect the RSC of the DFIG from the over-current in the rotor circuit, it has to be blocked. In such a case, the generator becomes a conventional SCIG and starts to absorb reactive power; the GSC can be set to control the reactive power and voltage at the PCC. However, the reactive power control capability of the GSC is limited because of its small power capacity. Moreover, due to the unbalance between the mechanical shaft torque and the generator's electromagnetic torque, the induction generator speeds up and draws more reactive power from the grid. This contributes further to the PCC voltage collapse [2].

Moreover, many WTGs are installed in remote, rural areas. These remote areas usually have electrically weak power grids, characterized by low short circuit ratios and under-voltage conditions. In such grid conditions and during a grid fault, the DFIGs may not be able to provide sufficient reactive power support. Without any external dynamic reactive compensation, there can be a risk of voltage instability in the power grid [2]. It has been reported recently that incorporation of wind farms into the East Danish power system could cause a severe voltage recovery problem following a three-phase fault on the network [18]. To prevent such contingencies, utilities typically immediately disconnect the WTGs from the grid, and reconnect them when normal operation has been restored. This is possible, as long as wind power penetration remains low. However, with the rapid increase in penetration of wind power in power systems, tripping of many WTGs in a large wind farm during grid faults may begin to influence the overall power system stability. Therefore, it will become necessary to require WTGs to support the network voltage and frequency not only during steady-state conditions but also during grid disturbances. Due to this requirement, the utilities in many countries have recently established grid codes [5], [19] that specify the range of voltage sags (in duration and voltage level) for which WTGs must remain connected to the power system, as shown in

Figure 1.4, where V and V_n are the magnitudes of the actual and nominal voltages at the connection point of WTGs, respectively. According to this grid-fault/low-voltage ride-through specification, the WTGs should remain connected to the grid and supply reactive power when the voltage at the point of connection falls in the gray area. The successful integration of WTGs into some weak power grids will therefore require dedicated local shunt FACTS devices, e.g., the STATCOM, to provide rapid, smooth, and step-less reactive compensation and voltage support [2], [20] in order to satisfy the relevant grid codes.

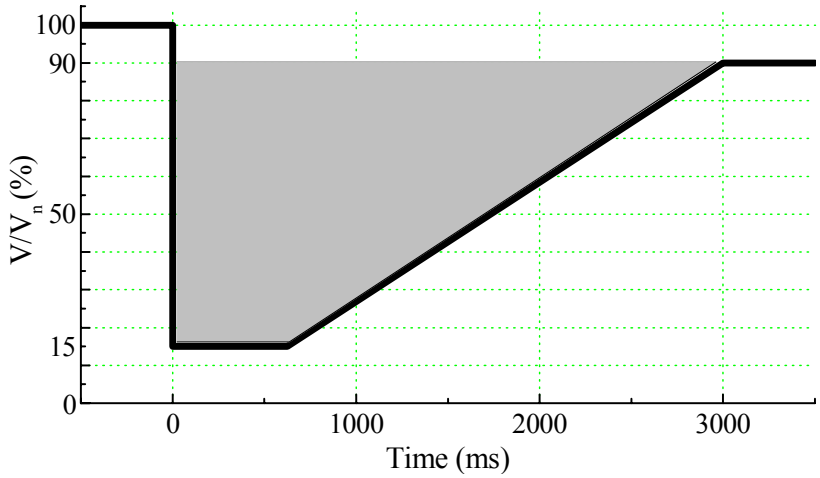

Figure 1.4: Typical grid-fault/low-voltage ride-through requirement of WTGs.

On the other hand, the VFC of the DFIG can be applied to control the reactive power and voltage. This reduces the demands of dynamic reactive compensation from the local FACTS devices. In order to achieve certain operational and economical benefits, it is necessary to coordinate the control actions of the wind farms and the local FACTS devices so that the WTGs will behave like other traditional sources of generations to assist in maintaining grid voltage and frequency stability, particularly during transient conditions. However, because of the stochastic and nonlinear nature of the power system, the traditional mathematical tools are not sufficient or too complicated

to design such a coordinated control scheme based on the analytical models of the integrated system.

1.3 Wide-Area Monitoring and Coordinating Control of the Power Systems with Wind Power Integration and FACTS Devices

Power systems are large-scale, nonlinear, nonstationary, multivariable, complex systems distributed over large geographic areas. System-wide disturbances are a challenging problem for the utility industry. When a major power system disturbance occurs, protection and control actions are required to stop the power system degradation, restore the system to a normal state, and minimize the impact of the disturbance. The standard power system controllers, such as the AVR, speed governor, PSS, and FACTS controllers, are local noncoordinated linear controllers. Each of them controls some local quantities to achieve a local optimal performance, but has no information on the entire power system performance. Consequently, the entire power system is normally operated at a nonoptimal operating condition. In addition, the possible interactions between these local controllers might lead to adverse effects causing inappropriate control effort by different controllers. As a result, when severe disturbances or contingencies occur, these local controllers are not always able to guarantee stability [21]. Further, many of the power system stability and dynamic security computations are applicable only for offline analysis or not frequently enough to take advantage of the immediate information on the state and topology of the system [22]. The operator must therefore deal with a very complex situation and rely on heuristic solutions and policies.

On the other hand, because of the new constraints placed by economical and environmental factors, the trend in power system planning and operation is toward maximum utilization of existing electricity infrastructure, with tight system operating margins and less redundancy. In the mean time, addition of nonutility generators and independent power producers, increased penetration of new generation sources such as wind power, increased energy transactions over the grid, and an increasingly competitive

environment make the power system more complex to operate and to control, and, thus, more vulnerable to a disturbance.

During the past two decades, tremendous efforts have been made by power engineers and control researchers to improve power system stability. With the increased availability of advanced computer, communication and measurement technologies, and new paradigms such as fuzzy logic and neural networks, the development of adaptive system-wide monitoring and control is becoming feasible [21]-[24].

A WACC based on the wide-area measurements can be designed to coordinate the actions of the local controllers, in order to optimize some global performance measure function to achieve system-wide dynamic optimization and stability. The WACC could be used to adjust set points or reference values of the various local controllers to achieve certain optimal steady-state operating conditions. When a disturbance occurs, the WACC could guarantee that at each moment an optimal control action is taken and ensure that the power system returns to the desired operating point as fast as possible after the disturbance with a minimum control effort. Each local controller communicates with the WACC, reports to and receives coordination/control signals from the WACC, to help attain system-wide performance goals. Obviously, this multilevel hierarchical control structure provides an attractive solution for the system-wide disturbance problems.

However, designing the WACC needs some knowledge of the entire system dynamics. Because of the stochastic, nonlinear, and complex nature of the power system, it might be difficult to design the WACC based on the analysis of system models. Further, the WACC involves designing a real-time optimal control scheme in order to achieve certain optimal performance of the power system. For a large-scale complex system, the traditional mathematical tools may not be sufficient to design such a real-time optimal control algorithm.

1.4 Missing Sensor Measurements and Fault-Tolerant Control

The nonlinear plants in power systems are normally monitored and controlled based on a set of measurements, which are read directly from sensors, and a set of abstract mathematical variables calculated from these measurements. These two sets of data contain the plant inputs, outputs, and state variables which describe the status of the system. The control and operation of power systems depend on the availability and quality of these two sets of data.

However, measurements are inevitably subjected to faults caused by sensor failure, broken or bad connections, bad communication, or malfunction of some hardware or software, etc. If some sensors fail to provide the correct information, the controllers cannot provide the correct control behavior for the plant based on the faulty input data. As a result, the plant may have to be disconnected from the power system.

In a power system, there are many devices (e.g., FACTS devices) that play a crucial role in system regulation, control, and stability. For instance, the SSSC is typically placed in series on a critical transmission line of the power network for power flow control and power oscillation damping. Unexpected tripping of such an SSSC due to missing sensor measurements may result in overloading of some transmission lines and reduce the operating margin of the power system. If a severe disturbance occurs under such a condition, further contingencies may happen and the system may lose stability. To prevent such contingencies, fault-tolerance is an essential requirement for power system control and operation.

A fault-tolerant control system [25] should be able to mitigate the effects of the sensor faults to an acceptable level by detecting and restoring the missing sensor data. This will improve the reliability, maintainability and survivability of the power system. In principle, in order to achieve fault-tolerance, system redundancy is necessary. For many systems, certain degrees of redundancy are present among the data collected from various sensors. If the degree of redundancy is sufficiently high, the readings from one or more

missing sensors may be able to be accurately restored from the remaining healthy sensor readings.

1.5 Neural Networks and Adaptive Critic Designs

System characterization and identification are fundamental problems in the field of systems and controls [26]. The problem of characterization is concerned with the mathematical representation of a system; while the objective of system identification is to provide a time-dependent model approximating the behavior of a system. Classical approaches for system identification are carried out using a family of parameterized linear models, such as moving average (MA), autoregressive (AR), and/or their combination autoregressive moving average (ARMA) or with an exogenous (X) variable, e.g., autoregressive with an exogenous variable (ARX) or autoregressive moving average with an exogenous variable (ARMAX) to optimize a given figure of merit (e.g. a mean-squared error function) [27]. Because of its simplicity, a linear model does not always adequately approximate a generic nonlinear system throughout its entire working environment. Other difficulties increase when the model ruling the system is unknown; in this case, the system needs to be treated as a black-box model.

Neural networks, because of their intrinsic nonlinearity and computational simplicity, are natural candidates to approximate a given dynamic model for the representation of a nonlinear plant [26]. In fact, the nonlinear models obtainable with neural networks for system identification extend their linear counterparts; among them are the nonlinear AR (with an exogenous variable) [NAR(X)] and nonlinear ARMA (with an exogenous variable) [NARMA(X)] subfamilies. There are numerous types of neural networks proposed in the literature for function approximation. These include multilayer perceptron neural networks (MLPNNs), radial basis function neural networks (RBFNNs), recurrent neural networks (RNNs), etc [28].

Once the system dynamics are identified/modeled by a neural network (called the identifier or model network), it can be used to train another neural network (called the controller or action network) based on one time step ahead errors. The action network generates the control signals for the plant to achieve certain control objectives. This control architecture, called indirect adaptive neurocontrol, has been demonstrated to be superior over conventional linear control techniques for controlling complex nonlinear systems [26]. However, this particular neurocontrol architecture is short-sighted and normally results in a nonoptimal control. This shortcoming can be overcome by using adaptive critic designs (ACDs) [29], [30].

Adaptive critic designs are a neural network based optimization and control technique which solves the classical nonlinear optimal control problem by combining concepts of *approximate dynamic programming* and *reinforcement learning*. Dynamic programming may provide the best approach to design the optimal control for highly constrained nonlinear systems [31]. In dynamic programming, such an optimal control is obtained by solving the Bellman equation which optimizes some cost-to-go function J of the system, defined as

$$J(k) = \sum_{q=0}^{\infty} \gamma^q U(k+q) = \gamma J(k+1) + U(k) \tag{1.1}$$

where $U(\cdot)$ is the utility function (user-defined function) which represents the one-stage cost or performance measure function of the system at each time step, and γ is a discount factor for finite horizon problems ($0<\gamma<1$). Equation (1.1) describes the basic principle of dynamic programming: optimizing $J(\cdot)$ in the short term is equivalent to optimizing $U(\cdot)$ in the long term and vice versa. This principle can be explained in more details as follows. If $J(k)$ is optimal, then $J(k+1)$ and $U(k)$ are both optimal; if $J(k+1)$ is optimal, then $J(k+2)$ and $U(k+1)$ are both optimal; and so on. In other words, if $J(k)$ is optimal, then $U(n)$, for $n = k, k+1, \cdots, \infty$, are all optimal, and vice versa. Therefore, if a control action optimizes the

cost-to-go function $J(\cdot)$ at time step k, then it optimizes the utility function $U(\cdot)$ from time step k and onwards.

The conventional dynamic programming approaches require an accurate analytical model of the system, as well as knowledge of the system comprehensive dynamics known a priori to develop an appropriate cost function $J(\cdot)$. These however are normally unavailable for many complex nonlinear systems. Therefore, it is difficult to obtain an accurate solution (i.e., an optimal control) for such systems in dynamic programming. The ACD method provides an approach to find an approximate solution to dynamic programming.

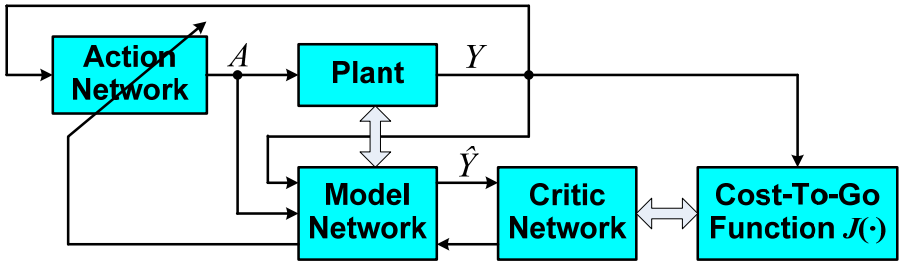

Figure 1.5: Schematic diagram of adaptive critic designs.

ACDs are capable of optimization over time under conditions of noise and uncertainty. For a given series of control actions that must be taken sequentially, and not knowing the effect of these actions until the end of the sequence, it is difficult to design an optimal controller using the traditional supervised learning artificial neural network (ANN). The ACD method determines optimal control laws for a system by successively adapting two ANNs, namely a *critic neural network* and an *action neural network*, as shown in Figure 1.5. The critic network learns to approximate the cost-to-go function $J(\cdot)$ in (1.1) or its derivatives and uses the outputs of the action network as one of its inputs, directly or indirectly; the action network provides the control actions for the plant. These two ANNs approximate the Hamilton-Jacobi-Bellman equation of optimal control theory.

In ACDs, a model network might be used to provide a dynamical model of the plant for training the critic and action networks.

Different types of critics have been proposed in the literature [29], [30]. A critic which approximates J is called the heuristic dynamic programming (HDP); one that approximates the derivatives of the function J with respect to its states, is called the dual heuristic programming (DHP); and a critic approximating both J and its derivatives is called the globalized DHP (GDHP). The ACD method determines optimal control laws for a system by successively adapting the critic and action networks. The adaptation process starts with a nonoptimal control by the action network; the critic network then guides the action network towards the optimal solution at each successive adaptation through reinforcement learning. This method punishes a bad control effort and rewards a good control effort based on the performance measured by the critic network. During the adaptations, neither of the networks needs any information of the desired control trajectory, only the desired cost needs to be known.

The use of ANNs to develop advanced neurocontrollers removes the need of a mathematical model for the nonlinear plant. The resulting nonlinear neurocontrollers can provide improved or optimized control performance over a wide system operating range.

1.6 Particle Swarm Optimization (PSO)

Particle swarm optimization [32]-[34] is a population based stochastic optimization technique. It searches for the optimal solution from a population of moving particles, based on a fitness or performance measure function. Each particle represents a potential solution and has a position (vector x_i) and a velocity (vector v_i) in the problem space. Each particle keeps track of its individual best position $x_{i,pbest}$, which is associated with the best fitness it has achieved so far, at any step in the solution. Moreover, the best position among all the particles obtained so far in the swarm is kept track of as x_{gbest}.

This information is shared by all particles. At each time instant k, a new velocity for particle i ($i = 1, 2, \cdots, N$) is updated by

$$v_i(k+1)=w\cdot v_i(k)+c_1\phi_1(x_{i,pbest}(k)-x_i(k))+c_2\phi_2(x_{gbest}(k)-x_i(k)) \tag{1.2}$$

where c_1 and c_2 are positive constants representing the weighting of the acceleration terms that guide each particle toward the individual best and the swarm best positions $x_{i,pbest}$ and x_{gbest}, respectively; ϕ_1 and ϕ_2 are uniformly distributed random numbers in [0, 1]; w is a positive inertia weight that controls a particle's exploration and exploitation capabilities during a search; N is the number of particles in the swarm. The first term in (1.2) enables each particle to perform a global search by exploring a new search space. The last two terms in (1.2) enable each particle to perform a local search around its individual best position $x_{i,pbest}$ and the swarm best position x_{gbest}. Based on the updated velocity, each particle changes its position according to the following equation.

$$x_i(k+1)=x_i(k)+v_i(k+1) \tag{1.3}$$

The final value of x_{gbest} is regarded as the optimal solution of the problem.

Unlike the traditional model-based optimization algorithms, e.g., Newton's method, the PSO algorithm does not need a mathematical model of the problem. The only information required by the PSO to search for the optimal solution is a performance measure function. Compared to other evolutionary computation algorithms, e.g., genetic algorithms, PSO has some attractive features including simple implementation, small computational load, and fast convergence. Therefore, it is fast and efficient to solve many complex problems for which it is difficult to find accurate mathematical models. In many cases, the PSO algorithm yields superior performance over the traditional model-based optimization algorithms and other evolutionary computation algorithms [35].

1.7 Problem Statement

The worldwide continued growth of wind power penetration and the trend to maximally utilize the existing electricity infrastructure have brought new challenges to power system operation, control, stability, and reliability. The use of FACTS devices can enhance the controllability of the ac transmission systems, and therefore, allow more efficient utilization of the existing infrastructure. The successful integration of WTGs into the power network often requires dedicated local FACTS devices to assist with voltage support. To achieve certain optimal operating performance and economical benefits, the control system of each individual power system component should be suitably designed.

The standard power system controllers are local noncoordinated linear controllers. They are designed around a specific operating point and therefore could not provide an acceptable performance over a wide system operating range. In addition, these local controllers only control some local quantities to achieve a local optimal performance, but have no information on the entire system performance. Consequently, the entire power system is normally operated at a nonoptimal operating condition. Further, the possible interactions among these local controllers might lead to adverse effects causing inappropriate control effort by different controllers. As a result, when severe system-wide disturbances or contingencies occur, these local linear controllers are not always able to guarantee stability. These problems can be overcome by using intelligent control techniques to design advanced nonlinear local decentralized or coordinating controllers with improved local dynamic performance and wide-area coordinating controllers to achieve some system-wide control objectives.

Further, any automatically controlled system is inevitably subjected to faults such as missing sensor measurements. These faults may result in the failure of the power system controllers and consequently severe contingencies in the power system. To avoid such contingencies and improve the system reliability, maintainability and survivability, fault-tolerance is an essential requirement for system control and operation.

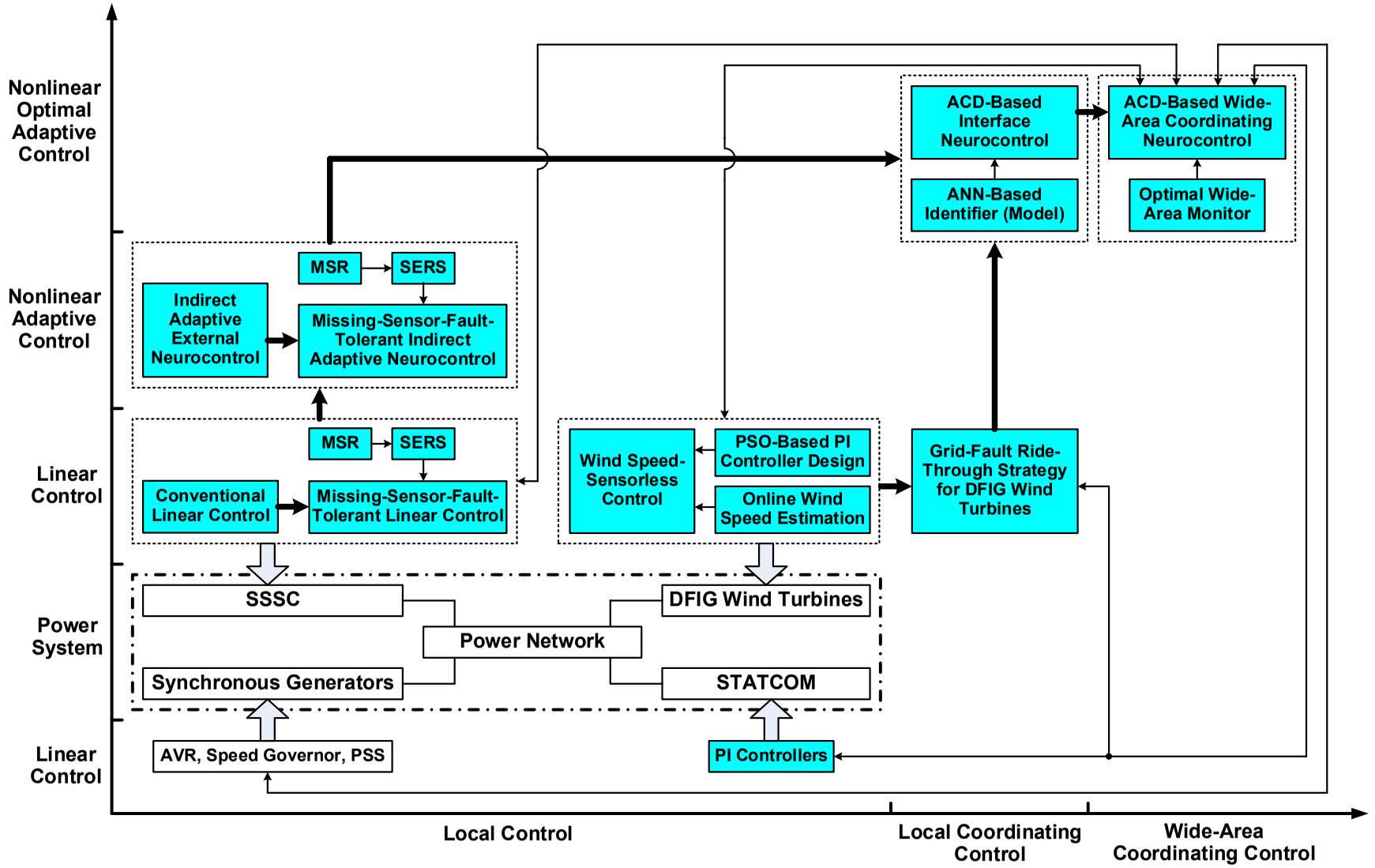

Figure 1.6: Outline of the dissertation.

This work focuses on the development of advanced intelligent control systems to improve the stability, reliability, and dynamic performance of the power systems which include wind power generation and FACTS devices. Figure 1.6 outlines the dissertation. The key issues to be investigated include:

- Developing intelligent indirect adaptive internal and external control schemes for the SSSC FACTS device using ANNs;
- Developing an intelligent missing sensor restoration (MSR) algorithm using an autoassociative neural network and a PSO;
- Based on the MSR algorithm, developing an intelligent online sensor evaluation and (missing sensor) restoration scheme (SERS) to provide fault-tolerant sensor measurements for the SSSC controllers;
- Based on the SERS, developing intelligent missing-sensor-fault-tolerant linear control and missing-sensor-fault-tolerant indirect adaptive neurocontrol schemes for the SSSC FACTS device to improve the reliability, maintainability and survivability of the SSSC and the power network;
- Developing a Gaussian radial basis function network (GRBFN)-based online wind speed estimation algorithm for WTGs, which removes the need for mechanical sensors to measure wind speeds;
- Based on the GRBFN-based wind speed estimation algorithm, developing a wind speed-sensorless output maximization control for the DFIG wind turbines, which reduces the cost and improves the reliability of the WTG systems;
- Developing a particle swarm optimization (PSO)-based intelligent approach to design the optimal parameters of the proportional integral (PI)-type controllers used by the RSC of the DFIGs, which improves the dynamic and transient performance of the DFIG wind turbines;

- Investigating the application of the STATCOM to enhance the grid fault ride-through capability of the DFIG wind turbines;
- Developing a heuristic dynamic programming (HDP)-based nonlinear adaptive interface neurocontroller to provide the optimal coordinated reactive power control for a wind farm (equipped with DFIG wind turbines) and a STATCOM;
- Developing a wide-area monitor and coordinating control strategy for a power system which includes wind power generation and multiple FACTS devices. It coordinates the local linear controllers used by the synchronous generators, DFIG wind turbines, SSSC and STATCOM to improve the system-wide dynamic performance and stability of the power system. Based on PSO, radial basis function neural networks (RBFNNs), and dual heuristic programming (DHP), this wide-area control strategy is a nonlinear optimal adaptive control and takes into account the effect of delays involved in transmitting the remote wide-area signals.

The proposed control schemes and design approaches are verified by simulation studies, experimental studies, as well as real-time implementations using Real Time Digital Simulator (RTDS) and TMS320C6701 Digital Signal Processor (DSP) Platform.

1.8 Dissertation Outline

A comprehensive literature review on existing techniques related to this work is summarized in Chapter 2. An indirect adaptive neurocontroller using the RBFNNs are developed in Chapter 3, for the external damping control of an SSSC. In Chapter 4, an SERS is proposed for online sensor evaluation and missing sensor restoration. Based on the SERS, a fault-tolerant indirect adaptive neurocontrol (FTIANC) strategy is then developed for missing-sensor-fault-tolerant control of an SSSC FACTS device. Chapter 5 proposes a comprehensive MSFTC strategy for real-time control of the SSSC FACTS device. This MSFTC is validated by real-time implementation results on an SSSC connected to the IEEE 10-machine 39-bus power system using a RTDS and

TMS320C6701 DSP Platform. In Chapter 6, a wind speed estimation based sensorless output maximization control scheme is developed for controlling the DFIG wind turbines. Chapter 7 proposes a PSO-based intelligent approach to design the optimal PI controllers used by the RSC of the DFIG wind turbines. The application of a STATCOM to achieve the uninterrupted operation of the DFIG wind turbines is investigated in Chapter 8 by real-time implementations using a RTDS. Chapter 9 proposes a HDP-based nonlinear adaptive interface neurocontroller (INC) for the optimal coordinated reactive power control of a wind farm and a STATCOM. In Chapter 10, a wide-area measurements based nonlinear optimal adaptive wide-area coordinating neurocontroller (WACNC) is proposed for controlling a power system with wind power generation and multiple FACTS devices, while considering the effect of signal transmission delays. Finally, Chapter 11 summarizes the concluding remarks and contributions of the dissertation, and gives some recommendations for further study.

CHAPTER 2

SUMMARY OF PREVIOUS WORK

This chapter briefly reviews the previous related work done by others. The topics to be covered include: 1) control and operation of SSSC FACTS devices, 2) modeling, control, and grid integration of the DFIG wind turbines, 3) local and wide-area coordinating control of multiple devices in a power system, and 4) missing sensor restoration and fault-tolerant control.

2.1 Internal and External Control of the SSSC

Conventional control schemes for an SSSC are based on linear control techniques [12]-[15], [36]-[38]. By extending the original work of Ooi *et al* [12] for an SSSC based on a voltage source PWM converter, Rigby and Harley [13] reported an improved internal control scheme for the SSSC. Based on this work, they also proposed a power oscillation damping scheme by applying a suitably designed conventional external linear controller (CONVEC) to the SSSC [14]. The work in [13] and [14] is briefly summarized as follows.

Figure 2.1 shows an SSCC with its internal and external linear controllers connected to a single machine infinite bus (SMIB) power system. The three three-phase transmission lines represent the different loops between the sending-end bus and the infinite bus at the receiving end. The SSSC is modeled as a sinusoidal PWM controlled GTO converter with a dc-link capacitor, which is connected in series at the receiving end of line 3 through a series injection transformer.

The schematic diagram of the internal control scheme for the SSSC is shown in Figure 2.2. The main objective of this internal control scheme is to inject a controllable voltage (by injecting a desired compensating reactance X_C^*) at the ac terminals of the

inverter which remains in quadrature with the transmission line current, as well as to keep the dc terminal voltage of the inverter constant at steady state.

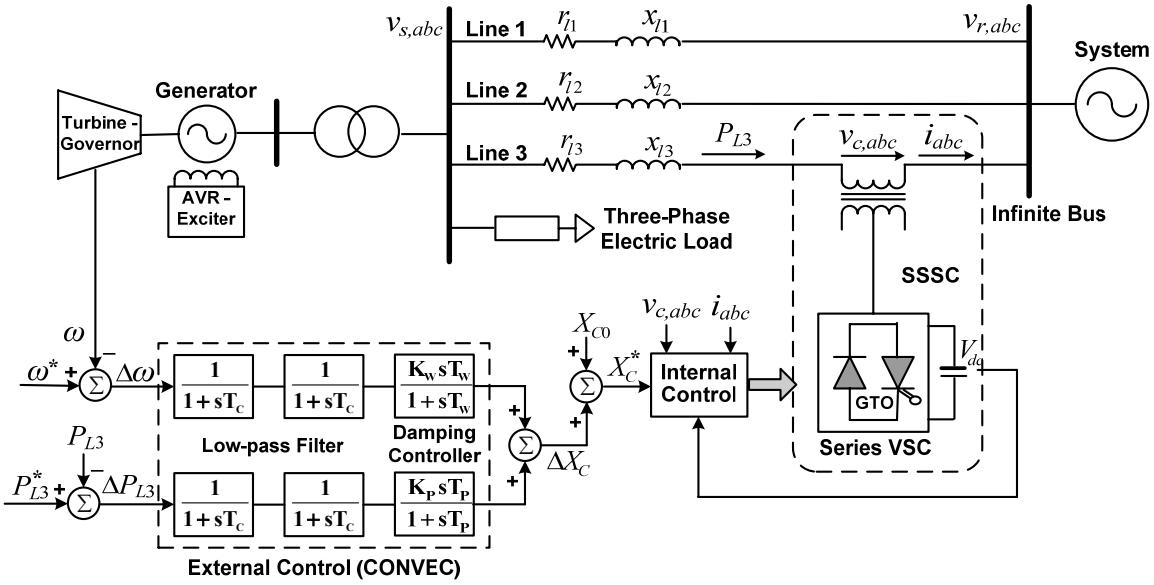

Figure 2.1: An SSSC with its internal and external linear controllers connected to an SMIB power system.

In Figure 2.2, the instantaneous three-phase currents of line 3, i_{abc}, are sampled and transformed into *d-q* components i_d and i_q by applying the synchronously rotating reference frame transformation [109]. The peak magnitude of the current vector, $\sqrt{i_d^2 + i_q^2}$, is multiplied by the desired value of compensating reactance X_C^* to determine the modulation index m_i.

The internal control scheme of the SSSC consists of an inner power control loop as well as an outer voltage control loop. The dc terminal voltage V_{dc} is fed back and compared with the reference value V_{dc}^* to generate the voltage error ε_V in the outer loop, which is passed through a proportional gain K_{VP} to form the commanded power P^*. The instantaneous real power P_i at the ac terminal of the inverter is fed back and subtracted

from the commanded power P^* to form the error ε_P in the inner loop, which is then converted into an equivalent error ε_θ in commanded phase angle of the injected voltage vector. The power to angle conversion in the inner loop ensures that the dynamics of the voltage regulator are not dependent on the amount of power transmitted by the transmission line. Finally, the error ε_θ is passed through a PI compensator to generate the commanded phase angle α for the PWM converter.

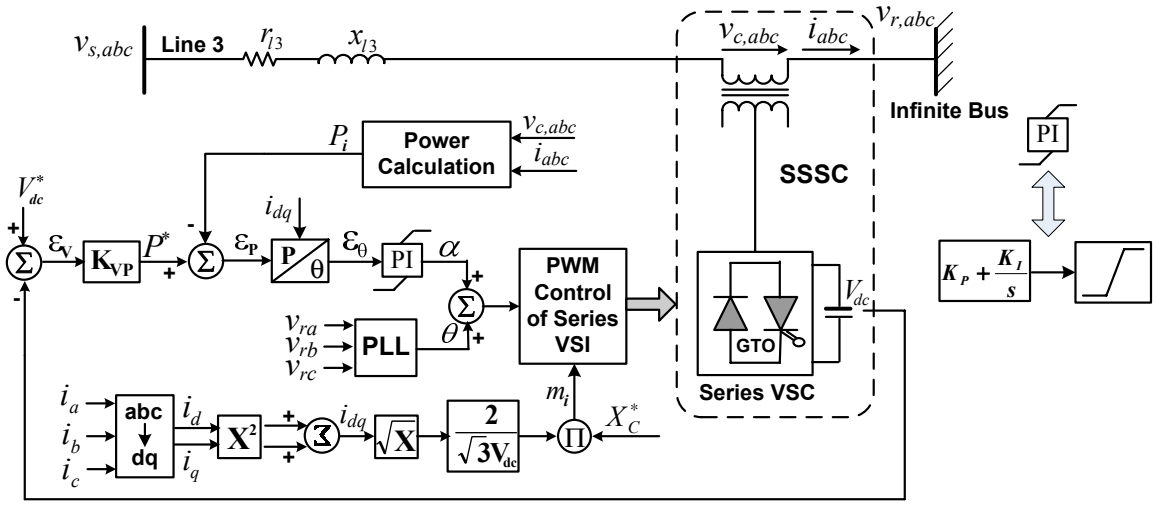

Figure 2.2: Schematic diagram of the internal control scheme for the SSSC.

The objective of the CONVEC (Figure 2.1) is to damp the transient power oscillations of the system. This external controller is able to rapidly change the compensating reactance X_C injected by the SSSC, thus providing a supplementary damping during transient power swings [14].

It was reported in [39] that the speed deviation $\Delta\omega$ of a generator can be used to produce the supplementary control signal ΔX_C from the external control. In Figure 2.1, the transmitted active power deviation ΔP_{L3} by line 3 is also used as the input of the CONVEC, which can provide the CONVEC with more damping ability compared to the case in which only $\Delta\omega$ is used as the input of the CONVEC [40], [41]. Moreover, this

design could be useful for the study of supervisory level control in a large-scale power system.

In Figure 2.1, the deviation signals $\Delta\omega$ from the synchronous generator and ΔP_{L3} from line 3 are passed through two first-order low-pass filters and a damping controller (consisting of a proportional gain and a washout filter) to form a supplementary control signal ΔX_C, which is then added to a steady-state fixed set-point value X_{C0} to form the total commanded value of the compensating reactance X_C^* at the input of the internal control for the SSSC. The washout filter is a high-pass filter that removes the dc offset, and without it the steady changes and/or dc offsets in active power P_{L3} and/or speed ω would modify the value of compensating reactance. The use of two low-pass filters is based on two reasons: 1) filtering the electrical noise in the measurements; 2) phase compensation to ensure that the variations in compensating reactance are correctly phased with respect to the transient power oscillations in order to provide supplementary damping.

If an SSSC is equipped with an energy storage system [15] or is located as the series branch of an UPFC [36]-[38], a *P*-*Q* decoupled control scheme can be developed to achieve independent active and reactive power flow control. This is the most powerful operating mode of the SSSC.

However, any linear controllers are only designed around a specific operating point, and a shortcoming is that their performance degrades at other operating points. Because of the wide operating range of the power system, when a severe disturbance or contingency occurs, the linear controllers may not be able to guarantee stability [42].

To overcome the shortcoming of linear controllers, Park *et al* [40] proposed to use a nonlinear neurocontroller, which was designed by utilizing the MLPNN and the ACD technique, as an alternative to the CONVEC for the SSSC. This external neurocontroller has an improved damping capability. However, it has been reported that the RBFNN has some advantages over the MLPNN with regard to training and locality of

approximations, thereby making the RBFNN an attractive alternative for designing nonlinear adaptive neurocontrollers [43]-[45].

2.2 Modeling, Control, and Grid Integration of DFIG Wind Turbines

Much research effort has gone into modeling, control, and grid integration of the DFIG wind turbines, as well as studying their impact on the dynamic performance and stability of the associated power system [2]-[5], [16], [17], [46]-[53]. The basic configuration of a DFIG wind turbine is shown in Figure 1.3. It consists of a wind turbine, a DFIG (with a VFC), and a mechanical shaft system connected between them.

2.2.1 Wind Turbine Aerodynamic Model

The aerodynamic model of a wind turbine can be characterized by the well-known C_P-λ-β curves. C_P is the power coefficient, which is a function of both tip-speed-ratio λ and the blade pitch angle β. The tip-speed-ratio λ is defined by

$$\lambda = \frac{\omega_t R}{v_w} \tag{2.1}$$

where R is the blade length in m, ω_t is the wind turbine rotor speed in rad/s, and v_w is the wind speed in m/s. The C_P-λ-β curves depend on the blade design and are given by the wind turbine manufacturer. For instance, the mathematical representation of the C_P curves used for a 3.6 MW wind turbine is obtained by curve fitting, given by [55]:

$$C_P(\beta, \lambda) = \sum_{i=0}^{4} \sum_{j=0}^{4} \alpha_{ij} \beta^i \lambda^j \tag{2.2}$$

where the coefficients α_{ij} are given in Table 4-7 of [55]. The resulting C_P curves (as functions of λ with β as a parameter) are shown in Figure 2.3. The curve fit is a good approximation for values of $2 < \lambda < 13$. Values of λ outside this range represent very high and low wind speeds, respectively, that are outside the continuous rating of the machine.

Given the power coefficient C_P, the mechanical power that the wind turbine extracts from the wind is calculated by [2]:

$$P_m = \frac{1}{2}\rho A_r v_w^3 C_P(\lambda, \beta) = f(v_w, \omega_t, \beta) \tag{2.3}$$

where ρ is the air density in kg/m^3, $A_r = \pi R^2$ is the area swept by the rotor blades in m^2. At a specific wind speed, there is a unique wind turbine rotational speed to achieve the maximum power coefficient, C_{Pm}, and thereby extract the maximum mechanical (wind) power. If the wind speed is below the rated value, the wind turbine operates in the variable-speed mode, and the rotational speed is adjusted such that C_P remains at the C_{Pm} point. In this operating mode, the wind turbine pitch control is deactivated. However, if the wind speed increases above the rated value, the pitch control is activated to increase the wind turbine pitch angle to reduce the mechanical power extracted from wind.

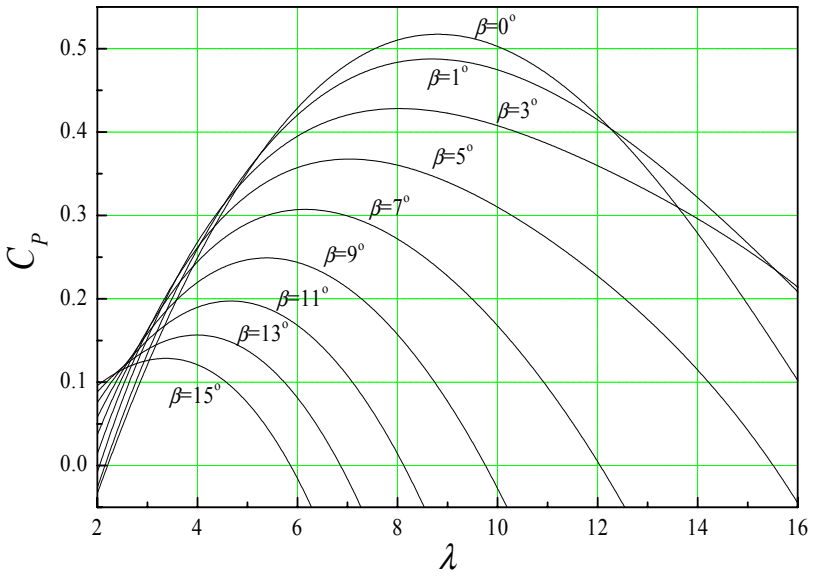

Figure 2.3: C_P-λ-β curves of a 3.6 MW wind turbine.

2.2.2 Modeling of the Shaft System

The shaft system of the DFIG wind turbine can be represented either by a two-mass system or by a single lumped-mass system [2], [46], [55]. In [2], [4], [46], [47], [49], [52], [55], the shaft system is simply modeled as a single lumped-mass system with the lumped inertia constant H_m, calculated by

$$H_m = H_t + H_g \tag{2.4}$$

where H_t and H_g are the inertia constants in seconds of the turbine and the generator, respectively. The electromechanical dynamic equation in the per-unit system as described in Appendix H is then given by

$$2H_m \frac{d\omega_m}{dt} = T_m - T_e - D_m\omega_m \tag{2.5}$$

where T_m and T_e are the mechanical torque in pu applied to the turbine and the electromagnetic torque of the generator, respectively; ω_m is the rotational speed in pu of the lumped-mass system; D_m is the damping coefficient in pu of the lumped system.

However, in transient studies of wind turbines and the power network, the two-mass model should be used because of a possible risk of the torsional oscillations of the wind turbines and the electrical quantities [1], [46]. In the two-mass model [1], [46], [55], separate masses are used to represent the low-speed turbine and the high-speed generator, and the connecting resilient shaft is modeled as a spring and a damper. According to the shaft system representation in Figure 2.4, in the per-unit system (see Appendix H), the electromechanical dynamic equations are then given by

$$2H_t \frac{d\omega_t}{dt} = T_m - D_t\omega_t - D_{tg}(\omega_t - \omega_r) - T_{tg} \tag{2.6}$$

$$2H_g \frac{d\omega_r}{dt} = T_{tg} + D_{tg}(\omega_t - \omega_r) - D_g\omega_r - T_e \tag{2.7}$$

$$\frac{dT_{tg}}{dt} = K_{tg}(\omega_t - \omega_r) \tag{2.8}$$

where ω_t and ω_r are the turbine and generator rotor speed in pu, respectively; T_{tg} is an internal torque in pu of the model; H_t and H_g are the inertia constants in seconds of the turbine and the generator, respectively; D_t and D_g are the damping coefficients in pu of the turbine and the generator, respectively; D_{tg} is the damping coefficient in pu of the flexible coupling (shaft) between the two masses; K_{tg} is the shaft stiffness in pu. In Figure 2.4, N_t/N_g is the gear ratio of the gearbox.

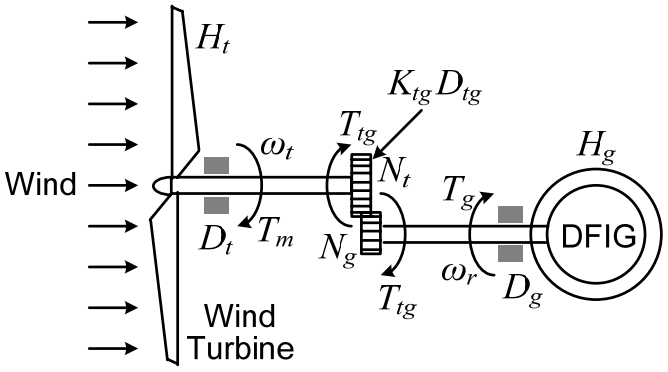

Figure 2.4: DFIG wind turbine shaft system representation.

2.2.3 Modeling of the DFIG

The dynamic equation of a three-phase DFIG can be written as follows in a synchronously rotating *d-q* reference frame [56]:

$$v_{ds} = r_s i_{ds} - \omega_s \lambda_{qs} + \frac{d\lambda_{ds}}{dt} \tag{2.9}$$

$$v_{qs} = r_s i_{qs} + \omega_s \lambda_{ds} + \frac{d\lambda_{qs}}{dt} \tag{2.10}$$

$$v_{dr} = r_r i_{dr} - s\omega_s \lambda_{qr} + \frac{d\lambda_{dr}}{dt} \tag{2.11}$$

$$v_{qr} = r_r i_{qr} + s\omega_s \lambda_{dr} + \frac{d\lambda_{qr}}{dt} \tag{2.12}$$

where ω_s is the rotational speed of the synchronous reference frame, $s\omega_s = \omega_s - \omega_r$ is the slip frequency, and the flux linkages are given by

$$\lambda_{ds} = L_{ls} i_{ds} + L_m (i_{ds} + i_{dr}) = L_s i_{ds} + L_m i_{dr} \tag{2.13}$$

$$\lambda_{qs} = L_{ls} i_{qs} + L_m (i_{qs} + i_{qr}) = L_s i_{qs} + L_m i_{qr} \tag{2.14}$$

$$\lambda_{dr} = L_{lr} i_{dr} + L_m (i_{ds} + i_{dr}) = L_m i_{ds} + L_r i_{dr} \tag{2.15}$$

$$\lambda_{qr} = L_{lr} i_{qr} + L_m (i_{qs} + i_{qr}) = L_m i_{qs} + L_r i_{qr} \tag{2.16}$$

where $L_s = L_{ls} + L_m$; $L_r = L_{lr} + L_m$; L_{ls}, L_{lr} and L_m are the stator leakage, rotor leakage, and mutual inductances, respectively. The electromagnetic torque of the DFIG is calculated by

$$T_e = \frac{3}{2}\frac{p}{2}L_m(i_{qs}i_{dr} - i_{ds}i_{qr}) \tag{2.17}$$

where p is the number of poles of the induction machine. Neglecting the power losses associated with the stator resistances, the active and reactive stator powers are given by

$$P_s = \frac{3}{2}(v_{ds}i_{ds} + v_{qs}i_{qs}) \tag{2.18}$$

$$Q_s = \frac{3}{2}(v_{qs}i_{ds} - v_{ds}i_{qs}) \tag{2.19}$$

and the active and reactive rotor (slip) powers are given by

$$P_r = \frac{3}{2}(v_{dr}i_{dr} + v_{qr}i_{qr}) \tag{2.20}$$

$$Q_r = \frac{3}{2}(v_{qr}i_{dr} - v_{dr}i_{qr}) \tag{2.21}$$

2.2.4 Control of the DFIG Wind Turbine

By adjusting the shaft speed optimally, the variable-speed WTGs can achieve the maximum wind power generation at various wind speeds within the operating range. To implement maximum wind power extraction, most controller designs of the variable-speed WTGs employ anemometers to measure wind speed in order to derive the desired optimal shaft speed for adjusting the generator speed. In most cases, a number of anemometers are placed surrounding the wind turbine at some distance to provide adequate wind speed information. These mechanical sensors increase the cost (e.g., equipment and maintenance costs) and reduce the reliability of the overall WTG system [57].

Recently, mechanical sensorless maximum power point tracking (MPPT) controls have been reported in [57]-[60], in which the wind speed is estimated [57]-[59] for MPPT, or the maximum power point is determined without the need of the wind speed information [60]. For instance, Bhowmik *et al*. [58] use a polynomial to approximate the wind turbine power coefficient; based on the estimated turbine mechanical power, the wind speed is then estimated online by calculating the roots of the polynomial using an iterative algorithm (e.g., Newton's method or bisection method). However, this method neither accurately estimates the power losses nor takes into account the dynamics of the WTG system. Therefore, it does not provide an accurate estimate of the turbine mechanical power from the measured WTG output electrical power. In addition, real-time calculation of the polynomial roots may result in a complex and time-consuming calculation, therefore, reducing system performance.

In [59], Tan and Islam propose using an autoregressive statistical model to predict the wind speed from the historical data. This method however may result in a complex computation and the predicted wind speed is not accurate for online MPPT control.

In MPPT control of the variable-speed WTGs, the maximum power point is commonly determined online from the WTG power-speed curves using a lookup table based mapping [57]. If the mechanical output power from the wind turbine is known, this lookup table in turn can be used to estimate the wind speed. However, to obtain an accurate wind speed estimation and MPPT, this method requires significant memory space and may result in a time-consuming search for the solution.

In [60], the MPPT is achieved by a fuzzy-logic-based control. For a particular wind speed, the fuzzy control adaptively performs an incremental/decremental search for the WTG shaft speed along the direct to increase the output wind power, until the system settles down at the maximum output power condition. However, if the wind speed changes significantly from moment to moment, this method may require a long searching time to locate the maximum power point.

ANNs are well known as a tool to implement nonlinear time-varying input-output mapping. To overcome the drawbacks of the methods in [58]-[59], Li *et al*. [57] propose a MLPNN-based wind speed estimation method for a direct-drive small WTG system. This method provides a fast and smooth wind speed estimation from the measured generator electrical power. However, it is based on a lumped-mass shaft model and does not take into account the power losses of the WTG. For a WTG with a gearbox, such as the DFIG wind turbine, this method could not accurately estimate the wind speed because of the nonnegligible power losses and the complex shaft system dynamics of the WTG.

The control system of a DFIG wind turbine generally consists of two parts: the electrical control of the DFIG and the mechanical control of the wind turbine blade pitch angle. Control of the DFIG is achieved by control of the VFC, which includes control of the RSC and control of the GSC Figure 1.3. Due to their simple structures, conventional linear (e.g., PI or PID) controllers are still the most commonly used techniques to control the DFIG wind turbines. Unfortunately, tuning PI/PID controllers is tedious and it might be difficult to tune the PI/PID gains optimally due to the nonlinearity and the high complexity of the system. Over the years, heuristic search based algorithms such as genetic algorithms (GAs), tabu search algorithm, and simulated annealing have been used for linear controller design [61]-[63]. However, when the parameters being optimized are highly correlated, the performance of these heuristic search algorithms degrades [64].

Recently, a new PSO-based technique has been successfully used for single- and multi-objective nonlinear optimization. The use of PSO to design a single PID controller in the AVR system of a conventional turbo generator has been reported in [66].

2.2.5 Grid Integration and Fault Ride Through of the DFIG Wind Turbines

In a DFIG wind turbine, the VFC and its power electronics (IGBT-switches) are the most sensitive part when subjected to transient disturbances in the power network. As a result of such disturbances, the RSC of the DFIG may have to be blocked (it stops

switching and trips) by a crow-bar circuit in order to protect it from over-current in the rotor circuit [2]-[5]; and the WTG might be tripped from the system to prevent further contingencies. Therefore, one of the key issues related to the operation of the DFIG wind turbines is the grid fault or low-voltage ride-through capability.

One solution to enhance the grid fault ride-through capability of the DFIG wind turbines is to improve the control scheme of the RSC. In [65], the authors proposed an improved dc-link voltage control strategy for a DFIG wind turbine. It reduced the magnitude of dc-link voltage fluctuations during grid faults. However, the issues of rotor current transients, which are a major factor on the operation of a DFIG wind turbine during grid faults, were not investigated. A nonlinear controller and a fuzzy controller have been proposed in [19] and [67], respectively, for controlling the RSC. Compared with the conventional linear control schemes, these control schemes reduce the over-current in the rotor circuit during grid faults. However, in a weak power network, there can be a risk of voltage instability which may result in the tripping of WTGs [2].

In [2], the author proposed an uninterrupted operation feature of a DFIG wind turbine during grid faults. In this feature, the rotor circuit is short-circuited through a crow-bar circuit (an external resistor); the generator becomes a conventional SCIG and starts to absorb reactive power. The WTG continues its operation to produce some active power and the GSC can be set to control the reactive power and voltage. The pitch angle controller might be activated to prevent the WTG from fatal over-speeding. When the fault has been cleared and when the voltage and the frequency in the power network have been reestablished, the RSC restarts and the WTG returns to normal operation. In this uninterrupted operation feature, voltage stability is a crucial issue. However, many WTGs are installed in remote, rural areas which usually have electrically weak power grids. In such grid conditions and during a grid fault, the GSC cannot provide sufficient reactive power and voltage support due to its small power capacity. Without any external dynamic reactive compensation, there can be a risk of voltage instability in the power

grid. As a result, the RSC will not restart and the WTG will be immediately disconnected from the grid, and reconnected when normal operation has been restored. This is possible, as long as wind power penetration remains low. However, with the rapid increase in penetration of wind power in power systems, tripping of many WTGs in a large wind farm during grid faults may begin to influence the overall power system stability. Therefore, it will become necessary to require WTGs to support the network voltage and frequency not only during steady-state conditions but also during grid disturbances.

In [68], the authors proposed two secondary voltage control schemes and a reactive power allocation strategy for a wind farm equipped with DFIG wind turbines. These control strategies improved voltage regulation performance of the wind farm. However, this supervisory voltage control capability of the wind farm is limited due to the small power ratings of the DFIG converters. In a weak power network, the WTGs may not be able to provide sufficient voltage control capability.

In order to meet power factor requirement (e.g., -0.95~0.95) at the PCC, most wind farms are equipped with switched shunt capacitors for static reactive compensation [2], [69]. Moreover, since many WTGs are connected to electrically weak power grids, the successful integration of WTGs will require local shunt FACTS devices, such as a static var compensator (SVC) and a STATCOM, to provide rapid and smooth steady-state and transient reactive compensation and voltage control [20]. The applications of a SVC or a STATCOM to a wind farm equipped with SCIGs have been reported in [70] for steady-state voltage regulation, and in [2], [71] for short-term transient voltage stability. However, in a weak power network which includes wind farms equipped with DFIG wind turbines, dynamic reactive compensations are also important to assist the WTGs to ride through grid faults. Further, it is necessary to coordinate the different control actions between the wind farms and the local shunt FACTS devices in order to achieve some optimal control and economical performance.

2.3 Wide-Area Coordinating Control

Real-time wide-area monitoring and coordinating control is becoming an important issue in the power industry. With the increased availability of advanced computer, communication and measurement technologies [e.g., phasor measurement units (PMUs) based on a global positioning satellite (GPS) system] [72], the development of WACC is becoming feasible. By employing the GPS synchronized PMUs, it is possible to deliver remote synchronized real-time signals to the control center at a speed of as high as 60 Hz sampling rate [72]. This sampling rate is high enough for damping control of the typical power system oscillating modes.

Reference [22] looks into the future state of power system operations and control based on a number of assumptions and provides an analysis of the direction that this area might take over the next 25 years. Issues related to development of techniques and requirements for fully coordinated, high-bandwidth, and robust controls for power system are discussed, and some methodologies are suggested. Proceeding toward this ultimate goal, system-wide automatic voltage control, system-wide automatic power control, and integrated system-wide automatic control concepts are introduced for coordination of shunt and series controllers for both active and reactive power.

2.3.1 Coordinating Control Based on Linear Control and Optimization

Various approaches have been addressed in the literature for coordinating the control action of different devices (e.g., synchronous generators, FACTS devices, etc.) in power systems. The first category of the coordinating control schemes is based on the linear design.

In [73], a simple linear controller based on the application of projective controls is designed to damp inter-area oscillations. The controller coordinates the control action of a thyristor controlled series capacitor (TCSC) and a thyristor controlled phase angle regulator (TCPAR) to allow for increased power transfers with improved system

damping. In [74], a method is developed for the simultaneous coordination of PSSs and FACTS device stabilizers in order to enhance the damping of the rotor modes oscillation in a multimachine system. The proposed coordination scheme is based on linear programming. However, because eigenanalysis using the QR algorithm [75] is required, the computational cost is high for large-scale systems.

In [76] and [77], the authors propose a coordinated linear optimal control using a hierarchical structure. The local-level controllers operate independently in parallel and handle the parameters according to operating conditions to ensure linear optimal control for the local system. The complementary control signals are generated at a global-level for ensuring the local system to be decoupled. By coordinating the local controllers globally, the proposed controller is effective in damping the inter-area oscillations in the system. However, it could not guarantee global optimality conditions.

Since the coordination schemes in [73]-[77] are based on small disturbance analysis that requires linearization of the system involved, they cannot properly capture complex dynamics of the system, especially during critical disturbances. To overcome the shortcomings of the linear design methods, nonlinear control and optimization techniques have been employed by some researchers to design the coordinating controllers.

2.3.2 Coordinating Control Based on Nonlinear Control and Optimization

The coordinating controls of generator excitation and different FACTS devices [TCSC, STATCOM, UPFC and thyristor controlled phase shifter (TCPS)] are proposed in [78]-[81] to enhance the transient stability, damping and voltage regulation of power systems. The feedback linearization technique is used to design these coordinating controllers. The influence of the uncertainties, caused by parameter variations and the inclusion of FACTS devices, is eliminated by applying robust nonlinear control theory.

The resulting coordinating controllers only use local measurements and are independent of the operating point.

Liu *et al* [82] propose an adaptive nonlinear coordinated excitation and STATCOM controller based on a robust L_2-gain control technique and Hamiltonian structure. It enhances the transient stability and voltage regulation of the overall system, regardless of different operating conditions.

Reference [23] proposes a decentralized/hierarchical structure to design the PSS with a supplementary input from remote PMUs. In this design, a remote/global feedback loop is built on top of the existing decentralized control system for each PSS. Both global and local control loops use linear controllers. Observability and controllability concepts are used to select the optimal signal to be measured and the appropriate location for the PSS, hence reducing the complexity of the system. A sequential nonlinear optimization procedure is used to tune the global and local control loops of the proposed controller.

Reference [24] proposes a wide-area control scheme based on a multiagent concept [83] for the PSSs. In the proposed multiagent damping controller structure, local PSSs (LPSSs) are installed in the system and tuned for damping local oscillation modes. They are represented as local agents, which are placed at the selected generator excitation loops and remain in the same location throughout their working lives. A supervisory level PSS (SPSS) using wide-area measurements is designed and operates as a global software agent. H_∞ controllers using selected wide-area measurements are embedded into the SPSS control loop to accommodate power system nonlinear dynamics and model uncertainties. The SPSS contains a fuzzy logic controller switch to select the appropriate robust controller (i.e., H_∞ controller) for the corresponding system operating condition. The coordination of the robust SPSSs and local PSSs is implemented based on the principles of multiagent system theory.

Despite the relative good performance of the wide-area control schemes in [23] and [24], they remain limited since the multivariable and nonlinear characteristics of the power system are not taken into account explicitly.

A two-level hierarchical controller based on wide-area measurements is proposed [21] to improve the stability of multimachine power systems. The solution consists of a local controller for each generator at the first level helped by a multivariable central controller at the secondary level. The secondary-level controller uses remote signals from all generators to synthesize decoupling control signals that improve the local controllers' performances. The first-level controllers, on the other hand, use only local signals to damp local oscillations. The wide-area signals based central controller is robust and combines a nonlinear decoupling control derived from the input-output linearization method with an adaptation algorithm. The latter continuously adapts controller parameters during a change in operating conditions or structure, thus considerably increasing the controller robustness.

In [84], the authors propose a supervisory controller for FACTS devices based on optimal power flow with multiple objectives in order to avoid congestion, provide secure transmission and minimize active power losses. However, this coordinating control scheme does not address the issues of system dynamic performance or transient stability.

The design of conventional nonlinear controllers requires an accurate system model and some knowledge of system parameters. Compared to linear controllers, they can provide good control capability over a wider operating range. However, they generally have sophisticated structures, complex control laws, and therefore, require much control effort and might be difficult for real-time implementation.

2.3.3 Some Issues and Challenges in Designing Wide-Area Coordinating Control

An unavoidable problem for designing a WACC is the delay involved between the instant of measurement and that of the signal being available to the controller. This

delay can typically be in the range of 0.01-1.0s [72], [85] depending on the signal transmission hardware, distance, protocol of transmission, etc. As the delay might be comparable to the time periods of some critical oscillating modes, it should be considered in the design of the WACC to ensure satisfactory control performance.

Moreover, designing the WACC needs knowledge of the entire power system dynamics to be available to the designers. Due to the large-scale, nonlinear, stochastic, and complex nature of power systems, the traditional mathematical tools and control techniques are not sufficient to design such a WACC. This problem can be overcome by using ANNs and ACDs based intelligent nonlinear optimal control techniques.

Finally, the existing designs of local or wide-area coordinating control algorithms are focused on conventional power systems with PSSs and/or FACTS devices. However, the coordinating control for the power systems with the penetration of renewable energy sources, i.e., wind power, has not yet been reported.

2.4 Missing Sensor Restoration

State estimation is commonly used to identify state variables that are not accessible for direct measurements [86], and could therefore be modified to restore missing sensor data. This technique is based on the analysis of a system model and the redundancy of system state variables. By deriving closed-form solutions for the variables corresponding to the missing sensors, the lost data are explicitly derived from the remaining available data. However for many systems, this model-based method converges slowly and the closed-form solutions can be unfeasible. Moreover, accurate system models are usually unavailable in real system applications.

The use of autoassociative neural networks (auto-encoder) [87]-[89] provides an alternative approach for missing sensor restoration. The auto-encoder is a feedforward multilayer neural network with a butterfly structure. It is trained to perform an identity mapping, where the network inputs are reproduced at the output layer. The network

contains a hidden "bottleneck" layer which has fewer nodes than the input and output layers. The dimensionality reduction through the input-to-hidden layer enables the network to extract significant features in data, without restriction on the character of the nonlinearities in the data (nonlinear feature extraction). Hence, the hidden layer captures the correlations between all input data. On the other hand, the dimensionality expansion through the hidden-to-output layer enables the network to reproduce the high dimensional inputs at the output layer. If one or more input data are missing, then the outputs of the auto-encoder cannot match its inputs. In this case, the correlations between the input data established by the auto-encoder can be used by some search algorithms to search for the optimal estimates of the missing data until an acceptable match between the input and output data is achieved.

Based on an auto-encoder, a missing sensor restoration (MSR) algorithm, as shown in Figure 2.5, has been designed in [87] to restore missing sensor data, which are constant values at steady state. However, the MSR relies on an external sensor evaluation scheme [87] to evaluate the integrity of sensor data and to detect which sensor or sensors are missing. Moreover, [87] does not explain how to design and implement such a sensor evaluation scheme, and does not specifically address the case when multiple sensors are missing; only one sensor measurement is assumed to be missing in the test. To restore multiple missing sensor measurements, the input space of the auto-encoder in [87] must be sufficiently high in order to provide the required degree of data redundancy. The resulting MSR must search in a multidimensional space with a high-dimensional auto-encoder in order to restore all missing data. This results in a time-consuming search. Consequently, the MSR is not fast enough and can not be used directly for online applications, such as the real-time control problem in this work, when multiple sensors are missing.

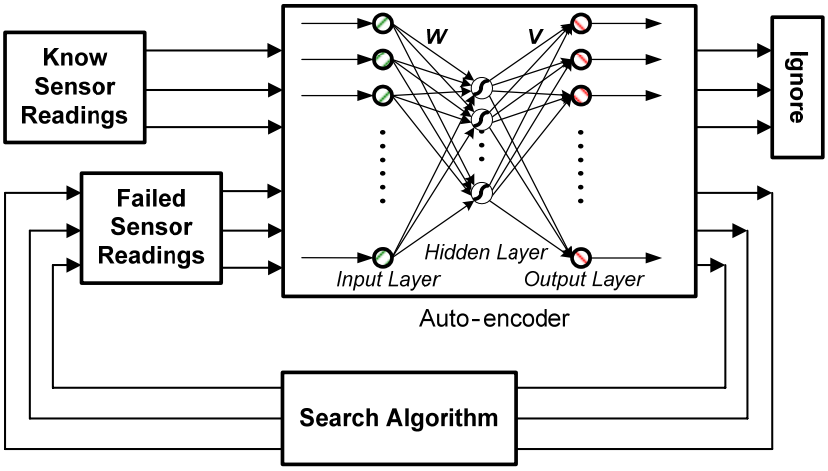

Figure 2.5: Schematic diagram of the missing sensor restoration (MSR) algorithm.

2.5 Chapter Summary

A comprehensive literature review on existing techniques related to this work has been summarized in this chapter. The trend of power system planning and operation is toward increased penetration of clean and renewable energy generation such as wind power and maximum utilization of the existing electricity infrastructure with tight system operating margins. This trend has brought new challenges to power system operation, control, stability, and reliability. However, due to the stochastic, nonlinear, and complex nature of modern power systems, traditional mathematical tools and control techniques are reaching a limit for system analysis and control. Therefore, innovative solutions based on advanced mathematical tools, optimal and intelligent control techniques, are required to improve the stability, reliability, dynamic and economical performance of modern power systems. This serves as the motivation and target of current research work.

CHAPTER 3

INDIRECT ADAPTIVE EXTERNAL NEUROCONTROL FOR AN SSSC IN DAMPING POWER OSCILLATIONS

The theory, operation and control of a static synchronous series compensator (SSSC) have been summarized in Chapter 2 based on the previous work done by others [13], [14]. Conventionally, linear control techniques are used to design the SSSC controllers around a specific operating point where the nonlinear system equations are linearized. However, at other operating points the performance of these linear controllers degrades. Nonlinear adaptive neurocontrollers offer an attractive approach to overcome this degradation problem.

This chapter proposes an indirect adaptive external nonlinear neurocontroller (INDAEC) to improve the damping performance of an SSSC compared to when it is equipped with a conventional external linear controller (CONVEC) [41]. This nonlinear INDAEC uses two radial basis function neural networks (RBFNNs) and needs no mathematical model of the SSSC or the power network. The improved damping performances of the INDAEC controlled SSSC are demonstrated by simulation results in PSCAD/EMTDC [90] on a single machine infinite bus (SMIB) as well as on a multimachine power system.

3.1 Modeling and Control of the SSSC

Figure 3.1 illustrates an SSSC with its internal and external controllers connected to a 160 MVA 15 kV (L-L) SMIB power system. The SSSC is modeled as a sinusoidal PWM controlled GTO converter with a dc-link capacitor, which is connected in series at the receiving end of line 3 through a series injection transformer. In the converter model, the operation of individual GTO switches is fully represented and the switching

frequency is 900 Hz. The generator is modeled together with its AVR/exciter and governor/turbine dynamics taken into account, as described in Appendix A. The three three-phase transmission lines represent the different loops between the generator and the system. The impedances of the three lines are $Z_1 = 0.02 + j0.4$ pu, $Z_2 = 0.03 + j0.6$ pu, and $Z_3 = 0.04 + j0.8$ pu, respectively. A three-phase balanced electric load draws a constant active power of $P_L = 0.1$ pu with a constant power factor 0.85 (lagging) from the generator bus.

The internal controller and the CONVEC (external controller) of the SSSC are the same as those in Figure 2.2 and Figure 2.1, respectively. The parameters of the controllers are designed at a certain operating point and the tuning procedure has been described in [13], [14], [41]. The final settings of the internal controller and the CONVEC parameter are provided in Table G.1 of Appendix G.

An INDAEC, based on RBFNNs, is developed to replace the CONVEC, as shown in Figure 3.1. Here the plant to be controlled by the INDAEC includes the SSSC with its internal controller as well as the SMIB power system.

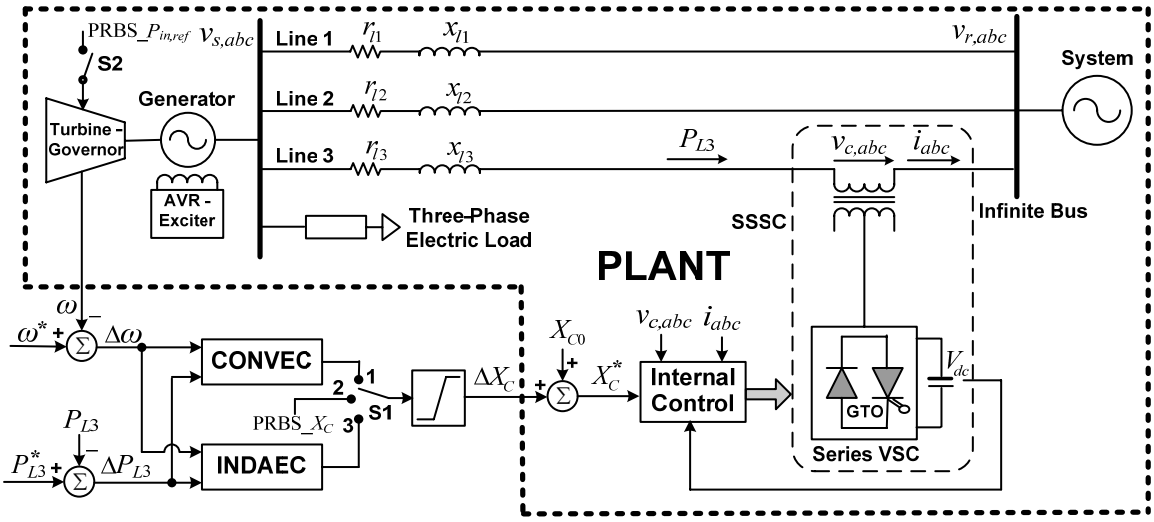

Figure 3.1: Single-line diagram of an SSSC with its internal and external controllers connected to an SMIB power system.

The external controllers (CONVEC and INDAEC) are able to rapidly change the compensating reactance X_C injected by the SSSC, thus providing supplementary damping during transient power swings. However, the maximum total compensating reactance must take into account the operating range of the SSSC. This can be represented by the degree of the series compensation k as follows:

$$k = \frac{X_C}{X_L} \tag{3.1}$$

where X_C is the compensating reactance of the SSSC and X_L is the transmission line reactance, respectively. In this application, $X_L = x_{l3}$ (Figure 3.1) and the value of k is limited to $-0.6 \leq k \leq 0.9$, where the negative value of k indicates an inductive reactance compensation and the positive value of k indicates a capacitive reactance compensation. Therefore, a limiter is placed at the output of the external controllers to limit the total compensating reactance of the SSSC within the desired range, as shown in Figure 3.1.

3.2 Radial Basis Function Neural Network

The neural networks used in this design are three-layer radial basis function (RBF) networks with the Gaussian density function as the activation function in the hidden layer (Figure 3.2) [41]. The overall input-output mapping for the RBF network, $\hat{f} : X \in R^n \rightarrow Y \in R^m$ is

$$\hat{y}_i = b_i + \sum_{j=1}^{h} v_{ji} \exp\left(-\frac{\left\| x - C_j \right\|^2}{\beta_j^2} \right) \tag{3.2}$$

where x is the input vector, $C_j \in R^n$ is the center of the j^{th} RBF units in the hidden layer, h is the number of RBF units, b_i and v_{ji} are the bias term and the weight between hidden and output layers respectively, and $\hat{y}_i$ is the i^{th} output.

One of the key issues in designing a RBFNN is to determine the number of RBF units in the hidden layer. In this design, the number of RBF units is chosen heuristically as a result of the tradeoff between the RBFNN performance and the computational cost.

Another key issue is to specify the locations of RBF centers. Basically, two different approaches can be used to determine the locations of RBF centers: 1) to determine them offline using a set of training patterns chosen from the operating space of the RBFNN, these centers are then fixed for online training of the RBFNN; 2) to update them online using each in-coming pattern or a batch of in-coming patterns. In the applications in power systems, it is feasible to determine the operating space of the nonlinear plants to be controlled. Therefore, the operating ranges of the RBFNN input and output variables can be specified. In addition, online updates of RBF centers are not feasible for online identification and control because of excessive memory requirement and computational complexity. Therefore, in this design, the locations of RBF centers are determined offline using a *k*-means clustering algorithm [91].

After locating the RBF centers, a good method to determine the RBF widths is the *p*-nearest neighbors heuristic [92], in which the width β_i of the i^{th} RBF unit is given by:

$$\beta_i = \left(\frac{1}{p} \sum_{j=1}^{p} \left\| C_i - C_j \right\|^2 \right)^{1/2} \tag{3.3}$$

where C_j are the *p*-nearest neighbors to the center C_i. In this design, *p* is chosen the same as the number of RBF units *h* in the hidden layer. In (3.2) and (3.3), $\|\cdot\|$ represents the Euclidean norm.

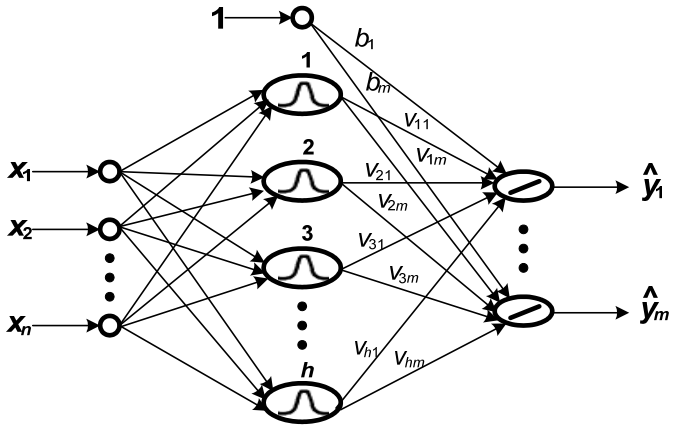

Figure 3.2: The three-layer radial basis function neural network.

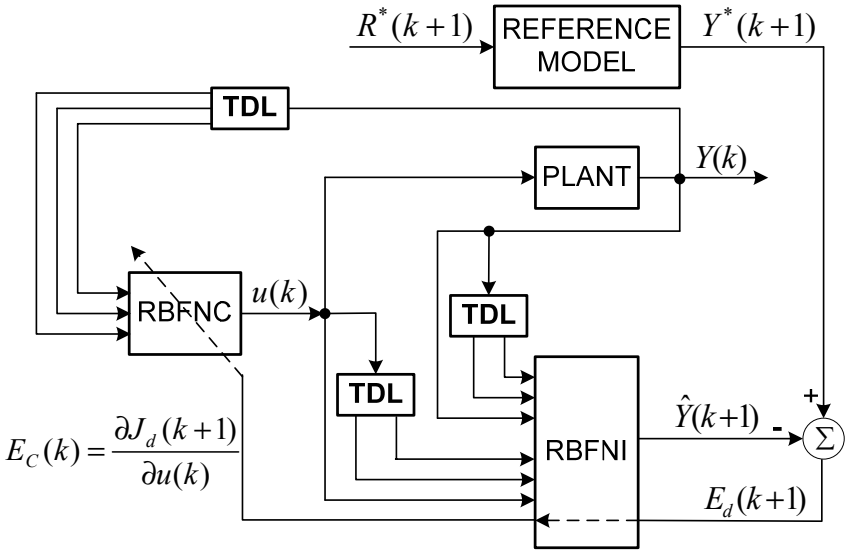

Figure 3.3: Structure of the proposed INDAEC.

3.3 Design of the Indirect Adaptive External Neurocontroller

The structure of the proposed INDAEC connected to the plant (shown as the dashed line block in Figure 3.1) is shown in Figure 3.3. It consists of two separate RBFNNs, namely one for the RBF neuroidentifier (RBFNI) and the other for the RBF neurocontroller (RBFNC) [41], [93]. TDL denotes time delays of the input and output signals. The RBFNI is developed using the nonlinear autoregressive moving average with exogenous inputs (NARMAX) model. It is used to provide a dynamic model of the plant at all times for training the RBFNC. The plant input $u = \Delta X_C$ and outputs $Y = [\Delta\omega, \Delta P_{L3}]$ at time k, k–1, and k–2 are fed into the RBFNI to estimate the plant output $\hat{Y} = [\Delta\hat{\omega}, \Delta\hat{P}_{L3}]$ at time k+1. The RBFNC has as its inputs the plant outputs at time k–1, k–2, and k–3; it in turn generates the control signals as the plant inputs to drive the plant outputs to the desired values. The reference model utilizes the reference inputs R^* to generate the desired plant outputs Y^* at each time step, which are used to guide the plant outputs $Y = [\Delta\omega, \Delta P_{L3}]$ to a desired steady-state set point. In this application, $R^* = [\omega^*, P_{L3}{}^*]$, which represent the steady-state values of the generator speed and the transmitted

active power by line 3 at a specific operating point, are used as the reference inputs; therefore $Y^* = [\Delta\omega^*, \Delta P_{L3}{}^*]$ are constant values, [0, 0], at each time step. The use of the variable ΔP_{L3} as the input of the INDAEC provides the RBFNI and RBFNC with additional information of the plant dynamics.

The entire training process of the INDAEC includes the training of the RBFNI and the training of the RBFNC. They are described as follows.

3.3.1 Training of the Radial Basis Function Neuroidentifier

The RBFNI is pretrained offline using a suitably selected training data set collected from two sets of training while the plant in Figure 3.1 is operating. The first set is called *forced training*, in which the plant is perturbed by injected small pseudorandom binary signals (PRBS) (with S1 in position 2 in Figure 3.1), given by

$$PRBS\_X_C(k) = 0.1 \cdot |X_{C0}| \cdot [r2(k) + r3(k) + r5(k)]/3 \tag{3.4}$$

where $r2$, $r3$, and $r5$ are uniformly distributed random numbers in [-1, 1] with frequencies 2 Hz, 3 Hz, and 5 Hz, respectively. The second training set is called *natural training*, in which the PRBS is removed; the plant is controlled by the CONVEC (with S1 in position 1 in Figure 3.1) and exposed to natural disturbances and faults in the power network. The forced training and natural training are carried out at different operating points to form the training data set, given by

$$\underline{\mathrm{A}} = \{\underline{\mathrm{X}}, \underline{\mathrm{Y}}\} = \left\{ \bigcup_{i=1}^{m} \underline{\mathrm{A}}_{\mathrm{F}i}, \bigcup_{i=1}^{m} \bigcup_{j=1}^{n} \underline{\mathrm{A}}_{\mathrm{N}ij} \right\} \tag{3.5}$$

where $\underline{\mathrm{A}}$ is the entire training data set selected from m operating points; $\underline{\mathrm{X}}$ and $\underline{\mathrm{Y}}$ are the input and output data sets of the RBFNI, respectively; $\underline{\mathrm{A}}_{\mathrm{F}i}$ is the subset collected from the forced training at the operating point i; $\underline{\mathrm{A}}_{\mathrm{N}ij}$ is the subset collected from the natural training caused by the j^{th} natural disturbance event at the operating point i. The selected training data set ensures that the RBFNI can track the system dynamics over a wide

operating range. After determining the training data set, the weights of the RBFNI are then calculated by singular value decomposition (SVD) method [28].

3.3.2 Training of the Radial Basis Function Neurocontroller

The RBFNC is trained online, again in two stages [41], [93]: *forced training* and *natural training*. The forced training of the RBFNC takes place with the pretrained RBFNI in cascade with the reference model (Figure 3.4). The forced PRBS, given by

$$PRBS\_P_{in,ref}(k) = 0.05 \cdot | P_{in,ref} | \cdot [r2(k) + r3(k) + r5(k)]/3 \tag{3.6}$$

is now added to the reference value of the turbine input power to disturb the plant (with switch S2 closed in Figure 3.1). During this stage, the plant and the RBFNI are driven by the CONVEC (with switch S1 in position 1 in Figure 3.1) instead of the RBFNC because the RBFNC has not yet learned the correct control behavior. The RBFNC is placed in parallel with the CONVEC to experience training and starts off with small random initial weights. In Figure 3.4, the error vector $E_d(k+1)$, which is the difference between the desired output of the reference model and the estimated output of the RBFNI at time $k+1$, is propagated back through the RBFNI (without changing its weights) to form the error signal $\Delta u_C(k)$ as follows.

$$\Delta u_C(k) = \frac{\partial J_d(k+1)}{\partial u(k)} = \frac{\partial D_I(k)}{\partial u(k)} V_I(k) E_d(k+1) \tag{3.7}$$

where $J_d(k+1)$ is the instantaneous total least-square error, given by

$$J_d(k+1) = \frac{1}{2} \| E_d(k+1) \|^2 = \frac{1}{2} \| Y^*(k+1) - \hat{Y}(k+1) \|^2 \tag{3.8}$$

and

$$\left[\frac{\partial D_I(k)}{\partial u(k)} \right]_j = \frac{\partial D_{I,j}(k)}{\partial u(k)} = \frac{2[C_{jl} - u(k)]}{\beta_j^2} D_{I,j}(k) \tag{3.9}$$

where $j = 1, 2, \cdots, h$; C_{jl} is the l^{th} element of the j^{th} RBF center corresponding to the input $u(k)$. The error signal $\Delta u_C(k)$ is added to the control signal $u(k)$ produced by the

CONVEC to form the target signal for training the RBFNC. This ensures that the RBFNC learns a better control behavior than that of the CONVEC at each time step. The plant outputs Y at time k–1, k–2, and k–3 are fed forward through the RBFNC to produce the estimated control signal $\hat{u}$ at time k, which is then compared with the target signal $[u(k)+\Delta u_C(k)]$ to form the training error vector $E_C(k)$. The backpropagation algorithm [94] is then used to train the RBFNC. This is carried out by minimizing the following total least-square error $J_C(k)$.

$$J_C(k) = \frac{1}{2} \| E_C(k) \|^2 = \frac{1}{2} \| u(k) + \Delta u(k) - \hat{u}(k) \|^2 \tag{3.10}$$

The updates of the weight matrix V_C and the bias term vector B_C between the hidden layer and the output layer are given by:

$$V_C(k+1) = V_C(k) + \Delta V_C(k) \tag{3.11}$$

$$B_C(k+1) = B_C(k) + \Delta B_C(k) \tag{3.12}$$

$$\Delta V_C(k) = -\gamma \frac{\partial J_C(k)}{\partial V_C(k)} = \gamma \frac{\partial \hat{u}(k)}{\partial V_C(k)} E_C(k) = \gamma D_C(k) E_C^T(k) \tag{3.13}$$

$$\Delta B_C(k) = -\gamma \frac{\partial J_C(k)}{\partial B_C(k)} = \gamma \frac{\partial \hat{u}(k)}{\partial B_C(k)} E_C(k) = \gamma E_C(k) \tag{3.14}$$

where γ is the learning rate with the value $0<\gamma<1$; and $D_C(k)$ (called decision vector) is the output vector of the Gaussian activation functions in the hidden layer.

Once the RBFNC has learned the correct control behavior, the PRBS is removed and the forced training is terminated. The CONVEC is now removed and the RBFNC is applied to control the plant (with switch S1 in position 3 in Figure 3.1), as shown in Figure 3.3. The system is operated at a normal operating condition and the natural training continues as the plant is exposed to natural disturbances and faults such as a three-phase short circuit. During this time, the RBFNC is continuously trained online without any PRBS (with switch S2 open in Figure 3.1). During the training of the

RBFNC, the RBFNI can also be trained online simultaneously (if necessary) to adapt to the operating conditions that were not covered by the pretraining.

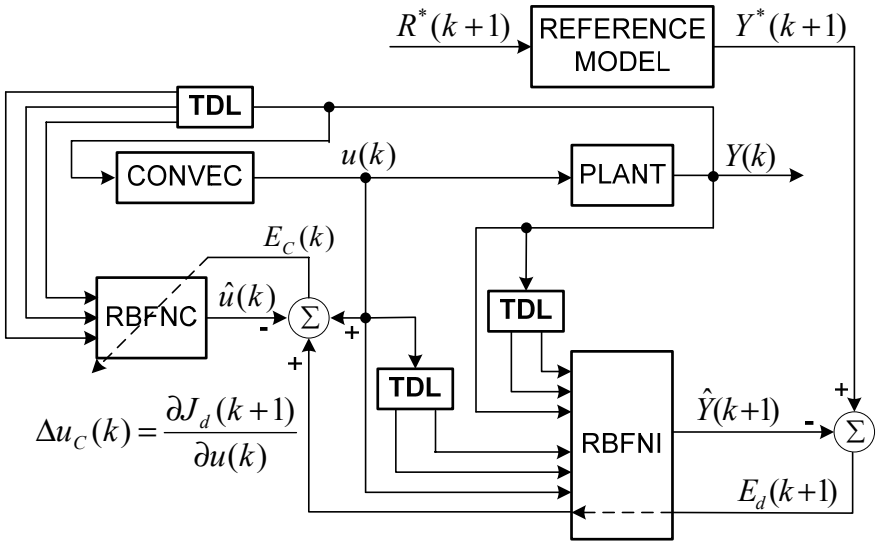

Figure 3.4: Forced training of the RBFNC.

3.4 Simulation Study on an SMIB Power System

This section presents simulation results of the system in Figure 3.1. The dynamic damping performances of the SSSC with a fixed set-point value of X_C^* (without any external controller), with the CONVEC, and with the INDAEC are compared at two different operating points by applying three-phase short circuits.

3.4.1 Tests at the Operating Point Where Controllers are Designed

The RBFNC is trained and the CONVEC is tuned at a specific operating condition (called OP-I), where the generator operates with a prefault power angle of 56.7º, output active power P_t = 0.8 pu, and output reactive power Q_t = 0.12 pu; the fixed set-point value X_{C0} = 0.25 pu; line 1 remains open during this entire test, and the transmitted steady-state active powers at the receiving end of line 2 and line 3 are P_{L2} = 0.30 pu and P_{L3} = 0.37 pu, respectively. At this operating point, the active power flow in

line 3 is heavier than that in line 2. Thereafter, a 100 ms three-phase short circuit is applied to the receiving end of line 2 at t = 15 s to evaluate the dynamic damping performances of the different controllers.

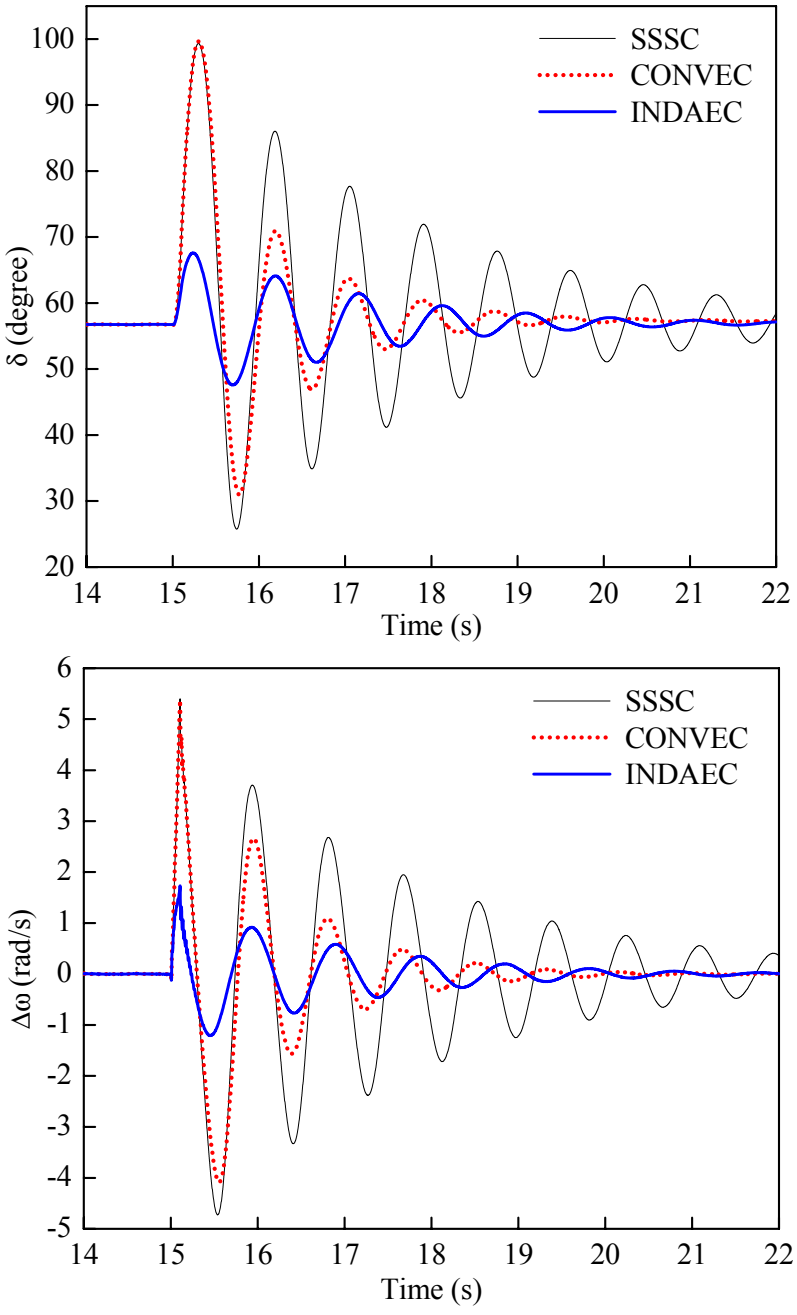

Figure 3.5: A 100 ms three-phase short circuit test at OP-I: δ (degree) and $\Delta\omega$ (rad/s).

Figure 3.5 shows the rotor angle δ and the speed deviation $\Delta\omega$ of the synchronous generator, respectively. The curve SSSC indicates the system response without the external controller applied to the SSSC. These results clearly show that the damping control of the low-frequency power oscillations by the INDAEC during the post-fault transient state is much better than those of the SSSC and the CONVEC. During the first half cycle of the power swings after the fault is applied, the CONVEC is unable to provide any damping; but the INDAEC is already providing significant damping during this period.

To compare directly the dynamic responses of the CONVEC and the INDAEC, Figure 3.6 shows their outputs ΔX_C during this transient disturbance. During the first half cycle of the power swings after the fault is applied, the CONVEC is unable to generate a sufficient ΔX_C that contributes to damping because of the time-delay responses of the two low-pass filters; on the contrary, the INDAEC is already providing a sufficient ΔX_C for the SSSC internal controller. This ΔX_C from the INDAEC reduces the reactance between the generator bus and the infinite bus during the fault. In addition, the use of INDAEC reduces the magnitudes of the voltage sag at the generator bus during the fault, as shown in Figure 3.7. Therefore, more active power can be transmitted from the generator to the system which reduces the unbalance between the generator input mechanical power and the output electrical power during the fault. This contributes to improving the damping of the system during the first as well as the post-fault power swings, as demonstrated in Figure 3.5. In this application, because X_{C0} is set at 0.25 pu, the value of ΔX_C is limited in the range of [-0.5, 0.5] pu, as discussed in Section 3.1 and shown in Figure 3.6.

The results in Figure 3.5-Figure 3.7 indicate that the INDAEC has neither a problem with the phase compensation between ΔX_C and transient power oscillations nor a problem with any electrical noise present in the measurements. Therefore, it works effectively without the two low-pass filters in the CONVEC shown in Figure 2.1.

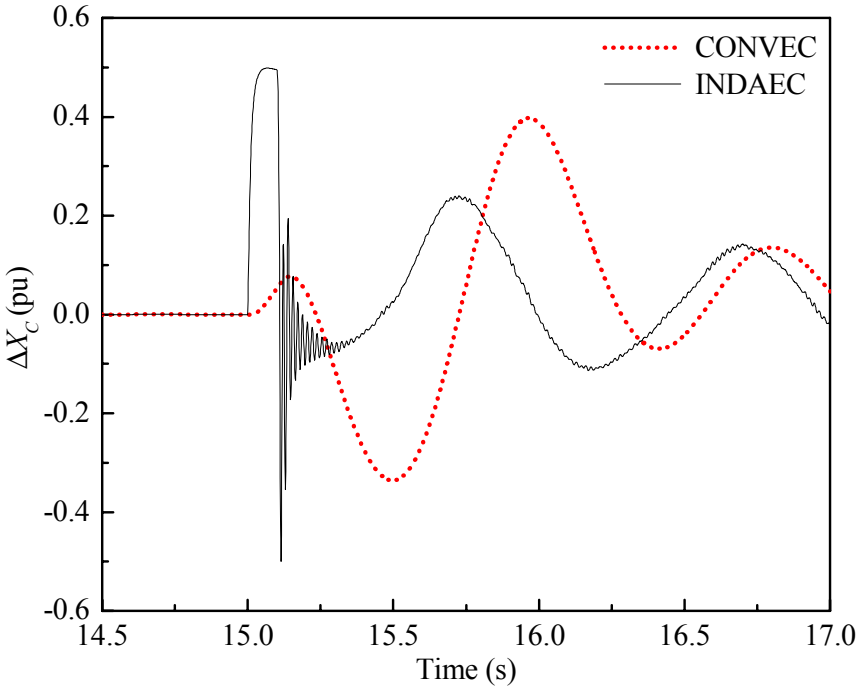

Figure 3.6: A 100 ms three-phase short circuit test at OP-I: ΔX_C (pu).

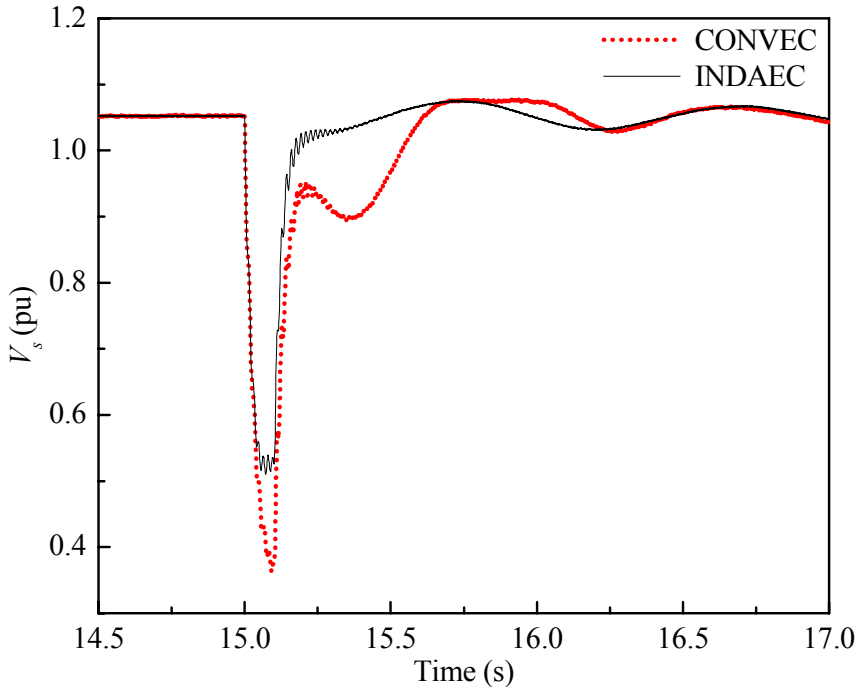

Figure 3.7: A 100 ms three-phase short circuit test at OP-I: V_s (pu).

3.4.2 Tests at a Different Operating Point

The dynamic damping performances of the controllers are now reevaluated at a different operating point (OP-II), where the prefault power angle of the generator changes to 52º (P_t = 0.88 pu, Q_t = 0.22 pu); line 1 is now kept closed during this entire test, and the transmitted steady state active powers by line 1, line 2 and line 3 are P_{L1} = 0.28 pu, P_{L2} = 0.21 pu and P_{L3} = 0.27 pu, respectively. At this operating point, most of the active power is transmitted by lines 1 and 2. However, the parameters of the controllers are the same as those used in the test at OP-I, i.e., the RBFNC has not been trained and the CONVEC has not been tuned for OP-II.

The same 100 ms three-phase short circuit is then applied to the receiving end of line 2 at t = 15 s, and thereafter, line 2 is tripped off from the system. The simulation results appear in Figure 3.8, which again clearly show that the INDAEC has the best damping performance compared with the CONVEC and the SSSC, and the CONVEC is also more efficient than the SSSC. However, comparing Figure 3.8 with Figure 3.5, the damping performance of the CONVEC degrades at this different operating point (OP-II) where it has not been tuned; but the INDAEC still provides the improved damping performance over the CONVEC at this new operating point (OP-II) where the RBFNC has also not been trained. Again, during the first half cycle of the power swings after the fault is applied, the CONVEC is unable to provide any damping; but the INDAEC is already providing significant damping during this period.

The outputs ΔX_C of the external controllers and the voltage magnitudes at the generator bus are again compared for this test, as shown in Figure 3.9 and Figure 3.10. During the first half cycle of the power swing after the fault is applied, the INDAEC is already providing a sufficient ΔX_C which reduces the reactance between the generator bus and the infinite bus during the fault, as shown in Figure 3.9. In addition, the use of INDAEC reduces the magnitudes of the voltage sag at the generator bus during the fault, as shown in Figure 3.10. Again, both the reduced reactance and the reduced voltage sag

contribute to improve the damping of the system during the first as well as the post-fault power swings, as demonstrated in Figure 3.8.

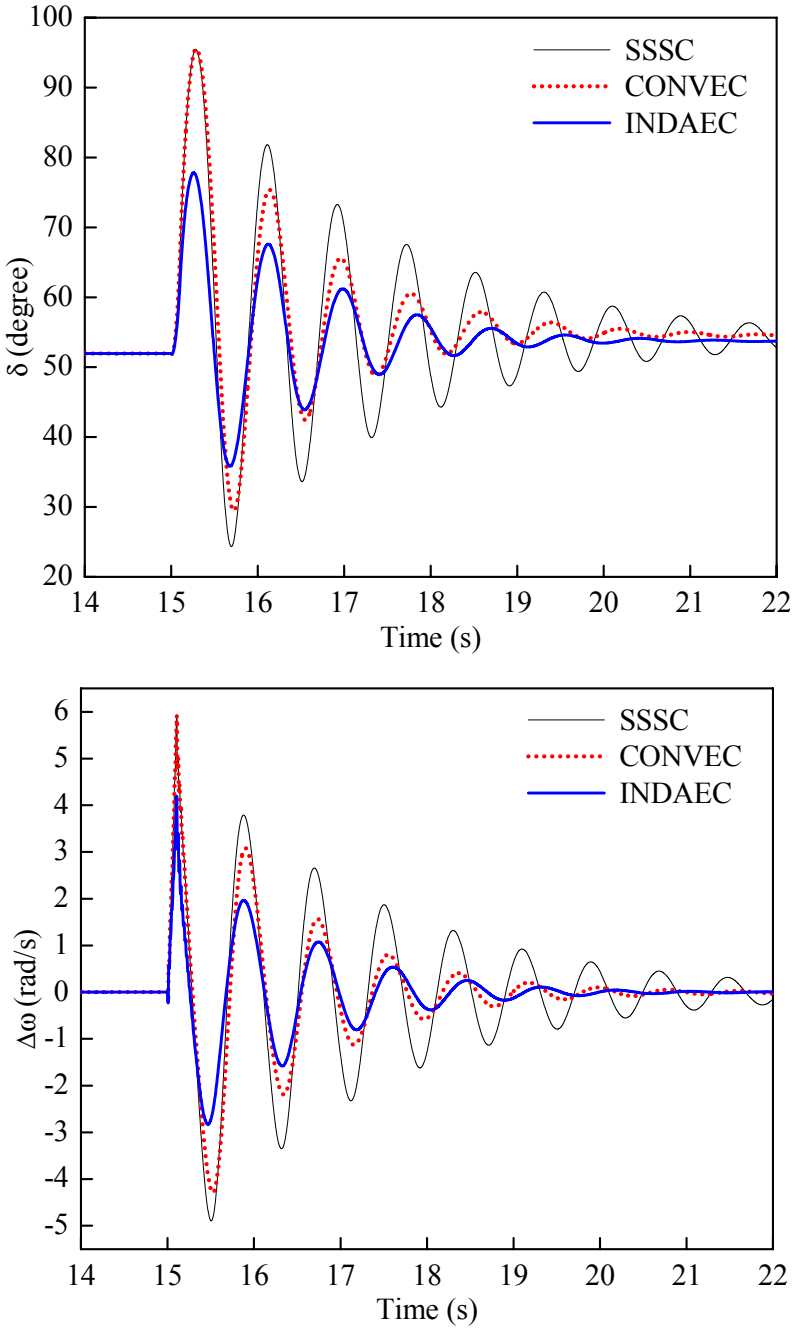

Figure 3.8: A 100 ms three-phase short circuit test at OP-II: δ (degree) and $\Delta\omega$ (rad/s).

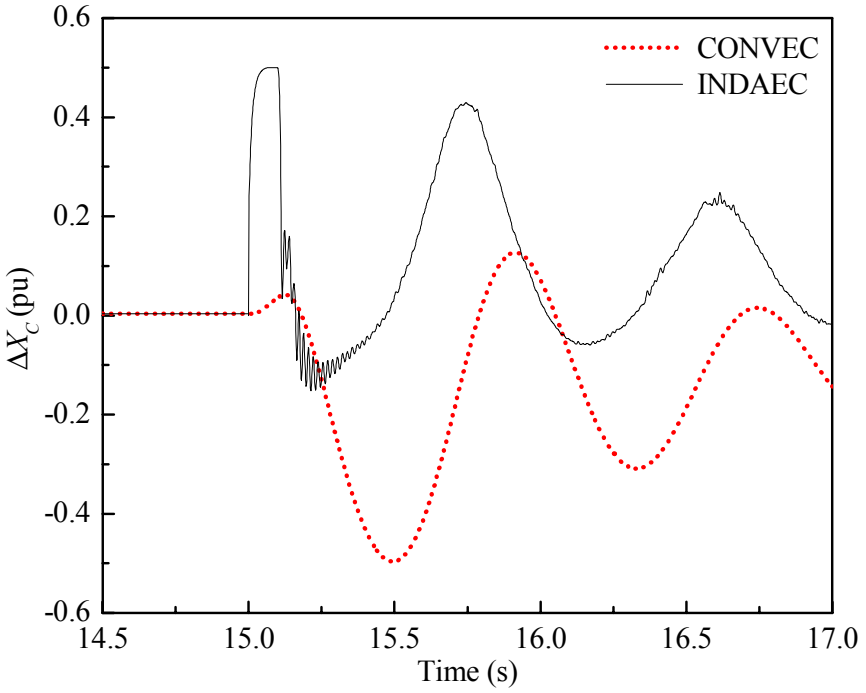

Figure 3.9: A 100 ms three-phase short circuit test at OP-II: ΔX_C (pu).

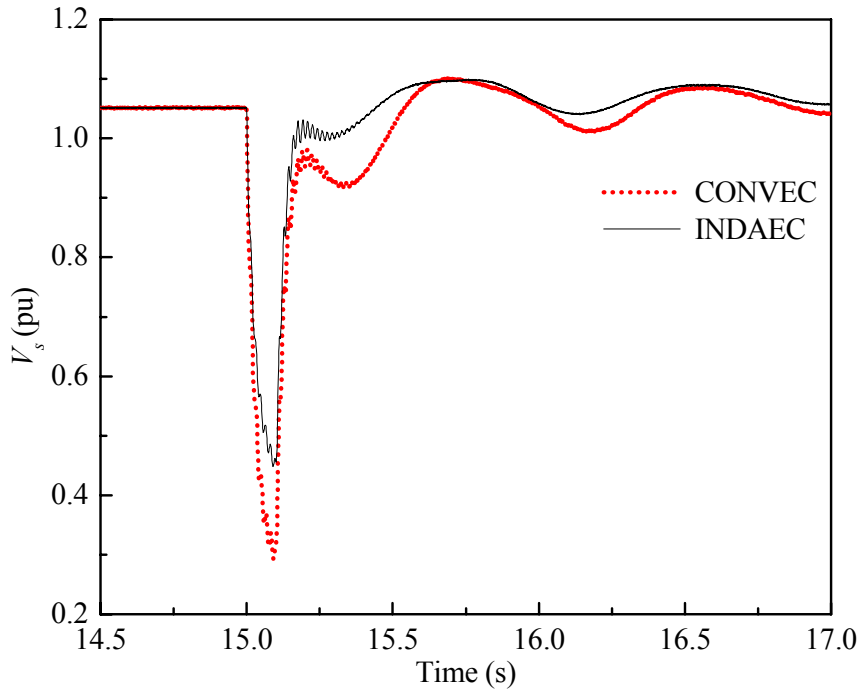

Figure 3.10: A 100 ms three-phase short circuit test at OP-II: V_s (pu).

3.5 Simulation Study on a Multimachine Power System

In order to further evaluate the usefulness of the proposed INDAEC, the equivalent multimachine power system of Figure 3.11 is now considered. This circuit model has been used for the study of voltage stability in [95] and [96]. In Figure 3.11, the sending area has two generators (Gen 1 and Gen 2) transmitting power to the load area through five 500 kV, 200 km transmission lines. Gen 1 is given a large inertia to represent a large interconnected power system, so that it functions as the slack bus. It is, however, relatively small electrically (5000 MVA) so that it provides only limited reactive power support for the load area.

The load area in Figure 3.11 consists of a generator (Gen 3), an industrial load (3000 MW, 1800 MVar) at bus 10 served directly from the transmission system, a residential load (3000 MW) served from bus 9, and shunt compensations (890 MVar at bus 6, 300 MVar at bus 7, and 1500 MVar at bus 10). The steady-state data of Gen 2 and Gen 3 at this operating point (called OP-III) are as follows:

- Gen 2: P_{t2} (at bus 2) = 0.682 pu, Q_{t2} = 0.0214 pu (leading), V_{t2} = 0.968 pu, δ_2 = 57.1º (with respect to bus 2).
- Gen 3: P_{t3} (at bus 3) = 0.6844 pu, Q_{t3} = 0.0781 pu (leading), V_{t3} = 0.962 pu, δ_3 = 60.5º (with respect to bus 3).

where P_t and Q_t are the active and reactive powers at generator terminals, respectively. V_t is the generator terminal voltage, and δ is the power angle.

The generators are modeled together with their conventional AVR, exciter, and turbine governor dynamics taken into account. The detailed steady-state and dynamic data for this multimachine power system, including the parameters of Gen 2 and Gen 3 [97], the AVR and exciter combination transfer function, and the turbine and governor combination transfer function [98] are provided in Appendix B.1.

The SSSC is installed between buses 6 and 11 to control the power flowing through the two 500 kV transmission lines between buses 5 and 11. It is assumed that the

SSSC is close enough to Gen 3 so that the external controllers (CONVEC and INDAEC) can receive the speed deviation signal from Gen 3 without any significant time delay.

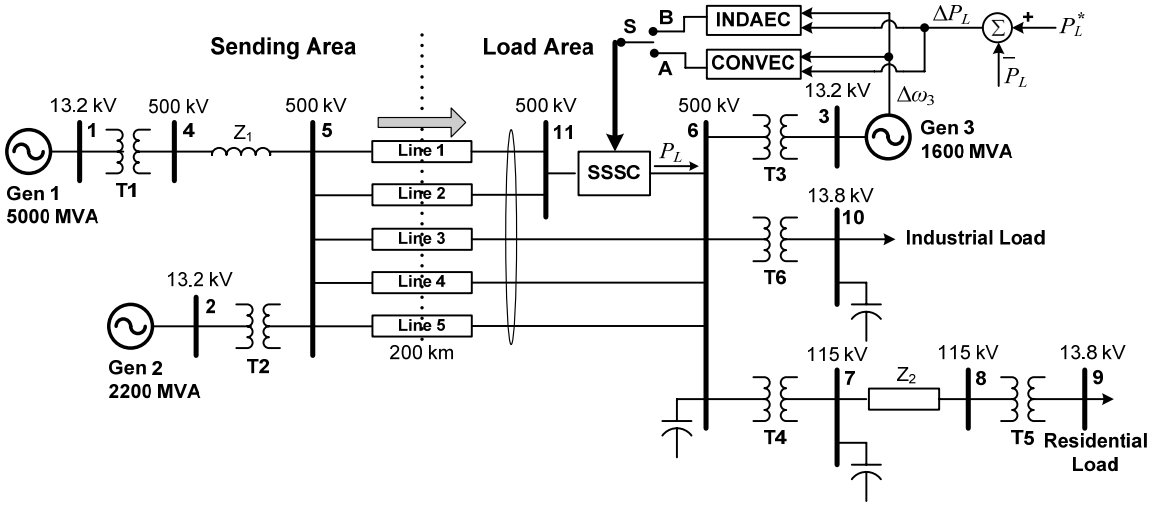

Figure 3.11: Single-line diagram of the multimachine power system.

The deviation signals $\Delta\omega_3$ from Gen 3 and ΔP_L from line 1 and line 2 (the deviation of the total transmitted active power by line 1 and line 2) in Figure 3.11, are now used as the inputs to the CONVEC as well as the INDAEC. The parameters of the internal controller and the CONVEC are given in Table G.1 of Appendix G. The design and training procedure of the INDAEC for the SSSC connected to this multimachine power system, are the same as those for the SMIB system in Figure 3.1. As in the SMIB system, the dynamic damping performances of the controllers are now evaluated at two different operating points by applying three-phase short circuits to bus 8.

3.5.1 Tests at the Operating Point Where Controllers are Designed

The INDAEC is trained and the CONVEC is tuned at OP-III. A 300 ms three-phase short circuit is applied to bus 8 at t = 15 s to compare the dynamic damping performances of the SSSC with different controllers. Figure 3.12 shows the speed ω_3 of Gen 3 by applying different controllers. These results show that the INDAEC provides

improved damping of the low-frequency power oscillations than those of the SSSC (without an external controller) and even with the CONVEC.

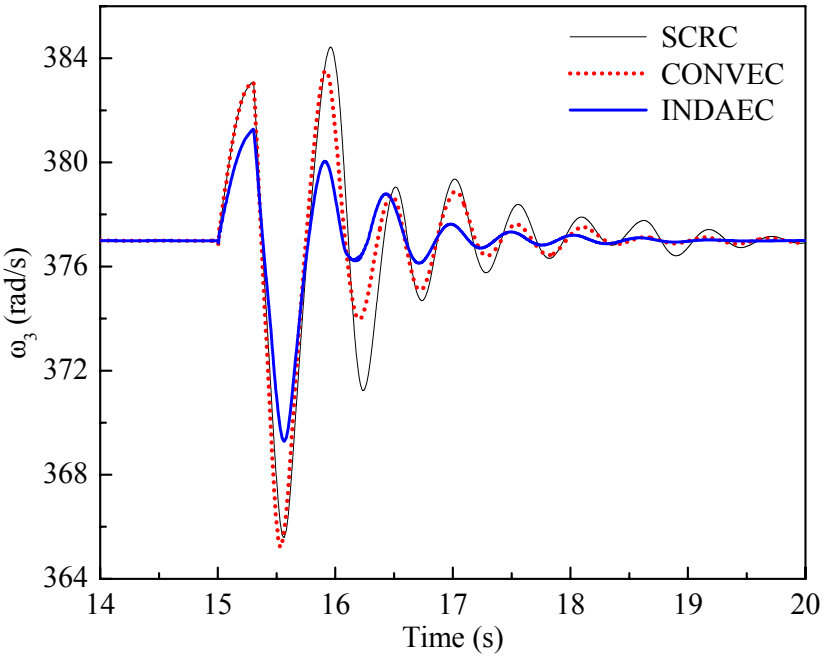

Figure 3.12: A 300 ms three-phase short circuit test at OP-III: ω_3 (rad/s).

3.5.2 Tests at a Different Operating Point

The dynamic damping performances of the controllers are now reevaluated at a different operating point (OP-IV). The parameters of the controllers at this new operating point are the same as those used in the test at OP-III, i.e., the RBFNC has not been trained and the CONVEC has not been tuned for OP-IV. Line 4 and line 5 are now open, and the steady-state data of Gen 2 and Gen 3 change to:

- Gen 2: P_{t2} (at bus 2) = 0.682 pu, Q_{t2} = 0.006 pu (leading), V_{t2} = 0.962 pu, δ_2 = 56.3º (with respect to bus 2).
- Gen 3: P_{t3} (at bus 3) = 0.684 pu, Q_{t3} = 0.0938 pu (leading), V_{t3} = 0.933 pu, δ_3 = 62.6º (with respect to bus 3).

A 250 ms three-phase short circuit is then applied to bus 8 at t = 15 s. The results of ω_3 appear in Figure 3.13, which again show that the INDAEC has the best damping

performance compared with the CONVEC and the SSSC, although it has not been trained at OP-IV. In contrast to the INDAEC, the damping performance of the CONVEC degrades at this new operating point (OP-IV) where it has not been tuned.

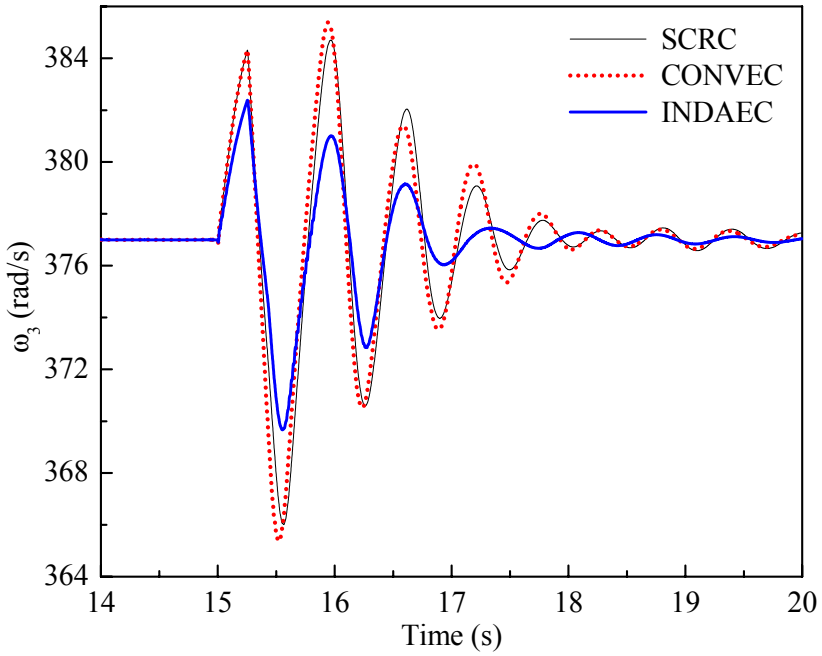

Figure 3.13: A 250 ms three-phase short circuit test at OP-IV: ω_3 (rad/s).

3.6 Chapter Summary

An indirect adaptive external neurocontroller (INDAEC) using two radial basis function neural networks (RBFNNs) has been designed to improve the damping of an SSSC connected to a power network. This nonlinear INDAEC needs no mathematical model of the SSSC or the power network.

The damping performance of the INDAEC has been evaluated and compared with those of the SSSC (without an external controller) and the conventional external linear controller (CONVEC) in a single machine infinite bus (SMIB) power system as well as a small multimachine power system. Results have shown that the damping performance of the CONVEC degrades, as expected, at the operating point where it has not been tuned.

Compared to the CONVEC, the INDAEC provides a better damping performance at the operating point where these external controllers have been designed, as well as at different operating points where these external controllers have not been designed. This proves that the proposed INDAEC can provide the improved damping capability over the CONVEC over a wide range of system operating conditions. Moreover, in contrast to the CONVEC, which cannot provide damping during the first half cycle of the power swing after the fault is applied, the INDAEC is able to provide damping during this period. This happens because the INDAEC works efficiently without the use of any low-pass filters, which however are important in the design of the CONVEC.

The SSSC controllers presented in Chapter 2 and in this chapter provide correct control actions to the SSSC under the condition that all the required sensor measurements are available. However, measurements are inevitably subjected to faults caused by physical sensor failure, broken or bad connections, bad communication, or malfunction of some hardware or software, etc. In order to ensure the correct actions of the controllers under such faulty conditions, fault-tolerance is an essential requirement for SSSC control. The next two chapters will present two novel missing-sensor-fault-tolerant control strategies for the SSSC FACTS device.

CHAPTER 4

MISSING-SENSOR-FAULT-TOLERANT INDIRECT ADAPTIVE NEUROCONTROL FOR SSSC FACTS DEVICE

As discussed in Chapters 1 and 2, control and operation of the SSSC FACTS device rely on the availability and quality of sensor measurements. Measurements can be corrupted or interrupted due to physical sensor failure, broken or bad connections, bad communication, or malfunction of some hardware or software. These faults in turn may cause the failure of SSSC controllers and consequently severe contingencies in the power system.

To prevent such contingencies, this chapter proposes an online sensor evaluation and (missing sensor) restoration scheme (SERS) by using autoassociative neural networks (auto-encoders) and particle swarm optimizer (PSO). Based on the SERS, a missing-sensor-fault-tolerant indirect adaptive neurocontrol (FTIANC) is developed for controlling an SSSC with an energy storage system connected to a power network [102]. This FTIANC is able to provide effective control to the SSSC when single or multiple crucial time-varying current sensor measurements are not available. Therefore, it improves the reliability, maintainability and survivability of the SSSC and the power system.

4.1 Missing Sensor Restoration (MSR) Algorithm

An auto-encoder can learn the data correlations through inspection of historical data. Once trained, data correlations established by the auto-encoder can be used by some search algorithms (e.g., PSO) to restore missing data if the data dependency is sufficiently strong. This completes a MSR algorithm, as shown in Figure 4.1. The unique point of convergence of the MSR rests on the concepts of contractive and nonexpansive mappings [99] and the operating point determined by the healthy sensor data.

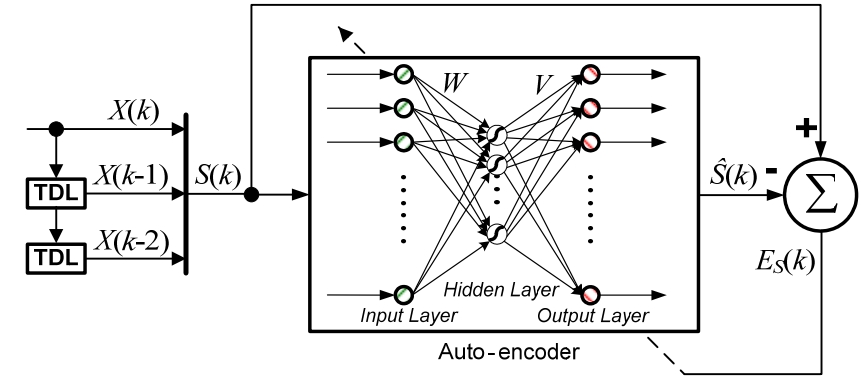

(a) Training of the auto-encoder.

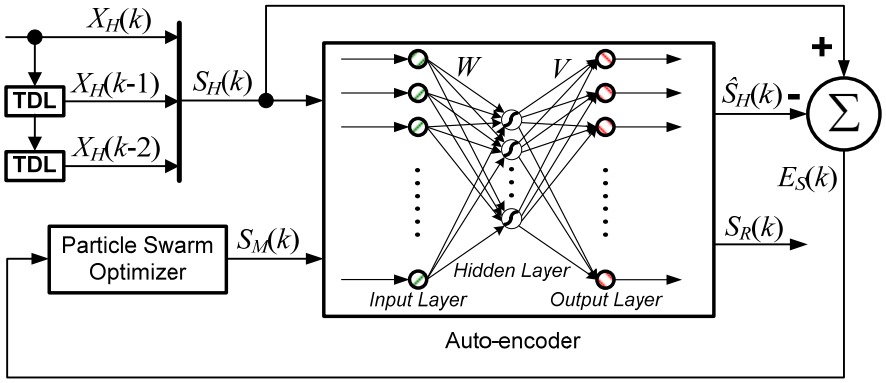

(b) Online restoration of missing sensor data.

Figure 4.1: Overall structure of the MSR.

4.1.1 Auto-encoder [Figure 4.1(a)]

The auto-encoder [100]-[104] is a three-layer feedforward neural network with sigmoidal nonlinearity in the hidden layer. It is trained to perform an identity mapping, where the network inputs are reproduced at the output layer. The overall input-output mapping for the auto-encoder, $\hat{g}$: $S \in R^P \rightarrow \hat{S} \in R^P$ is

$$\hat{S}_i = \hat{g}(S, W, V_i) = V_i \cdot d(S, W) = \sum_{j=1}^{q} V_{ij} d_j(S, W_j) \tag{4.1}$$

where $i = 1, 2, \cdots, p$; p is the dimension of the input and output vectors; q is the number of hidden-layer neurons; S is the input vector; $\hat{S}_i$ is the i^{th} output; W and V are the input and

output weight matrices, respectively; $d_j(S, W_j)$ is the sigmoid activation function of the j^{th} hidden layer neuron, given by

$$d_j(S, W_j) = \frac{1}{1 + e^{-a_j}} \tag{4.2}$$

where

$$a_j = W_j \cdot S = \sum_{i=1}^{p} W_{ji} S_i \tag{4.3}$$

Suppose the vector $X = [x_1, x_2, \cdots, x_n]$ consists of the measured time-varying sensor data at each time sampling k. In a power system, the time-varying variables are generally periodic and in the sinusoidal form, given by

$$x_i(k) = A_i \sin(\omega_i k + \phi_i) \quad i = 1, \cdots, n \tag{4.4}$$

Each periodic time-varying variable $x_i(k)$ is autocorrelated and its feature is determined by the magnitude A_i, the angular frequency ω_i, and the phase angle ϕ_i. Autocorrelations can be used to extract the significant features buried in a periodic time-varying signal, and therefore, are useful to restore the missing time-varying sensor measurements. The autocorrelation of each variable in the vector X can be captured by the auto-encoder using the time-delayed inputs. As shown in Figure 4.1(a), the inputs of the auto-encoder, S, consist of the vector, X, at the present time step as well as at the previous two time steps (i.e., $S(k) = [X(k), X(k–1), X(k–2)]$).

The auto-encoder is firstly trained without any missing sensor. It starts off with small random initial weights. By feeding the data through the auto-encoder and adjusting its weight matrices (using backpropagation algorithm [94]), W and V, the auto-encoder is trained to reproduce its input data at its output layer. Once trained, the cross-correlations between different sensor data as well as the autocorrelations of each sensor data in the vector X, are established by the auto-encoder.

There exist other complex structures, instead of the simple three-layer structure, for the auto-encoder. For instance, reference [105] proposed a four-layer autoassociative

neural network for missing sensor detection and restoration; reference [106] used a five-layer autoassociative neural network for nonlinear principal component analysis. Generally, the autoassociative networks with more complex structures are able to solve more sophisticated autoassociation problems, and therefore, can provide better performance for missing sensor detection and restoration. However, the use of complex autoassociative neural networks increases the computational cost, and consequently is not suitable for the applications of real-time system identification and control.

4.1.2 Missing Sensor Restoration [Figure 4.1(b)]

After training the auto-encoder, the inputs of the auto-encoder are reproduced at its output layer. If one or more sensor measurements are missing, the outputs of the auto-encoder, $\hat{S}$, no longer match its inputs S and the error signal E_S in Figure 4.1(a) becomes significant. In such a case, the PSO module in the feedback search loop of the MSR is activated and only the healthy sensor data S_H are fed directly into the auto-encoder. The error signal, E_S, is then used by the PSO as a fitness signal to search for the optimal estimates of the missing sensor data, based on the correlations between the healthy data and the missing data, established by the auto-encoder. At each iteration for each particle i (i = 1, 2, ···, N), its velocity and position vectors are updated by equations (1.2) and (1.3), respectively. The updated position vector, which represents the estimated missing sensor data, S_M, is then output from the PSO and fed together with the healthy sensor data, through the auto-encoder to reduce the value of the following fitness measure function f for each particle, defined by:

$$f = \| E_S \| = \| S_H - \hat{S}_H(S_H, S_M) \| \tag{4.5}$$

where S_H represents the actual healthy sensor data, $\hat{S}_H$ represents the reproduced healthy sensor data from the auto-encoder, and

$$\hat{S}_{Hj}(S_M) = \hat{g}(S_H, S_M, W, V_j) = \sum_{l=1}^{q} V_{jl} d_l(S_H, S_M, W_l) \tag{4.6}$$

is the j^{th} variable in the vector $\hat{S}_H$. Theoretically, good estimates of the missing sensor data should drive the fitness signal $||E_S||$ from the auto-encoder to zero, indicating a perfect match. In practical applications, once the error $||E_S||$ is below a predetermined threshold, the output of the auto-encoder, S_R, is regarded as the best estimates of the missing sensor data.

The use of the auto-encoder does not need an explicit plant model. In addition, the PSO algorithm provides a fast and efficient search for the optimal solution, because of its attractive features including simple implementation, small computational load, and fast convergence. Therefore, the MSR algorithm is suitable for on-line application.

4.1.3 Convergence of the Missing Sensor Restoration Algorithm

The unique convergence of the MSR can be shown through the concepts of contractive and nonexpansive mapping. An operator, Θ, mapping $\Re^N \rightarrow \Re^N$, is contractive if, for any vectors $x \in \Re^N$ and $y \in \Re^N$, it follows that $||\Theta x - \Theta y|| < ||x - y||$, where $||\cdot||$ denotes the Euclidean norm. The operator, Θ, is nonexpansive if $||\Theta x - \Theta y|| \leq ||x - y||$. According to the ***Banach Fixed-Point Theorem*** [107], if Θ is a contractive mapping, then there exists a unique fixed point x_0 for which $\Theta x_0 = x_0$; if Θ is nonexpansive, then there may exist a plurality of fixed points x_0 for which $\Theta x_0 = x_0$.

A well-trained auto-encoder constructs a nearly nonexpansive mapping $\hat{g}$ between its input space $\underline{S} \subset R^P$ and output space $\hat{\underline{S}} \subset R^P$, because for any vector $S \in \underline{S}$, there exists a unique vector $\hat{S} \in \hat{\underline{S}}$ such that $\hat{S} = \hat{g}(S) = S$. The auto-encoder performs a data compression through the input-to-hidden layer to extract significant features in the data. To avoid losing any significant information in the data, a necessary condition is that the dimension of the hidden layer, q, must equal or exceed the number of degrees of freedom in the input data, n.

Suppose r sensor data in S are missing, then the number of healthy sensor data is $p-r$. If the degree of data redundancy is sufficiently high, i.e., $(p-r)>q$, then the

"operating point" defined by the set of healthy sensor data, S_H, is the same as that defined by the full set of sensor data, $S = [S_H, S_M]$, because the missing sensor data S_M are redundant. Therefore, given an "operating point" defined by the set of healthy sensors, there exists a unique point of convergence for a well-trained auto-encoder. This convergence point should be reached regardless of how the missing sensors are initialized.

However, if the degree of data redundancy is not sufficiently high, i.e., $(p–r)<q$, then there may exists different sets of missing sensor data S_{M1} and S_{M2} such that $S_1 = \hat{g}(S_1)$ and $S_2 = \hat{g}(S_2)$, where $S_1 = [S_H, S_{M1}]$ and $S_2 = [S_H, S_{M2}]$. Here S_{M1} and S_{M2} are the correct values of the missing sensor data. In other words, given the set of healthy sensor data S_H, the missing sensor data might be restored as different values by the MSR. To avoid such a result, a necessary condition for the auto-encoder to work correctly is that the number of healthy inputs must equal or exceed the number of degrees of freedom in the hidden layer [105].

Generally, with a well-trained auto-encoder, the unique convergence of the MSR is achieved if two conditions are satisfied: 1) $q>n$, and 2) $(p–r)>q$, and vice versa.

4.2 SSSC in an SMIB Power System

Figure 4.2 shows an SSSC with its controllers connected to an SMIB power system. The generator (with 500 MW power rating) is modeled together with its AVR, exciter, and turbine governor dynamics taken into account [108], as described in Appendix A. The generated power is transmitted to a power system through three 230 kV three-phase transmission lines, which represent the different loops between the generator and the power system. The impedances of the three lines are $Z_1 = 0.02 + j0.4$ pu, $Z_2 = 0.03 + j0.6$ pu, and $Z_3 = 0.04 + j0.8$ pu (on 500 MW, 230 kV bases), respectively. A three-phase balanced electric load draws a constant active power of $P_L = 0.1$ pu with a constant power factor of 0.85 from the sending-end bus of the 230 kV transmission lines.

The SSSC is connected at the receiving end of line 3 through a series injection transformer for dynamic power flow control. It is modeled as a detailed switching-level voltage source converter (VSC) with an energy storage system coupled with the dc-link.

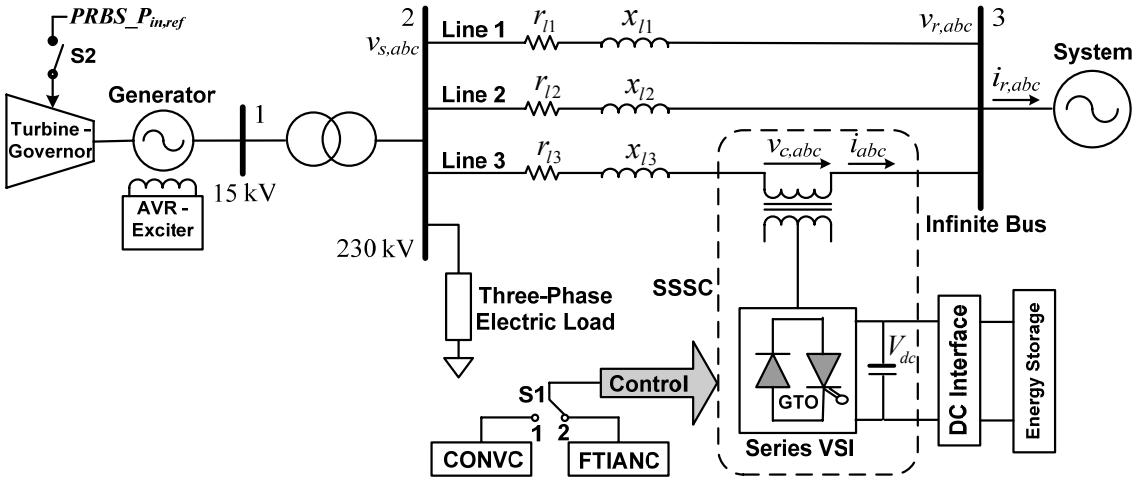

Figure 4.2: Single-line diagram of an SSSC in an SMIB power system.

The SSSC is controlled by a P-Q decoupled power flow control scheme using two conventional PI controllers (PI_d and PI_q, called CONVC) as described in [42]. The details of this linear control scheme are presented in Appendix C and the parameters of the two PI controllers are given in Table G.2 of Appendix G. In Figure 4.3, P^* and Q^* are the desired reference values of the transmitted real and reactive powers at the receiving end of line 3, which are used to determine the reference values of the *d*-axis component i_d^* and the *q*-axis component i_q^* of the line current at the SSSC ac terminal, respectively. The instantaneous three-phase currents of line 3, i_a, i_b and i_c, are sampled and transformed into *d*-axis and *q*-axis components i_d and i_q by applying the synchronously rotating reference frame transformation (SRRFT) [109]. The actual *d-q* current signals are compared with the corresponding reference signals to generate the *d*-axis and *q*-axis current deviations, respectively, which are then passed through the two PI controllers. The outputs of the PI controllers in turn determine the modulation index m_i and phase

shift α applied to the PWM module to drive the GTO thyristors of the inverter. The main objective of this SSSC is to control the transmitted active and reactive power at the receiving end of line 3. The reference values, P^* and Q^*, can be determined by the results of the power flow calculation at a specific operating point to achieve some form of optimal operation (e.g., optimal power flow) of the network, while considering the operating limits of the SSSC.

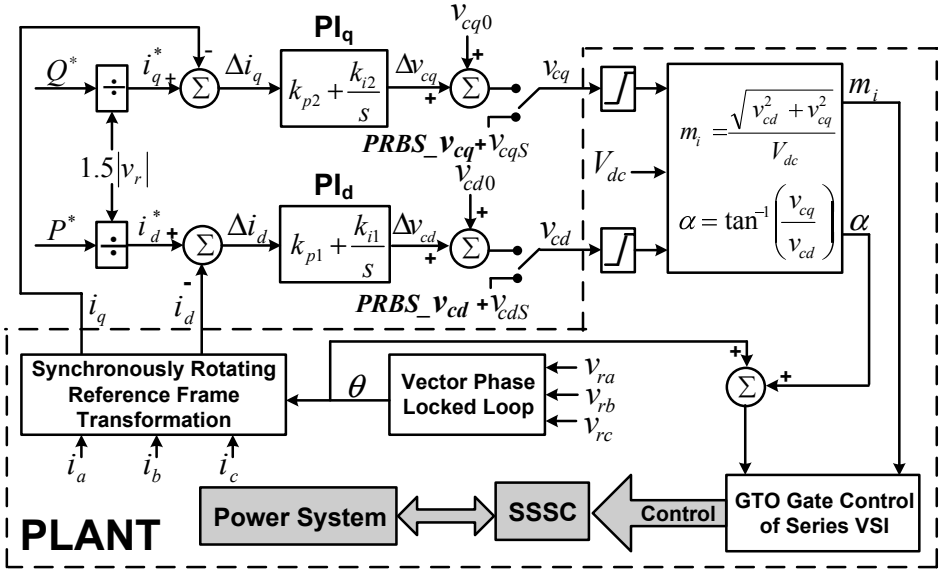

Figure 4.3: P-Q decoupled control scheme for the SSSC.

4.3 Design of the Fault-Tolerant Indirect Adaptive Neurocontrol

4.3.1 Overall Structure

The schematic diagram of the proposed FTIANC connected to the plant (the dash-line block in Figure 4.3) is shown in Figure 4.4. The FTIANC consists of an SERS, a radial basis function neuroidentifier (RBFNI) and a radial basis function neurocontroller (RBFNC). The RBFNI is trained to provide a dynamic predictive plant model at all times; this plant model is then used for training the RBFNC; the RBFNC in turn generates the control signals to drive the outputs of the actual plant to the desired values.

In Figure 4.4, $U = [v_{cd}, v_{cq}]$ and $Y = [i_d, i_q]$ are the plant input and output vectors, respectively. In this application, i_d and i_q are two crucial variables to determine the behaviors of the RBFNI and the RBFNC. The values of i_d and i_q are calculated from the three-phase currents i_a, i_b, and i_c ($i_{abc} = [i_a, i_b, i_c]$) of line 3 (Figure 4.2), which are time-varying variables measured by the metering current transformers (called current sensors in this work). Therefore in this application, i_a, i_b, and i_c are three crucial measurements; missing any of them results in the loss of both i_d and i_q.

The vector $v_{c,abc} = [v_{ca}, v_{cb}, v_{cc}]$, consists of the injected three-phase voltages of the SSSC, measured by the metering potential transformers (called voltage sensors in this work). The vector $i_{r,abc} = [i_{ra}, i_{rb}, i_{rc}]$, measured by other current sensors, consists of the three-phase currents flowing from the infinite bus into the system. These two vectors, $v_{c,abc}$ and $i_{r,abc}$, are irrelevant to the performances of the RBFNI and RBFNC, but are used to build the correlations with the variables in the vector i_{abc}. The use of the extra measurements, $v_{c,abc}$ and $i_{r,abc}$, to form the input vector, $X = [i_{abc}, v_{c,abc}, i_{r,abc}]$, of the SERS, provides necessary data redundancy in order to restore two or three missing currents in the vector i_{abc}.

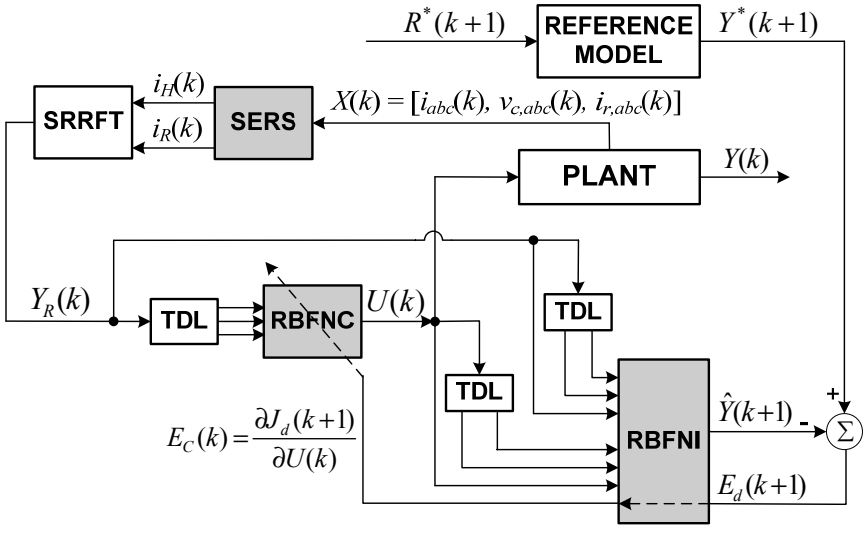

Figure 4.4: Schematic diagram of the FTIANC connected to the plant.

The SERS is designed by using the MSR algorithm and the features of the three-phase variables in power systems. It evaluates the integrity of the crucial vector i_{abc} which determines the behavior of the RBFNI and the RBFNC. If one or more sensor data in i_{abc} are missing, the SERS detects which sensor or sensors are missing. This information is then used by the PSO to search for the best estimates of all missing sensor data. In this design, a small population of particles (5 particles) is used in the PSO to reduce the computational cost of the PSO search algorithm for real-time implementation. The output vector of the SERS, i_R, contains the restored sensor data; but i_H, contains other healthy sensor data in the vector i_{abc}. The variables, [i_R, i_H], are transformed into the *d*-axis and *q*-axis current components, Y_R = [i_{dR}, i_{qR}], by applying the SRRFT. In this application, missing any of the three currents i_a, i_b and i_c results in the loss of both i_d and i_q. Therefore, the calculated currents i_{dR} and i_{qR} from the SRRFT block, by using the restored currents from the SERS, are then used by the RBFNI and the RBFNC as the restored actual plant outputs for continuous online identification and control. This provides a fault-tolerant control for the SSSC. If there are no sensors missing, the vector Y_R is exactly the same as the actual plant output vector Y.

4.3.2 Design of the Radial Basis Function Neuroidentifier

The RBFNI is developed using the nonlinear autoregressive moving average with exogenous inputs (NARMAX) model and radial basis function neural network (RBFNN) [28] (see Section 3.2). As shown in Figure 4.4, the plant inputs U = [v_{cd}, v_{cq}] and the restored plant outputs Y_R = [i_{dR}, i_{qR}] at time k, k–1, and k–2 are fed into the RBFNI to provide an estimate $\hat{Y} = [\hat{i}_d, \hat{i}_q]$ of the plant output at time k+1. The RBFNI is trained to provide a dynamic predictive plant model at all times; this model is then used for training the RBFNC.

The RBFNI is pretrained offline using a suitably selected training data set A, as discussed in Section 3.3.1. To form the training data set in the forced training, the two PI

controllers (PI_d, PI_q) are deactivated, and the small pseudorandom binary signals (PRBS), given by

$$PRBS\_v_{cd}(k) = 0.1 \cdot |v_{cdS}| \cdot [r2(k) + r3(k) + r5(k)]/3 \tag{4.7}$$

$$PRBS\_v_{cq}(k) = 0.1 \cdot |v_{cqS}| \cdot [r2(k) + r3(k) + r5(k)]/3 \tag{4.8}$$

are imposed from an external source and added to the steady-state plant inputs v_{cdS} and v_{cqS} as the forced disturbances to disturb the plant as well as the RBFNI at each time step k, as shown in Figure 4.3. In (4.7) and (4.8), $r2$, $r3$ and $r5$ are the uniformly distributed random numbers in [-1, 1] with frequencies 2 Hz, 3 Hz, and 5 Hz, respectively; $|v_{cdS}|$ and $|v_{cqS}|$ are the magnitudes of v_{cdS} and v_{cqS}, respectively.

The parameters of the RBFNI are determined as follows. The RBF centers are determined by a k-means clustering algorithm [91] using the selected training data set A; the RBF widths are then calculated by (3.3), in which p is chosen to be the same as the number of RBF units h in the hidden layer; the output weights of the RBFNI are then calculated by singular value decomposition (SVD) method [28]. However, the widths given by (3.3) are still nonoptimal and can be optimized to achieve an optimal RBFNN with fewer RBF units and a better performance [110]. Following the method in [110], the RBF widths are optimized by PSO algorithm for a given number of RBF units. By training the RBFNI with optimized widths over the training data set A, the performances of the RBFNI using different numbers of RBF units, are compared. It is found that any further increase of the RBF units over 25 gives negligible further improvement of the RBFNI performance. Therefore, the dimensions of the input, hidden, and output layers of the RBFNI are 12×25×6.

4.3.3 Design of the Radial Basis Function Neurocontroller

The RBFNC is used to replace two conventional PI controllers in Figure 4.3. As shown in Figure 4.4, the RBFNC uses the plant outputs $Y_R = [i_{dR}, i_{qR}]$ at time k–1, k–2,

and k–3 as its inputs, and then generates the control signals $U(k) = [v_{cd}(k), v_{cq}(k)]$ as the plant inputs to drive the plant outputs to the desired values.

The RBFNC is firstly pretrained offline to learn the dynamics of the CONVC. This ensures that the whole system, consisting of the FTIANC and the plant, remains stable. Similar to the pretraining of the RBFNI, the pretraining data set for the RBFNC is collected from two sets of training, forced training and natural training. During the forced training, the following forced PRBS

$$PRBS\_P_{in,ref}(k) = 0.05 \cdot |P_{in,ref}| \cdot [r2(k) + r3(k) + r5(k)]/3 \tag{4.9}$$

is added to the reference value of the turbine input power to disturb the plant (with switch S2 closed in Figure 4.2). In (4.9), $P_{in,ref}$ is the reference value of the turbine input power; $r2$, $r3$, and $r5$ are the same as those in (4.7) and (4.8). The forced and natural training are carried out at several different operating points to form the pretraining data set, given by

$$\underline{\mathrm{B}} = \{\underline{\mathrm{S}}, \underline{\mathrm{Z}}\} = \left\{ \bigcup_{i=1}^{m} \underline{\mathrm{B}}_{\mathrm{F}i}, \bigcup_{i=1}^{m} \bigcup_{j=1}^{n} \underline{\mathrm{B}}_{\mathrm{N}ij} \right\} \tag{4.10}$$

where $\underline{\mathrm{B}}$ is the entire pretraining data set selected from m operating points; $\underline{\mathrm{S}}$ is the output data sets of the plant and also the input data sets of the RBFNC; $\underline{\mathrm{Z}}$ is the input data sets of the plant and also the output data sets of the CONVC; $\underline{\mathrm{B}}_{\mathrm{F}i}$ is the subset collected from the forced training at the operating point i; $\underline{\mathrm{B}}_{\mathrm{N}ij}$ is the subset collected from the natural training caused by the j^{th} natural disturbance event at the operating point i. The selected pretraining data set ensures that the RBFNC can track the CONVC dynamics over a wide operating range. During this stage, the plant is controlled by the CONVC instead of the RBFNC (with switch S1 in position 1 in Figure 4.2) because the RBFNC has not yet learned the correct control behavior. Following the approach for the RBFNI, the parameters of the RBFNC, including the number of RFB units, the RBF centers, widths, and the output weights, are determined offline using the pretraining data set $\underline{\mathrm{B}}$.

Consequently, the dimensions of the input, hidden, and output layers of the RBFNC are 6×15×6.

Once the RBFNC has learned the dynamics of the CONVC, the RBFNC is applied to control the plant (with switch S1 in position 2 in Figure 4.2) and the output weights of the RBFNC are adapted further online to achieve better performance. Online training of the RBFNC takes place with the pretrained RBFNI in cascade with the reference model, as shown in Figure 4.4. The reference model utilizes the reference inputs R^* to generate the desired plant outputs Y^* at each time step, which are used to guide the plant outputs $Y = [i_d, i_q]$ to a desired steady-state set point. In this application, $R^* = [P^*, Q^*]$ are used as the reference inputs; thereby Y^* are calculated to be the constant values $[i_d^*, i_q^*]$ at each time step. The error signal $J_d(k+1)$ $(=½\|E_d(k+1)\|^2)$, where $E_d(k+1)$ is the difference between the desired outputs Y^* of the reference model and the estimated output $\hat{Y}$ of the RBFNI at time $k+1$, is propagated back through the RBFNI (without changing its weights) to form the error vector $E_C(k)$. This error vector is then used to train the RBFNC before the next sampling instant. During this stage, the output weights of the RBFNI can also be adapted online to the unexpected operating conditions where it has not been pretrained offline [26]. The online training is carried out at different operating points by applying the forced and natural training as well. When a desired performance is achieved, the training stops and the RBFNC with fixed parameters is then used to control the plant.

4.3.4 Design of the Sensor Evaluation and (Missing Sensor) Restoration Scheme

4.3.4.1 Overall Structure of the Sensor Evaluation and (Missing Sensor) Restoration Scheme

The SERS consists of three cascaded MSR blocks with different priorities as shown in Figure 4.5. Each MSR has the same structure as shown in Figure 4.1. Since the vectors $v_{c,abc}$ and $i_{r,abc}$ are irrelevant to the performances of the RBFNI and RBFNC, the

three MSR blocks are only used to evaluate and restore the three crucial current sensor measurements in the vector i_{abc}. However, the sensor data in $v_{c,abc}$ and $i_{r,abc}$ provide the necessary data redundancy among the inputs of the SERS. Therefore, a necessary condition for the SERS to work is that v_{ca}, v_{cb}, v_{cc}, i_{ra}, i_{rb}, and i_{rc} are all available. This condition is determined by the following relationships. Since the transmission systems of a power network normally operate under a nearly balanced three-phase condition, the three-phase voltages, v_{ca}, v_{cb} and v_{cc}, and the three-phase currents, i_{ra}, i_{rb}, and i_{rc}, should approximately satisfy the following equations.

$$v_{ca} + v_{cb} + v_{cc} = 0 \tag{4.11}$$

$$i_{ra} + i_{rb} + i_{rc} = 0 \tag{4.12}$$

The real systems are not ideally balanced. A realistic expression for (4.11) and (4.12) can be written as follows, which are usually true at the transmission level where an SSSC would be connected.

$$| v_{ca} + v_{cb} + v_{cc} | < \sigma_1 \tag{4.13}$$

$$| i_{ra} + i_{rb} + i_{rc} | < \sigma_2 \tag{4.14}$$

where σ_1 and σ_2 are predetermined small threshold values.

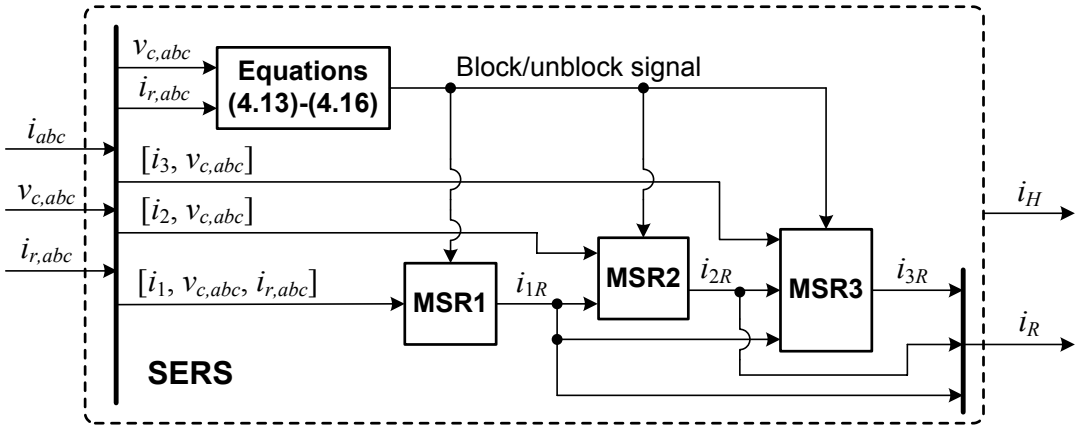

Figure 4.5: Structure of the SERS.

If the system is under normal balanced operating conditions, but the above relationships (4.13) or (4.14) are not satisfied, it indicates that one or more sensors in $v_{c,abc}$ and $i_{r,abc}$ are missing. However, if v_{ca}, v_{cb} and v_{cc} are all missing, there might be $v_{ca} = v_{cb} = v_{cc} = 0$ and therefore (4.13) is satisfied. To distinguish this case from the case of no missing sensor, another equation is used, given by

$$| v_{ca} | < \sigma_1 \text{ and } | v_{cb} | < \sigma_1 \text{ and } | v_{cc} | < \sigma_1 \tag{4.15}$$

Based on (4.13) and (4.15), there exists three scenarios of the sensor data in the vector $v_{c,abc}$: if (4.13) is satisfied but (4.15) is not satisfied, there is no sensor missing; if (4.13) is not satisfied, there are one or more sensors missing; if (4.13) and (4.15) are both satisfied, v_{ca}, v_{cb} and v_{cc} are all missing. A similar equation can be used for the vector $i_{r,abc}$, given by

$$| i_{ra} | < \sigma_2 \text{ and } | i_{rb} | < \sigma_2 \text{ and } | i_{rc} | < \sigma_2 \tag{4.16}$$

Equations (4.13)-(4.16) are implemented by the module "Equations (4.13)-(4.16)" (as shown in Figure 4.5) to evaluate the integrity of the sensor data in $v_{c,abc}$ and $i_{r,abc}$. If any sensor data in $v_{c,abc}$ and $i_{r,abc}$ is missing, it sends a signal to block the three MSR modules. Otherwise, it sends an unblock signal to the three MSR modules, which are then activated for sensor evaluation and missing sensor restoration.

Each MSR only performs a one-dimensional search to restore one missing sensor measurement. Therefore, the input current vector i_1 of MSR1 only consists of one current measurement (i.e., $i_1 = i_a$ or i_b or i_c). If i_1 is missing, it is restored by MSR1 and the restored value i_{1R} is then used as the healthy input for MSR2. Consequently, the input current vector i_2 of MSR2 consists of two current measurements: one is the same as i_1, the other is any one of the two currents not being used by MSR1. Finally, the input current vector i_3 of MSR3 consists of all of the three current measurements, i_a, i_b, and i_c. In addition, the input vector of each MSR also contains the voltage vector $v_{c,abc}$, which provides the required redundancy for missing sensor restoration. In this design, the three current vectors at the inputs of three MSR blocks are $i_1 = i_a$, $i_2 = [i_a, i_c]$, and $i_3 = i_{abc} = [i_a,$

i_b, i_c], respectively. The variables i_{1R} ($i_{1R} = i_{aR}$), i_{2R} ($i_{2R} = i_{aR}$ or i_{cR}), and i_{3R} ($i_{3R} = i_{aR}$ or i_{bR} or i_{cR}) represent the restored sensor data from MSR1, MSR2 and MSR3, respectively. If several MSR blocks end up restoring the same missing sensor data, the finally restored value is chosen from the MSR with the highest priority.

The use of the cascading structure to design the SERS is based on the following reasoning. 1) This structure enables the SERS itself to evaluate the status of the crucial sensor measurements and detect which sensor or sensors are missing, instead of relying on a sensor evaluation scheme in [87] or a sensor monitor in [100]. 2) Each MSR only searches in a one-dimensional space to restore one missing sensor measurement, which is faster than only using one MSR [87], [100] to search in a multidimensional space in order to restore multiple missing sensor measurements. In this application, each MSR converges within 20 iterations to restore one missing sensor measurement. 3) The required degree of data redundancy for restoring one missing sensor is lower than that of restoring multiple missing sensors for each MSR, and therefore, fewer sensor data need to be used.

The performance of the MSR relies on the data dependency at its input. Higher dependency among input data means a better performance of the MSR. During balanced operation, the three-phase currents, i_a, i_b, and i_c, approximately satisfy the following equation:

$$i_a + i_b + i_c = 0 \tag{4.17}$$

Therefore, a strong dependency is present among the three current variables i_a, i_b, and i_c and this relationship is used for designing the MSR3 block.

It is necessary to use three additional variables, $i_{r,abc} = [i_{ra}, i_{rb}, i_{rc}]$, as the inputs of MSR1 in order to provide enough redundancy among the input data of MSR1 (Other additional variables instead of I_r can be used). The effect of using or not using $i_{r,abc}$ on the performance of MSR1 is demonstrated by simulation studies as shown in Figure 4.6. Assuming that i_a is missing, Figure 4.6 shows the actual value i_a, the restored values i_{aR1}

by MSR1 without $i_{r,abc}$ as inputs [$i_{aR1}(4)$], and with $i_{r,abc}$ as inputs [$i_{aR1}(7)$]; the corresponding estimation/restoration errors $e_{a1}(4)$ and $e_{a1}(7)$ [$e_{a1}(\cdot) = |i_a(\cdot) - i_{aR1}(\cdot)|$] of MSR1 without and with $i_{r,abc}$ as inputs are also shown in Figure 4.6, respectively. The error $e_{a1}(7)$ (with $i_{r,abc}$ as the inputs of MSR1) is always kept within 0.025 kA at any time step, which is less than 3% of the magnitude of the missing sensor data i_a. However, the error $e_{a1}(4)$ (without $i_{r,abc}$ as the inputs of MSR1) is much larger than $e_{a1}(7)$ and reaches 0.2 kA (almost 25% of the magnitude of i_a) at some time steps. These results indicate that the performance of MSR1 is improved significantly by using three additional variables, $i_{r,abc} = [i_{ra}, i_{rb}, i_{rc}]$.

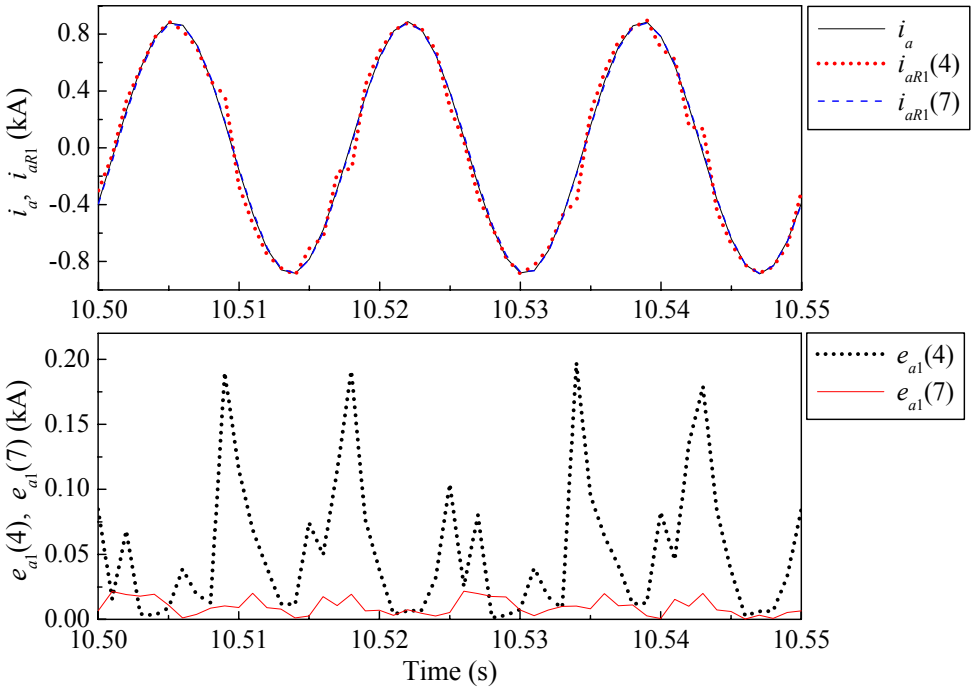

Figure 4.6: Comparison of performances of MSR1 with and without $i_{r,abc}$ as inputs.

In order to determine the order of priorities of the three MSR blocks, simulation studies are carried out to compare their performances for cases of missing sensor restoration; the results are shown in Figure 4.7. Assuming that i_a is missing and MSR1 uses $i_{r,abc}$ as inputs, Figure 4.7 shows the actual value i_a, the restored values i_{aR1} from

MSR1, i_{aR2} from MSR2, and i_{aR3} from MSR3, as well as the corresponding estimation errors e_{a1}, e_{a2}, and e_{a3} ($e_{a1} = | i_a - i_{aR1}|$), $e_{a2} = | i_a - i_{aR2}|$, $e_{a3} = | i_a - i_{aR3}|$), respectively. In this test, the PSO in all three MSR blocks uses the same fixed number of iterations to search for the estimated value of the missing sensor i_a at each time step. These results clearly indicate that MSR3 has the best performance, and the performance of MSR2 degrades a little compared to MSR3 but it is better than MSR1. Moreover, MSR2 and MSR3 use less sensor data than MSR1. Therefore, the priority of restoring the same missing sensor decreases in the following order - MSR3, MSR2, and MSR1.

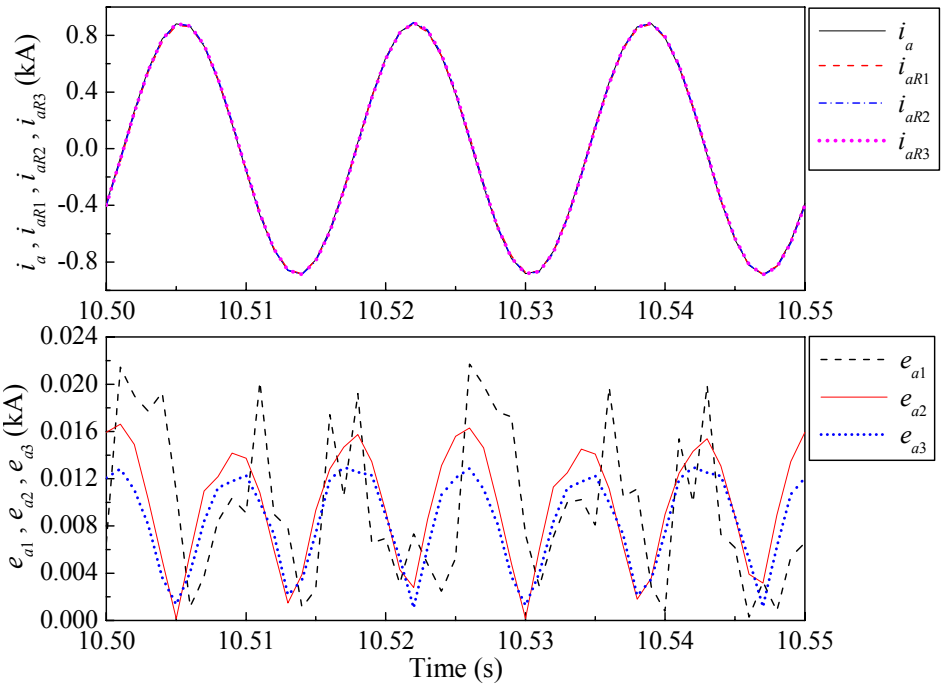

Figure 4.7: Comparison of performances of three MSR blocks.

To determine the number of hidden-layer neurons of the auto-encoder in each MSR, three requirements should be considered. First, a necessary condition for the auto-encoder to work correctly is that the number of healthy inputs must equal or exceed the number of degrees of freedom in the hidden layer. Second, the number of hidden-layer neurons should be as few as possible to reduce the real-time computational cost. Finally, to

reproduce the auto-encoder's inputs at its output layer, the number of hidden-layer neurons must be sufficient. Based on these requirements and the discussions in the previous paragraphs, the dimensions of the input, hidden and output layers of the auto-encoders in MSR1, MSR2 and MSR3 are chosen to be 21×12×21, 15×10×15, and 18×12×18, respectively. The output vector of the SERS, i_R, contains the total restored sensor measurements from all three MSR blocks; but i_H, contains other healthy sensor readings in the vector i_{abc}. The variables, [i_R, i_H], are transformed into the d-axis and q-axis current components, i_{dR} and i_{qR}, by applying the SRRFT.

4.3.4.2 Training of the Auto-Encoders

The training of the auto-encoder in each of the three MSR blocks requires that all sensor data in $v_{c,abc}$, $i_{r,abc}$, and i_{abc} are available. The integrity of the sensor data in $v_{c,abc}$ and $i_{r,abc}$ are evaluated by the module "Equations (4.13)-(4.16)" as shown in Figure 4.5. The integrity of the sensor data in the crucial vector i_{abc} can be preevaluated by two equations similar to (4.13)-(4.16), given by

$$| i_a + i_b + i_c | < \sigma_3 \tag{4.18}$$

$$| i_a | < \sigma_3 \text{ and } | i_b | < \sigma_3 \text{ and } | i_c | < \sigma_3 \tag{4.19}$$

If (4.18) is satisfied but (4.19) is not satisfied, there is no sensor in i_{abc} missing; otherwise, some sensors in i_{abc} are missing. The three auto-encoders are continuously trained online simultaneously without any missing sensor. By feeding forward the data through the auto-encoder and adjusting its weight matrices (using the backpropagation algorithm) W and V, the auto-encoder is trained to map its inputs to its outputs as shown in Figure 4.1(a). After training for every N_T time steps, the weights of each auto-encoder are frozen for N_E time steps to evaluate the convergence of the auto-encoder. During the evaluation, if the error $||E_S||$ of each auto-encoder is beyond a specified threshold value, μ, at any evaluation time step, the training resumes for the next N_T time steps. Otherwise, if the error $||E_S||$ of each auto-encoder is below the threshold value μ during the entire N_E time

steps, the training stops and the auto-encoder is used for sensor evaluation and missing sensor restoration. If the system changes to a new operating point, the error $||E_S||$ might be beyond the threshold value μ again. In such a case, if there is no sensor missing [determined by (4.13)-(4.16), (4.18) and (4.19)], the training resumes to adapt to this new operating point.

4.3.4.3 Sensor Evaluation and Missing Sensor Restoration

The entire sensor evaluation and missing sensor restoration procedure of the SERS is implemented in four stages as shown in Figure 4.8. In the first three stages, the SERS evaluates the status of the three current measurements i_a, i_b, and i_c by checking the value of the error signal $||E_S||$ of each auto-encoder as shown in Figure 4.1. During a normal operating condition, with a well-trained auto-encoder, $||E_S||$ should be acceptably small (In practical applications, a threshold value can be specified depending on the system properties). If one or more sensors are missing, the outputs of the auto-encoder no longer match its inputs and the value of $||E_S||$ becomes significant.

The sensor evaluation process is illustrated in Table 4.1, in which the positive sign, +, indicates that the value of $||E_S||$ of the corresponding MSR is significant; while the negative sign, -, indicates that the value of $||E_S||$ of the corresponding MSR is below a prespecified threshold value, ε. Table 4.1 gives all eight cases of the status of i_a, i_b, and i_c which can be determined in only three stages as follows. Stage I indicates that there is no restoration action from any MSR and all the MSR blocks are only used to check the value of $||E_S||$. Stage II indicates that MSR1 is activated to restore the missing current i_a, and all the MSR blocks are also used to check the value of $||E_S||$. Stage III indicates that MSR2 is activated to restore the missing current i_a or i_c, and all the MSR blocks are also used to check the value of $||E_S||$. In each stage, the restored missing data is used as the estimated healthy data required by the next stage.

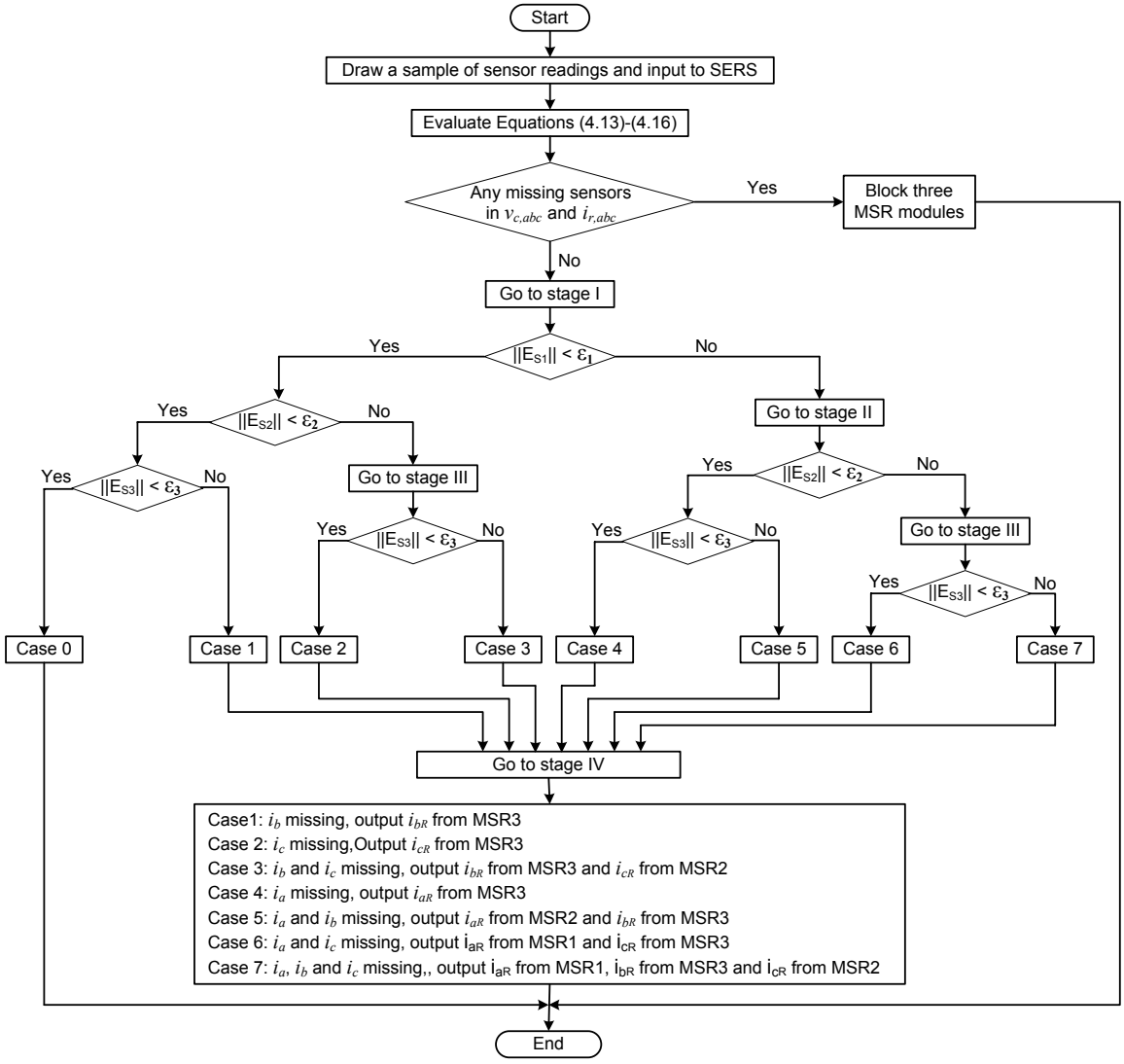

Figure 4.8: Flowchart of sensor evaluation and missing sensor restoration procedure.

The eight cases can be separated into four groups. The first group contains cases 0 and 1, which can be determined directly in stage I. The second group contains cases 2 and 3, which can be determined by stages I and III. In stage I, both cases indicate that i_a is not missing but that i_c is missing, therefore moving to stage III. In stage III, i_c is restored by MSR2, therefore cases 2 and 3 can be distinguished by the sign of MSR3. The third group contains cases 4 and 5, which is determined by stages I and II. The fourth group contains cases 6 and 7, which must be determined by all three stages. In

stage I, all of the four cases in groups 3 and 4 indicate the same results, i.e., i_a is missing, therefore going to stage II. In stage II, i_a is restored by MSR1. Group 3 is distinguished from group 4 because i_c is not missing, which is indicated by the sign of MSR2. Thereafter, cases 4 and 5 in group 3 are separated directly by checking the sign of MSR3. A positive sign of MSR2 in stage II indicates that the cases fall into group 4. Therefore the checking procedure goes to stage III, in which MSR2 restores the missing current i_c. Finally, cases 6 and 7 are separated by the sign of MSR3.

Table 4.1: Sensor evaluation

Group No.	Case No.	Missing Sensors	Stage I: No action			Stage II: MSR1 action			Stage III: MSR2 action		
			MSR1	MSR2	MSR3	MSR1	MSR2	MSR3	MSR1	MSR2	MSR3
1	0	none	–	–	–						
	1	i_b	–	–	+						
2	2	i_c	–	+	+				–	–	–
	3	i_b, i_c	–	+	+				–	–	+
3	4	i_a	+	+	+	–	–	–			
	5	i_a, i_b	+	+	+	–	–	+			
4	6	i_a, i_c	+	+	+	–	+	+	–	–	–
	7	i_a, i_b, i_c	+	+	+	–	+	+	–	–	+

If the SERS detects that one or more current sensors are missing, the procedure goes to the last stage IV, in which MSR3 is activated to restore one missing sensor. Other missing sensors (if they exist) take the values that are restored in the previous three stages. Table 4.2 shows the restored missing sensor by each MSR during stages II, III, and IV in each case. It is important to note that in any stage, each MSR only performs a one-dimensional search to restore one missing sensor. In addition, one missing sensor may be restored by more than one MSR during the four stages, e.g., i_a in case 4, or i_c in

cases 2 and 6. In order to select only one restored value for each missing sensor, the three MSR blocks are set with different priorities, as explained in Section 4.3.4.1. Since MSR3 has the highest priority, it is always activated to restore one missing sensor in the last stage IV. If the same missing sensor is restored by more than one MSR, the finally restored value comes from the MSR with the highest priority. In Table 4.2, the variables in the blank spaces with X represent the restored sensor values which are not used.

Table 4.2: Missing sensor restoration

Case No.	Missing Sensors	Restored Sensors		
		MSR1	MSR2	MSR3
1	i_b			i_{bR}
2	i_c		~~i_{cR}~~	i_{cR}
3	i_b, i_c		i_{cR}	i_{bR}
4	i_a	~~i_{aR}~~		i_{aR}
5	i_a, i_b		i_{aR}	i_{bR}
6	i_a, i_c	i_{aR}	~~i_{cR}~~	i_{cR}
7	i_a, i_b, i_c	i_{aR}	i_{cR}	i_{bR}

4.3.4.4 Unbalanced Operations

The balanced and unbalanced operations can be distinguished by using (4.13), (4.14), and (4.18). If (4.13), (4.14), and (4.18) are all not satisfied, the system is under unbalanced operating conditions, and vice versa. However, if only one or two of (4.13), (4.14), and (4.18) are not satisfied, the system is operated at a balanced operating condition and some sensors are missing. Here a reasonable assumption is that all three vectors $v_{c,abc}$, $i_{r,abc}$, and i_{abc}, simultaneously containing missing sensors will never happen.

Depending on the duration, the types of unbalanced operations can be divided into two main categories: long-term or steady-state unbalanced operations and short-term

unbalanced operations [111]. The long-term unbalanced operations are mainly caused by unbalanced load, transformer with different single phase units, untransposed transmission lines, etc. The effects of long-term unbalanced operations are normally small since the transmission system is still close to balanced operation [111].

The short-term unbalanced operations are mainly caused by unbalanced grid faults [111], including the single-phase-to-ground fault, phase-to-phase fault, etc. Under such conditions, the transmission systems experience a short-term strongly unbalanced operation (e.g., typically 50-200 ms) during the fault, and return to the balanced three-phase operation after the fault is cleared. If some sensor data are missing while an unbalanced fault occurs, (4.13)-(4.16), (4.18) and (4.19) will not be applicable to evaluate the status of the sensor data during the short-term unbalanced fault. Therefore, the following scenarios must be considered separately: 1) some sensor data are missing during normal operations and no unbalanced fault occurs; 2) some sensor data are missing from a moment during normal operations and thereafter an unbalanced fault occurs before the missing sensors are fixed; 3) some sensor data are missing from a moment during an unbalanced fault; 4) some sensor data are missing after the unbalanced fault is cleared and no further faults occur. Since the SERS is designed for balanced operating conditions, there is no problem of the SERS's operation for Scenarios 1) and 4). However for Scenario 2), the block signals from the "Equations (4.13)-(4.16)" module as shown in Figure 4.5 must be ignored during the short-term fault condition such that the SERS can continue to restore the missing sensors. The fault conditions can be detected by utilizing the signals from the protection devices that have been installed for the transmission lines. For Scenario 3), the three MSR modules are blocked during the fault and unblocked after the fault is cleared. Since the fault only exists for a very short time, Scenario 3) rarely happens. Even if it happens, blocking the MSR modules for a short period does not have any notable effect on the entire system performance.

4.4 Simulation Study on an SMIB Power System

The dynamic performance of the proposed FTIANC is evaluated at two different operating points by applying three-phase and single-phase short circuits to the system in Figure 4.2. During the simulations at each operating point, at first only two and then all of the three current sensors are assumed to be missing, respectively. In a practical system, if some sensors are missing, their values may be read as zeros, some noises or some uncertain error values. However, the forms of missing sensor readings do not affect the implementation of the SERS. Therefore, during the simulation, the sensor readings are simply set as zeros if they are missing.

4.4.1 Test on a Three-Phase Fault at the Operating Point Where Controllers are Designed

The RBFNC is trained and the CONVC is tuned at a specific operating condition (called OP-I), where the generator in Figure 4.2 operates with a prefault rotor angle of 42.6°, output active power P_t = 1.0 pu, and output reactive power Q_t = 0.56 pu; the transmitted active power and reactive power at the receiving end of line 3 are regulated by the SSSC at 0.45 pu and 0.22 pu, respectively. At this operating point, about half of the generator's output active power is transmitted by line 3. A three-phase short circuit is applied to the receiving end of line 2 at t = 15 s and 100 ms thereafter, line 2 is tripped off from the system. After this grid fault, the system changes to a new operating condition with only two lines (lines 1 and 3) in service. Two missing sensor tests are then applied during this post-fault transient state.

Case I – i_b and i_c Missing: From t = 15.1 s, the current sensors i_b and i_c are assumed to be missing and restored by the SERS. The restored values i_{bR} and i_{cR} are used with the healthy current i_a together, to calculate i_{dR} and i_{qR} by applying the SRRFT.

Case II – i_a, i_b and i_c Missing: In this extreme case, for the same initial conditions as in Case I, all three current sensors i_a, i_b, and i_c are assumed to be missing and restored by

the SERS from t = 15.1 s onwards. The restored values i_{aR}, i_{bR}, and i_{cR} are used to calculate i_{dR} and i_{qR} by applying the SRRFT.

In each of the two cases, the two current components i_{dR} and i_{qR} are used by the RBFNI and the RBFNC as the actual plant outputs for online training, identification, and control. Figure 4.9 and Figure 4.11 show the actual values i_d and i_q, the restored values i_{dR} and i_{qR} by the SERS, and the estimated values $\hat{i}_d$ and $\hat{i}_q$ by the RBFNI for Cases I and II, respectively, where the two curves i_{dR} and $\hat{i}_d$ (i_{qR} and $\hat{i}_q$) are lined up on top of each other. These results indicate that with a suitably designed SERS, the missing sensor data are correctly restored, and therefore, the SERS provides a set of correct estimates, [i_{dR}, i_{qR}], of the plant outputs and complete inputs to the RBFNI. As a consequence, the RBFNI tracks the transient dynamics of the actual plant outputs i_d and i_q with good precision.

Figure 4.10 and Figure 4.12 show the results of the rotor angle δ and the 230 kV sending-end bus voltage V_s for Cases I and II, respectively. The curves CONVC indicate the system response under the condition that the SSSC is controlled by the CONVC; the curves FTIANC indicate the system response under the condition that the SSSC is controlled by the FTIANC. These results clearly show that the damping control of the FTIANC is more efficient than the CONVC during the post-fault transient state. During the first swing after the fault is applied, the FTIANC is already providing significant damping compared to that provided by the CONVC. After the fault is cleared, the FTIANC drives the plant successfully and quickly to a new operating point with a rotor angle $\delta = 46.3^{\circ}$ at the steady state. Moreover, comparing the curves by FTIANC with and without missing sensors, the control performance of the FTIANC only degrades slightly due to missing sensor data. However, the transient performance of the FTIANC with missing sensor measurements is still better than the CONVC used by the SSSC without any missing sensor. These results prove that the proposed FTIANC provides a fault-tolerant control for the SSSC.

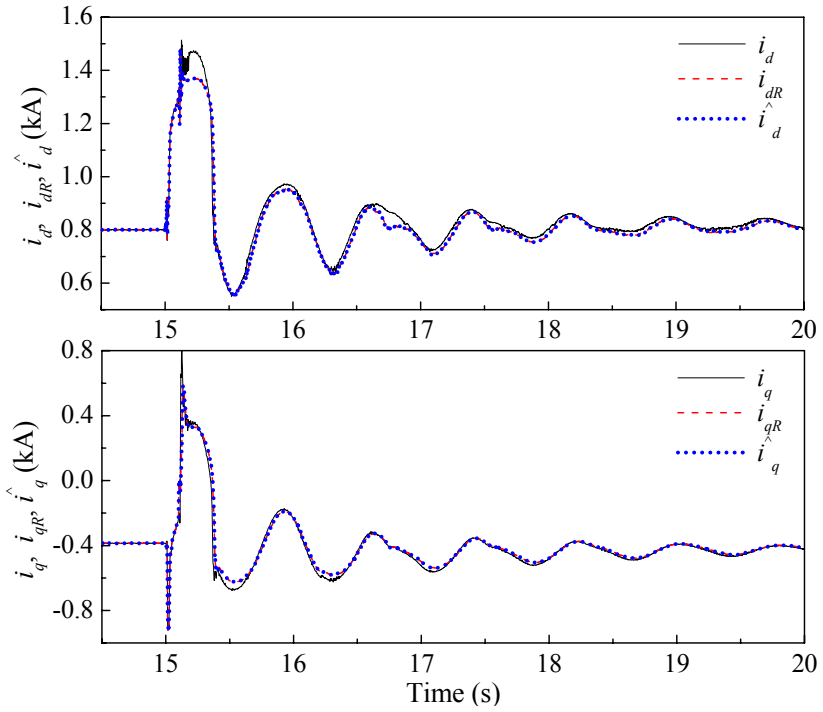

Figure 4.9: A 100 ms three-phase short circuit at 15 s at OP-I for Case I - i_b and i_c missing from 15.1 s.

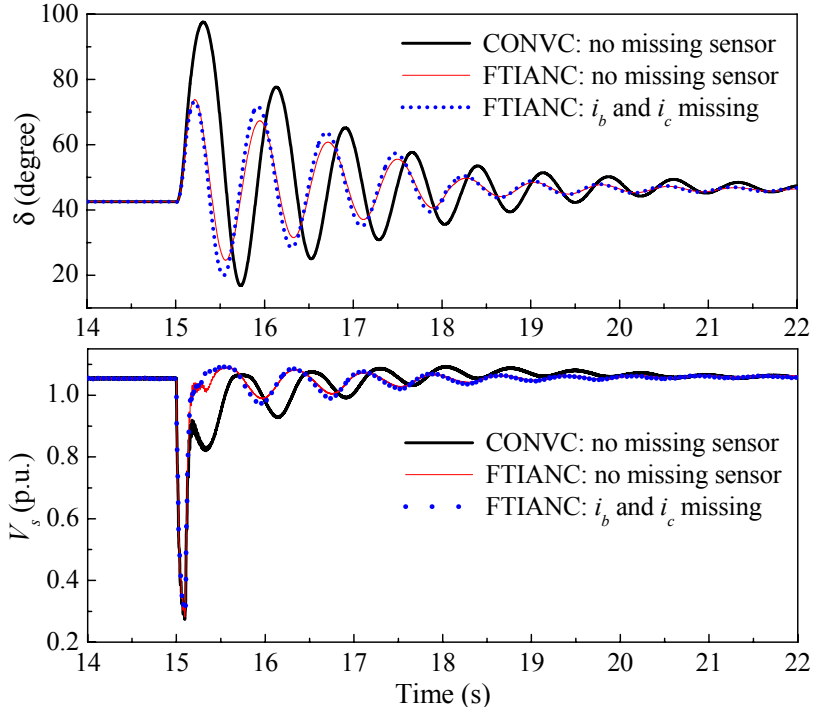

Figure 4.10: A 100 ms three-phase short circuit at 15 s at OP-I for Case I - i_b and i_c missing from 15.1 s: δ and V_s.

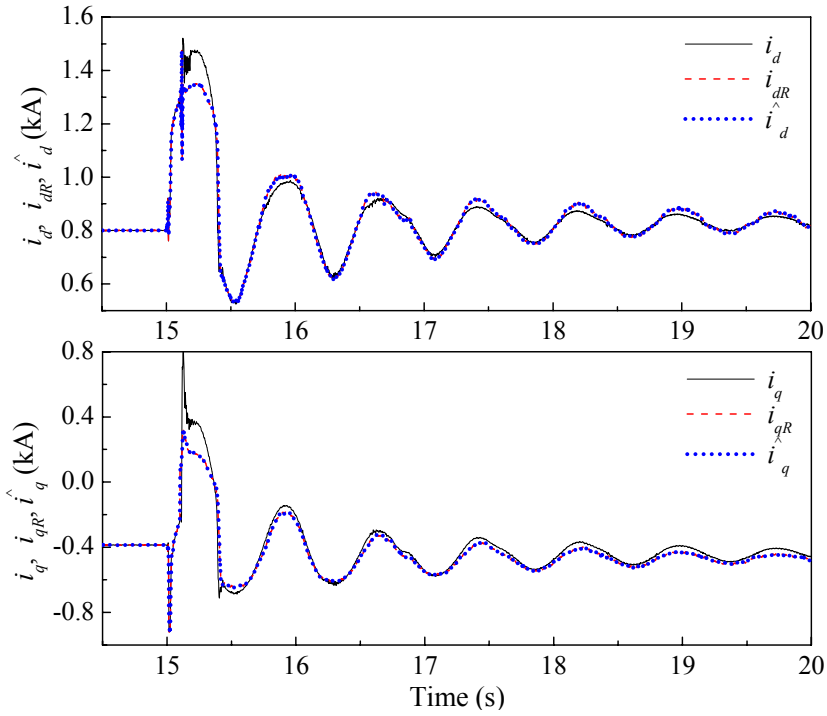

Figure 4.11: A 100 ms three-phase short circuit at 15 s at OP-I for Case II - i_a, i_b, and i_c missing from 15.1 s.

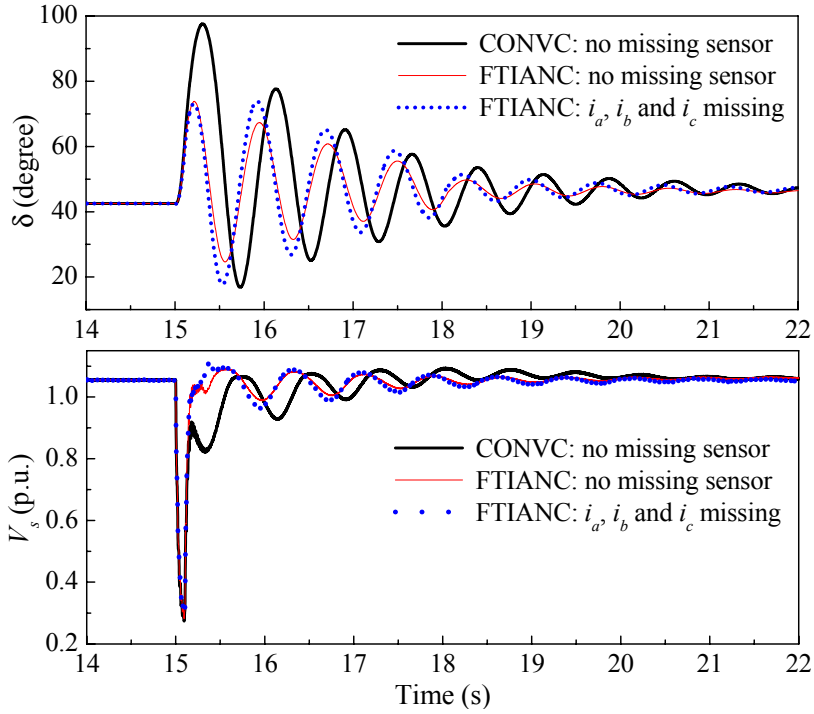

Figure 4.12: A 100 ms three-phase short circuit at 15 s at OP-I for Case II - i_a, i_b, and i_c missing from 15.1 s: δ and V_s.

4.4.2 Test on a Three-Phase Fault at a Different Operating Point

The transient performance of the FTIANC is now reevaluated at a different operating point (OP-II), where the prefault rotor angle of the generator changes to 50.1° (P_t = 1.0 pu, Q_t = 0.59 pu); P^* and Q^* are still chosen to be 0.45 pu and 0.22 pu, respectively; but line 1 is now kept open during this entire test. The parameters of the controllers are the same as those used in the test at OP-I, i.e., the RBFNC has not been trained and the CONVC has not been tuned for OP-II; but the SERS has been trained for this operating condition. A 100 ms three-phase short circuit is applied to the receiving end of line 2 at t = 15 s. Again, the same two missing sensor tests as in Section 4.4.1 are applied during this post-fault transient state: 1) Case I – from t = 15.1 s, the current sensors i_b and i_c are assumed to be missing and restored by the SERS. 2) Case II – for the same initial conditions as in Case I, all three current sensors i_a, i_b, and i_c are assumed to be missing and restored by the SERS from t = 15.1 s onwards.

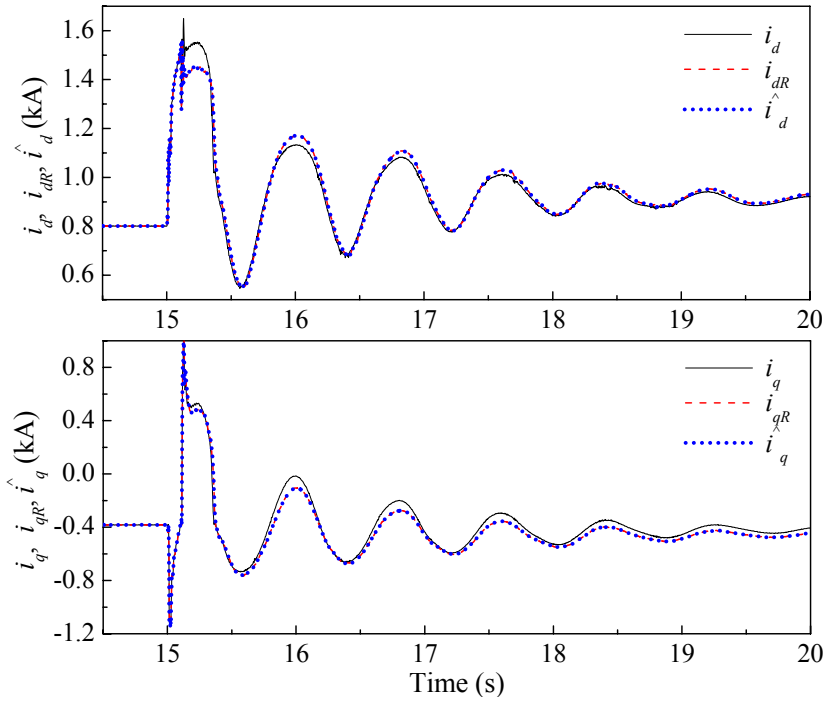

Figure 4.13: A 100 ms three-phase short circuit at 15 s at OP-II for Case I - i_b and i_c missing from 15.1 s.

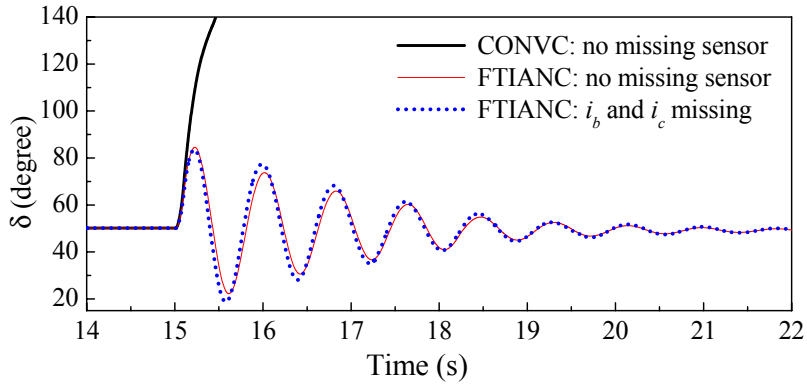

Figure 4.14: A 100 ms three-phase short circuit at 15 s at OP-II for Case I - i_b and i_c missing from 15.1 s: δ.

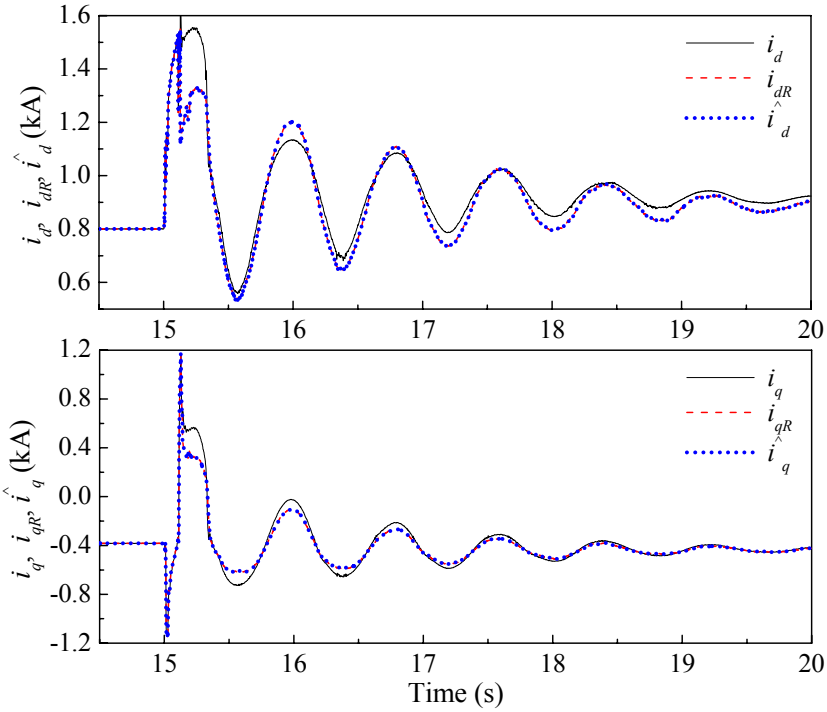

Figure 4.15: A 100 ms three-phase short circuit at 15 s at OP-II for Case II - i_a, i_b, and i_c missing from 15.1 s.

Figure 4.13 and Figure 4.15 show the actual values i_d and i_q, the restored values i_{dR} and i_{qR} by the SERS, and the estimated values $\hat{i}_d$ and $\hat{i}_q$ by the RBFNI for Cases I and II, respectively. Again, the plant outputs are correctly estimated by using the restored missing currents from the SERS as well as other healthy currents (if they exist). Consequently, the RBFNI tracks the transient dynamics of the plant with good precision.

Figure 4.14 and Figure 4.16 show the results of the rotor angle δ for Cases I and II, respectively. These results indicate that the CONVC fails to return the system back to the steady state after this large disturbance. However, the FTIANC still provides effective control, even if there are sensors missing or not. These results prove that the proposed FTIANC provides improved transient performance over the CONVC, and a fault-tolerant control for the SSSC over a wide system operating range.

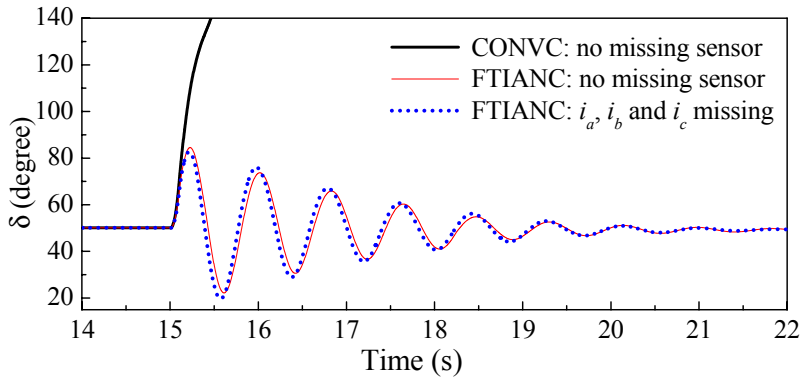

Figure 4.16: A 100 ms three-phase short circuit at 15 s at OP-II for Case II - i_a, i_b, and i_c missing from 15.1 s: δ.

4.4.3 Tests on a Single-Phase Fault at OP-II

In power system transient studies, three-phase short circuits are commonly used to evaluate the system transient performance and stability because they are the most severe faults in the power grid. However in the practical power system, most grid faults are unbalanced single-phase-to-ground faults. To further illustrate the robustness of the FTIANC, the system is now tested with a phaseA-to-ground fault at OP-II. This unbalanced fault is applied to the receiving end of line 2 at t = 15 s and is cleared after 150 ms. The system experiences an unbalanced operation during the fault, and returns to balanced three-phase operation after the fault is cleared. Two missing sensor tests are applied from t = 14 s before the fault: Case I – two current sensors i_b and i_c missing, and Case II – all three current sensors i_a, i_b, and i_c missing. Figure 4.17 and Figure 4.18 show

the results of the generator rotor angle δ and the 230 kV sending-end bus voltage V_s for Cases I and II, respectively. This single-phase fault causes a larger fault current in phase A than in phases B and C. The SERS has not been trained on this unbalanced condition, but it still provides the fault-tolerant measurements to the SSSC controllers. As a result, the control performances of the FTIANC with and without missing sensors are both superior to the CONVC without any missing sensor.

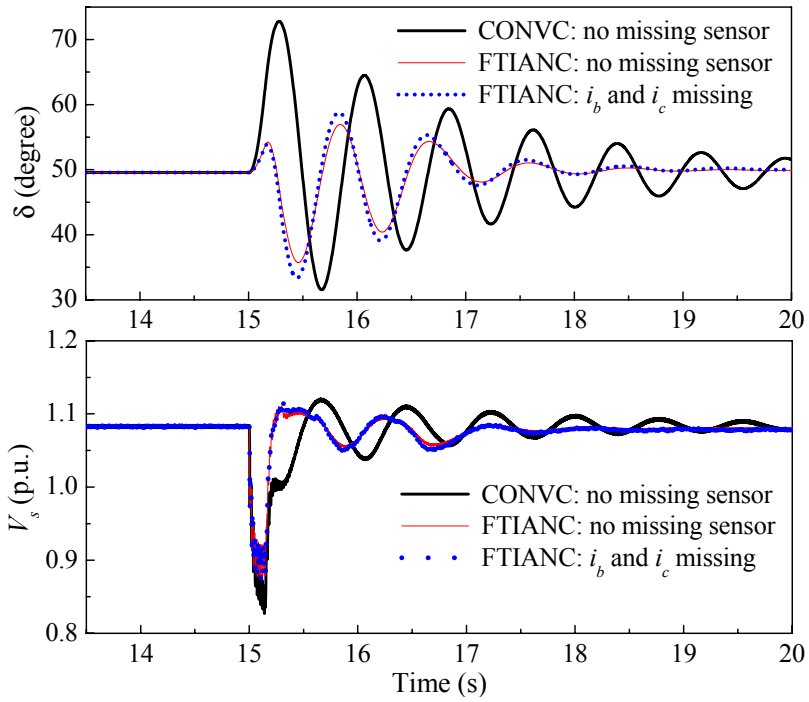

Figure 4.17: A 150 ms phaseA-to-ground short circuit at 15 s at OP-II for Case I - i_b and i_c missing from 14 s: δ and V_s.

The proposed FTIANC is also tested with other types of unbalanced faults, including the phase-to-phase fault and two-phase-to-ground fault. Results similar to those in Figure 4.17 and Figure 4.18 are obtained. The FTIANC provides effective control to the SSSC during various unbalanced faults even when two or three current sensors are missing. The simulation results in this section show that the FTIANC is able to provide a fault-tolerant robust control to the SSSC at any operating conditions in the

transmission system, including the steady-state operation, balanced and unbalanced grid faults, and change of operating conditions.

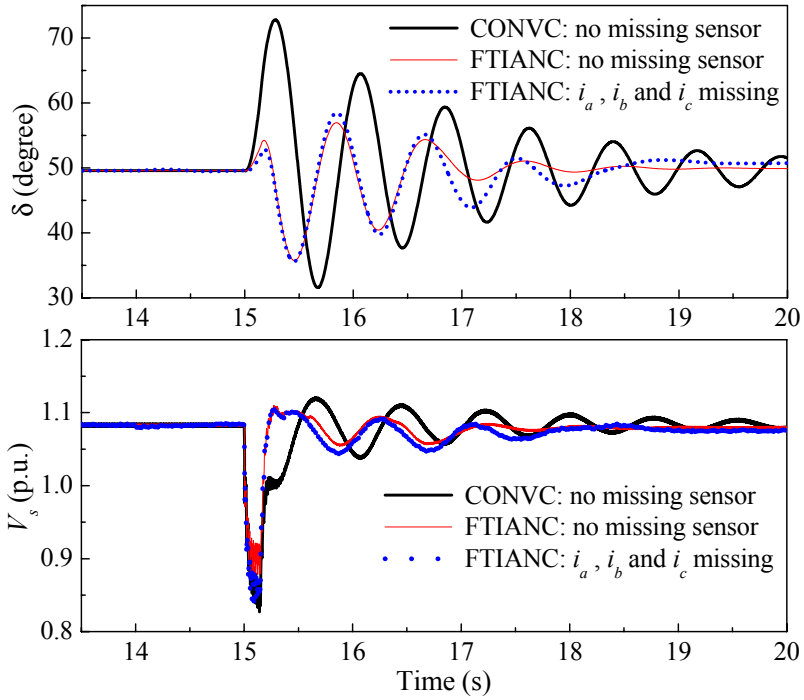

Figure 4.18: A 150 ms phaseA-to-ground short circuit at 15 s at OP-II for Case II - i_a, i_b, and i_c missing from 14 s: δ and V_s.

4.4.4 Test on a Steady-State Unbalanced Three-Phase Operation

Under balanced operation, missing one sensor might be simply restored using the relationship $i_a + i_b + i_c = 0$. However, power systems might experience unbalanced operations. In such a case, this relationship cannot be used to restore the missing sensor.

The operating condition of the system in Figure 4.2 is changed, now with line 2 open. Phase A of the electric load is open circuited causing an unbalanced operation, with phases B and C drawing a constant active power of $P_L = 0.1$ pu at a constant power factor 0.85 from the generator. It is assumed that the SERS has been trained for this unbalanced condition. Then the current sensor i_a is assumed to be missing from $t = 20$ s. The results are shown in Figure 4.19, in which $i_{aC} = 0 - i_b - i_c$. Obviously, the SERS restores the

missing current i_a correctly which cannot be calculated from the relationship $i_a + i_b + i_c = 0$.

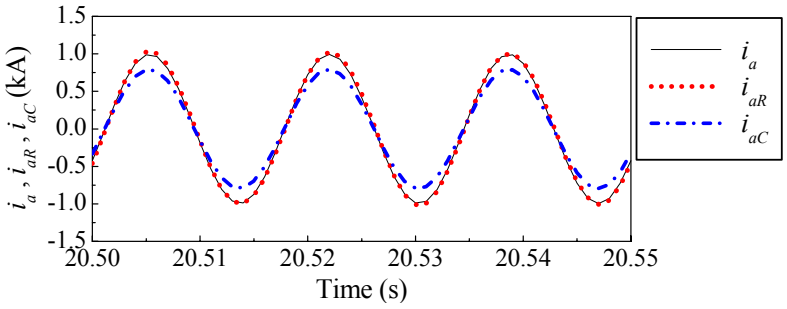

Figure 4.19: A steady-state unbalanced three-phase operation – i_a missing from 20 s: i_a, i_{aR}, and i_{aC}.

4.5 Simulation Study on the IEEE 10-Machine 39-Bus System

To demonstrate further the effectiveness of the proposed FTIANC, the IEEE 10-machine 39-bus New England system [112], [113] (see Appendix B.2) as shown in Figure 4.20 is now considered. An SSSC is connected to the bus 24 end of the transmission line 23-24 to regulate its power flows. This arrangement also improves the transient stability of this multimachine power system [114]. The same control schemes, CONVC and FTIANC, as in the SMIB system are applied to control the SSSC. In this study, G10 is modeled as a three-phase infinite source, while the other nine synchronous generators (G1-G9) are modeled in detail, with the governor/turbine and AVR/exciter dynamics taken into account, as described in Appendix B.2. The SSSC is represented by a detailed switching-level model, in which the PWM voltage source inverter is fully represented by individual GTO switches.

In this application, the crucial sensor measurements are the three-phase currents, i_a, i_b, and i_c, of line 22-24. The other two sets of measurements, which are the injected three-phase voltages of the SSSC, v_{ca}, v_{cb}, v_{cc}, and the three-phase voltages of bus 24, v_{24a}, v_{24b}, v_{24c}, are irrelevant to the performance of the SSSC controllers. They are used

by the SERS to provide the required data redundancy in order to restore the crucial missing sensor measurements.

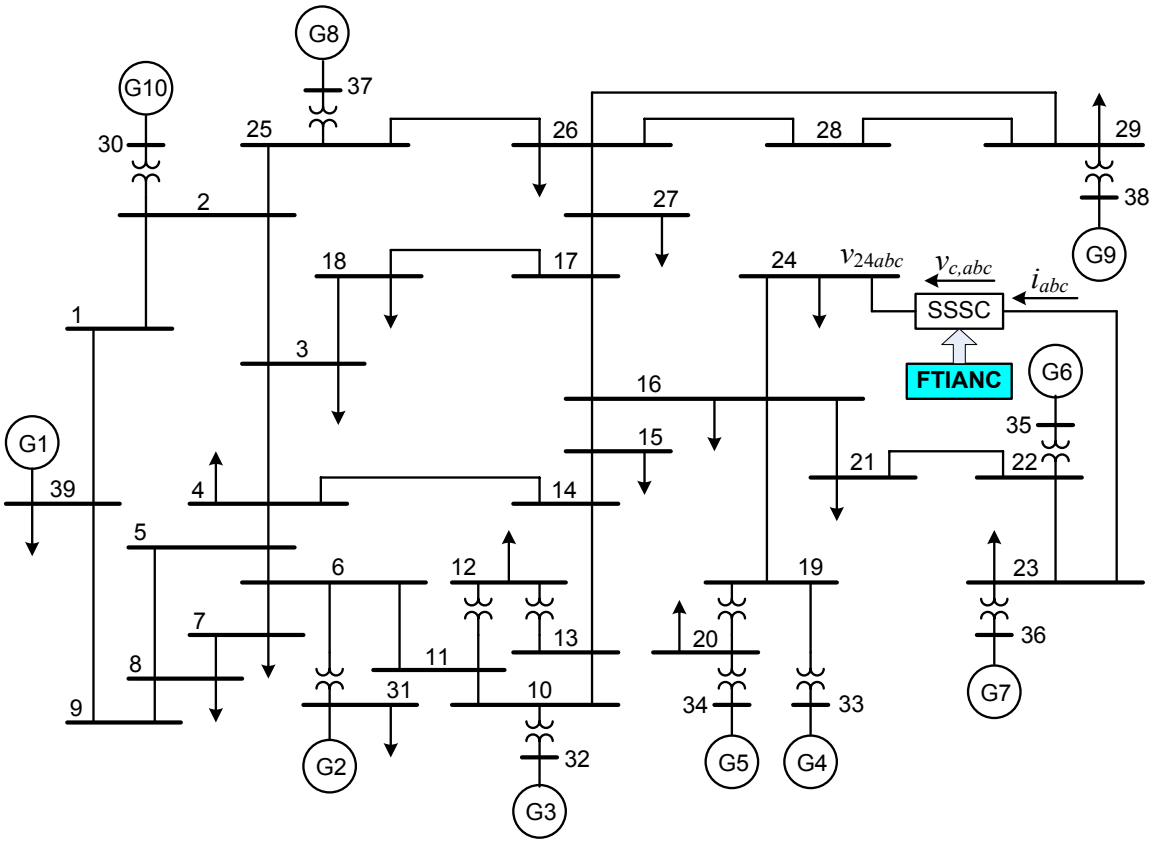

Figure 4.20: Single-line diagram of an SSSC (controlled by the FTIANC) connected to the IEEE 10-machine 39-bus New England system.

A three-phase short circuit is now applied to the bus 22 end of line 21-22 at t = 50 s, and is cleared after 150 ms. The same missing sensor tests as for the SMIB system (Cases I and II) are now applied, in which the sensor data are assumed to be missing from t = 50.15 s. Figure 4.21 and Figure 4.22 show the angular speeds of the generators 6 and 7, ω_6 and ω_7, for Cases I and II, respectively. Since the proposed SERS and FTIANC are independent of the system models, these results are similar to those in the SMIB system. The dynamic performance of the FTIANC is superior to the CONVC used by the SSSC. By using the fault-tolerant measurements from the SERS, the FTIANC provides effective

control to the SSSC when two and even all crucial current sensor measurements are missing. Moreover, the control performance of the FTIANC with missing sensors is almost the same as that without any missing sensors. Therefore, the proposed FTIANC improves the transient performance, stability, and reliability of the entire power system. The results at other operating conditions are similar to those in Figure 4.21 and Figure 4.22, and the SMIB system.

4.6 Chapter Summary

This chapter has proposed a fault-tolerant indirect adaptive neurocontrol (FTIANC) for an SSSC FACTS device. This FTIANC consists of a suitably designed sensor evaluation and (missing sensor) restoration scheme (SERS), a radial basis function neuroidentifier (RBFNI), and a radial basis function neurocontroller (RBFNC). It is able to provide effective control to the SSSC when single and multiple crucial time-varying current sensor measurements are missing.

The RBFNI is trained to provide a dynamic predictive plant model at all times; this plant model is then used for training the RBFNC. The RBFNC in turn generates the control signals to drive the actual plant outputs to the desired values. The SERS employs autoassociative neural networks as auto-encoders to capture the correlations between the redundant time-varying sensor measurements (through training). This enables the SERS to evaluate the integrity of the crucial time-varying current sensor measurements which determine the behaviors of the RBFNI and the RBFNC. If the SERS detects that one or more crucial sensor measurements are missing, it utilizes the particle swarm optimization (PSO) algorithm and the correlations established by the auto-encoders between the missing sensor data and the remaining healthy sensor data to quickly online restore the missing sensors. The restored missing sensor data are then combined with the healthy sensor data to provide a set of complete inputs for the RBFNI and the RBFNC. This provides a fault-tolerant control for the SSSC.

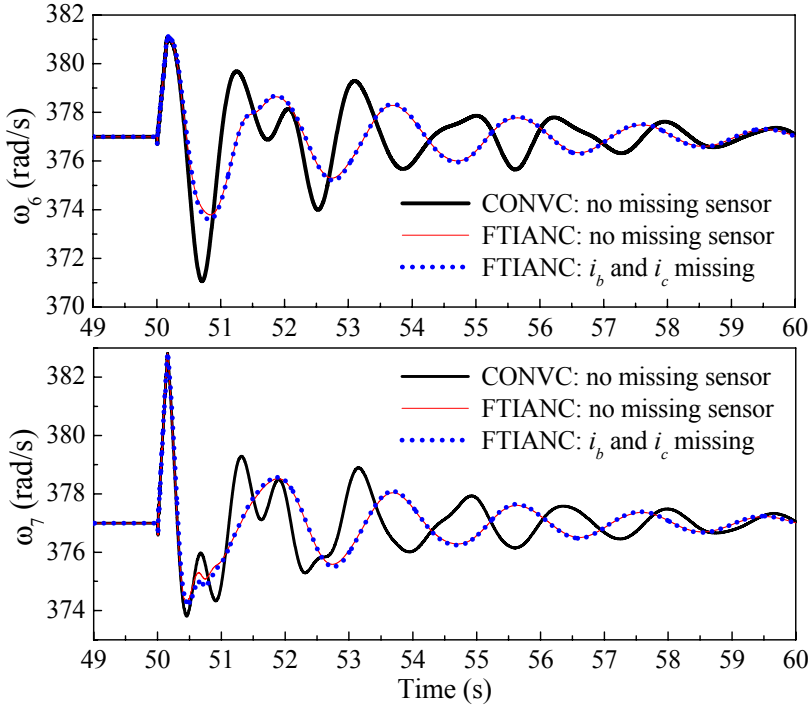

Figure 4.21: A 150 ms three-phase short circuit at 50 s for Case I - i_b and i_c missing from 50.15 s: ω_6 and ω_7.

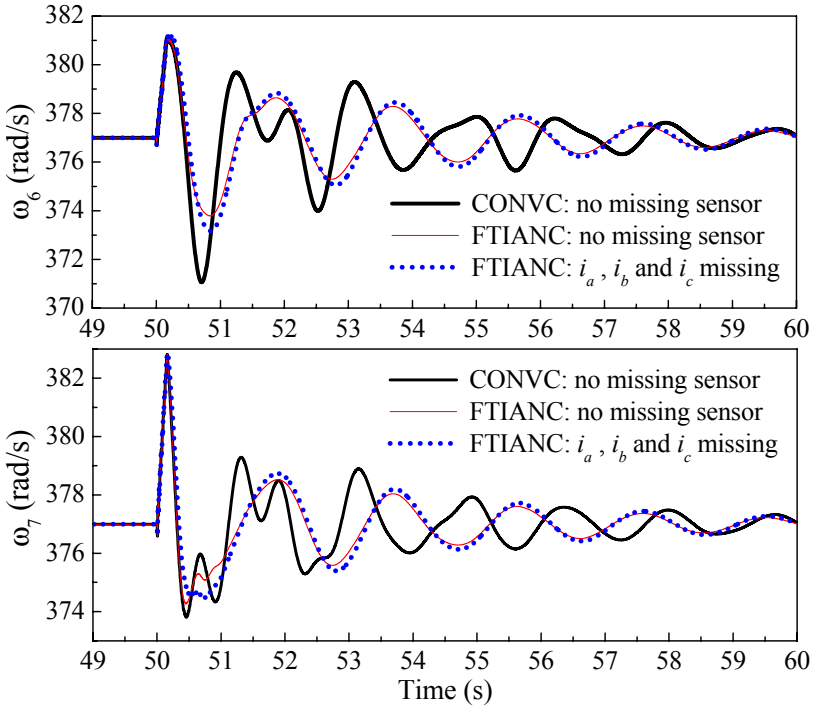

Figure 4.22: A 150 ms three-phase short circuit at 50 s for Case II - i_a, i_b, and i_c missing from 50.15 s: ω_6 and ω_7.

Simulation studies have been carried out for the SSSC connected to an SMIB power system as well as the IEEE 10-machine 39-bus power system. The proposed FTIANC with and without missing sensor measurements has been compared to a conventional PI control scheme used by the SSSC without any missing sensor measurements. Results have shown that the FTIANC improves the dynamic performance and reliability of the SSSC and the power network over a wide range of system operating conditions. The proposed fault-tolerant control is readily applicable to other plant models in power systems.

Since the proposed SERS and fault-tolerant control scheme require a certain amount of computational cost to implement, simulation studies may not be sufficient to demonstrate its effectiveness in a practical power system. In the next chapter, real-time implementations will be performed to demonstrate further the effectiveness of the SERS and the fault-tolerant control scheme using a Real Time Digital Simulator (RTDS) and DSP platform.

CHAPTER 5

MISSING-SENSOR-FAULT-TOLERANT CONTROL FOR SSSC FACTS DEVICE WITH REAL-TIME IMPLEMENTATION

Chapter 4 has proposed an online sensor evaluation and (missing sensor) restoration scheme (SERS). It provides a set of fault-tolerant complete phase current measurements for an static synchronous series compensator (SSSC) with an energy storage system. Based on the SERS, a fault-tolerant indirect adaptive neurocontrol (FTIANC) was developed to control the SSSC. The SERS and FTIANC were validated by simulation studies in PSCAD/EMTDC on a single machine infinite bus (SMIB) as well as a multimachine power system. However, an important issue related to the practical system applications was not considered. The SERS employs a particle warm optimization (PSO)-based iterative search algorithm for online missing sensor restoration. Compared to the normal sampling frequency when no sensors are missing, the restored missing sensor data might only be sent to the SSSC controllers at a reduced sampling frequency in a practical system in order to provide a sufficient period of time step to perform this online PSO search algorithm. The use of a reduced sampling frequency may have a significant effect on the controller performance. The simulation studies in Chapter 4 could not sufficiently evaluate the effect of sampling frequencies of the SERS in a practical power system. As a consequence, this issue is now investigated by real-time or hardware implementations in this chapter.

This chapter extends the work in Chapter 4 by proposing a missing-sensor-fault-tolerant control (MSFTC) for an SSSC in a power network [116]. This MSFTC contains a conventional internal and external control scheme [13], [14] (i.e., without any fault-tolerant design) cascaded with an SERS. The conventional control scheme provides the correct control actions for the SSSC under the condition that all the required sensor data

are available. The SERS is designed by using the auto-encoders and PSO. It evaluates the integrity of four sets of sensor data used by the SSSC controllers. If some sensor data are missing, it is able to detect and restore the missing sensor data and therefore provides a set of complete sensor measurements to the SSSC controllers. The resulting MSFTC therefore provides a missing-senor-fault-tolerant control for the SSSC. The proposed MSFTC is validated by a real-time implementation on an SSSC connected to the IEEE 10-machine 39-bus power system, using a Real Time Digital Simulator (RTDS) [117], [118] and TMS320C6701 DSP platform [119].

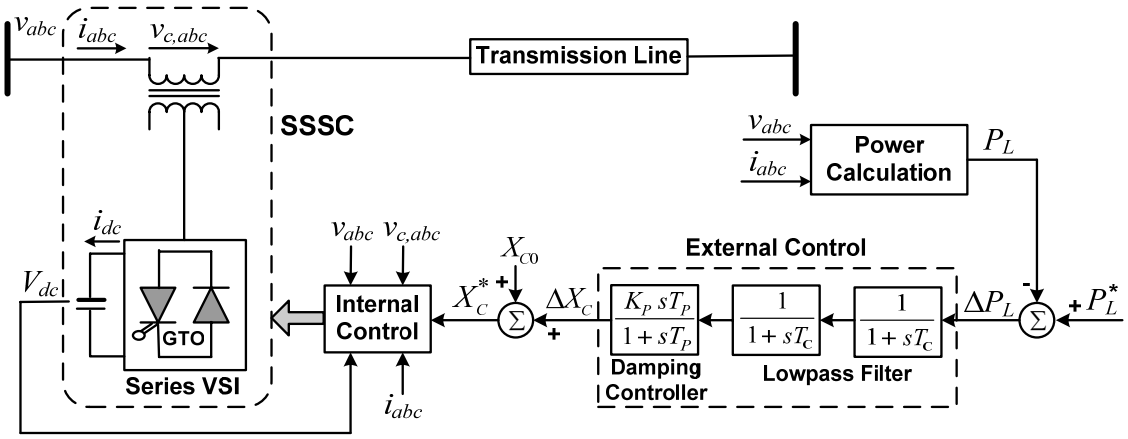

Figure 5.1: Schematic diagram of the SSSC with its conventional internal and external controllers (without fault-tolerant design).

5.1 SSSC and Its Conventional Internal and External Control

The schematic diagram of the SSSC and its conventional internal and external linear controllers are shown in Figure 5.1, in which the internal control scheme is shown in Figure 2.2. The objective of the SSSC external controller is to damp the transient power oscillations of the system. Similar to Figure 2.1, this external controller is able to rapidly change the compensating reactance X_C injected by the SSSC, thus providing supplementary damping during transient power swings. In a practical controller, it is usually desirable to choose a local signal. Therefore in this design, the active power

deviation ΔP_L on the transmission line measured at the connection point of the SSSC, is used as the input signal to the external controller. In Figure 5.1, ΔP_L is passed through two first-order low-pass filters and a damping controller (consisting of a proportional damping gain K_P and a washout filter) to form a supplementary control signal ΔX_C, which is then added to a steady-state fixed set-point value X_{C0} to form the total commanded value of compensating reactance X_C^* at the input of the SSSC internal controller [103].

5.2 Missing-Sensor-Fault-Tolerant Control

Control of the SSSC (Figure 5.1) relies on the availability and quality of four sets of sensor measurements: the three-phase currents i_{abc} of the transmission line, the three-phase bus voltages v_{abc}, the injected three-phase voltages $v_{c,abc}$ of the SSSC, and the dc-link voltage V_{dc}. Other variables, such as P_i and P_L, are calculated from these measured variables. In addition, the dc-link current i_{dc} is also measured to protect the inverter from over-current caused by a short-circuit fault on the dc-link [120]. However, the value of i_{dc} is irrelevant to the performance of the SSSC controllers. In this section, a MSFTC is designed for both internal and external control of the SSSC. This MSFTC provides fault tolerance to any faults in one of the sets of the major sensors (i_{abc}, v_{abc}, $v_{c,abc}$, and V_{dc}), based on two reasonable assumptions: 1) there are no multiple sets of sensors missing; 2) the power system operates under three-phase balanced condition at the transmission level.

5.2.1 Overall Structure of the Missing-Sensor-Fault-Tolerant Control

Figure 5.2 shows the overall structure of the MSFTC for the SSSC. It consists of an internal controller, an external controller, and an SERS. The four sets of sensor data used by the SSSC internal and external controllers are fed into the SERS, which evaluates the integrity of these sensor data. If the SERS detects that one or more sensors are missing, it is responsible for restoring all the missing sensor data. The output variables of the SERS with a subscript R represent the restored missing sensor data, while the output

variables with a subscript H represent the healthy sensor data. If there is no sensor missing, the outputs with a subscript H are exactly the same as the corresponding inputs (e.g., $i_H = i_{abc}$). The active power P_L used by the external controller is calculated from $[i_H, i_R]$ and $[v_H, v_R]$, and the active power P_i used by the internal controller is calculated from $[i_H, i_R]$ and $[v_{cH}, v_{cR}]$. Other sensor data used by the internal controller consist of $Z_H = [i_H, v_H, V_{dcH}]$ and $Z_R = [i_R, v_R, V_{dcR}]$. The SERS provides a set of complete sensor data to the SSSC controllers even when some sensors are missing. The resulting MSFTC therefore provides a fault-tolerant control strategy for the SSSC.

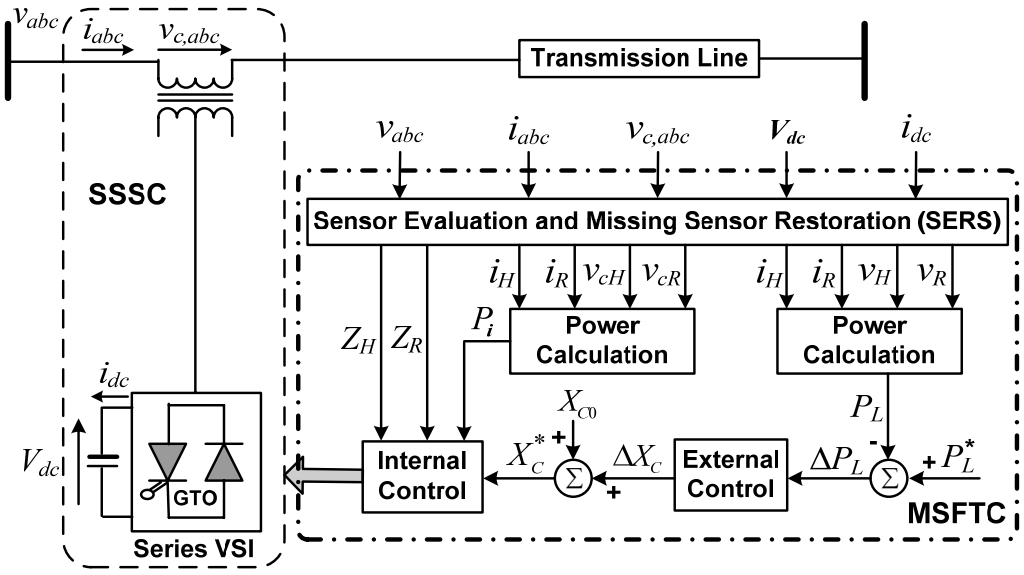

Figure 5.2: Overall structure of the proposed MSFTC strategy.

5.2.2 Design of the Sensor Evaluation and (Missing Sensor) Restoration Scheme

5.2.2.1 Three-Phase Current Sensor Measurements

Power transmission systems normally operate under almost balanced three-phase conditions. Therefore, the three-phase currents, i_a, i_b, and i_c, should approximately satisfy the following equation:

$$i_a + i_b + i_c = 0 \tag{5.1}$$

A more realistic expression for (5.1) can be written as

$$| i_a + i_b + i_c | < \sigma_1 \tag{5.2}$$

where σ_1 is a predetermined small threshold. Under balanced conditions, if the above relationship (5.2) is not satisfied, it indicates that one or more current sensors are missing. However, if i_a, i_b, and i_c are all missing, there might be $i_a = i_b = i_c = 0$ and therefore (5.2) is still satisfied. To distinguish such a case from the case of no missing sensor, another equation is used, given by

$$| i_a | < \sigma_2 \text{ and } | i_b | < \sigma_2 \text{ and } | i_c | < \sigma_2 \tag{5.3}$$

where σ_2 is a small threshold. If (5.2) is satisfied but (5.3) is not satisfied, there is no sensor missing; otherwise, one or more phase current sensors are missing.

If only one phase current sensor is missing, it can simply be restored by using (5.1). However, in order to detect and restore multiple missing current sensors, an SERS for the three-phase currents i_{abc} (called SERS-I) is designed, as shown in Figure 5.3. A necessary condition for SERS-I implementation is that all the sensor data in $v_{c,abc}$ and v_{abc} are available. How to determine this condition is discussed later on the overall structure of the SERS. Here it is simply assumed that this condition is satisfied. Under the assumption of balanced operating conditions, the SERS-I only contains two MSR blocks and a block that implements (5.1)-(5.2). Compared to the SERS in Chapter 4 that uses three MSR blocks, the computational cost of the SERS-I is reduced for real-time implementation. Each MSR block has the same structure as shown in Figure 4.1 and only evaluates the status of one current sensor measurement. If any MSR block detects that the current sensor is missing, its PSO module is then activated and only performs a one-dimensional search to restore the missing current. In Figure 5.3, i_a is evaluated by MSR1. If i_a is missing, it is restored by MSR1 and the restored value i_{aR} is then used as the healthy input for MSR2 and the block "Equations (5.1)-(5.2)"; if i_a is healthy, then $i_{aR} = i_a$. In a similar way, i_b is evaluated by MSR2. If i_b is missing, it is restored by MSR2

and the restored value i_{bR} is then used as the healthy input for the block "Equations (5.1)-(5.2)"; if i_b is healthy, then $i_{bR} = i_b$. i_c is evaluated by (5.2). If i_c is missing, it is calculated by (5.1). The output vector of the SERS-I, i_R, contains the total restored missing current sensor data; but i_H, contains other healthy current sensor data. These two vectors provide a set of complete current sensor measurements to the SSSC controllers. In this design, MSR1 needs to use the other six sensors' data $v_{c,abc}$ and v_{abc} in order to provide the required redundancy to restore the missing current i_a. However, the four sensors' data $v_{c,abc}$ and i_{aR} are enough to provide MSR2 with the required redundancy to restore the missing current i_b. The reason of using the cascading structure to design the SERS-I has been explained in Section 4.3.4.1.

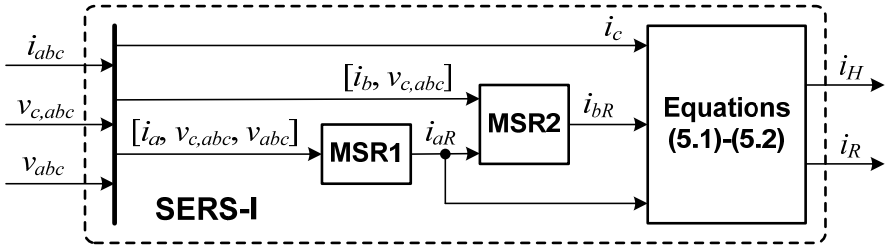

Figure 5.3: Structure of the SERS-I.

The implementation procedure of the SERS-I is shown as a flowchart in Figure 5.4, where ε_1 and ε_2 are predetermined small thresholds for MSR1 and MSR2, respectively. If for example the error signal $||E_{s1}||$ of MSR1 (Figure 4.1), is smaller than the threshold ε_1, it indicates that i_a, which is monitored by MSR1, is healthy; otherwise, if $||E_{s1}|| > \varepsilon_1$, it indicates that i_a is missing and is restored by MSR1. Similarly, if $||E_{s2}|| < \varepsilon_2$, then i_b is healthy; otherwise, if $||E_{s2}|| > \varepsilon_2$, then i_b is missing and is restored by MSR2.

In this application, each MSR converges within 15 iterations to restore one missing sensor measurement. Therefore, the maximum iteration number for PSO implementation in each MSR block is set at $M = 15$. In addition, a necessary condition for the MSR to work correctly, is that the number of healthy inputs of the auto-encoder

must equal or exceed the number of degrees of freedom in its hidden layer. Thus, the dimensions of the input, hidden, and output layers of the auto-encoders in MSR1 and MSR2 are chosen to be 21×12×21 and 15×10×15, respectively.

5.2.2.2 Dc-Link Voltage Sensor

Under normal operating conditions, the dc-link voltage is almost constant and its value is far from zero. The following power balance should be satisfied while taking into account the dynamics of the dc-link:

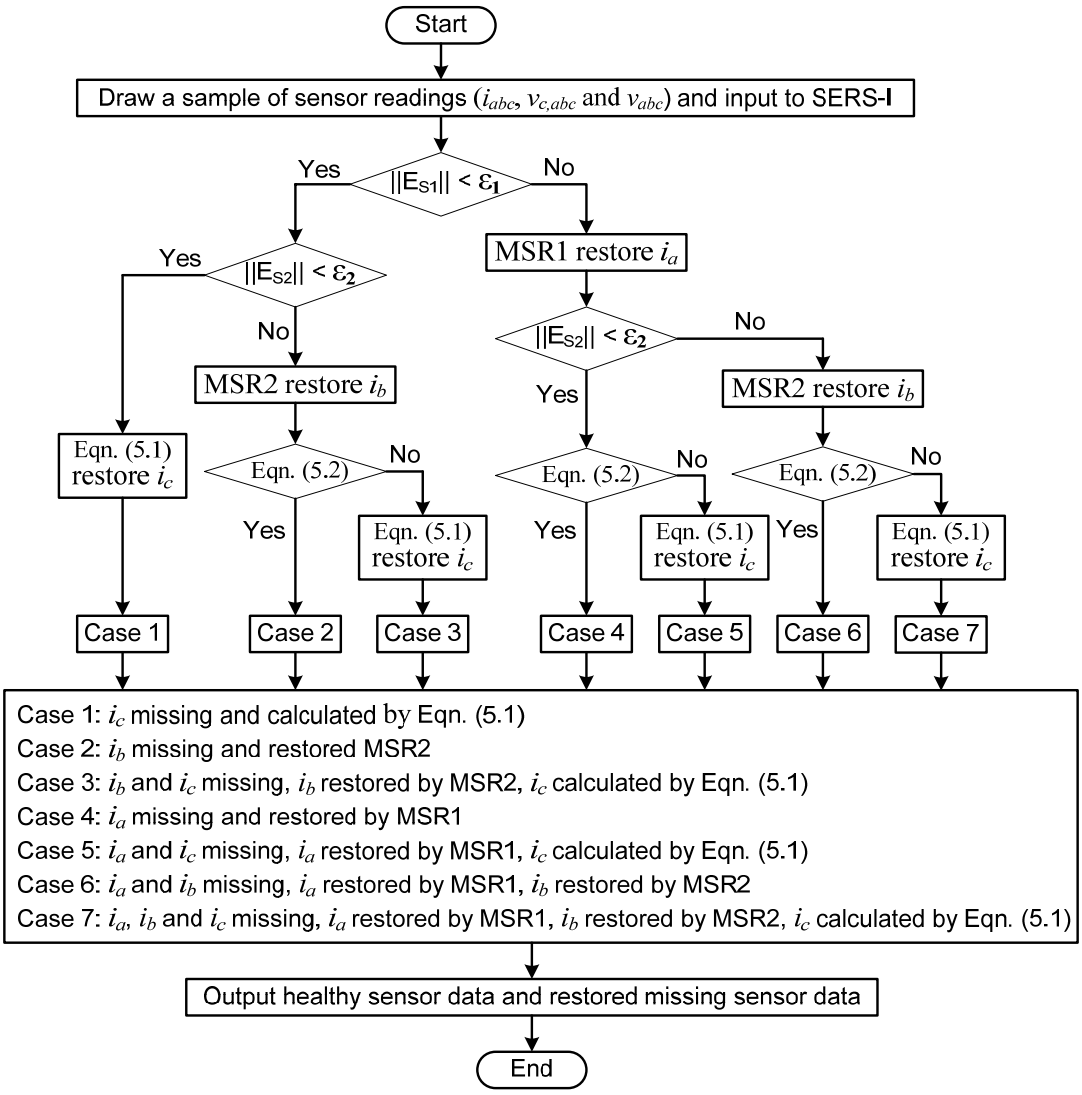

Figure 5.4: Implementation procedure of the SERS-I.

$$E = \left| P_i - P_{loss} - CV_{dc} \frac{dV_{dc}}{dt} \right| \tag{5.4}$$

where P_i is the measured active power injected to the SSSC (Figure 2.2); P_{loss} denotes the estimated power losses, including the copper loss, iron loss, switching loss, etc., in the SSSC. A simplified method to estimate the power losses in a three-phase converter has been discussed in [121]. In practice, if $E > \sigma_3$, where σ_3 is a predetermined threshhold, then the measured dc-link voltage is replaced by the calculated value using $V_{dc} = \int i_{dc} dt / C$.

5.2.2.3 Overall Structure of the Sensor Evaluation and (Missing Sensor) Restoration Scheme

Figure 5.5 shows the overall structure of the SERS. The structure and implementation of the SERS-I block have been shown in Figure 5.3 and Figure 5.4, respectively. The SERS-VC and SERS-V blocks, which have the same structures as the SERS-I block, are used to evaluate the sensor data and restore the missing sensor data in $v_{c,abc}$ and v_{abc}, respectively. The status of the sensor data in i_{abc}, $v_{c,abc}$, and v_{abc} is preevaluated by the equation evaluation block called "Equations (5.2)-(5.3) (5.5)-(5.6) (5.7)-(5.8)," where (5.5)- (5.8) are given by

$$| v_{ca} + v_{cb} + v_{cc} | < \sigma_4 \tag{5.5}$$

$$| v_{ca} | < \sigma_5 \text{ and } | v_{cb} | < \sigma_5 \text{ and } | v_{cc} | < \sigma_5 \tag{5.6}$$

$$| v_a + v_b + v_c | < \sigma_6 \tag{5.7}$$

$$| v_a | < \sigma_7 \text{ and } | v_b | < \sigma_7 \text{ and } | v_c | < \sigma_7 \tag{5.8}$$

where σ_4, σ_5, σ_6 and σ_7 are small threshholds. If (5.5) is satisfied but (5.6) is not satisfied, there is no sensor missing in $v_{c,abc}$; otherwise, one or more sensors in $v_{c,abc}$ are missing. If (5.7) is satisfied but (5.8) is not satisfied, there is no sensor missing in v_{abc}; otherwise, one or more sensors in v_{abc} are missing. If the equation evaluation block detects that any of the three vectors i_{abc}, $v_{c,abc}$, and v_{abc} contains missing sensor data, it will activate the corresponding SERS-X (X represents I, VC, or V) block to identify and restore the missing sensors. The healthy sensor data and restored missing sensor data are then

output from the SERS. If there is no missing sensor, the SERS outputs all the healthy sensor data. This procedure is shown in the flowchart of Figure 5.6.

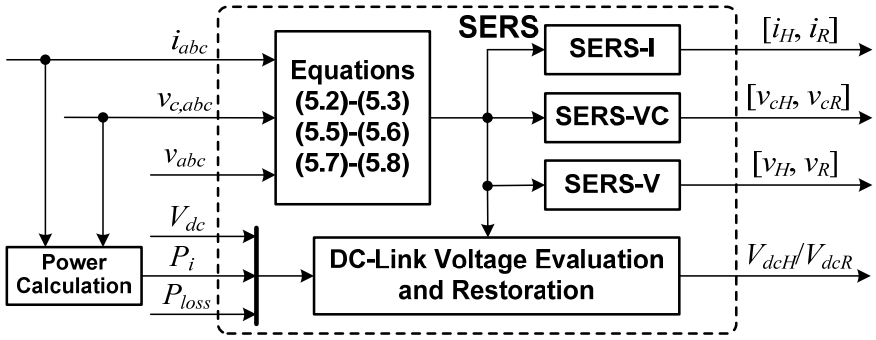

Figure 5.5: Overall structure of the SERS.

5.2.2.4 Training of the Auto-encoders

The auto-encoders in the two MSR blocks of each SERS-X are continuously trained online simultaneously without any missing sensors [determined by (5.2), (5.3), and (5.5)-(5.8)], as explained in Section 4.3.4.2. By feeding forward the data through the auto-encoder and adjusting its weight matrices, W and V, using backpropagation algorithm, the auto-encoder is trained to map its inputs to its outputs as shown in Figure 4.1(a).

5.2.3 Unbalanced Operations

The transmission system of a power network normally operates under a nearly balanced three-phase condition. As discussed in Section 4.3.4.4, the unbalanced operations are mainly caused by grid disturbances, such as unbalanced faults including a single-phase-to-ground fault, phase-to-phase fault, etc. Under these conditions, the transmission system experiences a short-term unbalanced operation (e.g., typically 50-200 ms) during the fault, and returns to its balanced three-phase operation after the fault is cleared. During the short-term unbalanced fault, (5.2), (5.3), and (5.5)-(5.8) are not

applicable to evaluate the status of the sensor data; therefore, the equation evaluation block "Equations (5.2)-(5.3) (5.5)-(5.6) (5.7)-(5.8)" in Figure 5.5 is temporarily deactivated, and the SERS continues to restore the missing sensors if they exist.

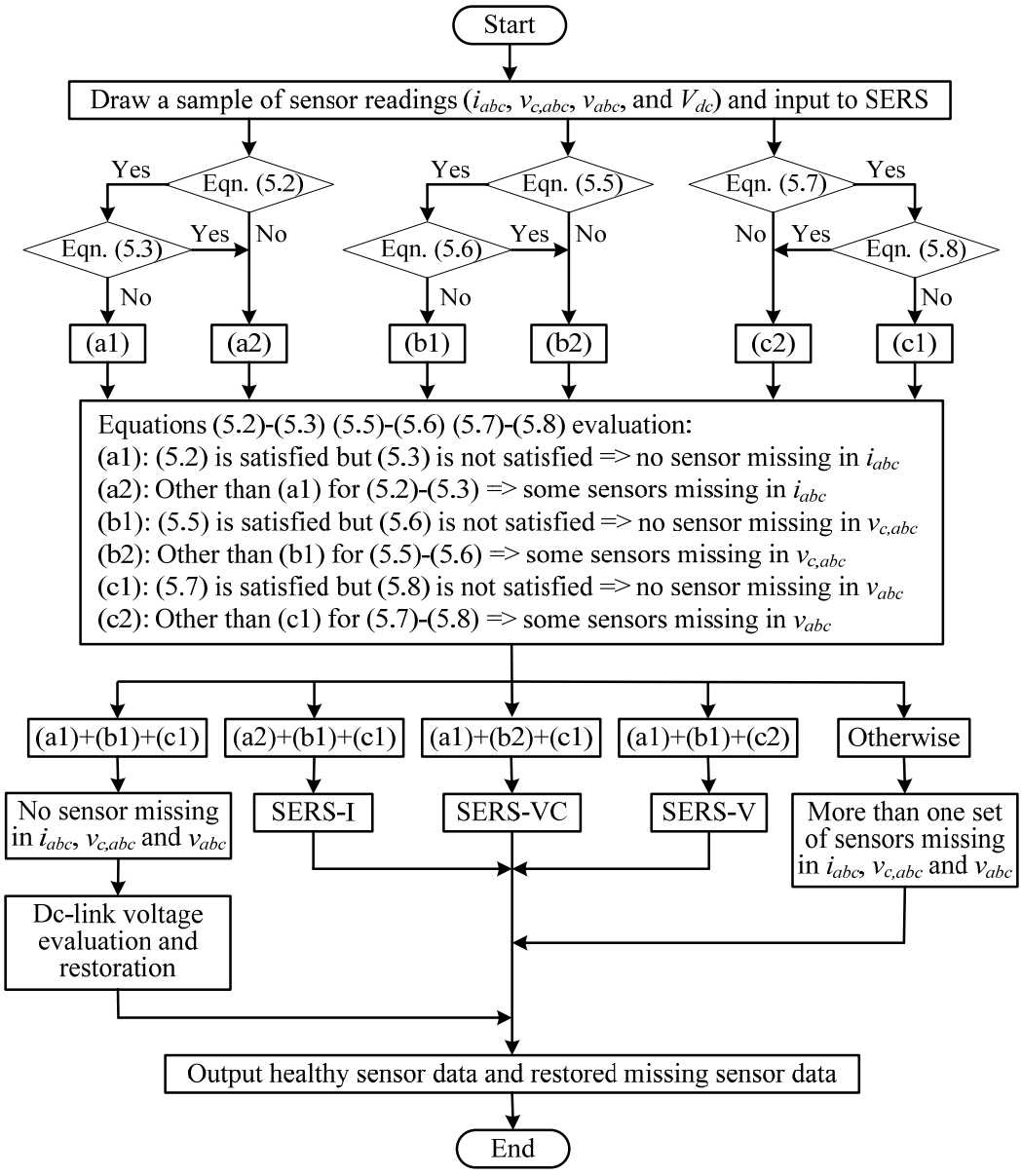

Figure 5.6: Implementation procedure of the SERS.

In addition, if three sensor data in one set of sensor measurements, e.g., the three current sensors, are all missing during an unbalanced operation, then the third missing

sensor cannot be accurately restored by (5.1). However, since the fault only exists for a very short period of time, it does not have any notable effect on the performance of the MSFTC.

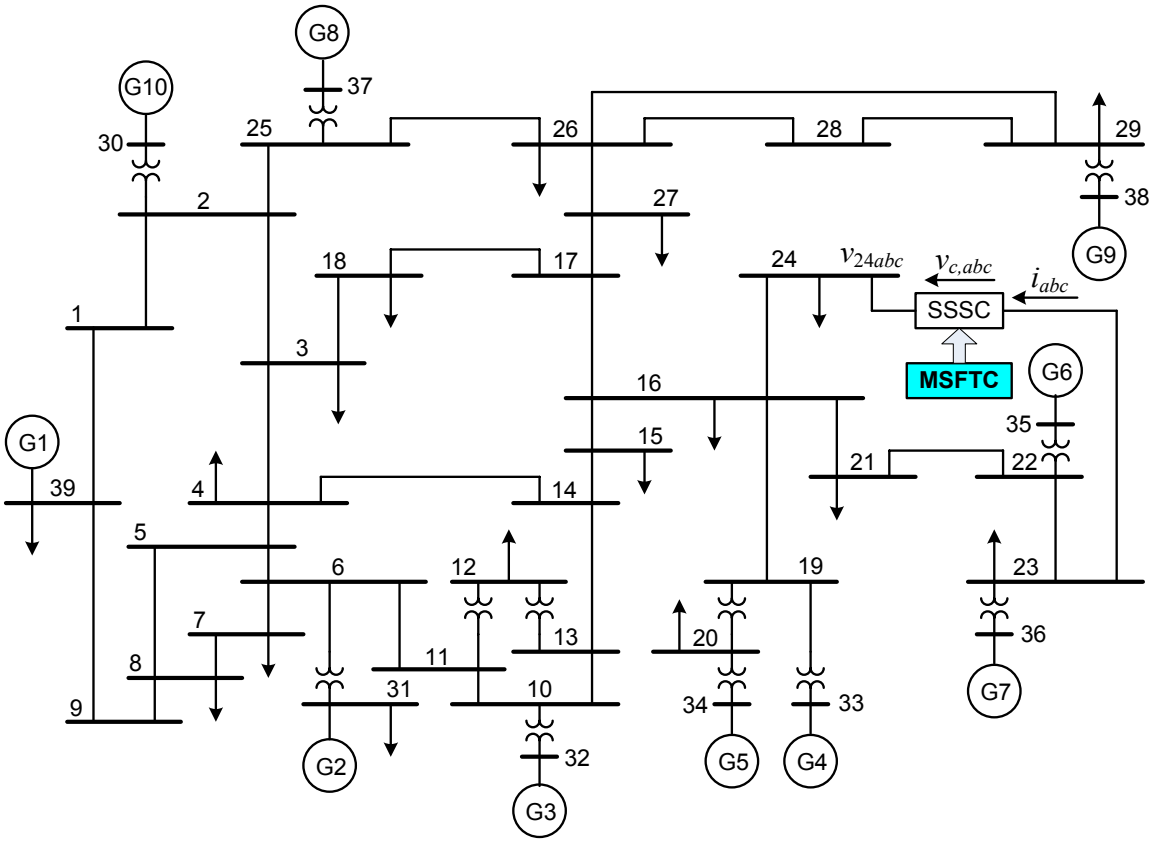

Figure 5.7: Single-line diagram of an SSSC (controlled by the MSFTC) connected to the IEEE 10-machine 39-bus New England system.

5.3 Real-Time Implementation Platform

To demonstrate the effectiveness of the MSFTC, the IEEE 10-machine 39-bus New England system as shown in Figure 4.20 is now reconsidered (see Section 4.5 and Appendix B.2). The MSFTC as shown in Figure 5.2 is applied to provide the fault-tolerant control for the SSSC, as shown in Figure 5.7. The parameters of the internal and external controllers in Figure 5.1 and Figure 5.2 are provided in Table G.1 of Appendix G. In this application, the operation and control of the SSSC rely on the availability and

quality of four sets of sensor measurements: the three-phase currents, i_a, i_b, i_c, of line 22-24; the injected three-phase voltages, v_{ca}, v_{cb}, v_{cc}, of the SSSC; the three-phase voltages, v_{24a}, v_{24b}, v_{24c}, of bus 24; and the dc-link voltage V_{dc}.

The proposed MSFTC for the SSSC is validated by a real-time implementation using a RTDS and an Innovative Integration M67 DSP card (based on a TMS320C6701-167 processor). Figure 5.8 shows the real-time implementation platform in the Real-Time Power and Intelligent Systems (RTPIS) Laboratory at the Missouri University of Science and Technology.

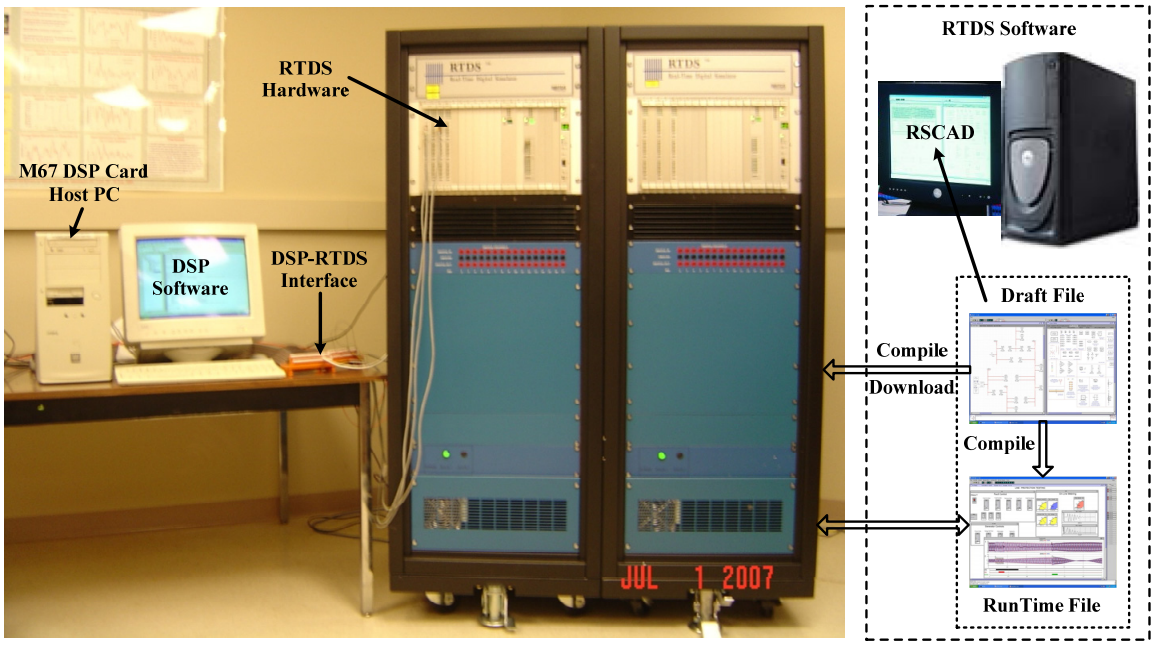

Figure 5.8: Real-time implementation platform.

The RTDS is a fully digital electromagnetic transient power system simulator capable of continuous, sustained real-time operation [117]. That is, it can solve the power system equations fast enough to continuously produce output conditions that realistically represent conditions in the real network. The RTDS has been widely accepted as an ideal tool for the design, development, and testing of power system protection and

control schemes. Because the solution is real-time, it can be connected directly to power system control and protective relay components.

The RTDS is a combination of advanced computer hardware and comprehensive software as shown in Figure 5.8. It has a custom parallel processing hardware architecture assembled in modular units called racks. Each rack contains both processing and communication modules. The mathematical computations for individual power system components and for network equations are performed using processor modules. The RTDS has a user friendly graphical interface – the RSCAD Software Suite [118], as the user's main interface with the RTDS hardware. The software is comprised of several modules designed to allow the user to easily perform all of the necessary steps to prepare and run a simulation and to analyze simulation output.

The SSSC and its internal and external controllers as well as the IEEE 39-bus power system are implemented on the RTDS; while the SERS is implemented on the M67 DSP card. This M67 DSP card communicates with the RTDS in real-time through a DSP-RTDS interface. The RTDS is equipped with analog input/output channels [117]. The sensor data used by the SSSC controllers are sent through the RTDS analog output channels and DSP-RTDS interface to the M67 DSP card for the implementation of the SERS. The M67 DSP card, operating at 167 MHz, is hosted on a Pentium III 433 MHz PC and equipped with two OMINBUS A4D4 I/O modules [119]. Each A4D4 module has four analog-to-digital (A/D) converters and four digital-to-analog (D/A) converters. The A4D4 modules receive the analog inputs (sensor data) from the DSP-RTDS interface and convert them to digital signals. They are then used by the SERS, running on the TMS320C6701-167 processor, for sensor evaluation and missing sensor restoration. The healthy sensor data and the restored missing sensor data are sent back to the RTDS, through the DSP-RTDS interface and RTDS analog input channels, for fault-tolerant internal and external control of the SSSC.

If there is no missing sensor, the SERS only performs the equation evaluation block "Equations (5.2)-(5.3) (5.5)-(5.6) (5.7)-(5.8)" to evaluate the integrity of the sensor measurements. Therefore, a high sampling rate such as 5 kHz can be used for the SERS implementation. However, if some sensors are missing, the SERS has to perform a PSO-based iterative search algorithm to restore the missing sensor data. In such a case, the sampling rate for the SERS implementation is reduced to 50 Hz to ensure that the missing sensors can be restored within one sampling period of 20 ms using the MSR algorithm with the maximum iteration number of 15. When designing the SSSC controllers, the measured three-phase voltage and current variables are normally transformed into a *d-q* synchronous reference frame variables, which are all dc quantities at steady state and oscillate at frequencies less than several Hz during disturbances. Other variables, such as generator speed, system frequency, active and reactive powers, have the same features. Therefore, the reduced sampling frequency of 50 Hz should be sufficient for the SSSC controllers to use these low-frequency or dc variables to provide correct control actions.

5.4 Real-Time Implementation Results

The dynamic performance of the SSSC equipped with the MSFTC is evaluated by applying different disturbances, such as unbalanced and balanced grid faults and change of load conditions, to the system in Figure 5.7 that is implemented on the RTDS (Figure 5.8). For each disturbance event, three (missing) sensor tests are performed and compared to evaluate the fault tolerance of the MSFTC: no sensor missing, two current sensors i_b and i_c missing, and three current sensors i_a, i_b, and i_c missing. In a practical system, if some sensors are missing, their values may be read as zeros, some noise or some uncertain error values. Since the forms of missing sensor readings have no effect on the implementation of the SERS, during the real-time tests, the sensor readings are simply set to zeros if they are missing.

5.4.1 Single-Phase-to-Ground (A-G) Fault

The system in Figure 5.7 is firstly operated at a normal operating condition without any missing sensor. The auto-encoder in each MSR block of the SERS is continuously trained online without any missing sensor, as discussed in Section 5.2.2.4. The online training of the auto-encoders converges within several minutes. Then, the training stops and the SERS continuously works online to evaluate the status of the sensor measurements and restore the missing sensor data. Thereafter, the first test is performed in which a temporary unbalanced phaseA-to-ground short circuit is applied at the bus 22 end of the transmission line 21-22. The fault is cleared 150 ms after it has been applied. After the system returns to steady state, the second test is then performed in which two phase current sensors i_b and i_c are set to be missing. Thereafter, the same phaseA-to-ground fault is applied to the system. Again, after the system returns to steady state, the third test is performed in which all of the three phase current sensors i_a, i_b, and i_c are set to be missing and the same grid fault is applied to the system.

If some phase current measurements are missing, they are detected and restored by the SERS. The restored missing phase current data are used to calculate the *d*-axis and *q*-axis current components by applying the synchronously rotating reference frame transformation [109]. The resulting *d*-*q* currents, i_d and i_q, in the three (missing) sensor tests are compared in Figure 5.9. Compared to the case of no sensor missing, the values of i_d and i_q calculated by using the restored missing phase currents deviate only slightly during the transient system oscillations. As discussed in Section 5.2.3, the unbalanced fault has no notable effect on the SERS performance since the unbalanced operation caused by the fault only exists for a very short period of time. These results indicate that the SERS correctly restores the missing current sensors during the steady state as well as the transient disturbance with a reduced sampling frequency of 50 Hz. Therefore, the SERS provides a set of fault-tolerant complete sensor data for the SSSC controllers.

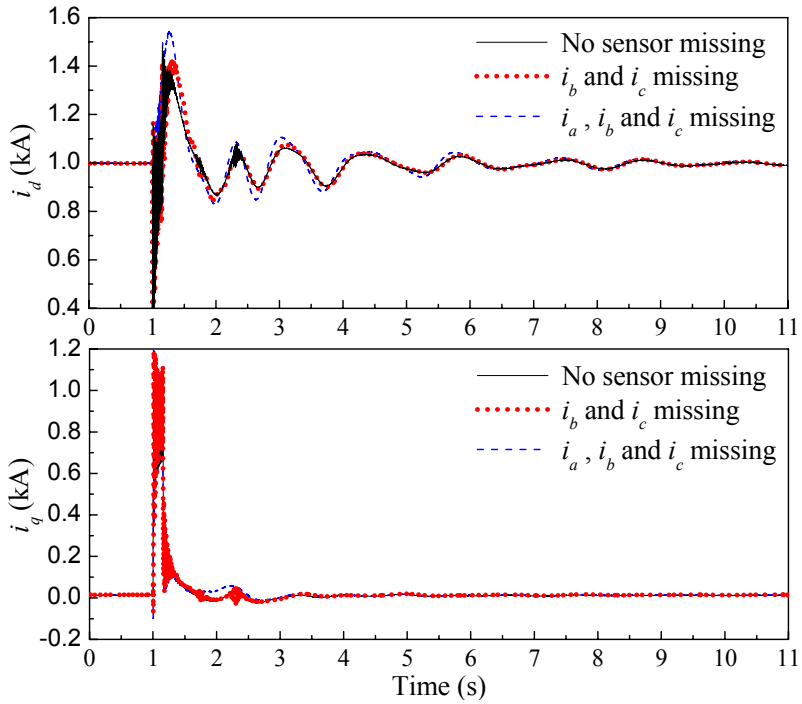

Figure 5.9: Dynamic performance of the MSFTC with different (missing) sensor tests during a single-phase-to-ground (A-G) fault: i_d and i_q.

Figure 5.10 compares the results of the generator G6 angular speed, ω_6, generator G7 angular speed, ω_7, and the transmitted active power, P_L, by the transmission line 23-24 for the three sensor tests. The responses of ω_6 and ω_7 when two or all of the three crucial phase current sensor measurements are missing, are almost the same as those in the case of no sensor missing. Compared to the synchronous generator angular speeds, the active power P_L is more sensitive to the missing-current-sensor faults because of the direct electrical relationship between the active power and the currents. As a result, the damping control of the MSFTC degrades slightly but is still effective when multiple current sensors are missing, as shown in Figure 5.10 for P_L. These results demonstrate that the MSFTC does provide fault-tolerant effective control for the SSSC and the power network even when multiple crucial phase current sensors are not available. In addition, neither the reduced sampling frequency at which the SERS provides the restored missing sensor data to the SSSC controllers, nor the short-term unbalanced operation caused by the fault has any notable effect on the performance of the MSFTC.

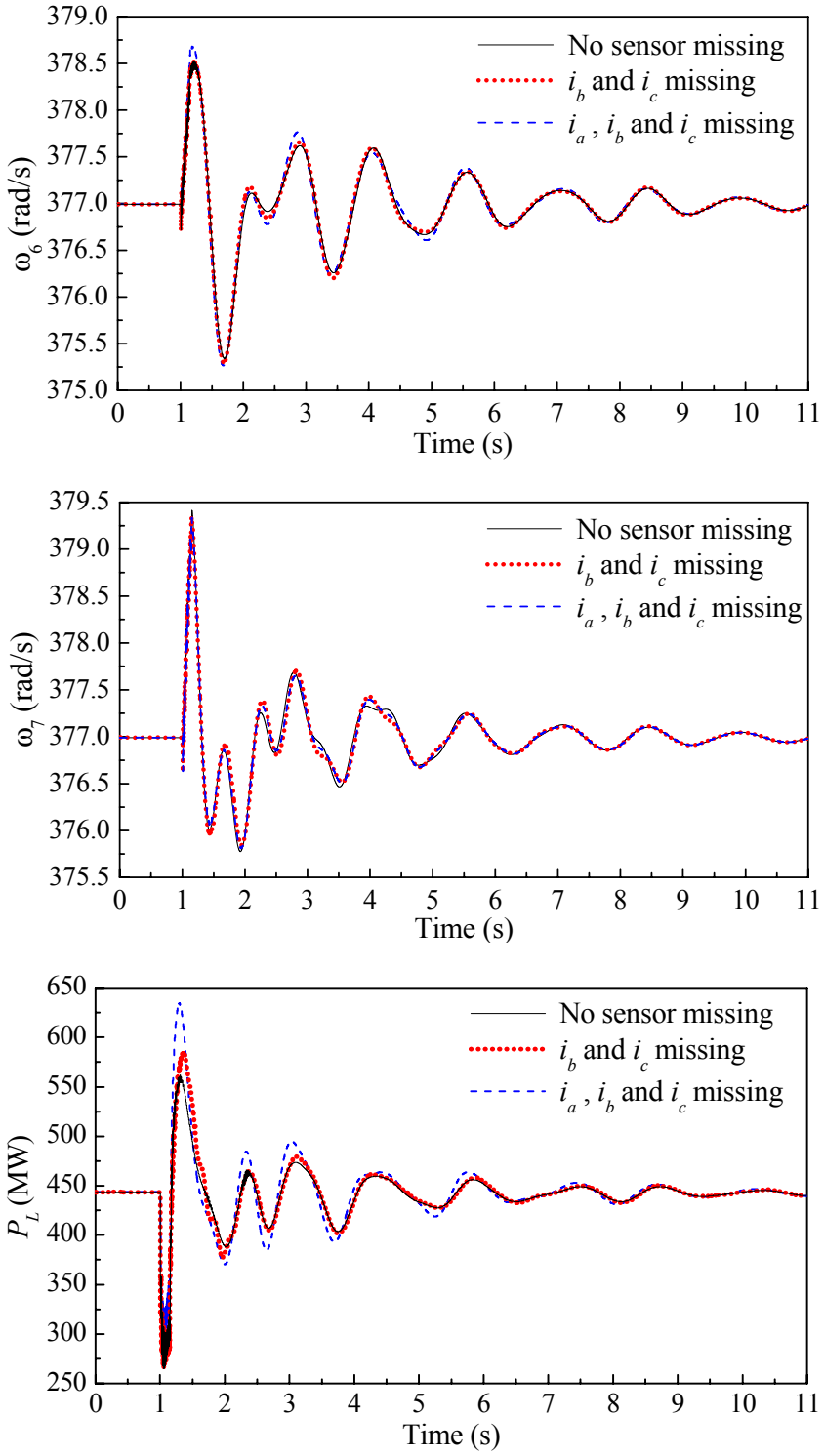

Figure 5.10: Dynamic performance of the MSFTC with different (missing) sensor tests during a single-phase-to-ground (A-G) fault: ω_6, ω_7, and P_L.

5.4.2 Two-Phase-to-Ground (AB-G) Fault

The dynamic performance of the MSFTC is now evaluated by applying a different 150 ms temporary fault between phases A and B-to-ground at the bus 22 end of the transmission line 21-22. The same three (missing) sensor tests as in the previous Section 5.4.1 are performed and Figure 5.11 compares the results of i_d and i_q. Again, these results indicate that the SERS correctly restores the missing current sensor data. The resulting responses of ω_6, ω_7, and P_L are compared in Figure 5.12 and similar results as in Figure 5.10 are obtained. The MSFTC therefore provides a fault-tolerant effective control for the SSSC and the power network when multiple crucial phase current sensor measurements are missing. Again, neither the reduced sampling frequency nor the short-term unbalanced operation caused by the fault has any notable effect on the performance of the SERS and the MSFTC.

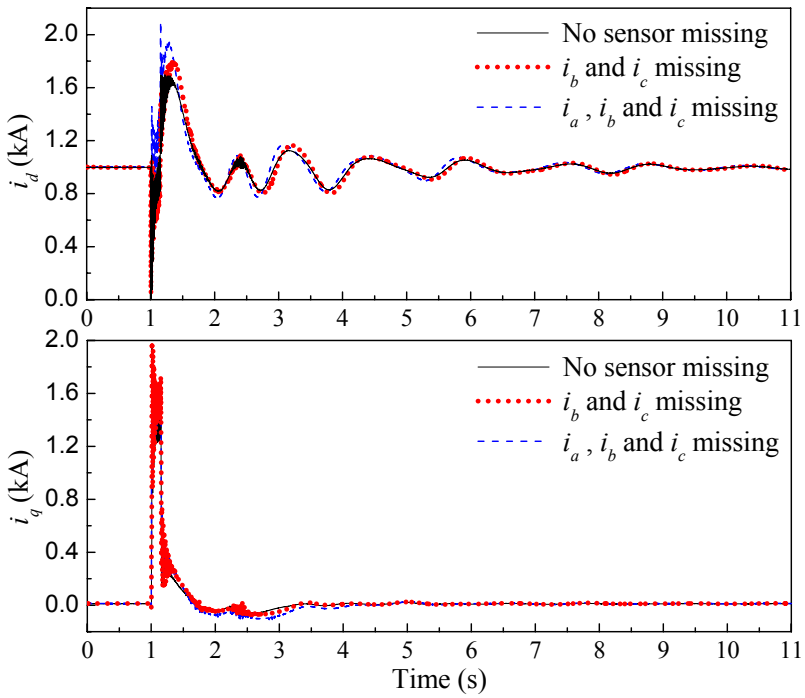

Figure 5.11: Dynamic performance of the MSFTC with different (missing) sensor tests during a Two-phase-to-ground (AB-G) fault: i_d and i_q.

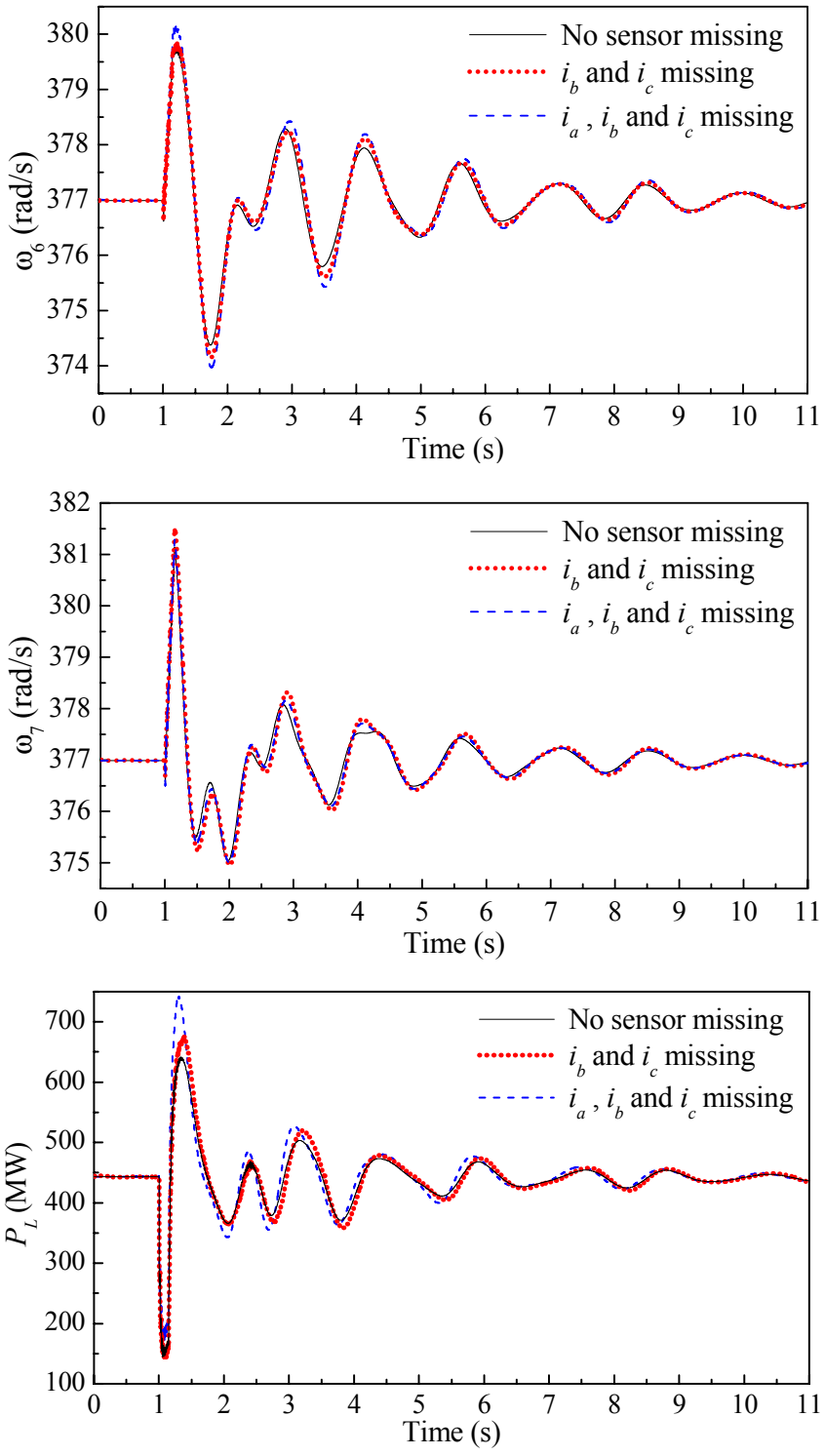

Figure 5.12: Dynamic performance of the MSFTC with different (missing) sensor tests during a Two-phase-to-ground (AB-G) fault: ω_6, ω_7, and P_L.

5.4.3 Three-Phase-to-Ground (ABC-G) Fault

A 150 ms temporary three-phase-to-ground short circuit is now applied at the bus 22 end of the transmission line 21-22 for the same three (missing) sensor tests as in the previous Section 5.4.1. Figure 5.13 compares the results of i_d and i_q, in the three (missing) sensor tests. Again, the SERS correctly restores the two and three missing current sensor data. The responses of ω_6, ω_7, and P_L are then compared in Figure 5.14. The MSFTC again correctly controls the SSSC and the power system back to the prefault steady-state operating condition even when multiple crucial phase current sensors are missing. These results show that the MSFTC provides fault-tolerant effective control for the SSSC and the power network during a balanced grid fault, and that the reduced sampling frequency has no notable effect on the performance of the SERS and MSFTC.

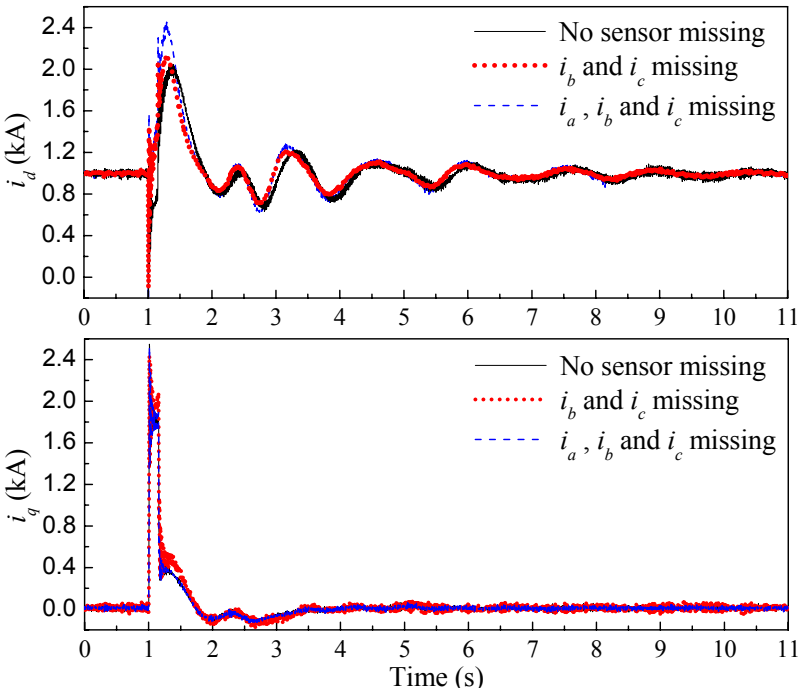

Figure 5.13: Dynamic performance of the MSFTC with different (missing) sensor tests during a three-phase-to-ground (ABC-G) fault: i_d and i_q.

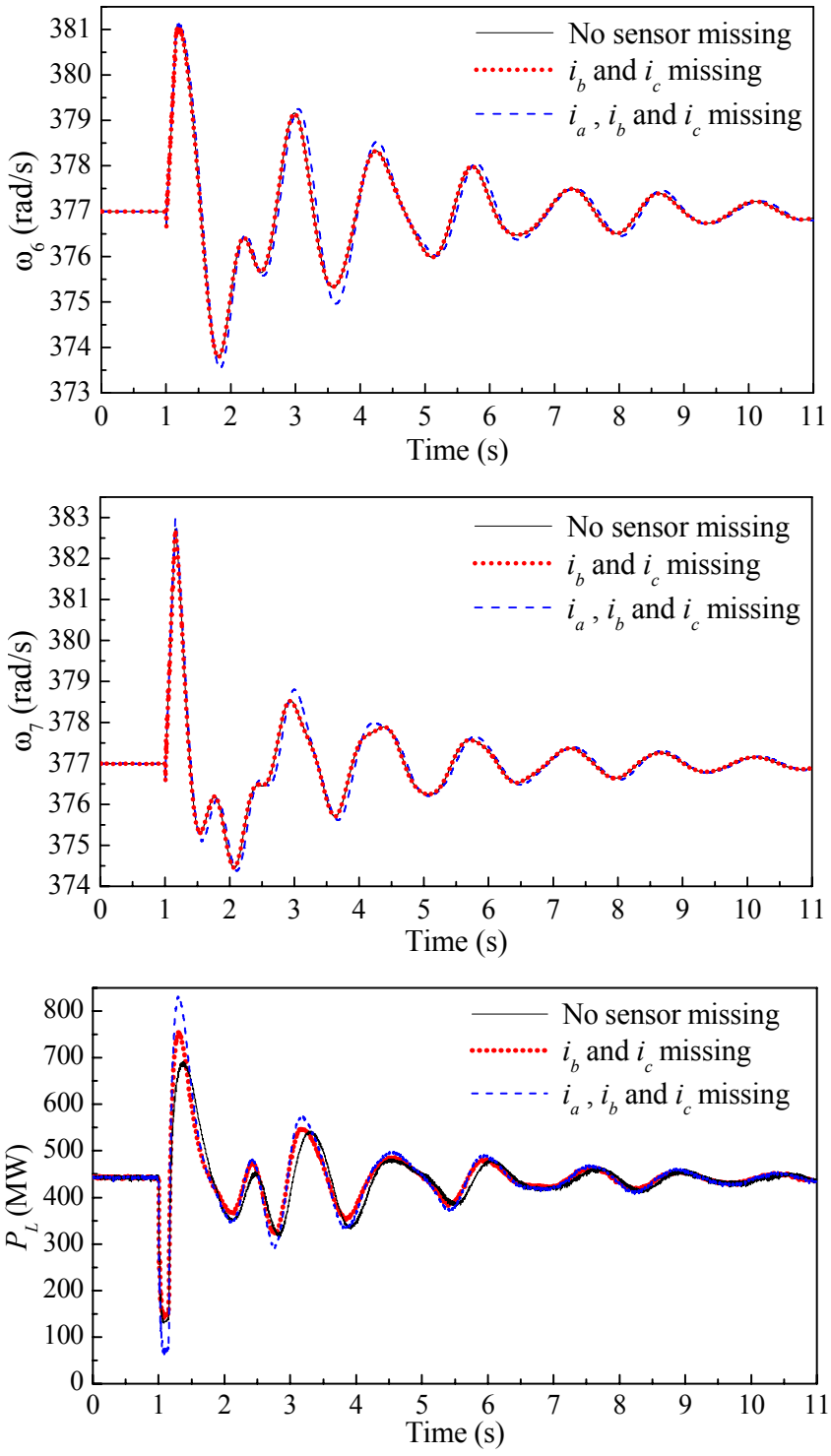

Figure 5.14: Dynamic performance of the MSFTC with different (missing) sensor tests during a three-phase-to-ground (ABC-G) fault: ω_6, ω_7, and P_L.

5.4.4 Change of Load Conditions

The same three (missing) sensor tests as in the previous three subsections are now performed. In each test, the three-phase electric load at bus 24 is increased at $t = 1$ s from 308.6 MW and -92 MVAr to 608.6 MW and -2 MVAr, respectively. After the change of the load condition, the system settles down to a new operating point. However, the auto-encoder in each MSR block of the SERS has not been trained at this new operating point since the sensors were missing before the load change.

Figure 5.15 shows the results of i_d and i_q, in the three (missing) sensor tests. The change of load condition results in a small transient in i_d and i_q. Their steady-state values change from 1.0 kA and 0.015 kA to 1.08 kA and -0.04 kA, respectively. The SERS correctly restores the two and three missing current sensor measurements when the system changes to a new operating condition.

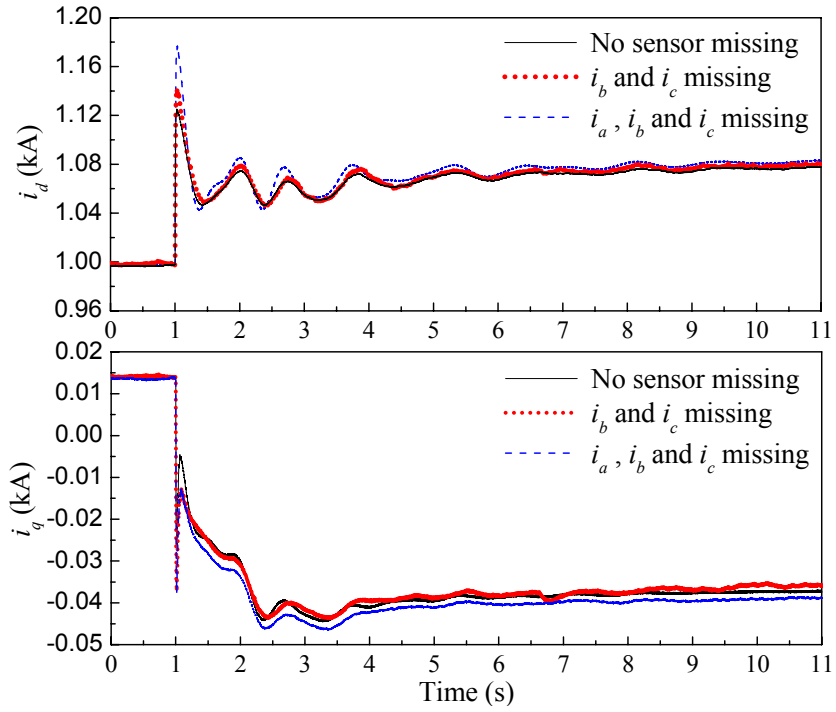

Figure 5.15: Dynamic performance of the MSFTC with different (missing) sensor tests during an increase of electric load at bus 24: i_d and i_q.

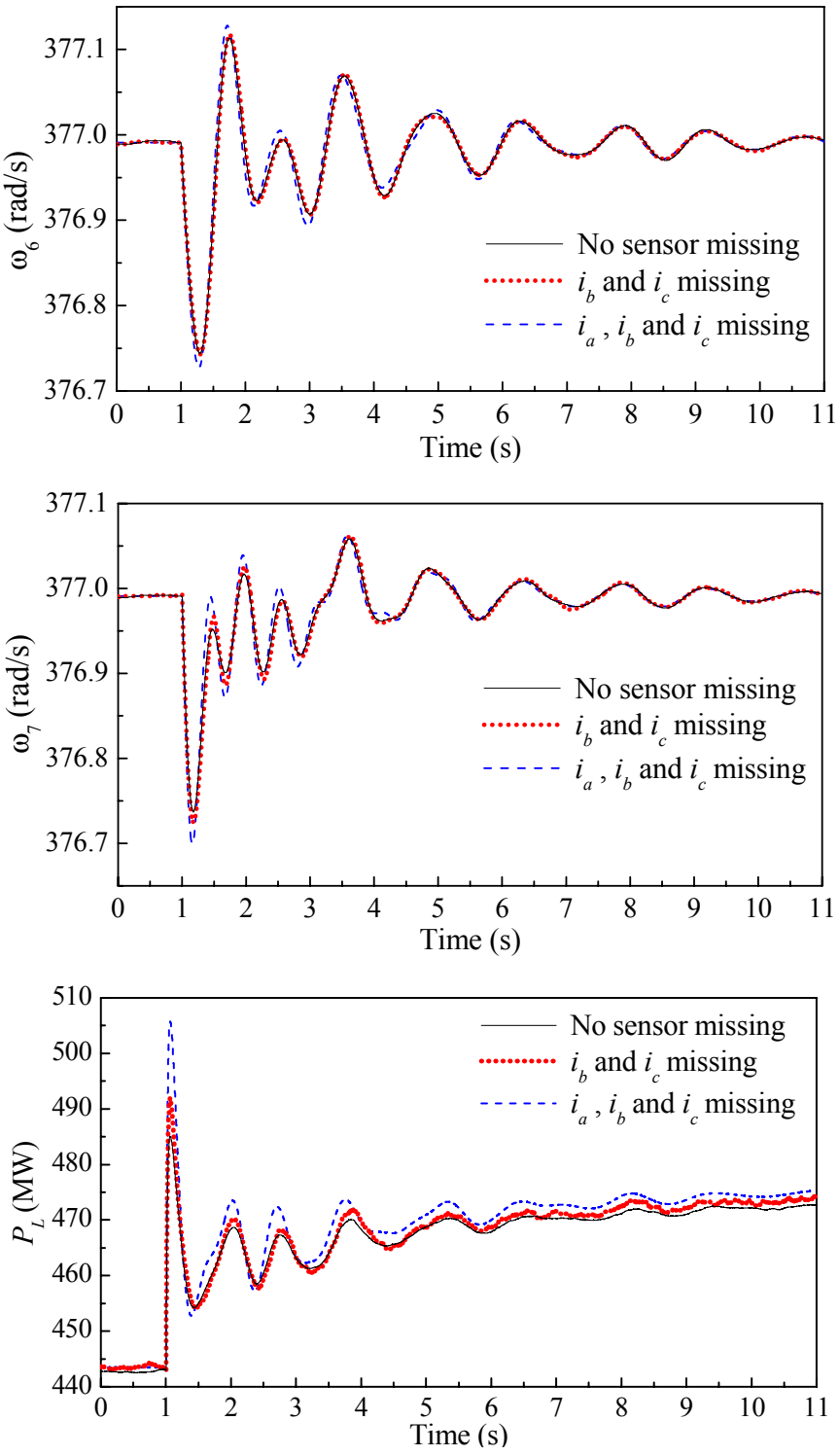

Figure 5.16: Dynamic performance of the MSFTC with different (missing) sensor tests during an increase of electric load at bus 24: ω_6, ω_7, and P_L.

The responses of ω_6, ω_7, and P_L are compared in Figure 5.16. Although the dynamic performance degrades slightly when multiple crucial phase current sensors are missing, the MSFTC still correctly controls the SSSC and power network to adapt to the new operating condition after the change of load condition. These results clearly show that the desired fault-tolerance is achieved by the MSFTC.

The missing sensor tests are also performed for two other set of sensor measurements, v_{ca}, v_{cb}, v_{cc}, and v_{24a}, v_{24b}, v_{24c}. Similar results as in Figure 5.9-Figure 5.16 are obtained.

5.5 Chapter Summary

Fault tolerance is an essential requirement for modern power system control. This chapter has proposed a missing-sensor-fault-tolerant control (MSFTC) strategy for controlling a static synchronous series compensator (SSSC) connected to a power network. The MSFTC consists of an online sensor evaluation and (missing sensor) restoration scheme (SERS) and a conventional internal and external SSSC control scheme (without any fault-tolerant design). The conventional control scheme provides the correct control actions for the SSSC under the condition that all the required sensor data are available. The SERS evaluates the integrity of the time-varying sensor measurements used by the conventional SSSC controllers. If some sensors are missing, it is able to detect and restore the missing sensor data. The restored missing sensor data are then used by the SSSC controllers, which provide a missing-sensor-fault-tolerant control for the SSSC.

The proposed MSFTC has been validated by a real-time implementation of an SSSC connected to the IEEE 10-machine 39-bus power system using a Real Time Digital Simulator (RTDS) and TMS320C6701 DSP platform. The SSSC and power network have been subjected to various grid disturbances and missing sensor faults (with two or three phase current sensor measurements missing). Results have shown that the SERS

correctly restores the data from multiple missing current sensors, and the resulting MSFTC provides fault-tolerant effective control for the SSSC and the power network during steady state, transient state of unbalanced and balanced grid faults, as well as a change of load conditions.

Because of the new constraints placed by the environmental and economical factors, the trend in power system planning and operation is toward maximum utilization of existing infrastructure with tight system operating and stability margins. This trend, together with a possible energy crisis, will bring critical challenges to electrical energy security, reliability and sustainability. These challenges require innovative solutions, such as new technologies for clean and renewable electrical energy (e.g., wind power) generation and distribution, efficient energy utilization, and enhancing the controllability, stability and reliability of the electric power system.

The capability of FACTS devices to enhance the controllability of power systems has been demonstrated in Chapters 3 and 4. This capability will be further extended in the rest chapters to enhance the performance and stability of power systems which include wind power generation.

The fault-tolerant control schemes in this chapter and the previous chapter significantly improve the reliability, maintainability and survivability of the FACTS device and the electric power system. In addition to the fault-tolerant design, the concept of sensorless control provides another approach to improve system reliability as well as to reduce the cost of using sensors. This concept will be demonstrated by a wind speed estimation based sensorless control strategy for wind power generation in the next chapter.

CHAPTER 6

WIND SPEED ESTIMATION BASED SENSORLESS OUTPUT MAXIMIZATION CONTROL FOR DFIG WIND TURBINES

At a certain wind speed, the shaft speed of a variable-speed wind turbine generator (WTG) can be adjusted optimally to achieve maximum wind power generation. In addition, during a strong wind, the WTG has to be stopped and disconnected from the power network to protect it from destruction. Therefore, control and protection of WTGs need wind speed information. A WTG normally uses one or several anemometers installed at certain locations around the wind turbine to measure wind speed. The use of anemometers increases the cost (although not significantly) but more importantly, reduces the reliability of the WTG system, as discussed in Section 1.2 of Chapter 1.

To solve the problems of using anemometers, this chapter proposes a novel online wind speed estimation algorithm [121]. It removes the need for mechanical sensors to measure wind speed. Based on the wind speed estimation algorithm, a sensorless output maximization control strategy is developed for variable-speed WTGs [121]. A specific design of the proposed control algorithm for a wind turbine driving a doubly fed induction generator (DFIG) is presented. The aerodynamic characteristics of the wind turbine are approximated by a Gaussian radial basis function network (GRBFN)-based nonlinear input-output mapping. Based on this nonlinear mapping, the wind speed is estimated from the measured generator output electrical power while taking into account the power losses in the WTG and the dynamics of the WTG shaft system. The estimated wind speed is then used to determine the optimal DFIG rotor speed command for maximum wind power extraction. The DFIG speed controller is suitably designed to effectively damp the low-frequency torsional oscillations. The resulting WTG system delivers maximum electrical power to the grid with high efficiency and high reliability

without mechanical anemometers. The validity of the proposed wind speed estimation and control algorithm is verified by simulation studies on a 3.6 MW WTG system. In addition, the effectiveness of the proposed wind speed estimation algorithm is demonstrated by experimental studies on a small emulational WTG system.

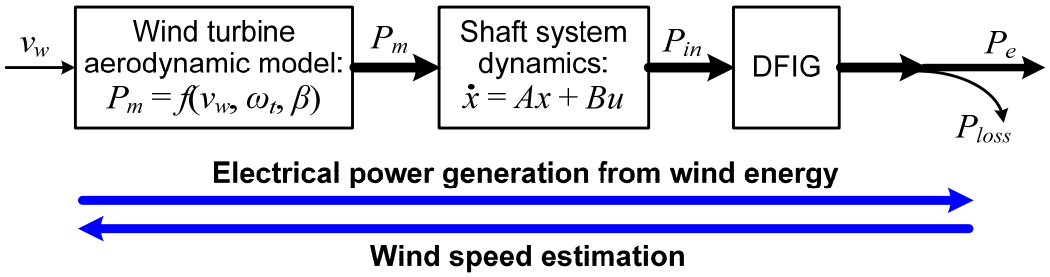

Figure 6.1: The principle of wind speed estimation algorithm.

6.1 Wind Speed Estimation

6.1.1 The Principle of Wind Speed Estimation Algorithm

For the DFIG wind turbine in Figure 1.3, the electrical power generation from wind energy can be described by the mathematical models in the flow chart of Figure 6.1. The wind energy to turbine mechanical power conversion is represented by a wind turbine aerodynamic model, as described by equation (2.3) in Chapter 2. In this model, the turbine mechanical power P_m is represented as a nonlinear function of the wind speed v_w. The dynamics of the shaft system, which include the low speed turbine shaft, high speed generator shaft and the gearbox, are represented by a set of differential equations (2.6)-(2.8). Consequently, the mechanical power is transferred from the turbine to the generator. The generator converts the mechanical power into electrical power P_e. The losses P_{loss} of the system (referred to the generator side) are considered in the model. The output electrical power P_e of the generator is measured. Therefore, if an inverse model can be developed from P_e to v_w, then the wind speed can be estimated from the measured

output electrical power. There are three key steps to develop such an inverse model. The first is power loss estimation. The second is the inverse model of the shaft system dynamics. The last is the nonlinear inverse mapping of the wind turbine aerodynamics.

6.1.2 Estimation of Power Losses in the Wind Turbine Generator

The total losses P_{loss} in the WTG takes into account the gearbox losses $P_{loss,GB}$, the induction generator losses $P_{loss,IG}$, the losses $P_{loss,RSC}$ in the RSC, the losses $P_{loss,GSC}$ in the GSC, the losses $P_{loss,T}$ in the step-up transformer, and the copper losses $P_{loss,F}$ in the R-L-C filter (see Figure 1.3), given by:

$$P_{loss} = P_{loss,GB} + P_{loss,IG} + P_{loss,RSC} + P_{loss,GSC} + P_{loss,T} + P_{loss,F} \tag{6.1}$$

The gearbox losses are calculated by [122]:

$$P_{loss,GB} = \eta P_m + \xi P_n \frac{\omega_r}{\omega_{rn}} \tag{6.2}$$

where η is the gear mesh losses constant, ξ is the friction constant, P_n is the nominal power of the WTG, and ω_{rn} is the nominal generator speed in rad/s. On the right hand side of (6.2), the first term denotes the gear mesh losses and the second term denotes the no-load losses in the gearbox. According to [123], for a 3.6 MW gearbox, values of 0.02 for η and 0.005 for ξ, are reasonable.

According to IEEE Std-112 part 5 [124], five types of losses should be taken into account in induction generators:

$$P_{loss,IG} = P_{s,loss} + P_{r,loss} + P_{core} + P_{fw} + P_{sl} \tag{6.3}$$

where $P_{s,loss}$, $P_{r,loss}$, P_{core}, P_{fw}, and P_{sl} are stator copper loss, rotor copper loss, core loss, windage and frication loss, and stray load loss, respectively. The stator copper loss is calculated by $P_{s,loss} = 3I_s^2 r_s$, where I_s is the per phase stator rms current and r_s is the stator resistance. The rotor copper loss is calculated by $P_{r,loss} = 3I_r^2 r_r + 3V_{sr} I_r$, where I_r is the per phase rotor rms current, r_r is the rotor resistance, and V_{sr} is the voltage drop across the slip-ring. The core loss is calculated by $P_{core} = 3I_m^2 r_m$, where I_m is the rms magnetizing

current and r_m is the equivalent core loss resistance. The windage and frication loss is assumed to be constant over the entire operating range, given by P_{fw} = 0.5% [125]. Finally, the stray load loss is assumed to be constant at P_{sl} = 0.9%, as specified by the IEEE Std-112 method E1 [124] for a 3.6 MW induction generator at rated load. By estimating each loss component separately, the resulting total losses can be estimated accurately (within ±2% error) from (6.3) [126].

An equivalent circuit of the IGBT PWM converter is shown in Figure 6.2, where each transistor is equipped with a reverse diode. The losses of the converter can be divided into switching losses and conduction losses [127], [128]. The switching losses of the transistors consist of turn-on and turn-off losses; while the switching losses of the diodes are mainly turn-off losses, i.e., reverse recovery energy. As shown in [122], the switching losses of the transistor and the inverse diode can be expressed as:

$$P_{s,T} = (E_{on} + E_{off}) \frac{2\sqrt{2} I_T}{\pi I_{Tn}} f_{sw} \tag{6.4}$$

$$P_{s,D} = E_{rr} f_{sw} \tag{6.5}$$

where E_{on} and E_{off} are the turn-on and turn-off energy losses of the transistor, respectively; I_{Tn} is the nominal current of the transistor; I_T is the rms value of the converter ac-side currents; E_{rr} is the reverse recovery energy of the diode; f_{sw} is the switching frequency.

To calculate the conduction losses, the transistor and the diode can be modeled as constant voltage drops, V_{CE} and V_F, and a resistor in series, r_{CE} and r_F, as shown in Figure 6.2. Simplified expressions of the transistor and diode conduction losses for a transistor leg are given by [129]:

$$P_{c,T} = \frac{\sqrt{2} V_{CE} I_T}{\pi} + \frac{V_{CE} I_T m_i \cos(\phi)}{\sqrt{6}} + \frac{r_{CE} I_T^2}{2} + \frac{r_{CE} I_T^2 m_i}{6\sqrt{3}\pi \cos(\phi)} - \frac{4 r_{CE} I_T^2 m_i \cos(\phi)}{45\sqrt{3}\pi} \tag{6.6}$$

$$P_{c,D} = \frac{\sqrt{2}V_F I_T}{\pi} - \frac{V_F I_T m_i \cos(\phi)}{\sqrt{6}} + \frac{r_F I_T^2}{2} - \frac{r_F I_T^2 m_i}{6\sqrt{3}\pi\cos(\phi)} + \frac{4 r_F I_T^2 m_i \cos(\phi)}{45\sqrt{3}\pi} \tag{6.7}$$

where m_i is the modulation index, and ϕ is the phase shift angle by which the modulation function leads the ac-side current of the converter. According to the values of the transistor and the diode parameters in this chapter, i.e., $V_{CE} \approx V_F$ and $r_{CE} \approx r_F$ (see Appendix E.1), the conduction losses in (6.6) and (6.7) can be further simplified to:

$$P_{c,T} + P_{c,D} = \frac{\sqrt{2}V_{CE} I_T}{\pi} + \frac{r_{CE} I_T^2}{2} + \frac{\sqrt{2}V_F I_T}{\pi} + \frac{r_F I_T^2}{2} \tag{6.8}$$

The total losses of the IGBT PMW converter that consists of three transistor legs are

$$P_{loss,COV} = 3(P_{s,T} + P_{s,D} + P_{c,T} + P_{c,D}) \tag{6.9}$$

Since the variable frequency converter (VFC) of a DFIG wind turbine (Figure 1.3) consists of two back-to-back IGBT PWM converters: the rotor side converter (RSC) and the grid side converter (GSC), the losses of both converters can be calculated by (6.4)-(6.9).

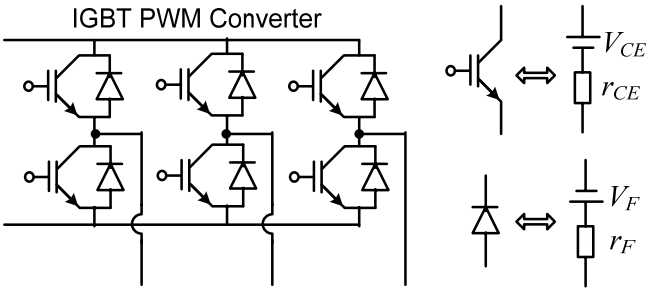

Figure 6.2: Equivalent circuit of the IGBT PWM converter.

Based on the no-load losses P_{nT} and copper losses P_{cT} (see Appendix E.1), the total losses of the transformer at a certain operating condition can be calculated by:

$$P_{loss,T} = P_{nT}\left(\frac{V_s}{V_{HT}}\right)^4 + P_{cT}\left(\frac{I_g}{I_{LT}}\right)^2 \tag{6.10}$$

where V_s is the measured per phase stator rms voltage of the DFIG, V_{HT} is the nominal per phase voltage at the transformer HV terminal, I_g is the measured ac-side rms current of the GSC, I_{LT} is the nominal rms current at the transformer LV terminal. Finally, the copper losses in the R-L-C filter are calculated as:

$$P_{loss,F} = 3I_g^2 r_g \tag{6.11}$$

Based on the measured generator electrical power P_e and estimated total power loss P_{loss} in the WTG, the turbine mechanical power P_m is then estimated from (6.13) which takes into account the dynamics of the WTG shaft system.

6.1.3 Estimation of Wind Turbine Mechanical Power

The turbine mechanical power P_m is estimated from the generator electrical power P_e while taking into account the power losses in the WTG as well as the dynamics of the WTG shaft system. Here the electrical power P_e is measured at the DFIG terminals and consists of the stator power P_s and the rotor (slip) power P_g, i.e., $P_e = P_s + P_g$ (Figure 1.3). Because of the use of the gearbox, there exist two different masses on the WTG shaft system with distinctly different mechanical parameters. This contributes to the dynamic difference between the instantaneous values of the mechanical power P_m and the electrical power P_e. Therefore, it is important to consider the dynamics of the WTG shaft system in order to estimate P_m from P_e.

Adding (2.6) and (2.7), and including the power losses in the WTG yields:

$$2H_t \frac{d\omega_t}{dt} + 2H_g \frac{d\omega_r}{dt} = \frac{P_m}{\omega_t} - \frac{P_e + P_{loss}}{\omega_r} \tag{6.12}$$

where P_{loss} is the total power losses in the WTG referred to the generator side. Rewriting (6.12) in the discrete-time format gives:

$$P_m(t) = \left[2H_t \frac{\omega_t(t) - \omega_t(t-1)}{\Delta t} + 2H_g \frac{\omega_r(t) - \omega_r(t-1)}{\Delta t} + \frac{P_e(t) + P_{loss}(t)}{\omega_r(t)} \right] \omega_t(t) \tag{6.13}$$

Equation (6.13) estimates the turbine mechanical power P_m at any time instant from the measured generator output electrical power P_e and the estimated total power losses P_{loss} in the WTG. In (6.12) and (6.13), all the variables are given as per-unit values.

6.1.4 GRBFN-Based Wind Speed Estimation Method

The wind speed v_w can be calculated from the roots [58] or the nonlinear inverse function of equation (2.3) provided that values are known for the turbine mechanical power P_m, the wind turbine rotational speed ω_t, and the blade pitch angle β. A commonly used method to implement an inverse function is using a lookup table. This method however requires much memory space and may result in a time-consuming search for the solution. In addition, real-time calculation of nonlinear function roots may result in a complex and time-consuming calculation, therefore, reducing system performance. Artificial neural networks (ANNs), well known as a tool for nonlinear complex time-varying input-output mapping, can be an ideal technique to solve this problem. Therefore, the proposed wind speed estimation algorithm in this work is based on an ANN-based input-output mapping that approximates the nonlinear inverse function of (2.3), as shown in Figure 6.3.

The ANN used in this application is a three-layer GRBFN, which has been shown to be a universal approximator [130]. The overall input-output mapping for the GRBFN is similar to (3.2), given by:

$$\hat{v}_w = b + \sum_{j=1}^{h} v_j \exp\left(-\frac{\left\| x - C_j \right\|^2}{\beta_j^2} \right) \tag{6.14}$$

where $x = [P_m, \omega_t, \beta]$ is the input vector, $C_j \in R^n$ is the center of the j^{th} RBF units in the hidden layer, h is the number of RBF units, b and v_j are the bias term and the weight between hidden and output layers respectively, and $\hat{v}_w$ is the output of the GRBFN that represents the estimated wind speed.

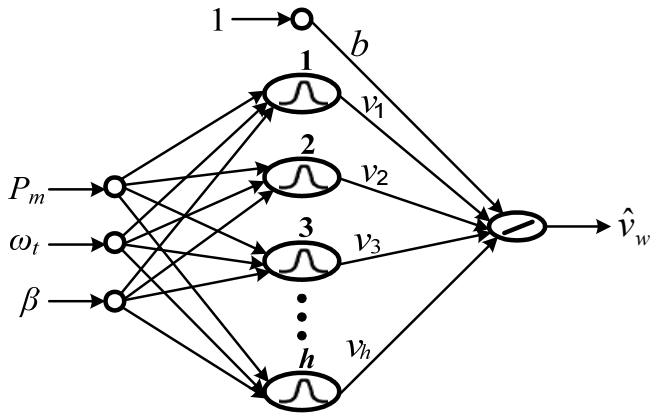

Figure 6.3: GRBFN-based wind speed estimation.

The GRBFN is trained offline using a training data set that covers the entire operating range of the WTG, defined by $\omega_{t,min}<\omega_t<\omega_{t,max}$, $v_{w,min}<v_w<v_{w,max}$, and $\beta_{min}<\beta<\beta_{max}$. In this design, the samples of turbine speed ω_t and wind speed v_w are generated evenly in the range $[\omega_{t,min}, \omega_{t,max}]$ and $[v_{w,min}, v_{w,max}]$ with the increments of $\Delta\omega_t$ = 0.01 rad/s and Δv_w = 0.02 m/s, respectively. The pitch angle β is fixed when the wind speed is below the rated value. The value of β is varied and sampled evenly in the range of $[\beta_{min}, \beta_{max}]$ with an increment of $\Delta\beta$ = 0.5 degree only when the wind speed exceeds the rated value. At each data sample of turbine speed, wind speed, and pitch angle, $\omega_t(i)$, $v_w(j)$, and $\beta(k)$, the turbine power sample $P_m(i, j, k)$ is calculated from (2.3). The entire training data set is then created by combining all the data samples of turbine speed, turbine power, pitch angle, and wind speed, given by

$$\underline{A} = \{\underline{X}; \underline{V}_w\} \tag{6.15}$$

where

$$\underline{X} = \{P_m(i, j, k), \omega_t(i), \beta(k) \mid i = 1, \cdots, I; j = 1, \cdots, J; k = 1, \cdots, K\} \tag{6.16}$$

$$\underline{V}_w = \{v_w(j) \mid j = 1, \cdots, J\} \tag{6.17}$$

are the input and output training data sets, respectively; I, J, and K are the maximum numbers of data samples for turbine speed, wind speed, and pitch angle, respectively, and given by:

$$I = (\omega_{t,max} - \omega_{t,max})/\Delta\omega_t + 1 \tag{6.18}$$

$$J = (v_{w,max} - v_{w,max})/\Delta v_w + 1 \tag{6.19}$$

$$K = (\beta_{max} - \beta_{max})/\Delta\beta + 1 \tag{6.20}$$

After determining the training data set, the parameters of the GRBFN, i.e., the number of RBF units, the RBF centers, widths, the output weights and bias term, are determined by an offline training and optimization algorithm [110], in which the RBF centers are determined by a *k*-means clustering algorithm; the output weights and bias term are calculated by singular value decomposition (SVD) method; the RBF widths are initially determined by *p*-nearest neighbors heuristic method, and then optimized together with the number of RBF units using the particle swarm optimization (PSO) algorithm. These parameters of the GRBFN are then fixed for subsequent online estimation of the wind speed. Since the training data set covers the entire operating range of the WTG, the resulting GRBFN provides an accurate wind speed estimation model over the entire WTG operating range.

6.1.5 Comparison of the GRBFN-Based Wind Speed Estimation Algorithm with Other Methods

The proposed wind speed estimation algorithm is compared with two other methods, i.e., a polynomial roots method and a lookup table method, in terms of the computational time and the required memory space. The data set described by (6.15)-(6.17), which covers the entire operating range of the WTG, is used to build the lookup table. It provides a nonlinear mapping of $(\omega_t, v_w, \beta) \rightarrow P_m$. For a particular operating point with the known information of P_m, ω_t, and β, the value of the wind speed v_w can be obtained by interpolation using the data from the lookup table. For the proposed method, the dimension of the three-layer GRBFN is 3×8×1, i.e, three inputs, eight RBF units in the hidden layer, and one output. The parameters of the GRBFN are calculated by an offline training and optimization procedure as described in Section 6.1.1 and in [110]. The three methods are implemented in MATLAB and the required computational time is

compared in Table 6.1. The proposed GRBFN-based method is seventeen times faster than the polynomial roots method and five times faster than the lookup table method.

In addition, the proposed method and the polynomial roots method only require a little memory space (less than two hundred bytes) to store the ANN parameters and the polynomial coefficients, respectively, for their implementation. On the contrary, the lookup table method requires a large amount of memory space to store the table data for its real-time implementation. For example, to store a three-dimensional table with the number of elements of 500×100×100 in a 4-byte float format requires 20 Megabytes of memory space. This obviously increases the cost of hardware and reduces system performance (especially when using the external memory).

Table 6.1: Comparison of different wind speed estimation methods

Wind speed estimation method	Computational time (ms)	Required memory (bytes)
Proposed GRBFN-based method	0.125	164
Polynomial roots method	2.172	100
Lookup table method	0.625	20,000,000

6.2 Output Maximization Control of the Wind Turbine Generator

The DFIG wind turbine (Figure 1.3) control system generally consists of two parts: the electrical control on the DFIG and the mechanical control on the wind turbine blade pitch angle, as shown in Figure 6.4. Control of the DFIG is achieved by control of the VFC, which includes control of the RSC and control of the GSC. The objective of the RSC is to govern both the stator-side active and reactive powers independently; while the objective of the GSC is to keep the dc-link voltage constant regardless of the magnitude and direction of the rotor power. The GSC control scheme can also be designed to regulate the reactive power or the stator terminal voltage of the DFIG.

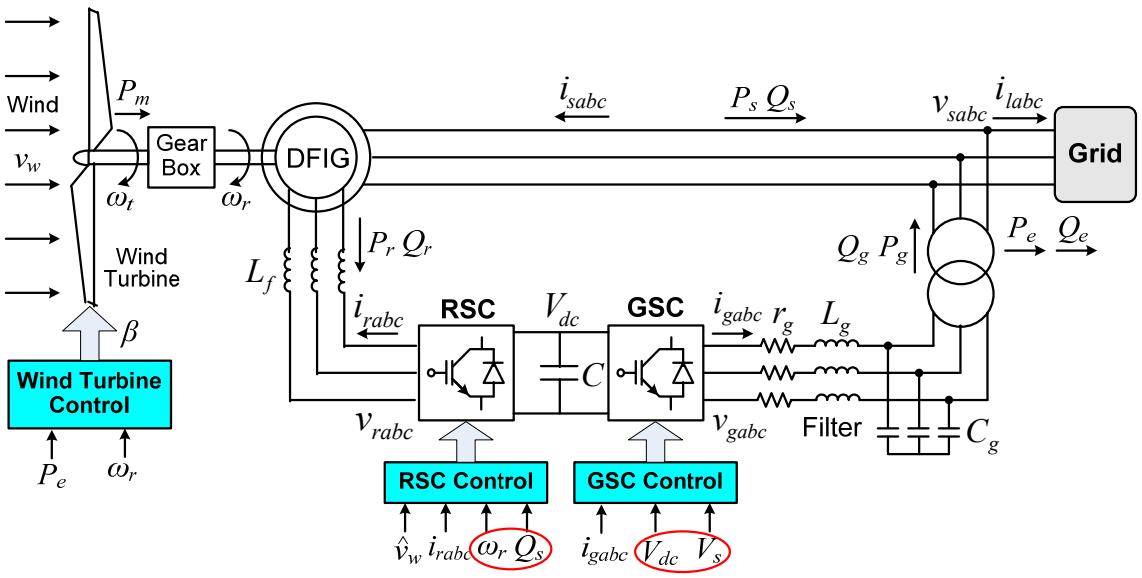

Figure 6.4: Configuration and control of a DFIG wind turbine.

6.2.1 Sensorless Maximum Wind Power Tracking

When the WTG operates in the variable-speed mode, the pitch angle is fixed. According to (2.2), the power coefficient C_p of a 3.6 MW wind turbine is a fourth-order polynomial of the tip-speed ratio λ. To extract the maximum active power from the wind, the shaft speed of the WTG must be adjusted to achieve an optimal tip-speed ratio λ_{opt}, which yields the maximum power coefficient C_{pm}. The value of λ_{opt} can be calculated from the roots of the derivative of the polynomial in (2.2). Then, based on the estimated wind speed $\hat{v}_w$, the corresponding optimal generator speed command ω_r^* for maximum wind power tracking is determined by

$$\omega_r^* = \frac{\lambda_{opt}\hat{v}_w}{R} \tag{6.21}$$

A block diagram of the GRBFN-based sensorless maximum wind power tracking algorithm is shown in Figure 6.5. Since the wind speed normally varies fast and randomly, but the responses of the WTG are relatively slow due to its inertia, a low-pass filter is necessary to provide a smooth rotor speed command to the DFIG. The bandwidth

of this low-pass filter should be less than or comparable to the bandwidth of the DFIG speed controller in order to achieve a stable speed tracking.

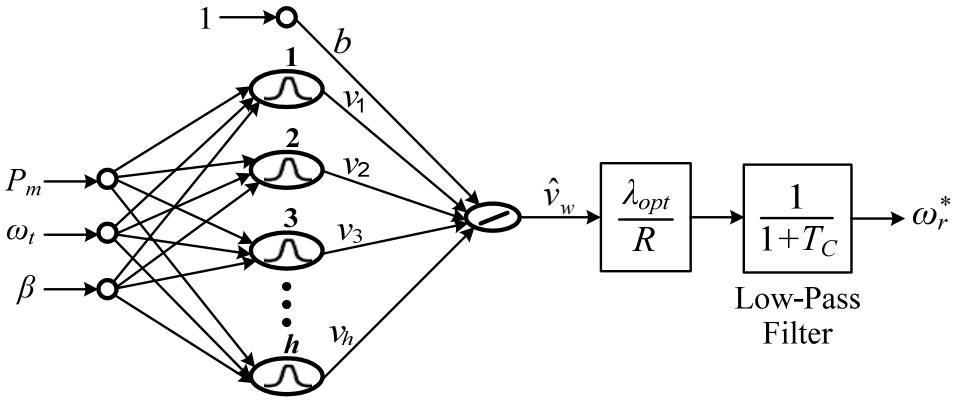

Figure 6.5: Block diagram of the GRBFN-based sensorless maximum wind power tracking.

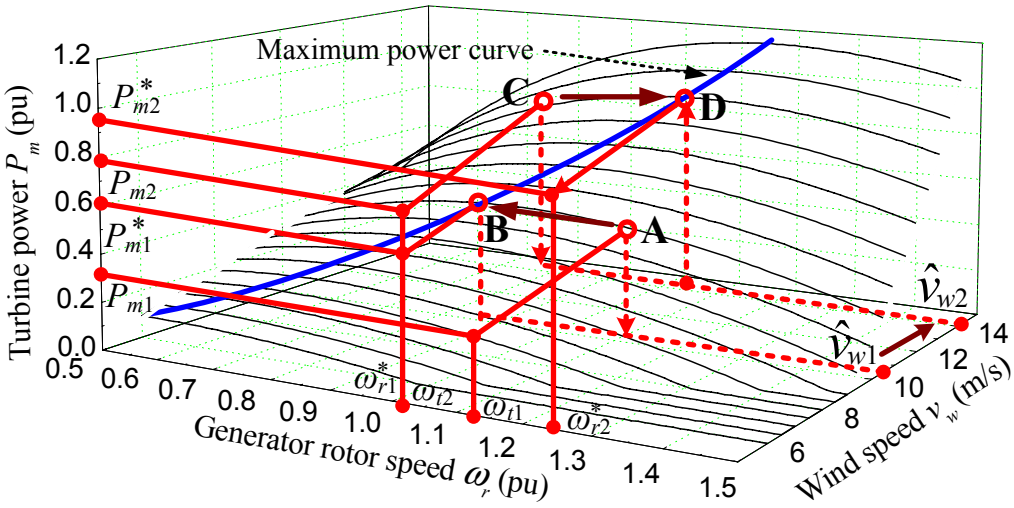

Figure 6.6: GRBFN-based sensorless maximum wind power tracking.

Figure 6.6 illustrates the principle of the GRBFN-based sensorless maximum wind power tracking algorithm. It is assumed that the WTG initially operates at a nonoptimal operating point A. The GRBFN estimates the wind speed $\hat{v}_{w1}$ from the turbine speed ω_{t1} and the estimated turbine mechanical power P_{m1} at point A. The

corresponding optimal generator speed reference ω_{r1}^* is determined by (6.21). The generator speed is then controlled to track the desired optimal speed reference where the WTG can extract the maximum active power P_{m1}^* from the wind. The operating point of the WTG therefore moves from A to the optimal operating point B at the wind speed $\hat{v}_{w1}$.

Thereafter, the wind speed changes while the WTG still operates with the turbine speed at $\omega_{t2} = \omega_{r1}^*$. As a result, the wind turbine mechanical power changes from P_{m1}^* to P_{m2} to adapt to the new wind speed. The operating point of the WTG now moves from B to a nonoptimal operating point C due to the variation of the wind speed.

Based on the turbine speed ω_{t2} and the estimated turbine mechanical power P_{m2} at point C, the proposed algorithm estimates the wind speed $\hat{v}_{w2}$ and determines the optimal generator speed reference ω_{r2}^*. The generator speed is then controlled to track the optimal speed reference to extract the maximum power P_{m2}^* from the wind. The operating point of the WTG therefore moves from C to the new optimal operating point D to adapt to the new wind speed $\hat{v}_{w2}$.

6.2.2 Design of the Speed Controller

A suitably designed speed controller for the WTG is essential to track the optimal generator speed reference ω_r^* for maximum wind power extraction. The design of such a speed controller should take into account the dynamics of the WTG shaft system. According to the two-mass shaft model (2.6)-(2.8), the transfer function from the generator electrical torque, T_e, to generator rotor speed, ω_r, for the DFIG wind turbine in Figure 1.3 (with $D_t = D_g = 0$) is given by:

$$\frac{\omega_r}{T_e} = \frac{1}{2(H_t + H_g)s} \frac{2H_t s^2 + D_{tg} s + K_{tg}}{\frac{2H_t H_g}{H_t + H_g} s^2 + D_{tg} s + K_{tg}} \tag{6.22}$$

which can be viewed as a lumped-mass system, $1/[2(H_t+H_g)s]$, on the left and a bi-quadratic function on the right. PI-type speed controllers are normally designed based on the assumption of a single lumped-mass system. However, the bi-quadratic function causes instability by altering the phase and gain of the lumped-mass system [131]. On most practical WTGs, the damping coefficient, D_{tg}, is small so that both the numerator and denominator of the bi-quadratic function exhibit lightly damped torsional oscillation modes, if no specifically designed damping control is present in the WTG controllers. The frequencies of these torsional oscillation modes are given by:

$$f_1 = \frac{1}{2\pi}\sqrt{\frac{K_{tg}}{2H_t}},\ f_2 = \frac{1}{2\pi}\sqrt{\frac{K_{tg}(H_t + H_g)}{2H_t H_g}} \tag{6.23}$$

where $f_1<f_2$. The value of f_2 is typically less than several Hz on most practical WTG systems.

To improve the damping of the low-frequency torsional oscillations of the WTG shaft system, the speed controller has to be designed so that the closed-loop system has a sufficiently low bandwidth less than f_1. The speed controller therefore acts as a low-pass filter to reduce the gains at the oscillating frequencies.

6.2.3 Control of the Rotor Side Converter

The RSC control scheme is expected to achieve the following objectives: 1) regulating the DFIG rotor speed for maximum wind power capture; 2) maintaining the DFIG stator output voltage frequency constant; 3) controlling the DFIG reactive power. In the DFIG-based wind generation system, these objectives are commonly achieved by rotor current regulation in the stator-flux oriented reference frame [56].

In the stator-flux oriented reference frame, the *d*-axis is aligned with the stator flux linkage vector λ_s, namely, $\lambda_{ds} = \lambda_s$ and $\lambda_{qs} = 0$. Therefore, according to the two-axis equations of the DFIG in Section 2.2.3, the following relationships can be obtained:

$$i_{qs} = -L_m i_{qr} / L_s \tag{6.24}$$

$$i_{ds} = L_m (i_{ms} - i_{dr}) / L_s \tag{6.25}$$

$$T_e = -\frac{3}{2}\frac{p}{2} L_m^2 i_{ms} i_{qr} / L_s \tag{6.26}$$

$$Q_s = \frac{3}{2}\omega_s L_m^2 i_{ms} (i_{ms} - i_{dr}) / L_s \tag{6.27}$$

$$v_{dr} = r_r i_{dr} + \sigma L_r \frac{di_{dr}}{dt} - s\omega_s \sigma L_r i_{qr} \tag{6.28}$$

$$v_{qr} = r_r i_{qr} + \sigma L_r \frac{di_{qr}}{dt} + s\omega_s \left(\sigma L_r i_{dr} + L_m^2 i_{ms} / L_s\right) \tag{6.29}$$

where

$$i_{ms} = \frac{v_{qs} - r_s i_{qs}}{\omega_s L_m} \tag{6.30}$$

$$\sigma = 1 - \frac{L_m^2}{L_s L_r} \tag{6.31}$$

Equations (6.22) and (6.26) indicate that the DFIG rotor speed ω_r can be controlled by regulating the q-axis rotor current components, i_{qr}; while (6.27) indicates that the stator reactive power Q_s can be controlled by regulating the d-axis rotor current components, i_{dr}. Consequently, the reference values of i_{dr} and i_{qr} can be determined directly from the stator reactive power (Q_s) and DFIG rotor speed (ω_r) regulation.

Figure 6.7 shows the diagram of the PI-type speed controller that generates the reference value i_{qr}^* for maximum wind power extraction. The speed command ω_r^* is determined from the maximum wind power tracking algorithm shown in Figure 6.5. To overcome the windup phenomenon of PI controllers, the anti-windup scheme [133] shown as the dash-line block is applied for the speed controller as well as all other PI controllers in this design. The gain k_a is given by $k_a = 1/k_p$.

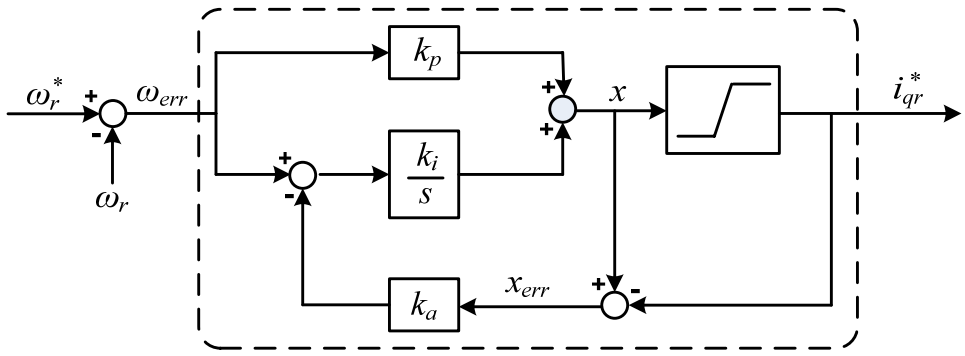

Figure 6.7: PI-type DFIG speed controller with anti-windup design.

In this application, the two oscillating frequencies of the DFIG WTG system are f_1 = 0.936 Hz and f_2 = 2.248 Hz. To sufficiently damp the low-frequency torsional oscillations, the basic principles to select the PI gains, k_p and k_i, of the speed controller (Figure 6.7) are as follows. First, the cutoff frequency of the speed controller, $f_{c,PI}$, should be less than $1/p$ of the oscillating frequency f_1.

$$f_{c,PI} < f_1/p \tag{6.32}$$

Generally, the value of p should be larger than 5. Second, the speed controller should reduce the gains of the system (6.22) at the oscillating frequencies by more than q dB, which means that

$$10 \cdot \log\left(\left| k_p + \frac{k_i}{s} \right| \right)_{\substack{s=j2\pi f_1 \\ s=j2\pi f_2}} < q \tag{6.33}$$

Generally, the value of q is selected less than -20 dB in order to provide the system with satisfactory damping. Based on (6.32) and (6.33), the ranges of k_p and k_i can be approximately determined. The final values of k_p and k_i can be obtained by investigating the system responses in the time-domain at the nominal or other desired operating conditions. The issues of selecting k_p and k_i will be further studied in Section 6.3 by time-domain simulations.

Figure 6.8 shows the overall vector control scheme of the RSC [121]. In the *d*-*q* reference frame, there exist cross-coupling terms between the *d*-axis and *q*-axis

components; as shown in (6.28) and (6.29), v_{dr} and v_{qr} depend on both i_{dr} and i_{qr}. The coupling may deteriorate the current loop response if it is not well compensated. To improve the transient performance of the current loops, a simple decoupling scheme [56] is applied in which the cross-coupling terms in (6.28) and (6.29) are not included in the current loop PI controller design. The resulting voltage components v_{dr1} and v_{qr1} only depend on *d*-axis and *q*-axis currents, i_{dr} and i_{qr}, respectively, and therefore can be regulated independently by i_{dr} and i_{qr}. This decoupling provides the current loop with fast response and improved dynamic performance. The outputs of the two current controllers are compensated by the corresponding cross-coupling terms, v_{dr2} and v_{qr2}, to form the total voltage signals, v_{dr} and v_{qr}. They are then used by the PWM module to generate the IGBT gate control signals to drive the IGBT converter. The reactive power control of the RSC can be applied to achieve the desired power factor at the connection point of the WTG. When the WTG feeds into a strong power system, the reactive power command of the RSC can be simply set to zero.

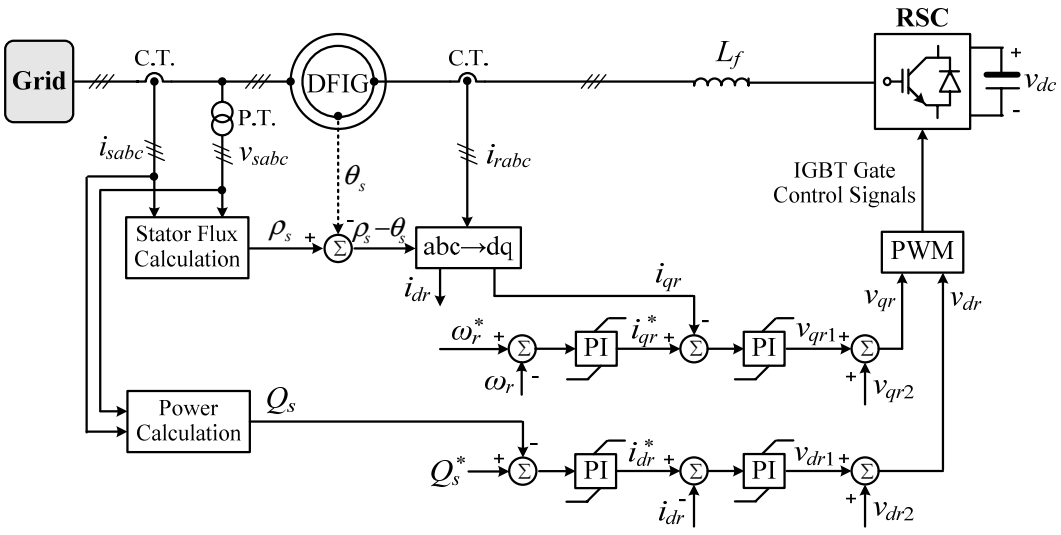

Figure 6.8: Overall vector control scheme of the RSC: $v_{dr2} = -s\omega_s\sigma L_r i_{qr}$, $v_{qr2} = s\omega_s(\sigma L_r i_{dr}+L_m^2 i_{ms}/L_s)$.

6.2.4 Control of the Grid Side Converter

The objective of the GSC is to keep the dc-link voltage constant regardless of the magnitude and direction of the rotor power. If the RSC has been arranged for reactive power control, then the GSC control scheme can be designed to regulate directly the stator terminal voltage of the DFIG. This arrangement can mitigate terminal voltage fluctuations of the DFIG caused by the variations of the wind speed, and therefore improve the power quality when the WTG is connected to a weak power network [134].

Figure 6.9 shows the overall control scheme of the GSC [121]. The control of the dc-link voltage and the DFIG stator terminal voltage (v_{dc} and V_s) is also achieved by current regulation in a synchronously rotating reference frame [109]. The output voltage signals, v_{dg} and v_{qg}, from the current controllers are used by the PWM module to generate the IGBT gate control signals to drive the GSC. Again, the *d-q* decoupled current control is applied to improve the transient performance of the inner current loop.

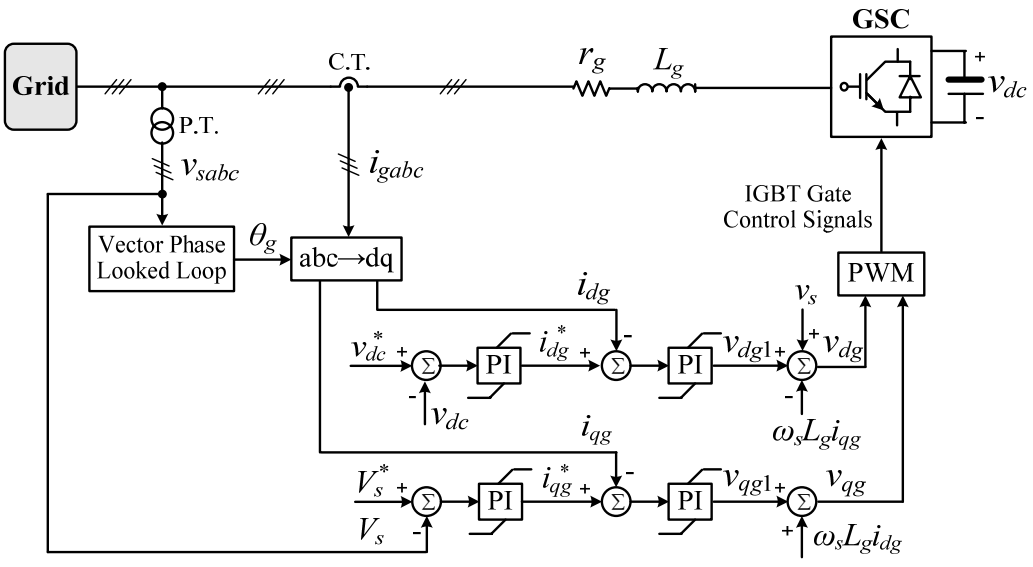

Figure 6.9: Overall vector control scheme of the GSC.

6.2.5 Pitch Angle Controller

The pitch angle controller is only activated at high wind speeds. In such situations, the rotor speed can no longer be controlled within its limits by increasing the generated power, as this would lead to overloading of the generator and/or the converter. Therefore, the pitch angle is controlled to reduce the mechanical power extracted from wind. Figure 6.10 shows the structure of the pitch angle controller [2], [121], in which P_e is the total output active power from the DFIG.

More details on modeling and control of a DFIG wind turbine and their models in PSCAD/EMTDC are presented in Appendix D.

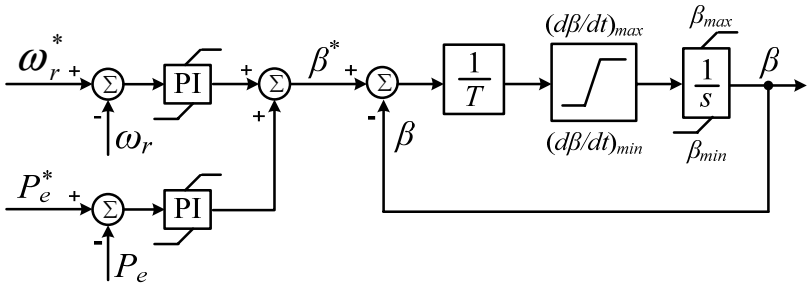

Figure 6.10: Wind turbine pitch angle controller.

6.3 Simulation Study

The wind speed estimation and control algorithm is firstly verified by simulation studies. Considering a grid connected DFIG wind turbine as shown in Figure 6.11. The WTG represents a 3.6 MW variable-speed DFIG wind turbine [55]. It is connected to the grid through a step-up transformer and two parallel lines. A three-phase balanced electric load at bus 3 draws a constant active power and reactive power from the system. The parameters of the DFIG wind turbine are provided in Appendix E.1. The parameters of the RSC controllers in Figure 6.8, the GSC controllers in Figure 6.9, and the wind turbine pitch angle controller in Figure 6.10 are provided in Tables G.3, G.4 and G.5,

respectively. The parameters of the power network (on 3.6 MVA, 34.5 kV bases) are given as follows. The equivalent reactance between WTG and the transformer is x_l = 0.001 pu; the total leakage reactance of the transformer is x_t = 0.03 pu; the equivalent resistances of Line 1 and Line 2 are r_{l1} = 0.02 pu and r_{l2} = 0.002 pu, respectively; the equivalent reactances of Line 1 and Line 2 are x_{l1} = 0.08 pu and x_{l2} = 0.008 pu, respectively.

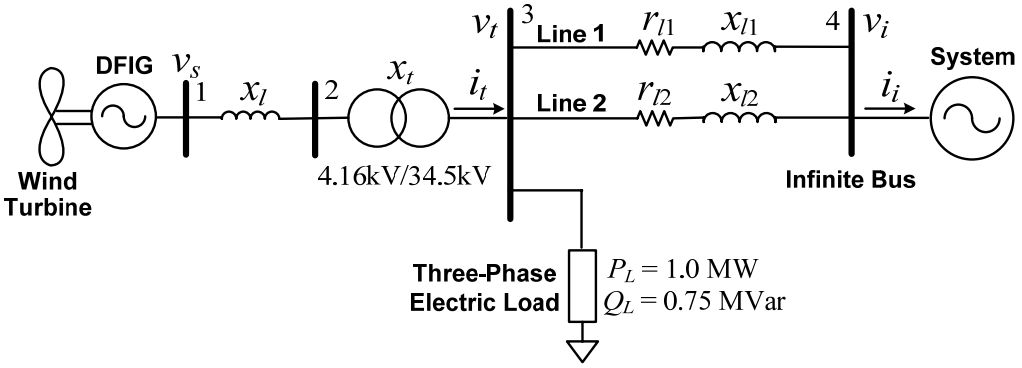

Figure 6.11: Single-line diagram of a DFIG wind turbine connected to a power system.

6.3.1 Wind Speed Estimation

Simulation studies are firstly carried out to evaluate the performance of the proposed GRBFN-based wind speed estimation algorithm. In the real system, the wind speed is always fluctuating. During the simulation, a four-component wind model (see Appendix D) as defined in [135] is used as the actual wind to drive the WTG. The speed of the wind is estimated by the proposed algorithm. To estimate the wind speed, the mechanical power that the wind turbine extracts from the wind is firstly estimated from the measured DFIG output electrical power based on (6.13)-(6.11). This estimation takes into account the losses of the WTG and the dynamics of the WTG shaft system. Figure 6.12 shows that the turbine mechanical power is accurately estimated with the estimation errors within ±0.1 MW, which is less than 3% of this WTG power rating.

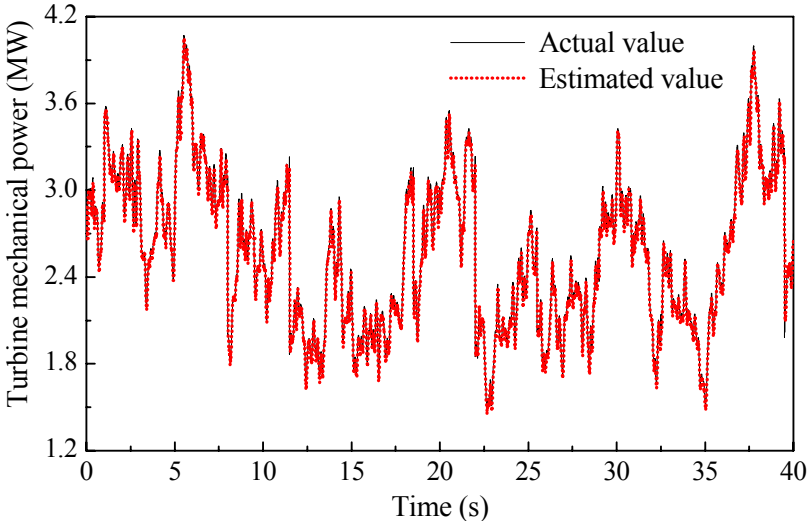

(a) Actual and estimated mechanical power that the wind turbine extracts from the wind.

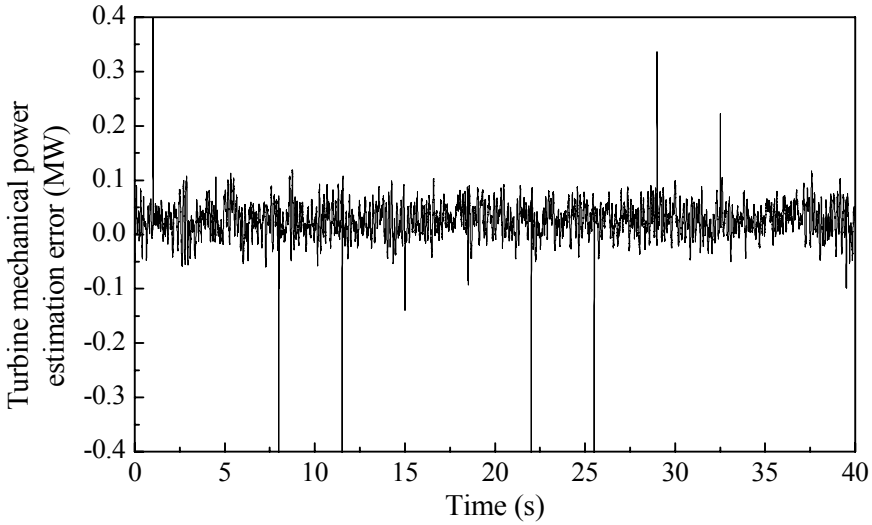

(b) Turbine mechanical power estimation errors.

Figure 6.12: Turbine mechanical power estimation results.

Based on the estimated turbine mechanical power, the wind speed is then estimated by the proposed algorithm (Figure 6.3). Figure 6.13 shows the wind speed estimation results. The estimated wind speed tracks the actual wind speed with good precision and the estimation errors are kept within about ±0.2 m/s [Figure 6.13(b)].

Based on the estimated wind speed, the optimal DFIG rotor speed command ω_r^* can now be determined for maximum wind power extraction (see Figure 6.5). This optimal speed command corresponds to the optimal tip-speed-ratio of the WTG at any

moment. Figure 6.14(a) shows that the rotor speed is well controlled to track its reference accurately during wind speed variations. The tracking errors are kept within ±0.2 rad/s as shown in Figure 6.14(b), which is less than 0.11% of the actual rotor speed. The resulting tip-speed-ratio of the wind turbine is varying around 6.0 as shown in Figure 6.14(c). The variations of tip-speed-ratio are caused by fast variations of the wind speed and the relatively slow responses of the WTG system. However, the average value of the tip-speed-ratio is 5.95, which is very close to the optimal tip-speed-ratio $\lambda_{opt} = 5.96$.

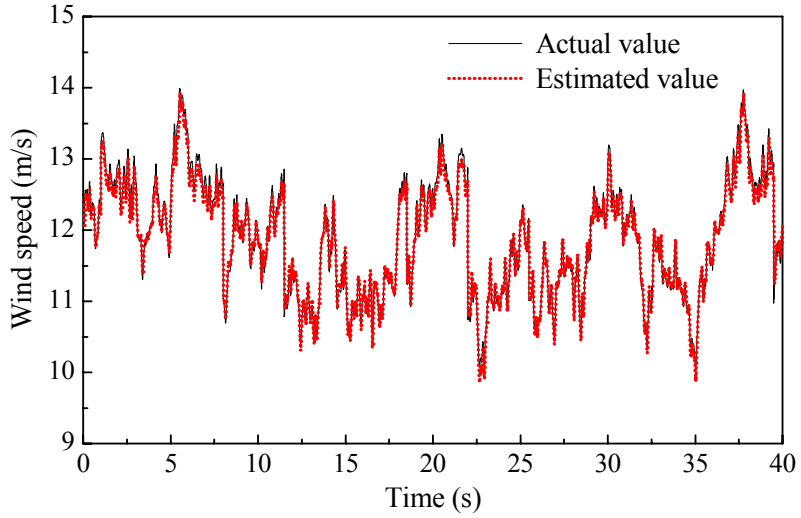

(a) Actual and estimated wind speed.

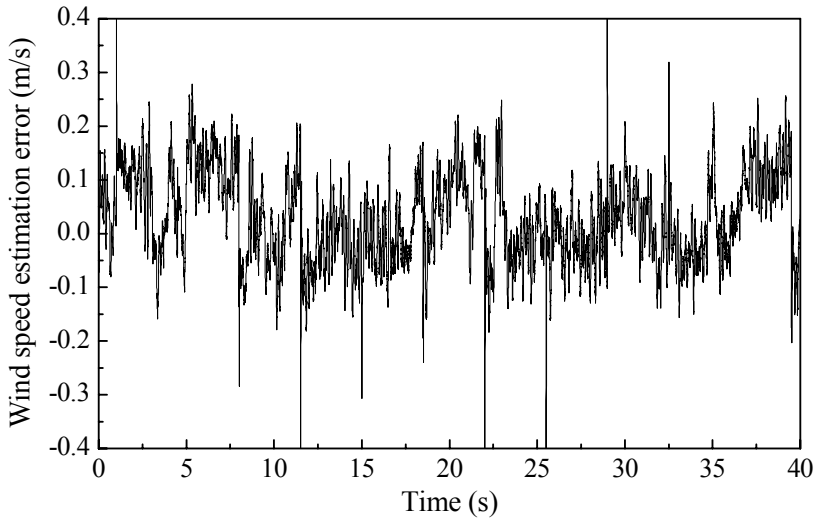

(b) Wind speed estimation errors.

Figure 6.13: Wind speed estimation results based on the scheme in Figure 6.3.

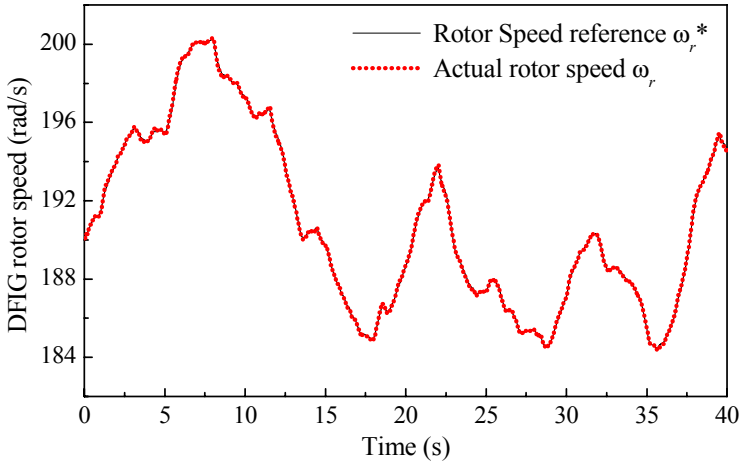

(a) Reference and actual rotor speed.

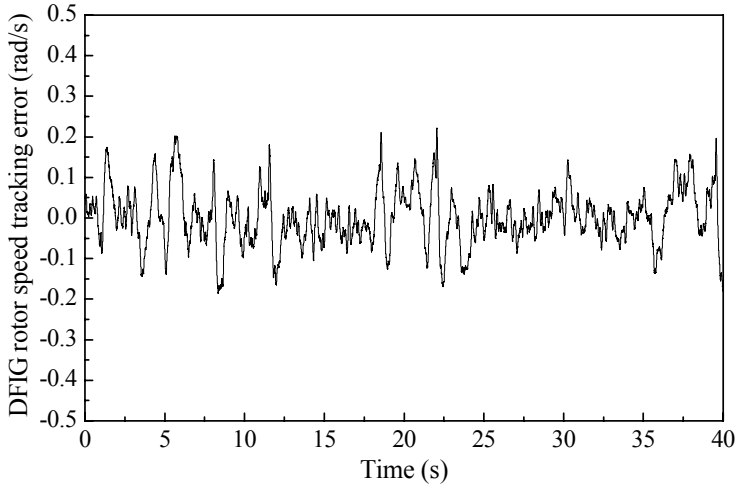

(b) Rotor speed tracking errors.

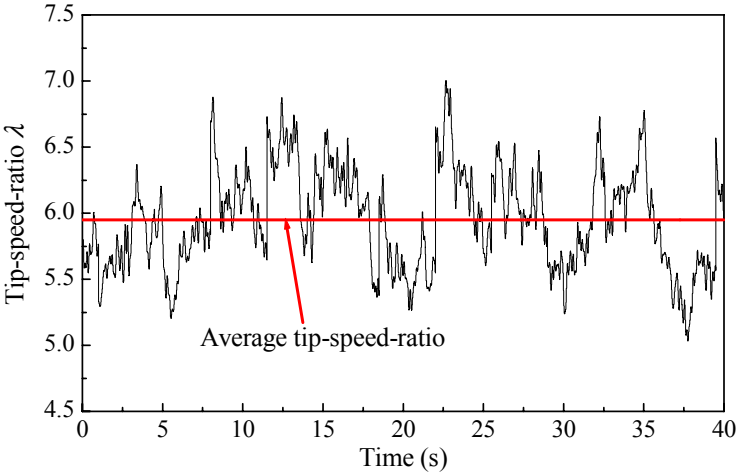

(c) Actual and average tip-speed-ratios of the wind turbine.

Figure 6.14: Performance of the DFIG speed controller for maximum wind power extraction.

Figure 6.15 shows the results of the DFIG output electrical power. Compared to the results in Figure 6.12, the dynamic difference between the turbine mechanical power and the DFIG electrical power is caused by the shaft system dynamics and the losses of the WTG.

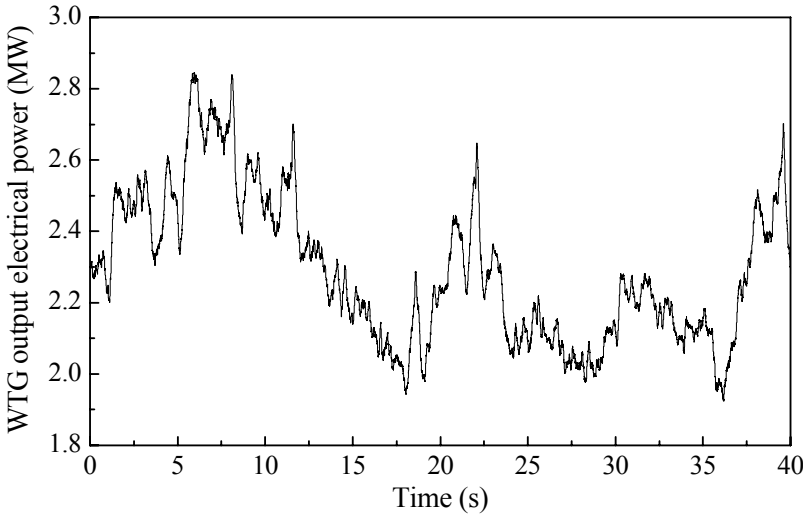

Figure 6.15: DFIG output electrical power.

6.3.2 DFIG Speed Controller for Damping Torsional Oscillations

Due to the electromechanical interaction between the WTG shaft system and the power network, grid disturbances may excite shaft torsional oscillations, primarily, in the shaft system equipped gearbox [2]. The torsional oscillation modes can be seen in the fluctuations of the generator rotor speed, which will also lead to the fluctuations of the electric variables of the generator, such as the electrical power and rotor current. Excessive speed fluctuations may cause an excessive rotor current to reach the trip limit of the converter. When the torsional oscillations of the shaft system are insufficiently damped, the WTG might have to be disconnected. As discussed in the previous Section 6.2.2, in order to damp low-frequency torsional oscillations of the WTG, the gain and bandwidth of the DFIG speed controller must be properly designed.

The ranges of the integral and proportional gains of the speed controller (Figure 6.7) can be firstly selected in the frequency domain using (6.32) and (6.33). The final values of k_p and k_i are then designed by time-domain simulations.

Assuming that the wind speed is step changed from 10 m/s to 13.5 m/s at t = 10 s, Figure 6.16 shows the responses of the DFIG output active power P_e when using fixed proportional gain k_p = 0.1 but different integral gains, where $k_{i1} < k_{i2} < k_{i3} < k_{i4}$ (k_{i1} = 0.1, k_{i2} = 0.2, k_{i3} = 1.0, and k_{i4} = 4.0). A larger integral gain k_i gives a higher bandwidth for the closed-loop system. These results indicate that the smallest gain k_{i1} should be used. It provides the closed-loop system with a sufficient low bandwidth so that the low-frequency torsional oscillations are sufficiently damped.

Figure 6.17 shows the responses of the DFIG wind turbine internal torque T_{tg} as described by (2.6)-(2.8) when using fixed proportional gain k_p = 0.1 but different integral gains. Again, the smallest overshoot and best damping of T_{tg} are obtained when using the smallest integral gain k_{i1} = 0.1, which minimizes the mechanical stress on the WTG shaft system during a significant transient event.

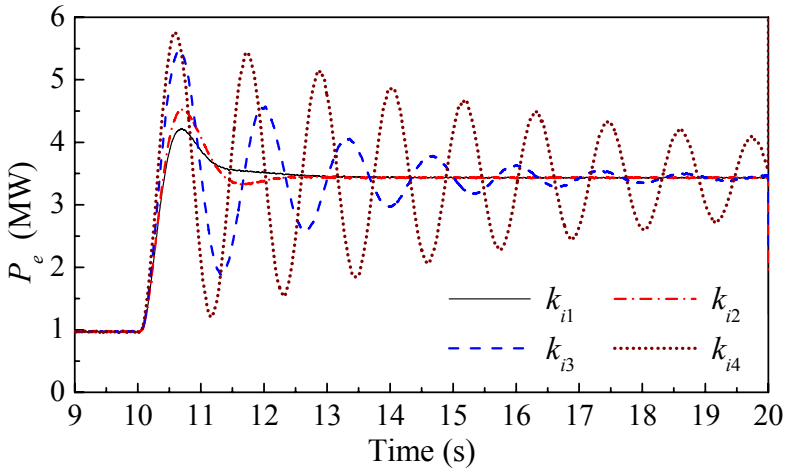

Figure 6.16: The responses of the DFIG output active power P_e to a step change of the wind speed when using different integral gains for the speed controller.

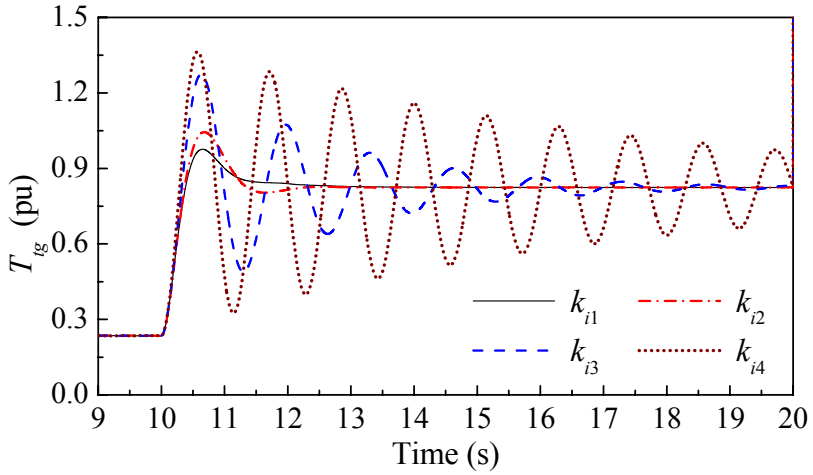

Figure 6.17: The responses of the DFIG wind turbine internal torque T_{tg} to a step change of the wind speed when using different integral gains for the speed controller.

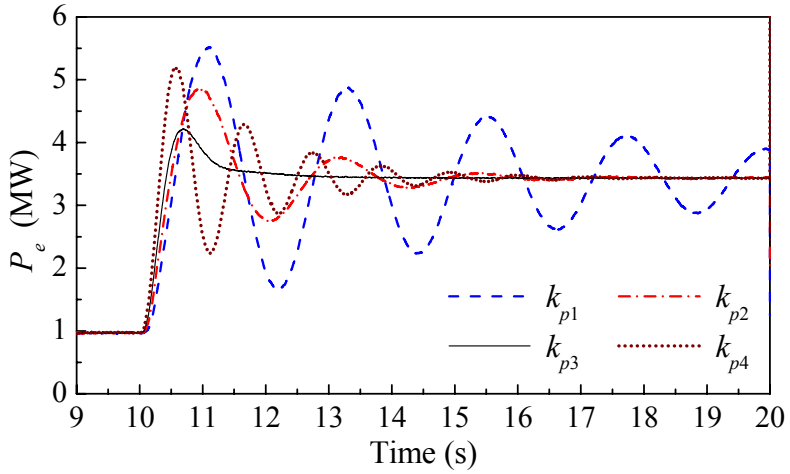

Figure 6.18: The responses of the DFIG output active power P_e to a step change of the wind speed when using different proportional gains for the speed controller.

Now the integral gain is fixed at $k_i = 0.1$. The same step change as in Figure 6.16 is applied to the wind speed at $t = 10$ s. Figure 6.18 and Figure 6.19 show the responses of P_e and T_{tg}, respectively, when using different proportional gains for the speed controller, where $k_{p1} < k_{p2} < k_{p3} < k_{p4}$ ($k_{p1} = 0.01$, $k_{p2} = 0.04$, $k_{p3} = 0.1$, and $k_{p4} = 0.5$). The best damping is achieved by using the gain k_{p3}. According to the results in Figure 6.16-Figure 6.19, the proportional and integral gains are chosen as $k_p = 0.1$ and $k_i = 0.1$,

respectively, which provide the best damping performance for low-frequency torsional oscillations and minimize the mechanical stress on the WTG shaft during a disturbance.

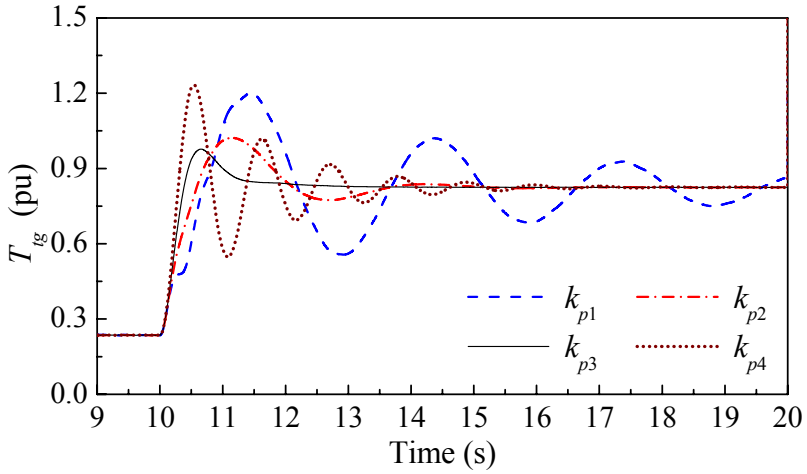

Figure 6.19: The responses of the DFIG wind turbine internal torque T_{tg} to a step change of the wind speed when using different integral gains for the speed controller.

6.3.3 Grid Disturbances

A three-phase short circuit is applied to the bus 4 end of line 2 (Figure 6.11) at t = 10 s; 200 ms thereafter, the fault is cleared and line 2 is tripped off from the system. Figure 6.20 compares the responses of the DFIG output active power P_e and terminal voltage V_s by using the measured and estimated wind speeds, respectively. In the decoupled control of the DFIG, the speed control and the resulting output active power depend on the estimated wind speed. During the transient state of this large disturbance, the performance of turbine mechanical power estimation degrades; so does the performance of wind speed estimation. Consequently, the performance of the DFIG speed control degrades slightly during the transient state when using the estimated wind speed. This causes slight differences of the DFIG output active power between the cases of using measured and estimated wind speeds, as shown in Figure 6.20(a). The performance of the DFIG speed control is improved when the system returns back to the

steady state. Figure 6.20(a) shows that the active power response of the WTG using the estimated wind speed is still close to that using the measured wind speed, and the differences are kept within the acceptable range, even during the transient disturbances.

On the other hand, the reactive power and voltage control of the DFIG are relatively independent of the wind speed. Therefore the DFIG stator voltage responses are almost the same for the WTG system using both the measured and estimated wind speeds, as shown in Figure 6.20(b).

The differences of the DFIG stator terminal voltage response between these two cases are shown in Figure 6.20(c). The range of the voltage differences with respect to the nominal voltage is within ±0.03% during the steady state but is increased to ±2% during the transient state. The reasoning is that the DFIG system is not ideally decoupled so that the rotor speed and the active power still have slight influence on the reactive power and the terminal voltage.

In conclusion, the results in Figure 6.20 show that the proposed wind speed estimation based sensorless control system provide an effective and accurate control to the WTG during large transient disturbances.

6.4 Experimental Verification

The proposed wind speed estimation based sensorless maximum wind power tracking control can be applied to other WTG systems. Here the essential part is the wind speed estimation because a high-performance maximum power tracking control relies on accurate wind speed information. To accurately estimate the wind speed for other WTG systems, the power losses in the WTG and the dynamics of the WTG shaft system need to be appropriately considered, as for the DFIG wind turbine system in Section 6.1.

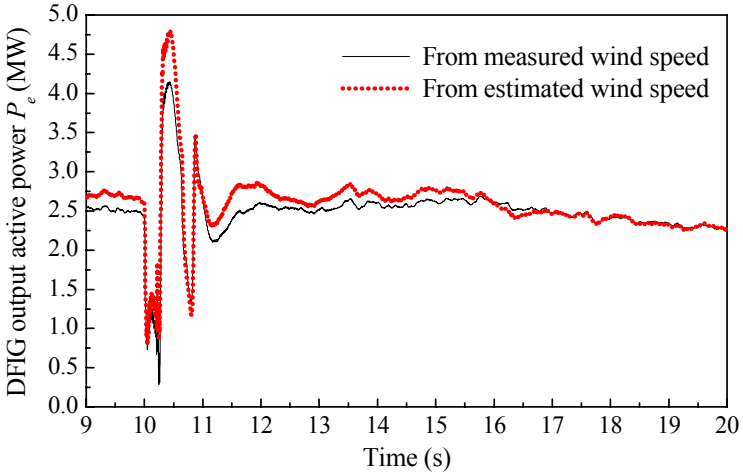

(a) DFIG output active power P_e.

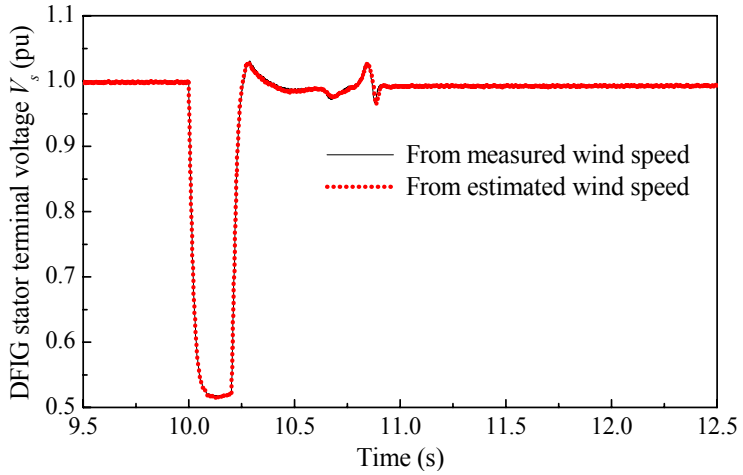

(b) DFIG stator terminal voltage V_s.

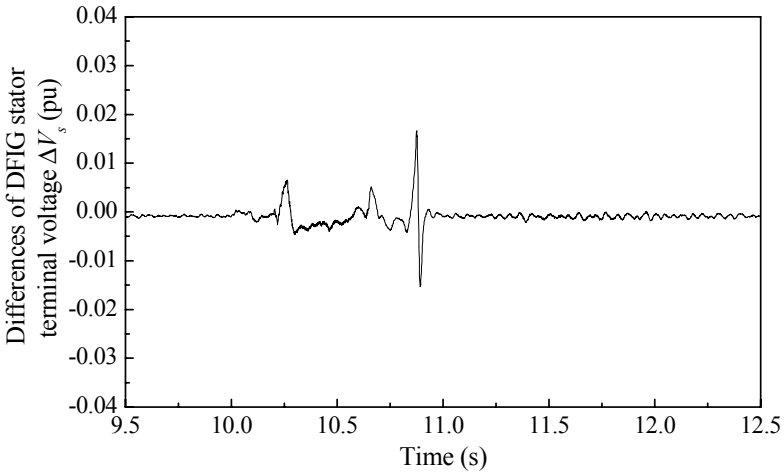

(c) Differences of the DFGI stator terminal voltage ΔV_s.

Figure 6.20: The responses of the DFIG during a three-phase short circuit.

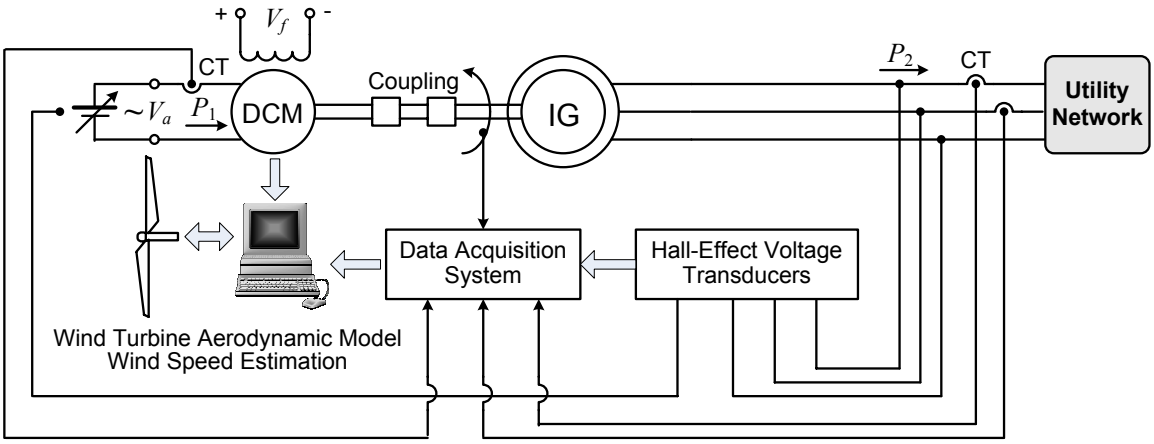

Figure 6.21: Hardware configuration of the experimental system.

Laboratory measurements are carried out to verify the proposed wind speed estimation algorithm using a small emulational WTG system. Figure 6.21 shows the hardware configuration of the experimental system. A squirrel-cage induction generator (SCIG) is driven by a dc motor with the fixed field voltage. This dc motor emulates a wind turbine. Its armature winding is connected to a reversible variable dc voltage source, so that the armature voltage can be varied to emulate the variations of the turbine mechanical power that are caused by wind speed variations. The wind turbine aerodynamic model is implemented on a lab computer to emulate wind energy to turbine mechanical power conversion. This aerodynamic model represents a nonlinear mapping from the wind speed to the emulated turbine mechanical power (i.e., the input electrical power, P_1, of the dc motor). The required voltages and currents are measured by Hall-effect voltage and current transducers. These measurements are input to the lab computer to calculate the generator output electrical power P_2, which is then used for the implementation of the proposed wind speed estimation algorithm.

The experiment setup is shown in Figure 6.22. The system parameters are provided in Appendix E.2.

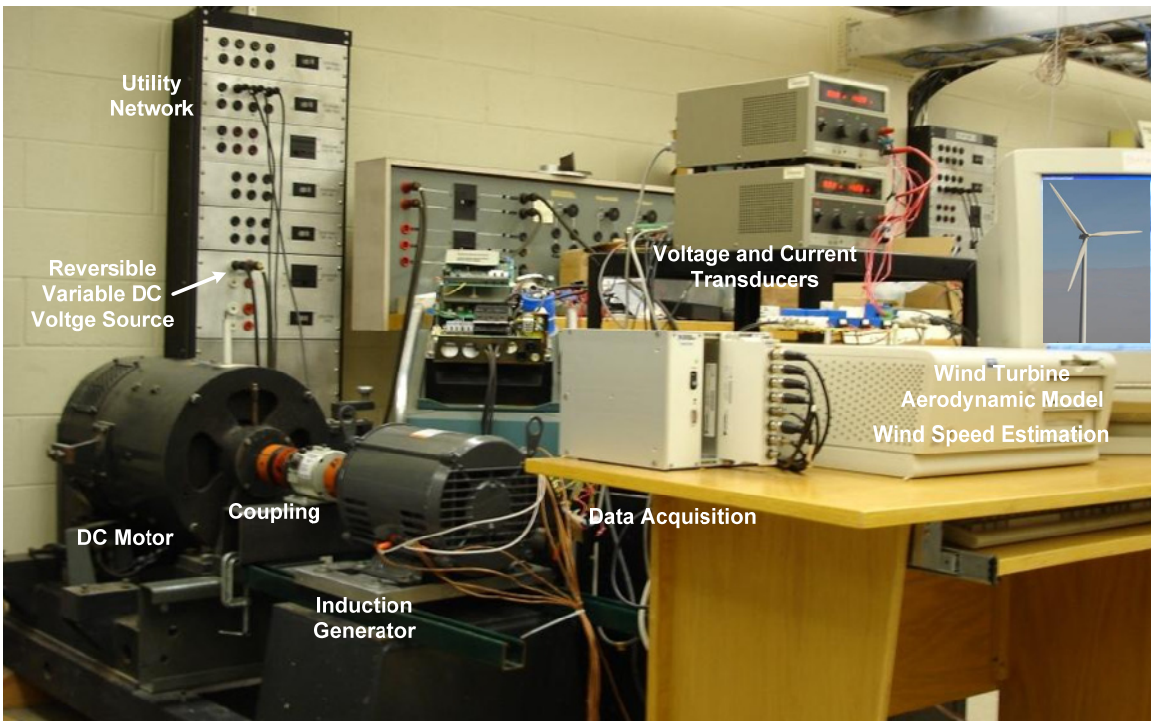

Figure 6.22: Experiment setup.

To demonstrate the performance of the proposed wind speed estimation algorithm, the armature voltage of the dc motor in Figure 6.22 is varied to emulate variable wind speed condition. The resulting emulated variable turbine mechanical power (i.e., the input electrical power, P_1, of the dc motor) is applied as the input to the dc motor. The emulated actual wind speed is then determined from the emulated actual turbine mechanical power (i.e., the measured value of P_1) on the lab computer by using the wind turbine aerodynamic model. The output electrical power of the system (i.e., P_2 in Figure 6.21) is measured at the point where the system is connected to the utility network, as shown in Figure 6.23(a). By appropriately considering the losses and the shaft dynamics of the system, the proposed algorithm estimates the emulated turbine mechanical power from the measured output electrical power P_2. Figure 6.23(a) compares the actual (i.e., the measured value of P_1) and estimated turbine mechanical power. These results indicate that the turbine mechanical power is accurately estimated;

the estimation errors [Figure 6.23(b)] are within ±0.15 kW, which are less than 3% of the system power rating. Compared to the DFIG WTG system in the previous sections, the moment of inertia of the experimental system is much smaller, and therefore, the system response is much faster. Consequently, the output electrical power and the emulated turbine mechanical power are almost in phase, as shown in Figure 6.23(a).

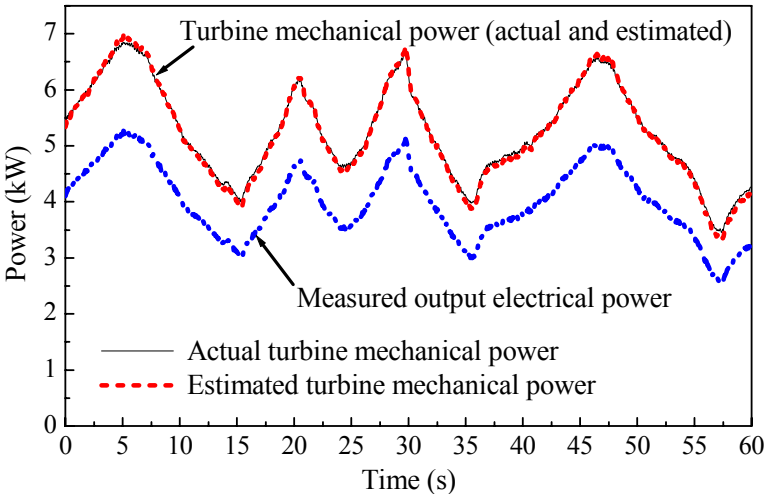

(a) Actual and estimated turbine mechanical power.

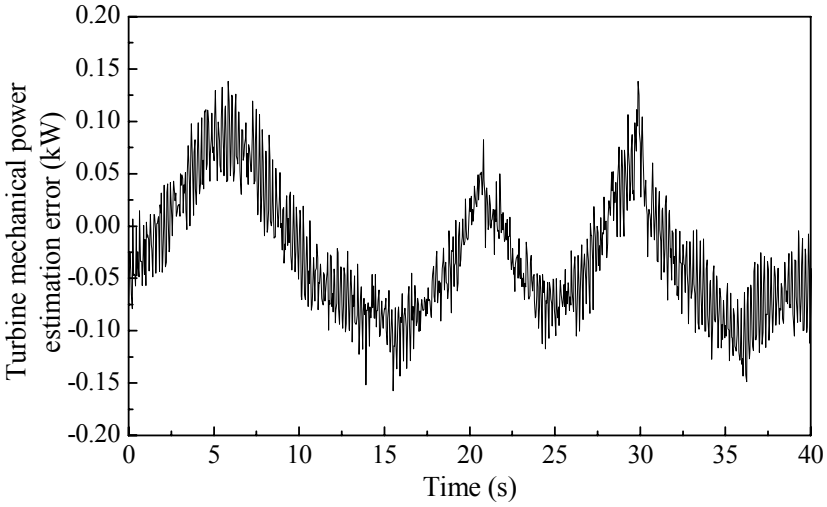

(b) Turbine mechanical power estimation errors.

Figure 6.23: Experimental turbine mechanical power estimation results.

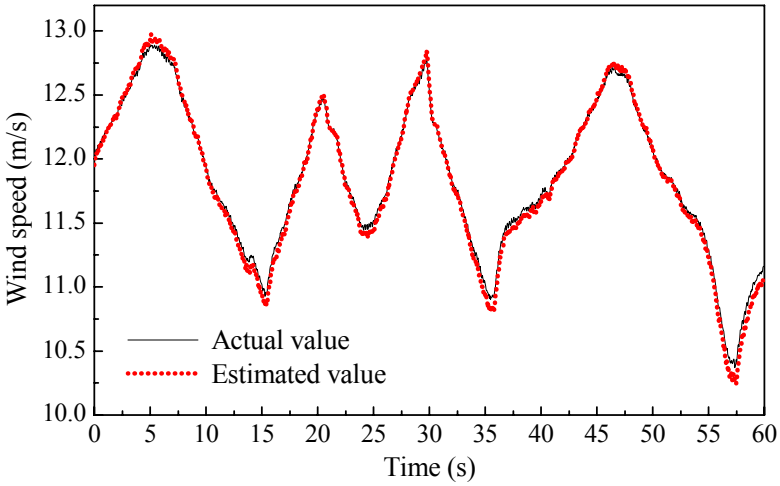

(a) Actual and estimated wind speed.

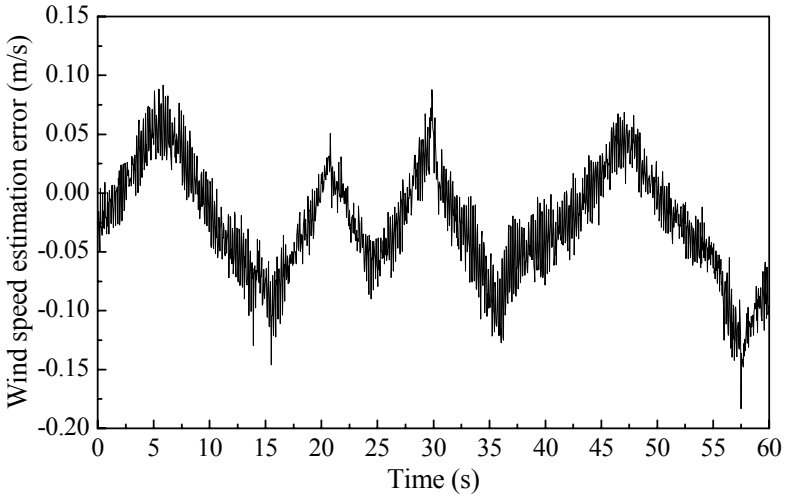

(b) Wind speed estimation errors.

Figure 6.24: Experimental wind speed estimation results.

Based on the estimated turbine mechanical power, the wind speed is then estimated by the proposed algorithm (Figure 6.3) and the results are shown in Figure 6.24. The wind speed varies within the range of 10 ~ 13 m/s. The estimated wind speed tracks the emulated actual wind speed with good precision and the estimation errors are within a small range of -0.15 ~ 0.1 m/s.

These experimental results show that the proposed wind speed estimation algorithm works perfectly to online estimate the wind speed by using the measured

output electrical power of the WTG. This is the essential part of the proposed control algorithm, because it provides the accurate wind speed information for implementing a high-performance maximum wind power tracking control without anemometers. The experimental results not only verify the theoretic and simulation studies of the proposed algorithm but also demonstrate the effectiveness of the proposed algorithm to more than one type of WTG systems.

6.5 Chapter Summary

This chapter has proposed a wind speed estimation based sensorless output maximum control for variable-speed wind turbine generator (WTG) systems. A specific design of the proposed control has been presented for a wind turbine driving a doubly fed induction generator (DFIG). A Gaussian radial basis function network (GRBFN) is used to provide a nonlinear input-output mapping for the wind turbine aerodynamic characteristics. The turbine mechanical power is estimated from the measured generator electrical power while taking into account the power losses of the WTG and the dynamics of the WTG shaft system. Based on the nonlinear GRBFN mapping, the wind speed is estimated from the turbine mechanical power and speed. The optimal DFIG rotor speed command is then determined from the estimated wind speed. To achieve the maximum wind power extraction, a DFIG speed controller has been suitably designed (gain and bandwidth) so that the low-frequency torsional oscillations of the WTG have been sufficiently damped. Other control issues, such as the reactive power and voltage control, have also been investigated in the entire control system design.

Simulation studies have been carried out on a 3.6 MW WTG system to verify the proposed sensorless control system. Results have shown that the wind speed was accurately estimated under both normal and transient operating conditions. The resulting WTG system delivered maximum electrical power to the grid with high efficiency and high reliability without mechanical anemometers. In addition, the proposed algorithm

can be applied to other WTG systems. Its effectiveness has been further demonstrated by experimental studies on a small emulational WTG system.

In this chapter, the parameters of the PI controllers in Figure 6.8 and Figure 6.9 are determined by the conventional linear design techniques, e.g., pole-zero placement and bode design. However, tuning PI controllers is tedious and it might be difficult to tune the PI gains optimally. In the next chapter, a particle swarm optimization (PSO) [32]-[34]-based intelligent approach will be proposed to design the optimal parameters of the rotor side converter controllers (Figure 6.8) of a DFIG wind turbine.

CHAPTER 7

DESIGN OF OPTIMAL PI CONTROLLERS FOR DFIG WIND TURBINES USING PSO

This chapter proposes an approach that uses the PSO algorithm to design the optimal PI controllers for the rotor side converter (RSC) of a wind turbine driving a doubly fed induction generator (DFIG) [136]. The proposed design approach is demonstrated by a specific design on an equivalent DFIG wind turbine in PSCAD/EMTDC.

7.1 Design of the Optimal PI Controllers for the Rotor Side Converter

In the RSC control loops (Figure 6.8), there are four PI controllers and each of them has a proportional gain and an integral time constant. In this section, the particle swarm optimization (PSO) [32]-[34] algorithm is applied to find the optimal parameters of the four PI controllers, namely, four proportional gains (K_ω, K_Q, K_d, and K_q) and four integral time constants (T_ω, T_Q, T_d, and T_q), to optimize some performance measure function (fitness function). Generally, the PI controller performance in the time domain can be measured by a set of parameters: the overshoot M_p, the rise time t_r, the settling time t_s, and the steady-state error E_{ss}. For example, if the objective is to minimize the over-current in the rotor circuit during grid faults, then a performance measure function can be defined as follows:

$$f(x) = \beta \cdot \Delta I_{r,max} + (1-\beta)(t_s - t_0) + \alpha \cdot |E_{ss}| \tag{7.1}$$

where $x = [K_\omega, K_Q, K_d, K_q, T_\omega, T_Q, T_d, T_q]$ represents the position vector of each particle; β and α are weighting factors; $\Delta I_{r,max}$ is the maximum rotor current magnitude deviation of the DFIG; t_0 is the starting time of the disturbance; and t_s is the settling time.

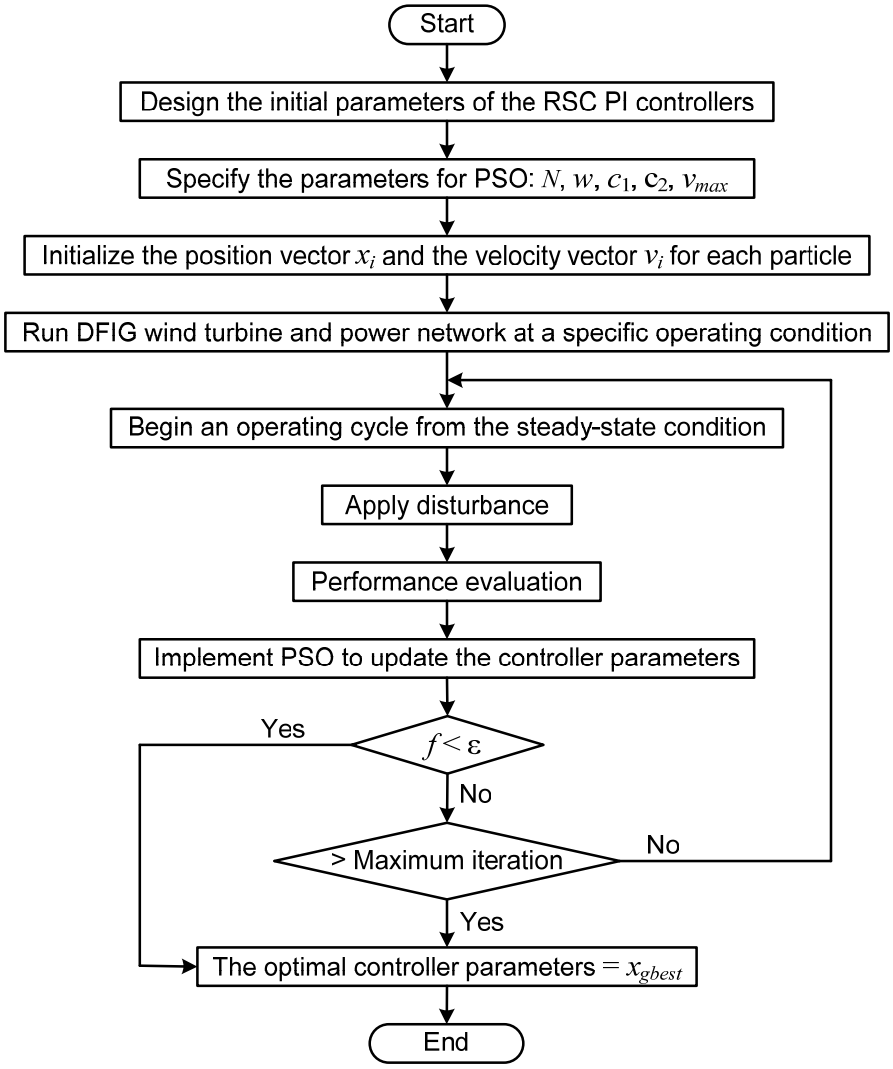

Figure 7.1: Procedure of designing the optimal PI controller parameters for the RSC.

The weighting factors β and α in the performance measure function $f(x)$ are used to satisfy different design requirements. If a large value of β is used, then the objective is to reduce the over-current in the rotor circuit. If a small value of β is used, then the objective is to reduce the settling time. The weighting factor α is introduced to minimize the steady-state error.

The proposed approach is implemented by a user-defined module which is integrated in the PSCAD/EMTDC simulator. The overall design procedure is shown in the flowchart in Figure 7.1. The DFIG RSC is firstly controlled by a set of initially

designed PI controllers with nonoptimal parameters. To obtain the optimal controller parameters, the following operating cycle is performed repetitively at a specific operating condition, e.g., the nominal condition, in the PSCAD/EMTDC simulator. During each operating cycle, the WTG and the power network are initially operated at the steady-state condition. A disturbance is then applied to the DFIG wind turbine or the power network in terms of the design objective. For example, the objective of this design is to minimize the overshoot of the rotor current during grid faults. Therefore, a severe grid fault, e.g., a three-phase short circuit, is applied at a certain location of the power network to which the WTG is connected. The performance of the RSC controllers is then evaluated by (7.1), which is used as a fitness function by the PSO algorithm to update the parameters of the RSC controllers. This operating cycle repeats until a desired performance, measured by (7.1), is obtained. The final outputs of the PSO are then regarded as the optimal parameters of the RSC controllers. In order to provide satisfactory performance over a wide operating range, the same design procedure can be performed at different operating conditions by applying different disturbances. The final optimal settings of the controller parameters are then selected as those that provide the best control performance.

7.2 A Specific Design

To demonstrate the effectiveness of the proposed design approach, the system in Figure 7.2 is now considered. In a practical power system, a large power plant is normally connected to the power network by multiple parallel power lines with certain capacity redundancy, not only because of the thermal limits of each single power line, but also to increase the reliability of the power transmission in the case of an outage of one power line. In this study a large wind farm is connected to a power network through a step-up transformer and two parallel lines. A three-phase balanced electric load at the sending-end bus is modeled as a constant impedance load. The parameters of the system components are given as follows (base power = 400 MVA and base voltage = 230 kV):

$r_{l1} = r_{l2} = 0.02$ pu, $x_{l1} = x_{l2} = 0.4$ pu, constant impedance load $Z_L = 4.5 + j2.18$ pu, transformer turn ratio: 22 kV/230 kV.

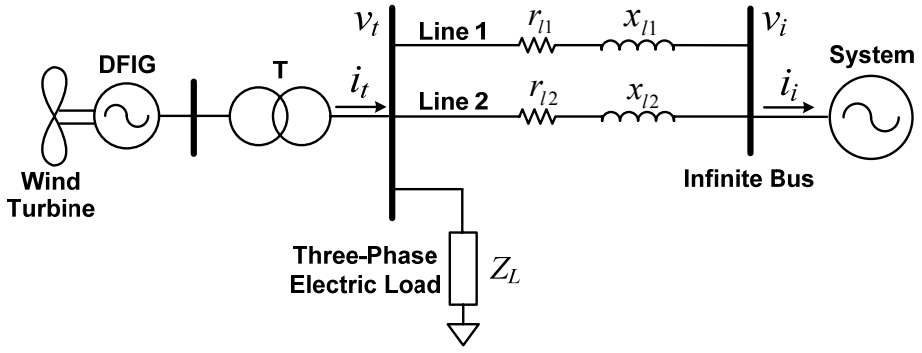

Figure 7.2: Single-line diagram of a wind farm connected to a power network.

The wind farm consists of over one hundred individual WTGs. Each individual wind turbine is equipped with a DFIG that represents a 3.6 MW WTG system [55], [121] (see Appendix E.1). It has been reported in [2] that with well-tuned converters, there is no mutual interaction between WTGs in a wind farm, independently from the conditions of the power grid. Therefore, the wind farm can be represented by an aggregated model in which over one hundred individual wind turbines and DFIGs are modeled as one equivalent DFIG driven by a single equivalent wind turbine [2], [137], [138]. Then the MVA-rating of the equivalent WTG is the sum of the MVA-ratings of all the individual WTGs, given by

$$S = \sum_{i=1}^{N} S_i \tag{7.2}$$

where N is the total number of WTG in the wind farm, S_i is the MVA-rating of the ith WTG in the wind farm. The mathematical model of this equivalent WTG is exactly the same as each individual WTG as described in Section 2.2. If the MVA-rating of the equivalent WTG is used as the base value, then the per-unit values of the equivalent WTG parameters, including the equivalent wind turbine parameters, equivalent shaft

system parameters, equivalent DFIG parameters, are exactly the same as those for each individual WTG in Figure 1.3, as provided in Appendix E.3. The parameters of the equivalent DFIG grid side converter (GSC) controllers (Figure 6.9) are given in Table G.4 of Appendix G.

The RSC PI controllers in Figure 6.8 are initially designed (but not optimal) at a specific operating point, where the equivalent WTG in Figure 7.2 is operating at a supersynchronous speed with the slip frequency around -0.2 pu, an output active power of 0.75 pu, an output reactive power of 0.125 pu (the RSC reactive power command is set to 0.125 pu), and a rotor current magnitude of 11.0 kA. The parameters of the RSC controllers are then optimized at this operating point using the proposed approach. Five particles are used in the PSO implementation and the position vector of the first particle is initialized as the initially designed parameters; while the position vectors of the other four particles are initialized with the values around the initially designed parameters using (1.2). The values of c_1 and c_2 in (1.2) are chosen as 2; the inertia constant $w = 0.8$. The weighting factors in (7.1) are chosen as $\alpha = 0$, $\beta = 1$ to limit the over-current in the rotor circuit during grid faults. The PSO is implemented with 30 trial runs (30×5 = 150 operating cycles) by applying a 100 ms three-phase short circuit at the receiving end of line 2. The initial values and the optimal values found by the PSO for the RSC controller parameters are listed in Table 7.1.

7.3 Simulation Results

Different grid faults are applied to the power system in Figure 7.2 to compare the performance of the optimal RSC controllers with that without the optimal design.

Table 7.1: Initial and optimal parameters of the RSC PI controllers

PI gains	K_ω	K_Q	K_d	K_q	T_ω	T_Q	T_d	T_q
Initial design	8.48	0.01	2.89	1.79	0.081	2.0	0.028	0.065
Optimal design	18.23	0.001	3.05	4.87	0.038	1.0	0.056	0.21

7.3.1 Case Study I: A Three-Phase Short Circuit Test at Receiving End of Line 2

A 100 ms temporary three-phase short circuit is applied to the receiving end of line 2 at t = 5.0 sec. Figure 7.3 shows the magnitudes of the DFIG rotor current for both designs. The rotor current magnitude is limited to 14 kA when applying the optimal design, which is much smaller than that of 19 kA when using the initial design. The reduction of the over-current in the rotor circuit avoids the blocking of the RSC and therefore achieves continuous operation of the WTGS during this grid fault. Due to the stator flux oscillations during the transient state after the grid fault, the rotor current oscillates with a frequency near the synchronous frequency, as discussed in [2].

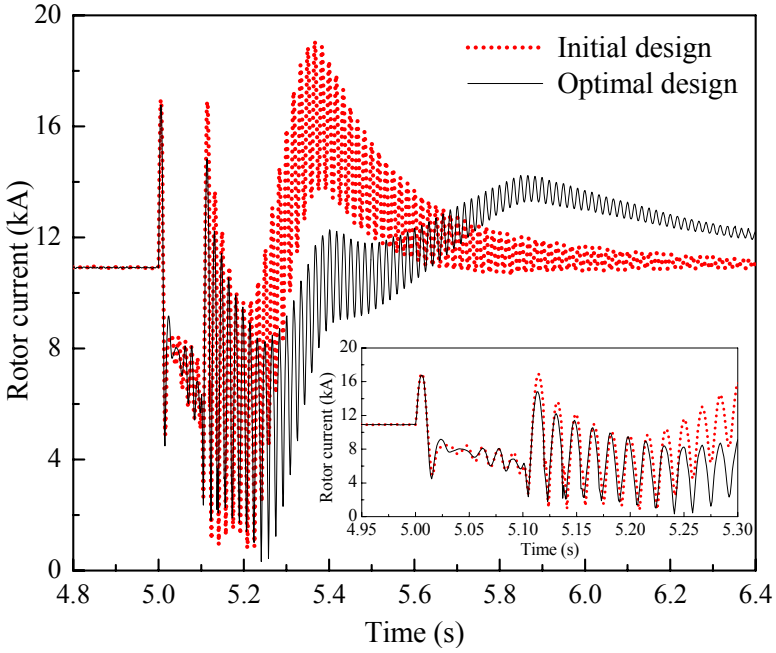

Figure 7.3: Comparison of the initial design and the optimal design in Case I.

7.3.2 Case Study II: A Three-Phase Short Circuit Test at Sending End of Line 2

The two designs are compared for another case, in which a three-phase short circuit is applied to the sending end of line 2 and 100 ms thereafter line 2 is tripped off from the system. In this case, the system in Figure 7.2 operates at a new operating point

after the fault is cleared. Figure 7.4 compares the magnitudes of the DFIG rotor current for both designs. Again, the magnitude of the post-fault rotor current is limited to 13.5 kA when applying the optimal design, which is much smaller than that of 24 kA when applying the initial design. It is concluded that the optimal design reduces the over-current in the rotor circuit effectively over a wide range of operating conditions.

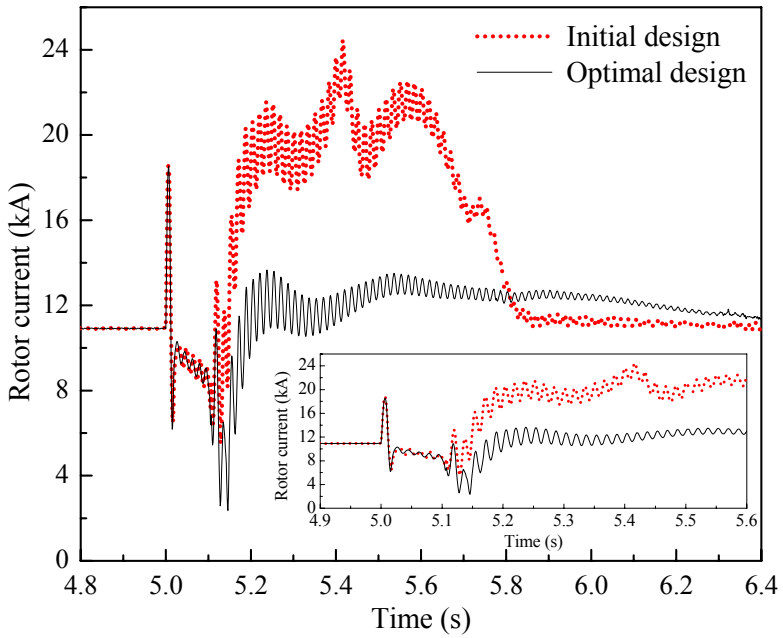

Figure 7.4: Comparison of the initial design and the optimal design in Case II.

7.4 Chapter Summary

A PSO-based approach has been proposed to design the optimal parameters of the rotor side converter (RSC) PI controllers for the wind turbines driving doubly fed induction generators (DFIGs). A specific design has been presented to minimize the over-current in the DFIG rotor circuit during grid faults. A time-domain fitness function has been defined to measure the performance of the controllers. Simulation studies have been carried out at the operating point where the optimal controllers have been designed, as well as at another operating point where the optimal controllers have not been

designed. Results have shown that the proposed design approach was efficient to find the optimal parameters of the RSC PI controllers. The resulting optimal controllers improved the transient performance of the wind turbine generator (WTG) system over a wide range of operating conditions. The proposed design approach can be readily applied to design other controllers in power systems.

Moreover, many WTGs are installed in remote, rural areas which usually have electrically weak power grids. In such grid conditions and during a grid fault, the DFIGs may not be able to provide sufficient reactive power support. Without any external dynamic reactive compensation, there can be a risk of voltage instability in the power grid [2]. To prevent such contingencies, external dynamic reactive compensator, e.g., the static synchronous compensator (STATCOM), may be required to provide transient voltage support to help WTGs ride through grid faults. This issue will be investigated in the next chapter.

CHAPTER 8

REAL-TIME IMPLEMENTATION OF A STATCOM ON A WIND FARM EQUIPPED WITH DFIG WIND TURBINES

Voltage stability is a key issue to achieve the uninterrupted operation of the wind turbines equipped with doubly fed induction generators (DFIGs) during grid faults. This chapter investigates the application of a static synchronous compensator (STATCOM) to assist with the uninterrupted operation during grid faults of a wind farm equipped with DFIG wind turbines, which is connected to a power network [139]. The control schemes of the DFIG wind turbine and the STATCOM are suitably designed and coordinated. The fault ride through enhancement of the wind turbine generators (WTGs) with the assistance of the STATOCM is demonstrated by real-time implementation results using a Real Time Digital Simulator (RTDS).

8.1 Wind Farm, STATCOM, and Power Network Model

In a practical power system, a wind farm generally consists of many individual WTGs. It has been reported in [2] that with well-tuned converters, there is no mutual interaction between WTGs in a wind farm, independently from the conditions of the power grid. Therefore in this study, only one WTG is used to represent the wind farm.

Figure 8.1 shows the single-line diagram of the power system used for this study. A 3.6 MW DFIG wind turbine (see Appendix E.1) is connected to a power grid through a transformer and two parallel lines ($r_{l1} = r_{l2} = 0.14$ pu, $x_{l1} = x_{l2} = 0.8$ pu). A three-phase balanced electric load at the sending end bus is modeled as a constant impedance load, $Z_L = 0.7 + j1.5$ pu. A STATCOM is shunt connected at the sending-end bus for steady-state as well as transient voltage support.

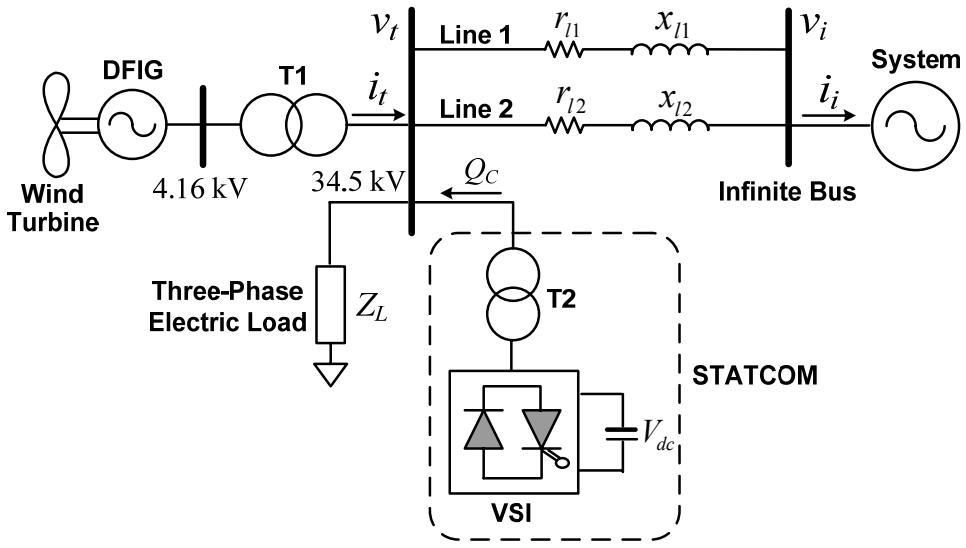

Figure 8.1: Single-line diagram of a DFIG wind turbine and a STATCOM in a single machine infinite bus (SMIB) power system.

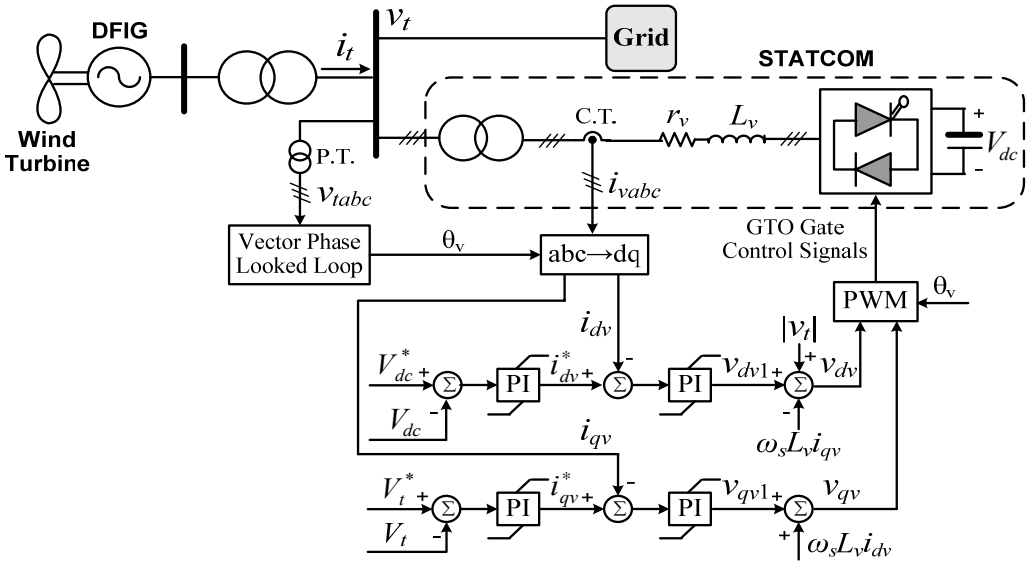

Figure 8.2: Overall control scheme of the STATCOM.

The configuration and control of the DFIG wind turbine are shown in Figure 1.3 and Figure 6.7-Figure 6.10. The detailed description of the WTG model and control systems is provided in Section 2.2 and Section 6.2.

The STATCOM is modeled as a GTO PWM converter with a dc-link capacitor. The objective of the STATCOM is to rapidly regulate the voltage at the point of common

coupling (PCC, i.e., 34.5 kV bus) in the desired range. It can enhance the capability of the WTG to ride through transient disturbances in the grid. The overall control scheme of the STATCOM is shown in Figure 8.2 [1]. It consists of two cascaded control loops. The outer voltage control loop regulates independently the PCC voltage and the dc-link voltage of the STATCOM, respectively; while the inner current control loop generates the *d*-*q* voltage components, v_{dv} and v_{qv}, at the ac-side of the voltage source inverter (VSI), and they are then used by the PWM module to generate the IGBT gate control signals to drive the VSI. To overcome the windup phenomenon of PI controllers, an anti-windup scheme in [133] is applied for all the PI controllers. More details on modeling and control of a STATCOM are presented in Appendix F and the parameters of the STATCOM controllers in this application are provided in Table G.6 of Appendix G.

8.2 Uninterrupted Operation of the DFIG Wind Turbine during Grid Faults

The idea behind the uninterrupted operation feature is that the WTG does not trip when the rotor side converter (RSC) has blocked during a grid fault. During the RSC blocking, the rotor circuit is short-circuited by a crow-bar circuit (Figure 1.3), which is simply implemented by connecting an external resistor across each phase of the rotor circuit. The value of the external resistance is chosen as $R_{ext} = 20 \cdot r_r$ [139]. The WTG continues its operation with the DFIG rotor short-circuited. During such an operation condition, the controllability of the RSC is naturally lost and there is no longer any independent control of active and reactive power in the DFIG. The DFIG becomes a conventional induction generator, which produces an amount of active power and starts to absorb an amount of reactive power. In order to prevent the wind turbine from over-speeding, the pitch angle controller (Figure 6.10) can be activated to keep the speed around the predefined value.

When the RSC is blocking, the grid side converter (GSC) can be set to control the reactive power exchanged between the DFIG and the grid. This controllability of the

GSC, however, is limited due to the small capacity of the converter. In a weak power network, as a result, there can be a risk of voltage instability and the subsequent tripping of the WTG. To prevent such a contingency, a STATCOM is used to provide transient voltage support to help the DFIG ride through grid faults. The STATCOM can also be used for steady-state voltage regulation and power factor control of the DFIG.

During the RSC blocking, the RSC control system (Figure 6.8) continues monitoring the generator rotor current, terminal voltage, active and reactive powers, and rotor speed. When the fault has cleared and when the terminal voltage and the rotor current return to their predefined ranges, the RSC restarts switching and the external resistors (crow-bar circuit) are disconnected. The voltage control of the GSC is deactivated and its reactive power command is reset to $Q_g^* = 0$ (Figure 6.9). When the RSC has restarted, the DFIG again has independent active and reactive power control and the WTG returns to normal operation.

The advantages of this uninterrupted operation feature include: 1) the WTG continues supplying the active power to the power network and therefore the demand for immediate power reserves is reduced; 2) the WTG contributes to maintaining the frequency in the power network during the transient state; 3) after a short-term blocking of the RSC, the WTG returns to normal operation quickly.

8.3 Real-Time Implementation Setup

The system in Figure 8.1 is implemented in real time on a RTDS, as shown in Figure 8.3. The RTDS hardware has a number of different types of processor cards available including the Triple Processor Card (3PC), the RISC Processor Card (RPC), and the Giga Processor Card (GPC). The 3PC contains three Analog Devices ADSP21062 (SHARC) processors each operating at 80 MHz. The 3PC is typically used to perform the computations required to model the user's power system and control systems with a typical time step of 50 microseconds. The RPC contains two IBM

PowerPC 750CXe RISC processors each operating at 600 MHz. The most recent GPC contains two IBM PowerPC 750GX RISC processors each operating at 1 GHz. In addition to the network solution and the simulation of standard components, the GPC can also be used to provide small time-step (< 2 microseconds) simulations of the VSCs with a high switching frequency. The RTDS provides a specially designed *small-dt* module to perform the small time-step simulations on the GPC card.

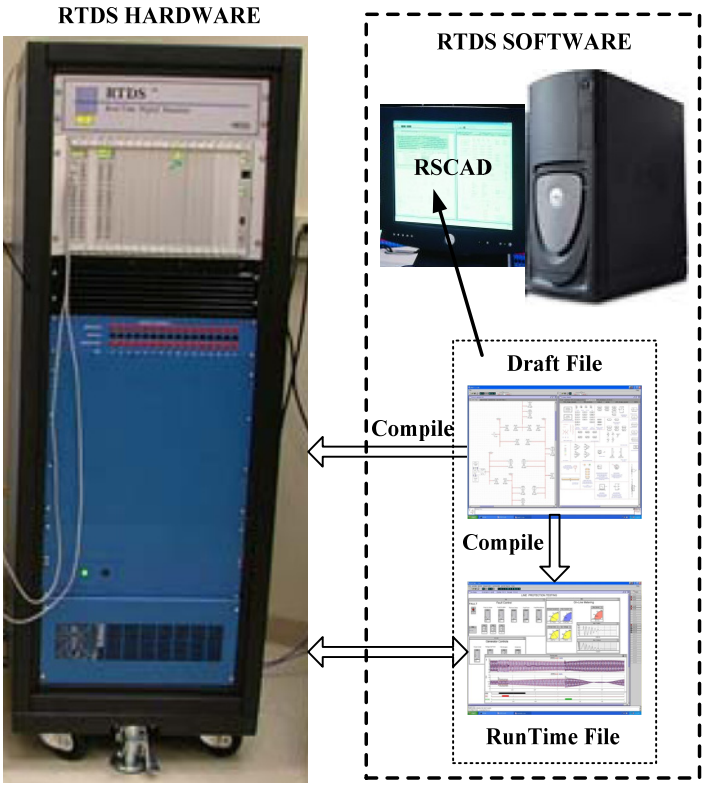

Figure 8.3: Real-time implementation setup using RTDS.

In this study, the variable frequency converter (VFC) of the DFIG contains two PWM IGBT converters with switching frequencies of 2 kHz each and therefore is simulated on the GPC card using the *small-dt* module. The power network model and the STATCOM are simulated on the 3PC and RPC cards. The control systems are simulated on the 3PC cards. Figure 8.4 shows the RTDS modules and the processor assignments

for real-time implementation of the system in Figure 8.1. Because the small time-step power system modules (< 2 microseconds) and the large time-step (50 microseconds) power system modules use different time steps during real-time implementations, they cannot be connected together directly. In RTDS, an interface transformer, which performs conversions between different time-step systems, is used to connect these two different time-step modules.

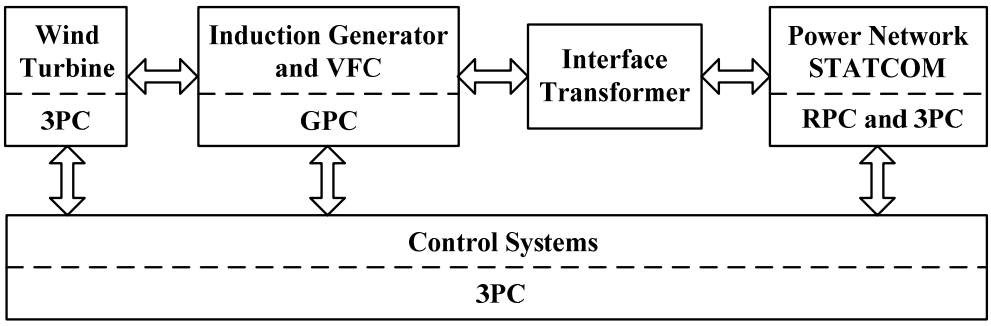

Figure 8.4: RTDS modules and processor assignments for real-time implementation.

8.4 Real-Time Implementation Results

This section presents the real-time implementation results of the system in Figure 8.1 at the following operating condition: 1) the wind speed is constant during the simulation (this assumption is reasonable for investigating the short-term voltage stability [2]); 2) the DFIG is running at a supersynchronous speed with the rotor speed at about 1.2 pu; 3) the DFIG does not exchange reactive power with the power system when applying the STATCOM by setting the reactive power commands of both RSC and GSC to zero.

8.4.1 Steady-State Voltage Regulation

The voltage command of the STATCOM controller (Figure 8.2), V_t^*, is step changed from 0.92 pu to 1.02 pu at t = 2 s and back to 0.92 pu at t = 5 s. Figure 8.5 shows the steady-state voltage regulation result and the corresponding reactive power, Q_c,

compensated by the STATCOM. Without any reactive compensation, the initial steady-state value of the PCC voltage V_t (Figure 8.2), is 0.92 pu which is below the acceptable lower limit value of 0.95 pu. With the STATCOM applied for reactive compensation, the PCC voltage is kept at the desired value of 1.02 pu. The response of the STATCOM to the step change of the voltage command is fast and smooth.

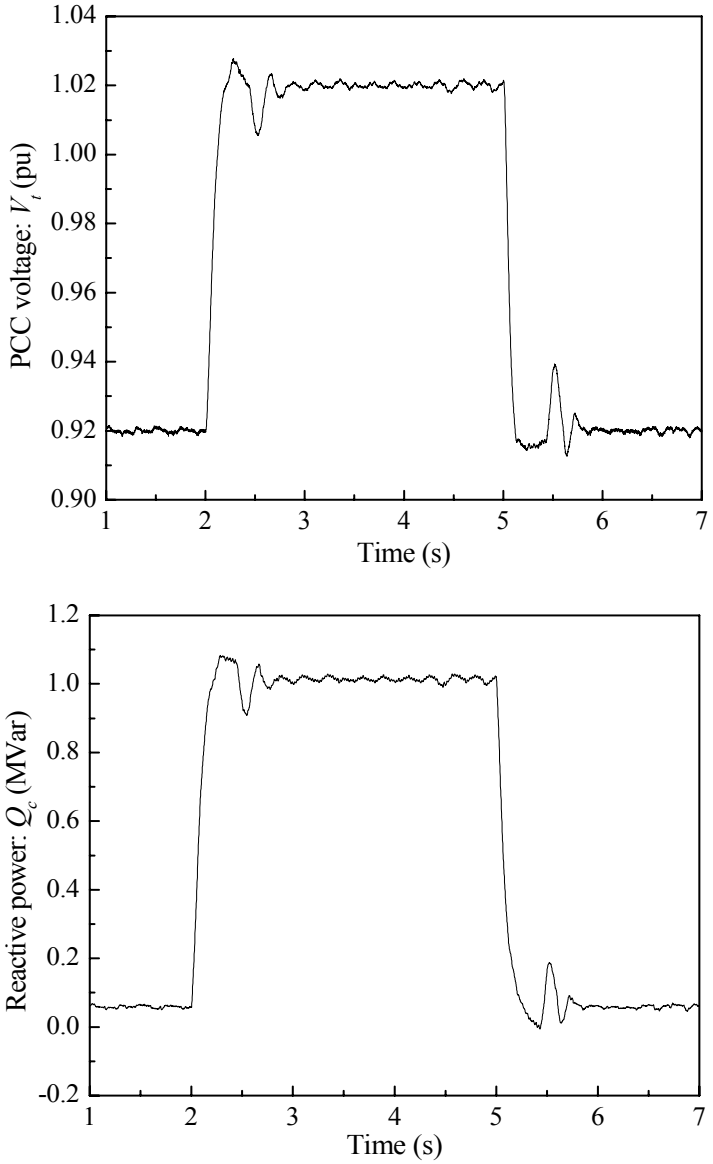

Figure 8.5: Steady-state voltage regulation result of STATCOM at PCC: V_t and Q_c, when the reference V_t^* has a step change.

8.4.2 A Three-Phase Short Circuit Test: Rotor Side Converter not Blocking

Grid faults, even far away from the location of the WTG, can cause voltage sags at the connection point of the WTG. Such a voltage sag results in an imbalance between the turbine input power and the generator output power, which initiates the machine stator and rotor current transients, the converter current transient, the dc-link voltage fluctuations, and a change in speed.

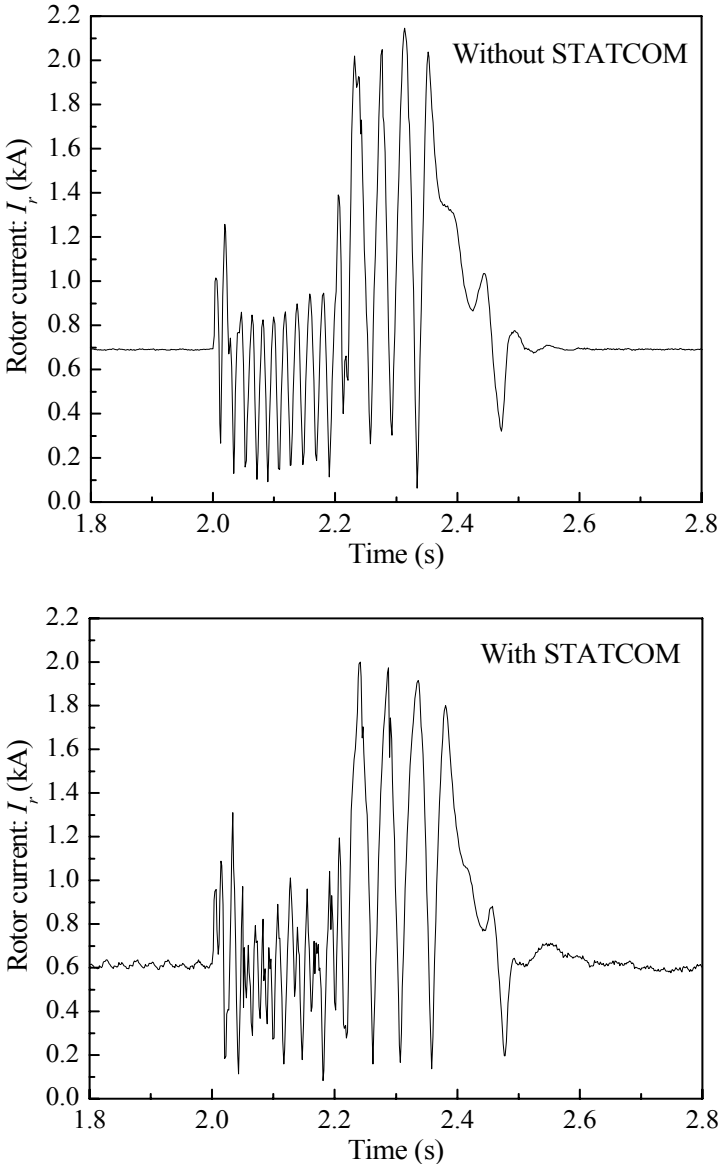

Figure 8.6: RMS rotor current I_r during a 200 ms three-phase short circuit at the infinite bus, RSC not blocking.

A temporary three-phase short circuit is applied for 200 ms to the infinite bus in Figure 8.1 at t = 2 s. The protective system of the wind turbine and the DFIG is disabled in this test. Figure 8.6 shows the rotor current, I_r, response with and without the STATCOM. In the case of no STATCOM, the reactive power command of the RSC is set to 0.28 pu in order to regulate the PCC voltage at 1.02 pu. These results show that during the fault and post-fault transient state, the rotor current exceeds its limit value (1.0 kA) in both cases. Therefore, the RSC must be blocked to avoid being destroyed by the over-current in the rotor circuit.

8.4.3 A Three-Phase Short Circuit Test without the STATCOM: Rotor Side Converter Blocking

The same three-phase short circuit test as in Figure 8.6, is applied at t = 2 s without using the STATCOM; but now 30 ms after applying the fault (at t = 2.03 s), the RSC is blocked to protect it from over-current in the rotor circuit. Figure 8.7 shows the voltage profiles at the PCC. The curve GSC is the result with the reactive compensation by the GSC (the reactive power command of the GSC is set to the maximum value 0.25 pu instead of 0) from 2.03 s; and the curve NC indicates the result without any reactive compensation from 2.03 s. In both the cases of GSC and NC, the reactive power command of the RSC is set to 0.28 pu instead of 0 before applying the fault in order to regulate the PCC voltage at 1.02 pu. The fault is cleared at t = 2.2 s. However, the PCC voltage can not be reestablished (even after several seconds in Figure 8.7) without the STATCOM or only using the GSC; therefore, the RSC cannot restart and the WTG will have to be tripped from the system.

Figure 8.8 shows the total active power, P_e, generated by the induction generator and the total reactive power, Q_e, exchanged between the induction generator and the grid. During the RSC blocking, the active power generated by the induction generator reduces significantly for both the GSC and the NC. After the fault has cleared (at t = 2.2 s) but the RSC is still blocking, the induction generator absorbs some reactive power (negative

values in Figure 8.8) from the grid. However, when only the GSC provides reactive compensation, the induction generator produces more active power to the power grid, and the reactive power absorbed by the induction generator is reduced, compared to the case of no compensation.

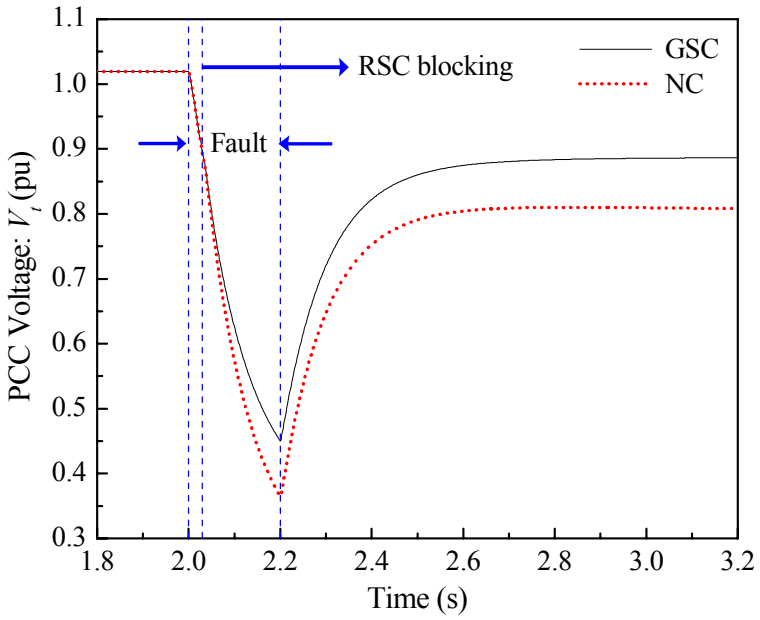

Figure 8.7: A 200 ms three-phase short circuit at the infinite bus, RSC blocking without STATCOM: PCC voltage V_t.

8.4.4 Uninterrupted Operation of the DFIG Wind Turbine with the STATCOM

A grid fault in the power network can be temporary or permanent. A permanent grid fault is normally cleared by disconnecting the power line on which the fault occurs, from the system. Line tripping reduces the operational and stability margins of the power system, and hence results in a relatively weaker power network. Therefore, a permanent grid fault with line tripping is more severe than a temporary fault without any line tripping for power system operation and stability.

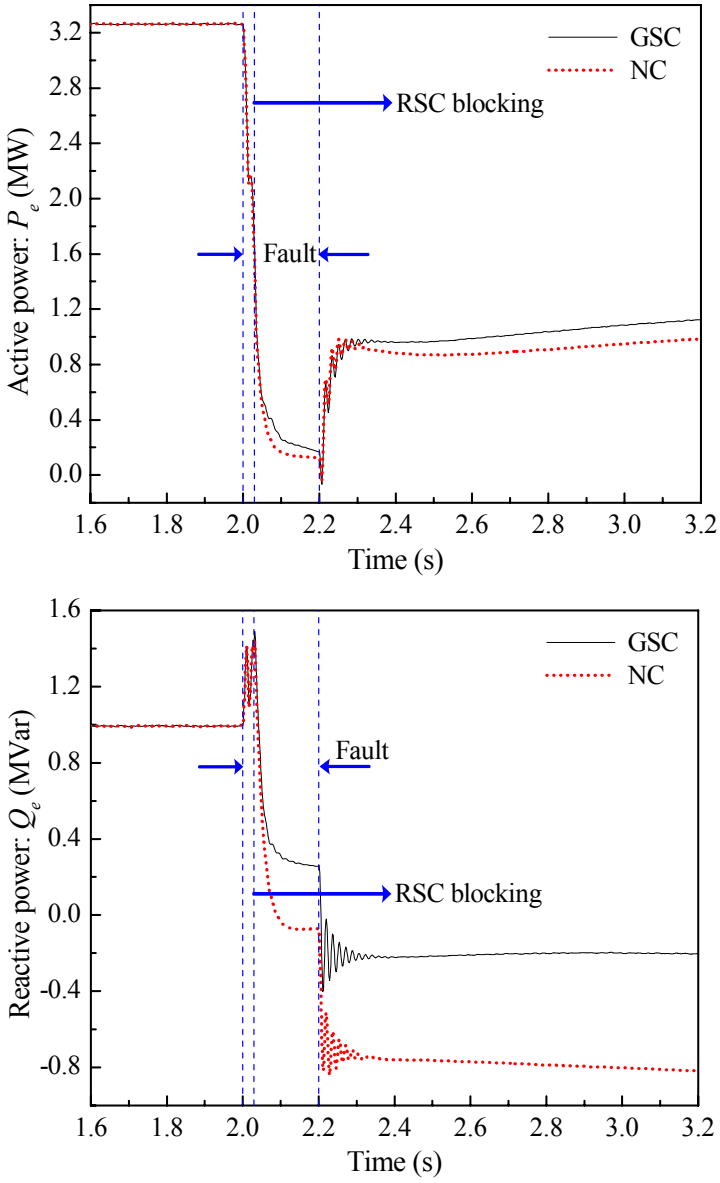

Figure 8.8: A 200 ms three-phase short circuit at the infinite bus, RSC blocking without STATCOM: P_e and Q_e.

To demonstrate the effectiveness of the STATCOM to help the WTG ride through grid faults, a three-phase permanent short circuit is now applied to the receiving end of line 1 at t_1 = 2 s, and is cleared by tripping line 1. The STATCOM is now used to help achieve the uninterrupted operation of the WTG. During the entire test, the reactive power command of the GSC is set to $Q_g^* = 0$. Figure 8.9 shows the voltage profiles at the PCC. Before $t = t_1$, the power system is at normal operation. 30 ms after applying the

short circuit (at t_2 = 2.03 s), the RSC is blocked to protect it from over-current in the rotor circuit. 200 ms after applying the short circuit (at t_3 = 2.2 s), the fault is cleared and line 1 is disconnected from the system. In contrast to the cases of no STATCOM as shown in Figure 8.7, with the STATCOM for transient voltage support, the PCC voltage is quickly reestablished shortly after the fault has cleared. When the PCC voltage returns to a predefined value, the RSC starts switching. Finally, 500 ms after blocking the RSC (at t_4 = 2.53 s), the RSC restarts successfully and the uninterrupted operation of WTG is achieved.

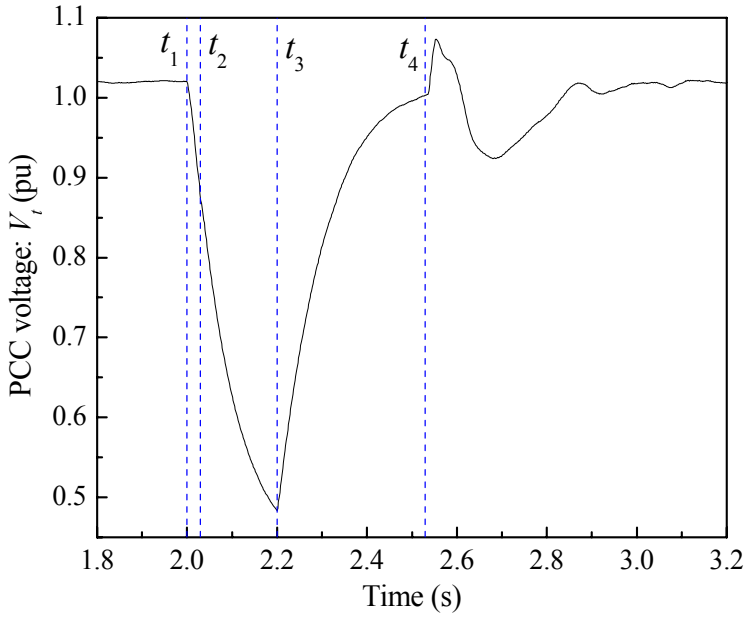

Figure 8.9: Uninterrupted operation of WTG with a STATCOM during a grid fault: V_t.

Figure 8.10 shows the magnitude of the rotor current, I_r. Compared to Figure 8.6, the rotor current transient is significantly reduced. During the RSC blocking, the rotor current magnitude is within its limit value (1.0 kA) by connecting a suitably selected external resistance to the rotor circuit. In addition, with a proper restarting procedure and a suitably designed control system, the RSC successfully restarts with only a small transient in the rotor current.

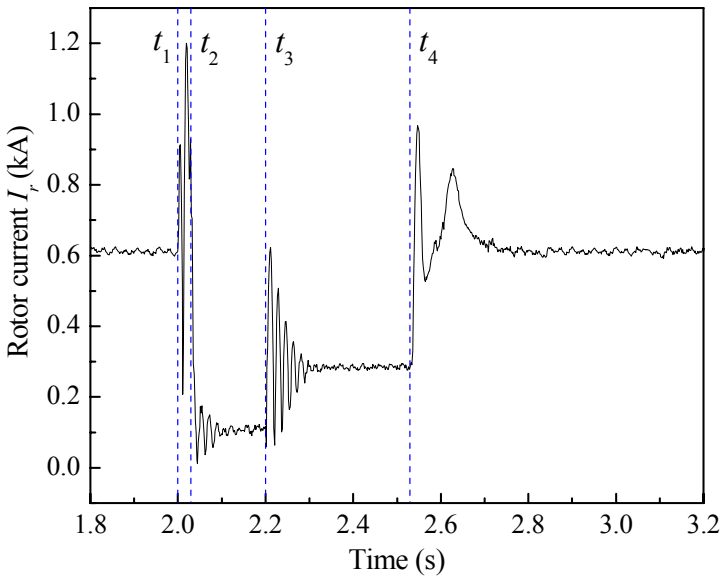

Figure 8.10: Uninterrupted operation of WTG with a STATCOM during a grid fault: I_r.

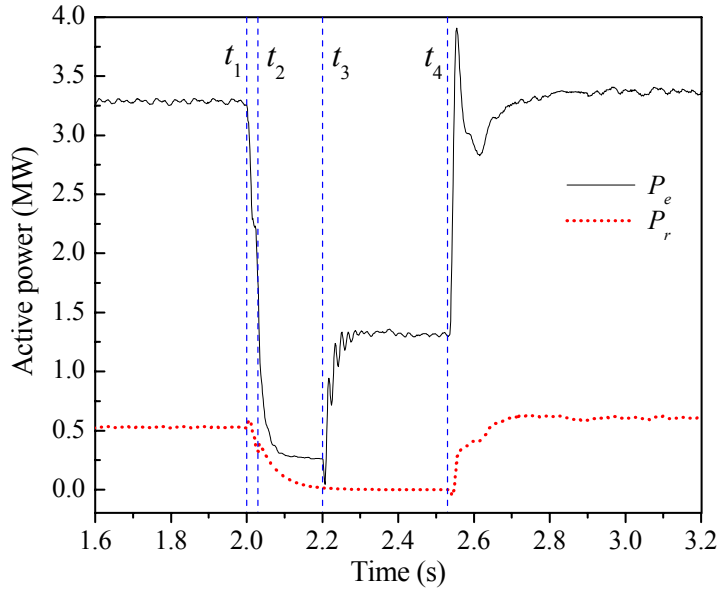

Figure 8.11: Uninterrupted operation of WTG with a STATCOM during a grid fault: P_e and P_r.

Figure 8.11 shows the total active power generated by the induction generator, P_e, and rotor active power, P_r. During the RSC blocking from t_2 to t_4, the total active power generated by the induction generator is reduced and no active power flowing through the rotor circuit ($P_r \approx 0$). However, compared to the results without the STATCOM in Figure

8.8, with the STATCOM now connected, the induction generator generates more active power to the power network when the fault has cleared (between time t_3 and t_4).

Figure 8.12 shows the total reactive power, Q_e, exchanged between the induction generator and the grid, and the rotor reactive power, Q_r. During the time period t_3 - t_4 (the fault has cleared but the RSC is still blocking), the induction generator absorbs a large amount of reactive power from the power grid, and therefore, the use of dynamic reactive power compensation is required.

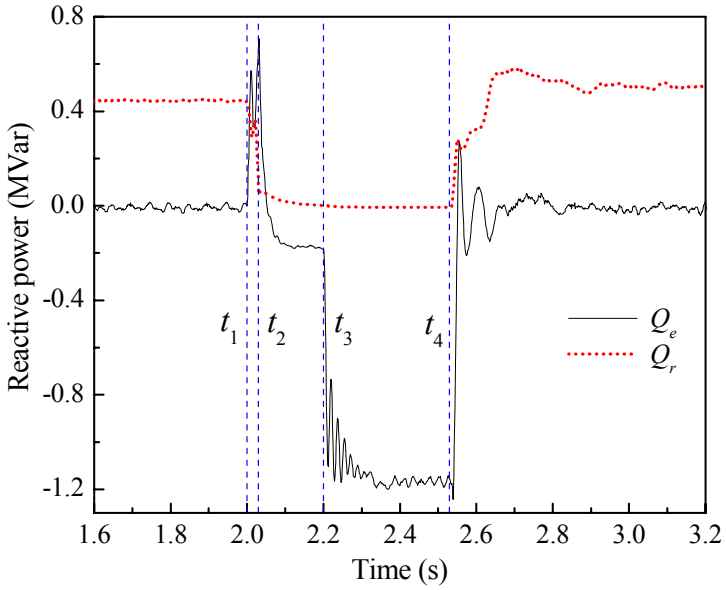

Figure 8.12: Uninterrupted operation of the wind turbine with a STATCOM during a grid fault: Q_e and Q_r.

During the time period t_3 - t_4 in Figure 8.13, the RSC is blocked, and the STATCOM is providing 2.3 MVar reactive power (Q_c). This could not have been provided by the GSC which has a rating of 0.9 MVA, and underlines the need for a STATCOM or some other form of reactive compensation.

Another requirement for the successful uninterrupted operation of the WTG is the dc-link voltage stability of the VFC. As shown in Figure 8.14, after the grid fault, the GSC controller successfully controls the dc-link voltage back to the nominal value of 4.0 kV.

The overshoot of the dc-link voltage after t_4 when the RCS restarts, is less than 10% of the nominal value, which is a necessary condition for the RSC to restart.

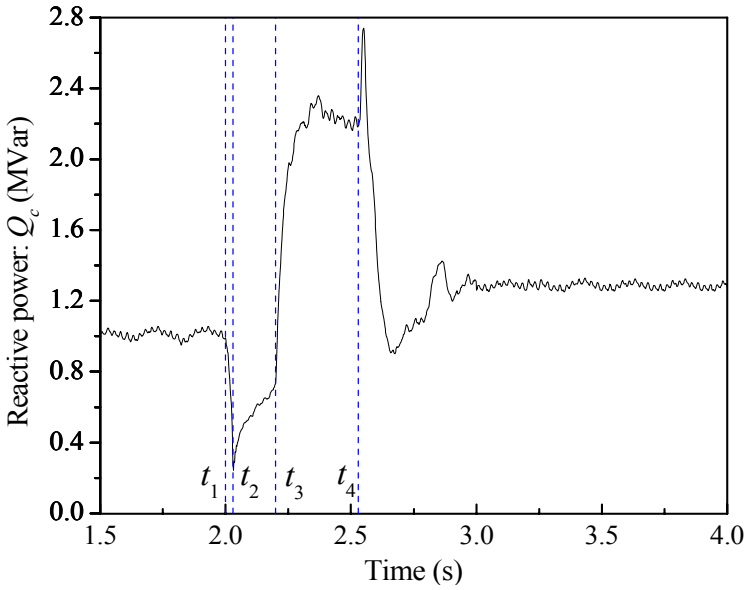

Figure 8.13: Uninterrupted operation of WTG with a STATCOM during a grid fault: Q_c.

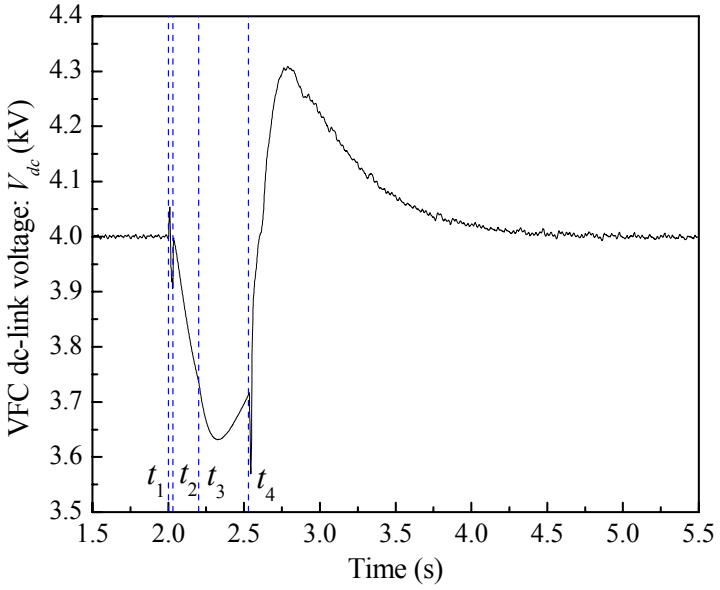

Figure 8.14: Uninterrupted operation of WTG with a STATCOM during a grid fault: V_{dc}.

The results in Figure 8.9-Figure 8.14 demonstrate that during the grid fault and with the assistance of the STATCOM, the DFIG wind turbine remains in service to supply active and reactive power to the grid. This satisfies the grid code requirements as shown in Figure 1.4.

8.5 Chapter Summary

The successful integration of wind farms to power systems may need dynamic reactive compensation to assist with voltage support, particularly during grid disturbances. This chapter has investigated the application of a static synchronous compensator (STATCOM) to achieve the uninterrupted operation of a wind turbine driving a doubly fed induction generator (DFIG) during grid faults. The STATCOM has been placed at the bus (PCC) where the DFIG is connected to the power grid, for steady-state voltage regulation and transient voltage support. The control schemes of the rotor side converter (RSC) and the grid side converter (GSC) of the DFIG and the STATCOM have been suitably designed and coordinated.

The system has been implemented on a RTDS and subjected to short-circuit grid faults. During grid faults, the RSC was blocked and restarted when the fault was cleared and the PCC voltage was reestablished. Real-time implementation results have shown that with the STATCOM providing dynamic voltage support, the PCC voltage could be reestablished shortly after grid faults and therefore the wind turbine generator (WTG) remained in service. However, without the STATCOM for voltage support, the PCC voltage could not be reestablished after grid faults so that the WTG had to be tripped from the power network. The STATCOM improved the transient voltage stability and therefore enhanced the grid fault ride-through capability of the WTG system.

Both DFIG and STATCOM can be used to control the reactive power and voltage. However, the reactive power controls of the DFIG and the STATCOM in this chapter are independent without coordination. In order to achieve certain optimal

operating performance and economical benefits, it is necessary to coordinate the control actions of the WTG and STATCOM. This issue will be investigated in the next chapter.

CHAPTER 9

COORDINATED REACTIVE POWER CONTROL OF A LARGE WIND FARM AND A STATCOM USING HEURISTIC DYNAMIC PROGRAMMING

A nonlinear adaptive interface neurocontroller (INC) is proposed for the coordinated reactive power control between a large wind farm and a static synchronous compensator (STATCOM) [140]. The wind farm consists of over one hundred individual wind turbines driving doubly fed induction generators (DFIGs). The heuristic dynamic programming (HDP) technique and radial basis function neural networks (RBFNNs) are used to design this INC. It effectively reduces the level of voltage sags as well as the over-currents in the DFIG rotor circuit during grid faults and therefore significantly enhances the fault ride-through capability of the wind farm. The INC also acts as a coordinated external damping controller for the wind farm and the STATCOM and therefore improves power oscillation damping of the system after grid faults. Simulation studies are carried out in PSCAD/EMTDC and the results are presented to demonstrate the effectiveness the proposed INC.

This work is a part of a joint National Science Foundation (NSF) project with the Real-Time Power and Intelligent Systems (RTPIS) Laboratory at the Missouri University of Science and Technology. The researchers there worked on the coordinating voltage control of a wind farm and a static var compensator (SVC), in which the wind farm is equipped with wind turbines driving synchronous generators [141].

9.1 Wind Farm, STATCOM, and Power System Model

The original 4-machine 12-bus benchmark power system in [115] is used as a platform system for studying FACTS device applications and integration of wind energy

generation. Figure 9.1 shows the single-line diagram of the extended 4-machine 12-bus power system which now includes a large wind farm and a STATCOM. The system consists of six 230 kV busses, two 345 kV busses and four 22 kV busses. It covers three geographical areas. Area 1 is predominantly a generation area with most of its generation coming from hydro power (represented by G1 and G2). Area 2, located between the main generation area (Area 1) and the main load center (Area 3), has a large 400 MW wind farm (represented by G4) but this is insufficient to meet local demand. Area 3, situated about 500 km from Area 1, is a load center with some thermal generation (represented by G3). Furthermore, since the generation unit in Area 2 has limited energy available, the system demand must often be satisfied through transmission. The transmission system consists of 230 kV transmission lines except for one 345 kV link between Areas 1 and 3 (between busses 7 and 8). Areas 2 and 3 contain switched shunt capacitors to support the voltage. A detailed description of the system is provided in Appendix B.3.

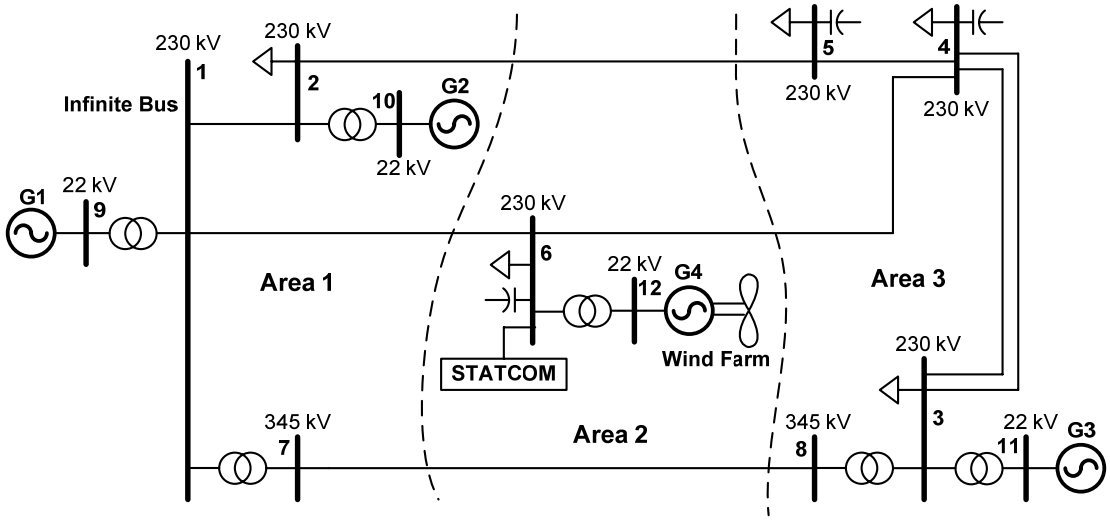

Figure 9.1: Single-line diagram of the 4-machine 12-bus power system which includes a large wind farm and a STATCOM.

The wind farm G4 is represented by an aggregated model in which over one hundred individual DFIG wind turbines are modeled as one equivalent DFIG driven by a single equivalent wind turbine. Each individual DFIG wind turbine represents a 3.6 MW wind turbine generator (WTG) system (Appendix E.1). The parameters of the equivalent DFIG wind turbine are given in Appendix E.3. The configuration and control of the DFIG wind turbine are shown in Figure 1.3 and Figure 6.7-Figure 6.10. A detailed description of the WTG model and control systems is provided in Section 2.2 and Section 6.2. In this design, the grid side converter (GSC) of the DFIG is arranged to regulate the reactive power exchanged between the GSC and the power network as shown in Figure 9.2. The parameters of the RSC and GSC controllers are provides in Tables G.3 and G.4 of Appendix G, respectively.

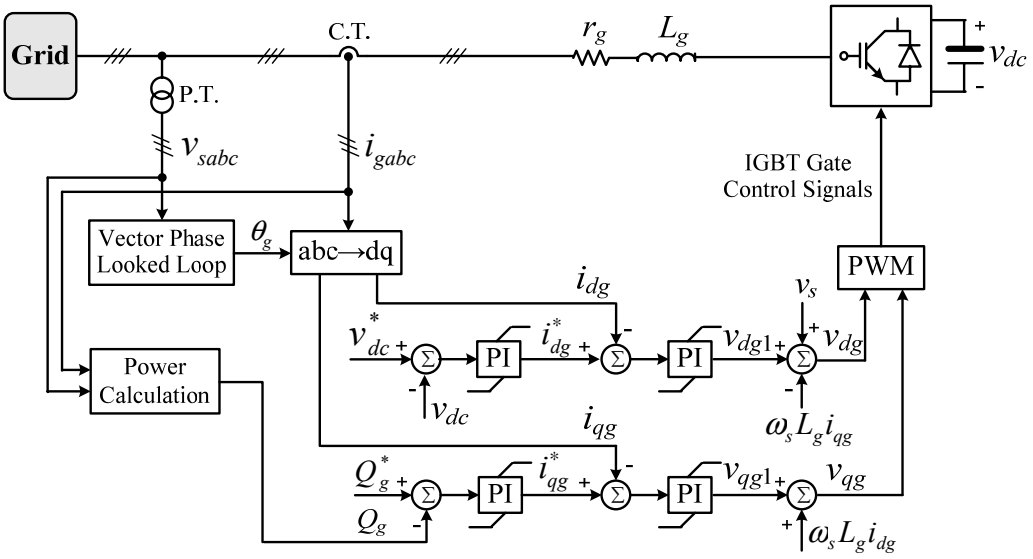

Figure 9.2: Overall vector control scheme of the GSC.

A STATCOM is placed at bus 6 to provide fast and smooth steady-state as well as transient voltage support for the wind farm. The overall control scheme of the STATCOM is shown in Figure 9.3 and the controller parameters are given in Table G.6 of Appendix G. The objective of the STATCOM is to provide the desired amount of

reactive compensation (with SW in position 1 in Figure 9.3) or to directly regulate the voltage at the point of common coupling (PCC) (bus 6) within the desired range (with SW in position 2 in Figure 9.3). This can enhance the capability of the wind farm to ride through grid disturbances in the grid. The block "Grid" in Figure 9.3 denotes the power network (Figure 9.1) to which the wind farm and the STATCOM are connected.

G1 is modeled as a three-phase infinite source, while the other two conventional generators (G2 and G3) are modeled in detail, with the exciter and turbine governor dynamics taken into account (see Appendix B.3).

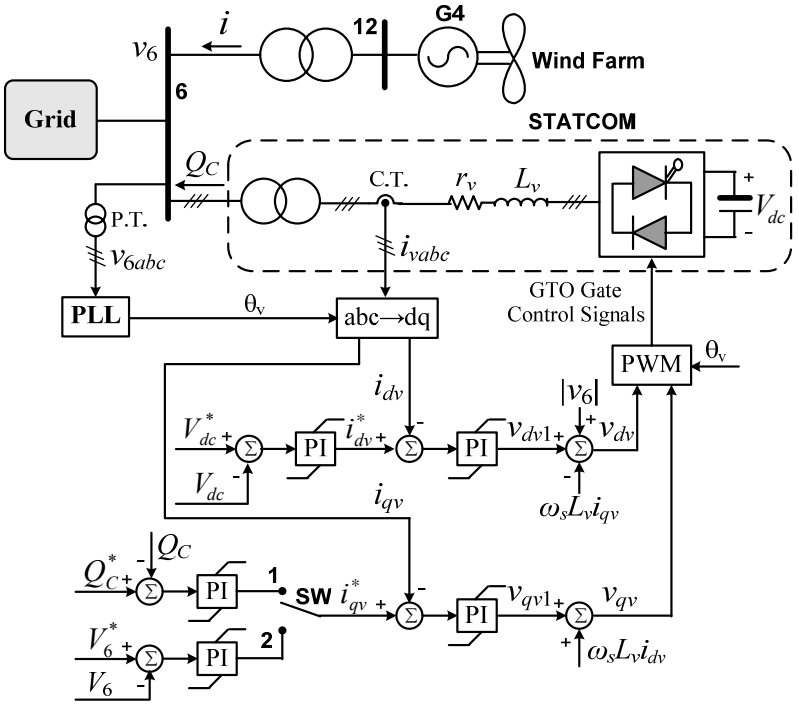

Figure 9.3: Overall control scheme of the STATCOM.

9.2 Design of the Interface Neurocontroller

Grid faults, even far away from the location of the wind farm, can cause voltage sags at the connection point of the wind farm. This voltage sag will result in an imbalance between the turbine input power and the generator output power and therefore a high

current in the stator windings of the DFIG. Because of the magnetic coupling between stator and rotor, this current will also flow in the rotor circuit and the converter. In addition, the power imbalance during the fault will excite low-frequency torsional oscillations on the WTG shaft system, which leads to oscillations of the shaft speed and the output active power. These oscillations are lightly damped if there is no specifically designed damping control for the WTG system.

In this section, an adaptive critic design (ACD) approach, the HDP, and RBFNNs are used to design an external interface controller (INC) for the coordinated reactive power control between the wind farm and the STATCOM, as shown in Figure 9.4. The dashed line block denotes the plant to be controlled by the INC. The voltage deviation, ΔV_6, at bus 6 and the active power deviation, ΔP_{g4}, of the wind farm are fed into the INC to produce two supplementary control signals, ΔQ_s and ΔQ_C. They are then added to the steady-state fixed set-point values, Q_{s0} and Q_{C0}, respectively, to form the total commanded values of the compensating reactive power, Q_s^* and Q_C^*, at the input of the DFIG rotor side converter (RSC) and the STATCOM controllers. A basic principle is that by rapidly varying the amount of reactive power provided by the DFIG and the STATCOM during grid faults, it is possible to reduce the level of voltage sags at the PCC and therefore control directly the transient imbalances between the electrical output power and the mechanical input power that are responsible for over-current in the rotor circuit. Because of the direct coupling between voltage magnitude and reactive power, it is straightforward to use the voltage deviation, ΔV_6, as an input signal of the INC. However, the active power deviation, ΔP_{g4}, of the wind farm is also used as an input of the INC because it provides the INC with additional information of the plant dynamics. In addition, ΔP_{g4} contains the information of system oscillations and can therefore be used by the INC to damp post-fault power oscillations of the system. The fixed set-point value Q_{s0} of the DFIG can be determined based on the desired stator-side or the net power factor of the induction machine. The choice of Q_{s0} is also subject to the limit of

the DFIG MVar rating. The value of Q_{C0} can be determined by the results of a power flow calculation at a specific operating point or to achieve some form of optimal power flow operation of the network.

The transfer functions from ΔV_6 and ΔP_{g4} to ΔQ_s and ΔQ_C are complex, nonlinear and depend on the network topology. A neural network can solve this problem and avoids having to derive such analytical functions.

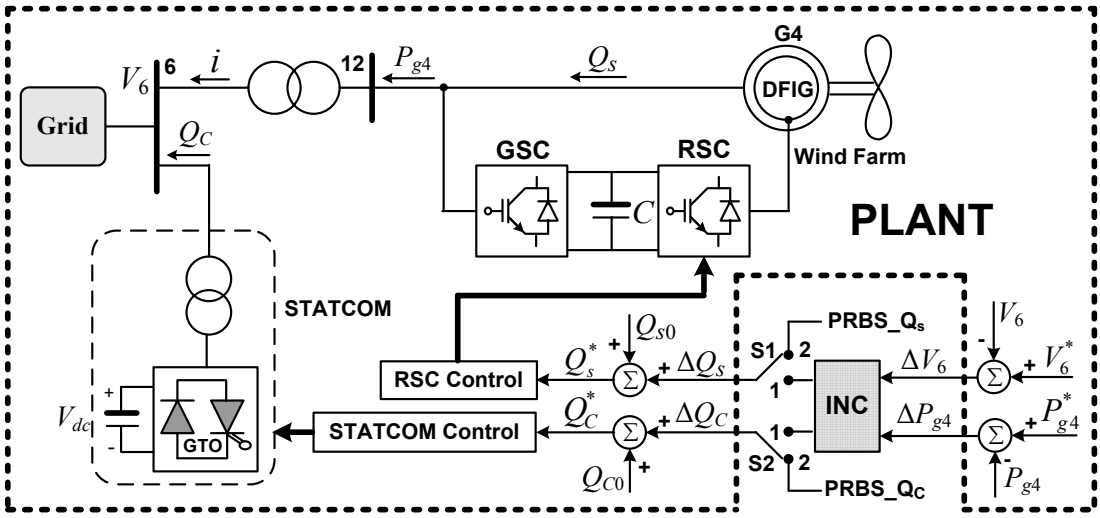

Figure 9.4: Schematic diagram of the wind farm and STATCOM coordinated by an interface neurocontroller (INC).

9.2.1 Heuristic Dynamic Programming (HDP)

The HDP method, belonging to the family of the ACDs, requires three neural networks, one for the *model*, one for the *critic*, and one for the *action network* for its implementation [29], [30]. The model network is used to provide a dynamical model of the plant for training the critic and action networks; the critic network estimates the cost function J in (1.1); the action network provides the optimal control for the plant. Based on an accurate model network, the HDP method determines optimal control laws for a system by successively adapting the critic and action networks. The adaptation process

starts with a nonoptimal control by the action network; the critic network then guides the action network towards the optimal solution at each successive adaptation.

9.2.2 Design of the Model Network

The model network is a three-layer RBFNN (Figure 3.2) with 25 hidden-layer neurons. The plant inputs $A = [\Delta Q_s, \Delta Q_C]$ and outputs $Y = [\Delta V_6, \Delta P_{g4}]$ at time k, k–1, and k–2 are fed into the model network to estimate the plant outputs $\hat{Y} = [\Delta \hat{V}_6, \Delta \hat{P}_{g4}]$ at time k+1, as shown in Figure 9.5. The sampling period for RBFNN implementation is 1 ms.

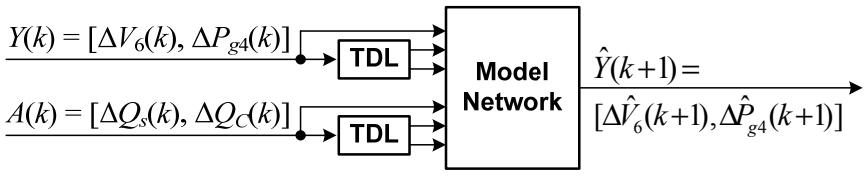

Figure 9.5: Structure of the model network.

The model network is pretrained offline using a suitably selected training data set collected from two sets of training, forced training and natural training. During the forced training, the plant is perturbed by injected small pseudorandom binary signals (PRBS) (with S1 and S2 both in position 2 in Figure 9.4), given by

$$PRBS\_Q_s(k) = 0.1 \cdot |Q_{s0}| \cdot [r0(k) + r1(k) + r2(k)]/3 \tag{9.1}$$

$$PRBS\_Q_C(k) = 0.1 \cdot |Q_{C0}| \cdot [r0(k) + r1(k) + r2(k)]/3 \tag{9.2}$$

where r0, r1 and r2 are uniformly distributed random numbers in [-1, 1] with frequencies of 0.5 Hz, 1 Hz and 2 Hz, respectively. During the natural training, the PRBS is removed (with S1 and S2 both in position 1 in Figure 9.4) and the system is exposed to natural disturbances and faults in the power network. The forced training and natural training are carried out at several different operating points to form the training data set, given by

$$\underline{\mathrm{A}} = \{\underline{\mathrm{X}}, \underline{\mathrm{Y}}\} = \left\{ \bigcup_{i=1}^{m} \underline{\mathrm{A}}_{\mathrm{F}i}, \bigcup_{i=1}^{m} \bigcup_{j=1}^{n} \underline{\mathrm{A}}_{\mathrm{N}ij} \right\} \tag{9.3}$$

where $\underline{\mathrm{A}}$ is the entire training data set selected from m operating points; $\underline{\mathrm{X}}$ and $\underline{\mathrm{Y}}$ are the input and output data sets of the model network, respectively; $\underline{\mathrm{A}}_{\mathrm{F}i}$ is the subset collected from the forced training at the operating point i; $\underline{\mathrm{A}}_{\mathrm{N}ij}$ is the subset collected from the natural training caused by the j^{th} natural disturbance event at the operating point i. Table 9.1 shows the selected five operating points for the natural training of the model network, in which v_w, ω_4, P_{g4}, Q_g, Q_s, and Q_C are the wind speed, DFIG rotor speed, output active power of the wind farm, reactive power of the GSC, reactive power of the RSC, and the compensated reactive power from the STATCOM, respectively. In this design, three different natural disturbances are applied at each operating point in Table 9.1: 1) a 150 ms temporary three-phase short circuit at the bus 1 end of line 1-6, 2) a 150 ms temporary phase A to ground short circuit at the bus 4 end of one of the parallel lines 3-4, 3) wind speed variations around the mean values in Table 9.1 using the wind model in [142], which causes the variations of P_{g4} in the range of ±50 MW at each operating point.

The selected training data set ensures that the model network can track the system dynamics over a wide operating range. After determining the training data set, the weights of the model network are then calculated by singular value decomposition (SVD) method [28].

Table 9.1: Operating conditions selected for natural training of the model network

Operating Conditions	v_w (m/s)	ω_4 (pu)	P_{g4} (MW)	Q_g (MVar)	Q_s (MVar)	Q_C (MVar)
OP-I	11.6	1.2	350	0	0	150
OP-II	11.0	1.2	300	0	0	165
OP-III	11.4	1.15	250	0	38	150
OP-IV	10.6	1.1	200	0	70	150
OP-V	9.7	1.05	150	0	1120	150

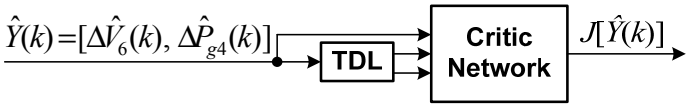

Figure 9.6: Structure of the critic network.

9.2.3 Design of the Critic Network

The critic network is a three-layer RBFNN with 15 hidden-layer neurons. The inputs to the critic network are the estimated plant outputs, $\hat{Y} = [\Delta\hat{V}_6, \Delta\hat{P}_{g4}]$, from the model network and its two time-delayed values. The output of the critic network is the estimate of the function J in (1.1) with respect to the estimated plant output $\hat{Y}$, as shown in Figure 9.6.

The critic network learns to minimize the following error measure over time [30]:

$$\|E_C\| = \tfrac{1}{2}\sum_k E_C^T(k)E_C(k) \tag{9.4}$$

where

$$E_C(k) = J[\hat{Y}(k)] - \gamma J[\hat{Y}(k+1)] - U(k) \tag{9.5}$$

The objective of the INC (Figure 9.4) is to provide an optimal coordinating control that minimizes the voltage deviations at bus 6, ΔV_6, as well as the active power oscillations, ΔP_{g4}, of the wind farm. Therefore, the utility function is defined as

$$\begin{aligned} U(k) = {} & \tfrac{1}{2}[\Delta V_6^2(k) + 0.5\Delta V_6^2(k-1) + 0.1\Delta V_6^2(k-2)] \\ & + \tfrac{1}{2}[\Delta P_{g4}^2(k) + 0.5\Delta P_{g4}^2(k-1) + 0.1\Delta P_{g4}^2(k-2)] \end{aligned} \tag{9.6}$$

In (9.6), it is natural to use time-delayed values of ΔV_6 and ΔP_{g4} because power systems are causal systems, in which an output depends on the present as well as past input values.

Generally, two critic networks are required in HDP to estimate the cost-to-go function J arising from the present state $\hat{Y}(k)$ and the future state $\hat{Y}(k+1)$, respectively. The critic's output $J(k+1)$ is necessary to generate the target signal $\gamma J(k+1)+U(t)$, for

training the critic network. In the case of minimization in the least mean square (LMS), the output weights of the critic network are updated by

$$\Delta W_C(k) = -\eta_C \{J[\hat{Y}(k)] - \gamma J[\hat{Y}(k+1)] - U(k)\} \frac{\partial J[\hat{Y}(k)]}{\partial W_C} \tag{9.7}$$

where $\eta_C = 0.05$ is a positive learning gain. The adaptation of the critic network in HDP is shown in Figure 9.7.

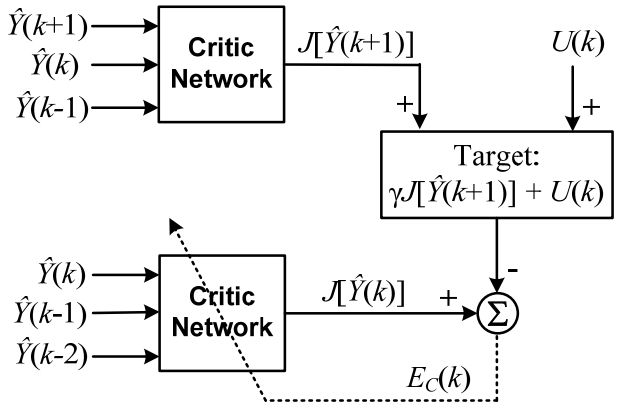

Figure 9.7: Adaptation of the critic network in HDP.

9.2.4 Design of the Action Network

The action network (Figure 9.8) is a three-layer RBFNN with 20 hidden-layer neurons. The inputs to the action network are the plant outputs $Y = [\Delta V_6, \Delta P_{g4}]$, at time k–1, k–2, and k–3. The outputs of the action network are the plant inputs, $A = [\Delta Q_s, \Delta Q_C]$, at time k.

The objective of the action network adaptation is to find out the optimal control trajectory, $\boldsymbol{A}_{opt}$, in order to minimize the cost-to-go function J over time:

$$A_{opt}(k) = \arg\min_A [J(k)] = \arg\min_A [U(k) + \gamma J(k+1)] \tag{9.8}$$

Such adaptation, as shown in Figure 9.9, is achieved by training the action network with the error signal, $E_A(k) = \partial J(k)/\partial A(k)$, which is obtained by propagating the constant,

$\partial J/\partial J=1$, back through the model to the action network [30]. The output weights of the action network are then updated by

$$\Delta W_A(k) = -\eta_A \frac{\partial J(k)}{\partial A(k)} \frac{\partial}{\partial W_A}\left[\frac{\partial J(k)}{\partial A(k)}\right] \tag{9.9}$$

where $\eta_A = 0.05$ is a positive learning gain.

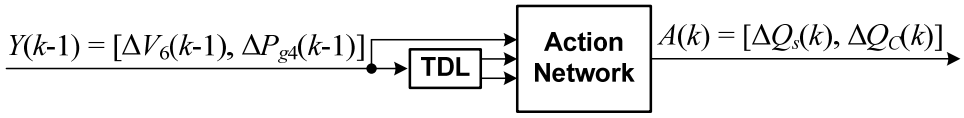

Figure 9.8: Structure of the action network.

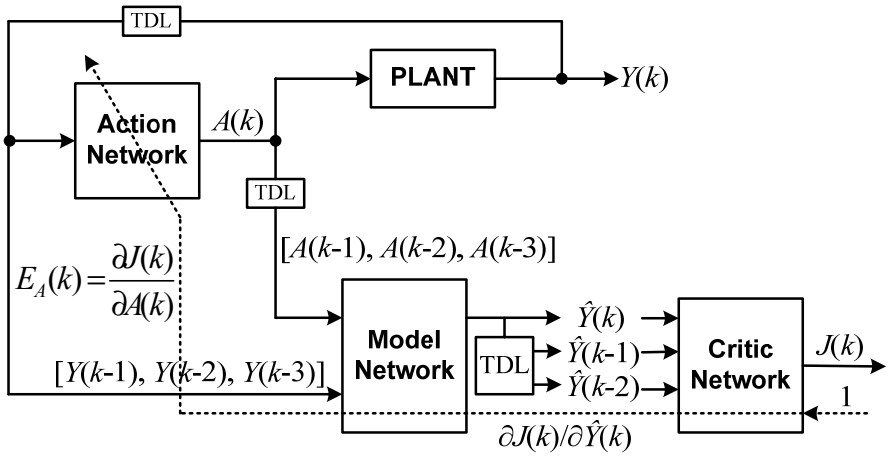

Figure 9.9: Adaptation of the action network in HDP.

9.2.5 Overall Training Procedure

The training procedure to implement the HDP algorithm consists of two training stages: one for the model network and the other for the critic/action networks. The model network is firstly pretrained offline to learn the plant dynamics before training the critic and action networks, as described in Section 9.2.2. During the training of the critic and action networks, the wind speed is varied over a certain range (e.g., ±2 m/s around the mean wind speed) using the wind model in [142] to simulate the real operation of the

wind farm. Consequently, the output active power of the wind farm varies significantly from time to time. During this time, the model network can be trained further to adapt to the operating conditions that are not covered by the pretraining.

The training stage of the critic/action networks contains two separate training cycles: one for the critic and the other for the action. The critic network is firstly pretrained by the procedure in Figure 9.7 to approximate the cost-to-go function J. During the critic's pretraining, the plant is perturbed by injecting small PRBS given by (9.1) and (9.2) to Q_{s0} and Q_{C0}, respectively (with S1 and S2 both in position 2 in Figure 9.4).

Once the critic's pretraining is over, S1 and S2 switch to position 1 and the INC is used to provide an external control for the STATCOM and the RSC of the DFIG. Then the critic's weights are fixed, the action network is trained by the procedure in Figure 9.9 for N_A cycles. Then the action's weights are fixed, and the critic network is trained further for N_C cycles. This process of training the critic/action networks is repeated one after the other until an accepted performance is achieved. Once the critic and action networks' weights have converged, the action network with the fixed weights is used to control the plant during the real-time operation.

9.3 Simulation Results

Simulation studies are carried out in this section to examine the responses of the system in Figure 9.4 when equipped with the proposed INC. The wind farm initially operates at an operating point with the wind speed v_w = 11.0 m/s, generator rotor speed ω_4 = 1.2 pu, output active power P_{g4} = 300 MW, and output reactive power Q_{g4} = 0. The reactive power command of the GSC is set at Q_g^* = 0. The steady-state fixed reactive power commands of the RSC and the STATCOM are set at Q_{s0} = 0 and Q_{C0} = 165 MVar, respectively. The voltage at bus 6 is regulated at V_6 = 1.02 pu. A three-phase short circuit is applied to the bus 1 end of line 1-6 at 1 s and is cleared after 150 ms. This scenario has been used in the pretraining of the model network, but has not been used for

training the critic and action networks. The dynamic performance of the wind farm, reinforced with the INC, is compared with the cases without the INC.

9.3.1 STATCOM in Reactive Power Control Mode in the Case of No Interface Neurocontroller

Figure 9.10-Figure 9.12 compare the system responses with and without the INC. In the case of no INC, the reactive power control is applied to the STATCOM (with SW in position 1 in Figure 9.3). In such a case, the reactive power commands of the RSC and the STATCOM are both constant. This control arrangement cannot contribute to improving the transient behavior of the wind farm or the damping of power oscillations in the system. On the contrary, the INC provides the RSC and the STATCOM with supplementary control capability in response to voltage sags and power oscillations during a transient disturbance. If the INC is well designed, it can contribute to improving the transient behavior of the wind farm and the damping of power oscillations. As shown in Figure 9.10, the INC significantly reduces the magnitudes of voltage sag and voltage overshot at bus 6 during the three-phase short circuit.

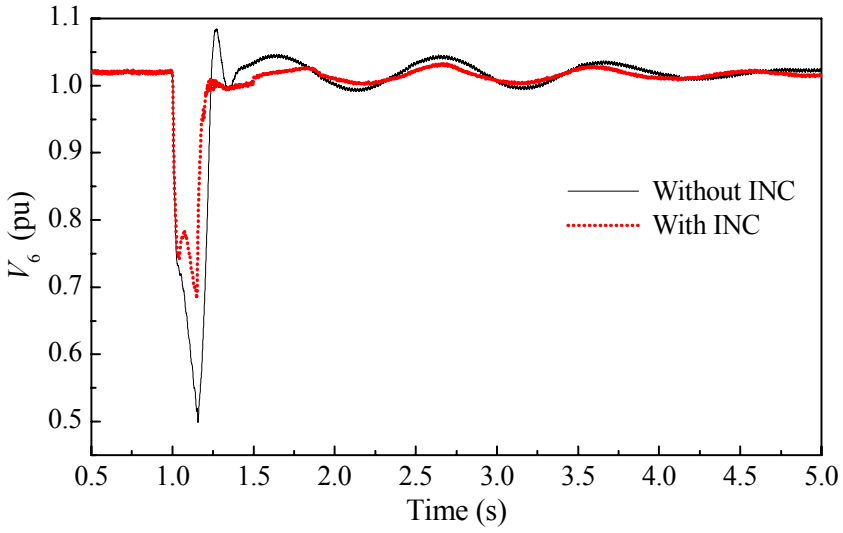

Figure 9.10: Comparison of the voltage magnitude at bus 6 with and without the INC (STATCOM in reactive power control mode in the case of no INC).

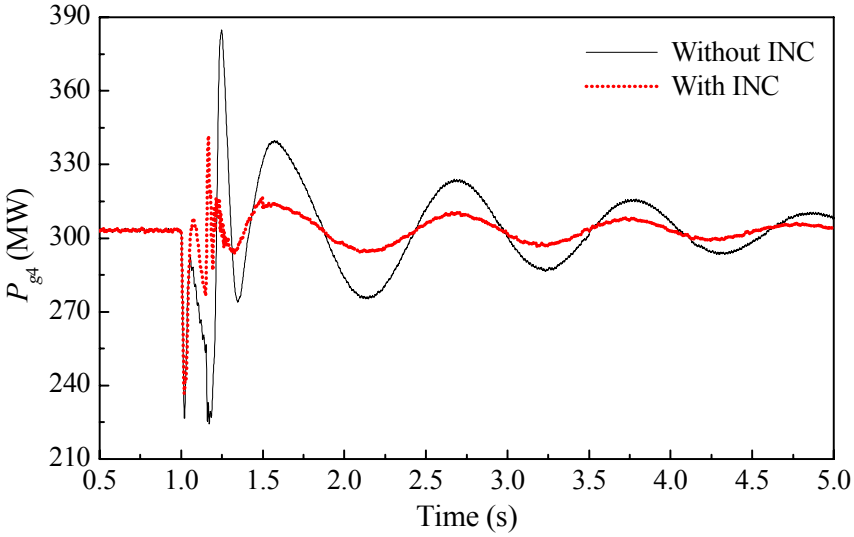

Figure 9.11: Comparison of the output active power of the wind farm with and without the INC (STATCOM in reactive power control mode in the case of no INC).

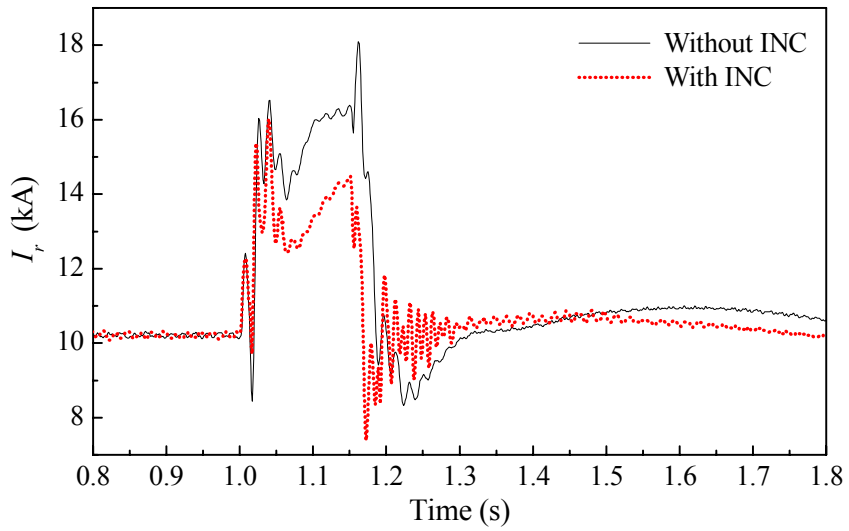

Figure 9.12: Comparison of the magnitude of rotor current with and without the INC (STATCOM in reactive power control mode in the case of no INC.

Figure 9.11 shows the output active power of the wind farm. By using the active power deviation signal, ΔP_{g4}, as an input to the INC, the power oscillation damping with the INC is much better than that without the INC.

Finally, the magnitudes of the DFIG rotor current, I_r, are shown in Figure 9.12. In this test, the reference values of the DFIG rotor currents, i_{dr}^* and i_{qr}^* in Figure 6.8, are

limited to 6.5 kA and 16 kA for both cases with and without the INC. The peak value of the transient rotor current (from 1.05 s onwards) without using the INC is about 18 kA, while this value reduces to 14 kA when using the INC. The INC significantly reduces the magnitude of the DFIG rotor current transient during the 150 ms short circuit, and therefore, it enhances the fault ride-through capability of the wind farm.

9.3.2 STATCOM in Voltage Control Model in the Case of No Interface Neurocontroller

Now the voltage control is applied to the STATCOM (with SW in position 2 in Figure 9.3). In this case, the reactive power command of the RSC is still constant, but the STATCOM controller can contribute to improving the transient behavior of the wind farm during voltage sags. As shown in Figure 9.13-Figure 9.15, the voltage sag at bus 6 (Figure 9.13) and the maximum rotor current (Figure 9.15) are almost the same for both cases with and without the INC; however, the voltage overshoot (Figure 9.13) and the magnitudes of active power oscillations (Figure 9.14) in the case of no INC are much larger than for an INC. These results are consistent with the design objectives, namely, the INC is optimally designed to minimize the voltage deviation at bus 6 as well as the magnitudes of active power oscillations in terms of the utility function U in (9.6).

Another important result is shown in Figure 9.16. It indicates that the amount of the compensated reactive power required by the STATCOM when using the INC, is less than half of that without the INC. Therefore, the size of the STATCOM can be significantly reduced when using the INC to provide the coordinated reactive power control for the wind farm and the STATCOM.

More reactive compensation from the STATCOM in the case of no INC (Figure 9.16) contributes to the rapid decay of the rotor current transient (Figure 9.15). On the other hand, in terms of the utility function (9.6), the INC actually optimally controls the reactive compensation from the RSC and the STATCOM to decay (or damp) the voltage (V_6) and active power (P_{g4}) transients as fast as possible. In this design, fast decay of the

rotor current (I_r) transient is not a control objective of the INC, but the rotor current is always controlled within its limit (e.g., 16 kA in this application) during the 150 ms grid fault, as shown in Figure 9.15. Moreover, the post-fault rotor currents (from 1.15 s) decay rapidly for both cases with and without the INC.

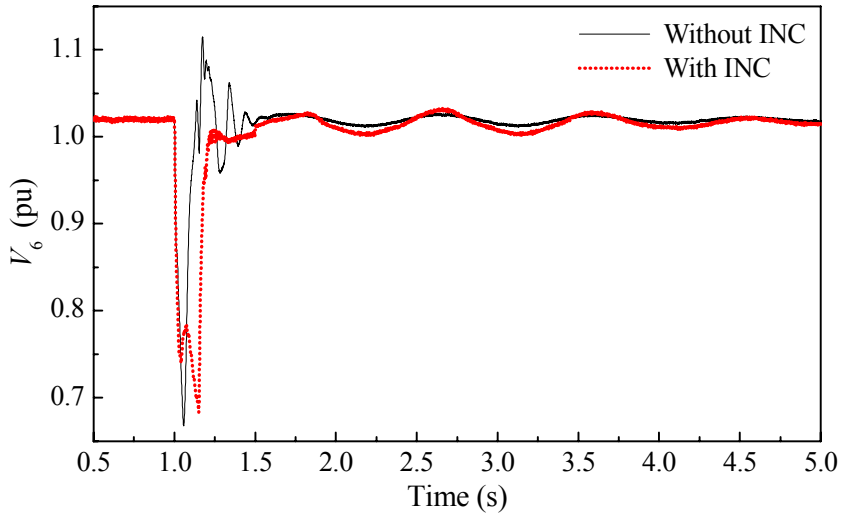

Figure 9.13: Comparison of the voltage magnitude at bus 6 with and without the INC (STATCOM in voltage control mode in the case of no INC).

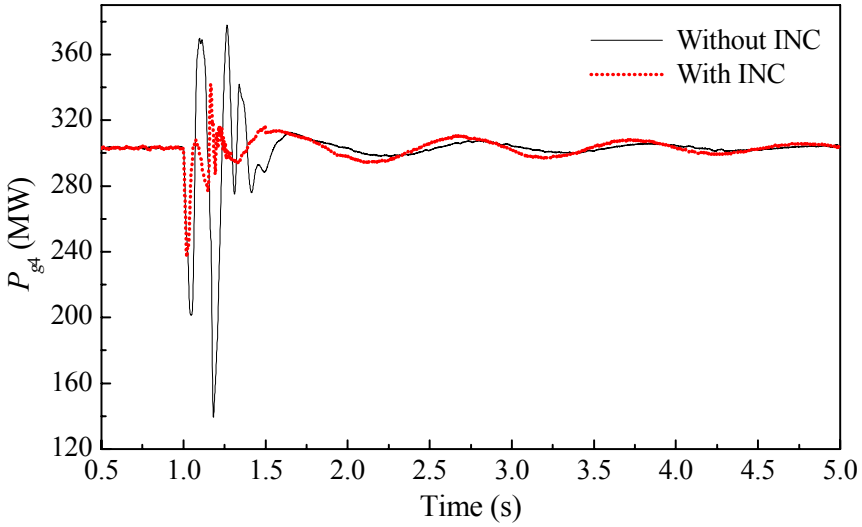

Figure 9.14: Comparison of the output active power of the wind farm with and without the INC (STATCOM in voltage control mode in the case of no INC).

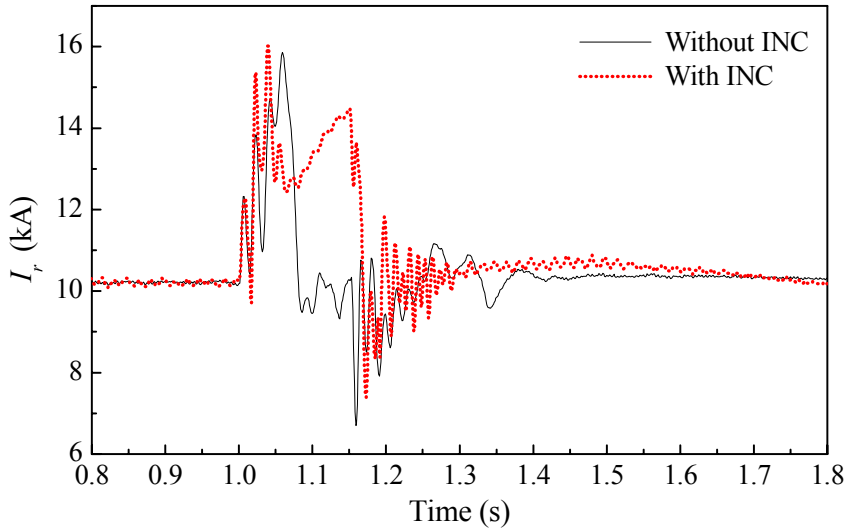

Figure 9.15: Comparison of the magnitude of rotor current with and without the INC (STATCOM in voltage control mode in the case of no INC).

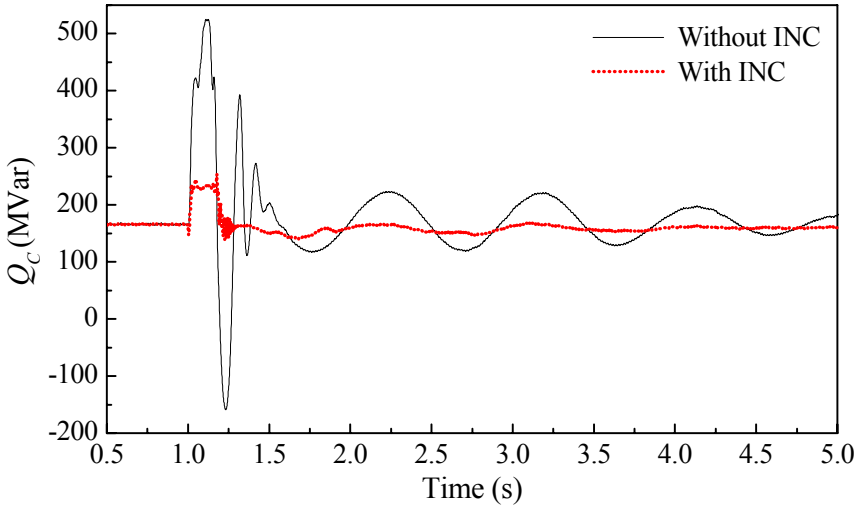

Figure 9.16: Comparison of the compensated reactive power by the STATCOM with and without the INC (STATCOM in voltage control mode in the case of no INC).

9.3.3 STATCOM in Voltage Control Mode with Reactive Power Limitation in the Case of No Interface Neurocontroller

In this test, the STATCOM is still operated in the voltage control mode (with SW in position 2 in Figure 9.3), but now the compensated reactive power Q_c of the STATCOM is limited to 250 MVar (by placing suitable limits to the current references

i_{dv}^* and i_{qv}^* in Figure 9.3). Figure 9.17 indicates that the maximum values of Q_c are limited to 250 MVar for both cases with and without the INC. However, the post-fault power oscillations of Q_c (Figure 9.17) and P_{g4} (Figure 9.18) in the case of the INC are damped more rapidly than for no INC. In addition, the peak value of the rotor current transient is reduced when using the INC, as shown in Figure 9.19. These results again confirm that the INC provides a smart coordinating control for the system. It improves the fault ride-through capability of the wind farm and power oscillation damping of the system during this transient disturbance.

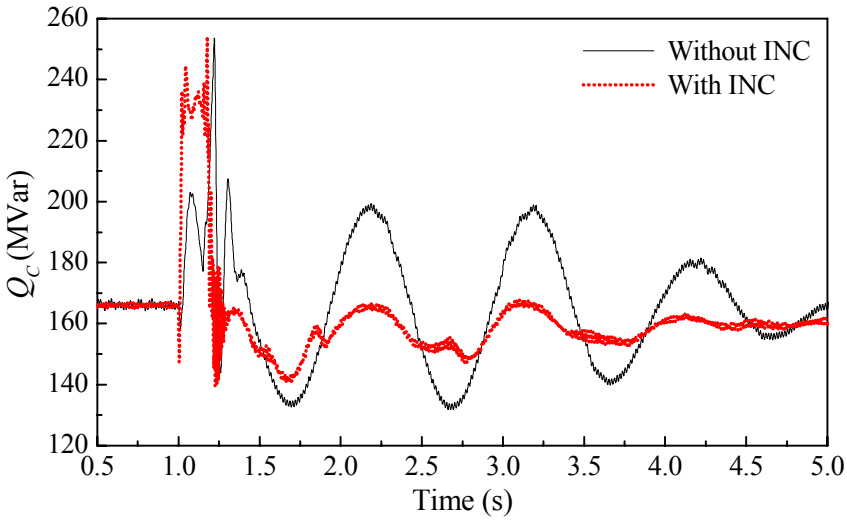

Figure 9.17: Comparison of the compensated reactive power by the STATCOM with and without the INC (STATCOM in voltage control mode with reactive power limitation in the case of no INC).

9.4 Chapter Summary

A large wind farm equipped with wind turbines driving doubly fed induction generators (DFIGs) has been integrated into a multimachine benchmark power system. A static synchronous compensator (STATCOM) has been placed at the bus where the wind farm is connected to the power network for steady-state and transient reactive power

compensation. The control schemes of the DFIG wind turbine and the STATCOM have been suitably designed.

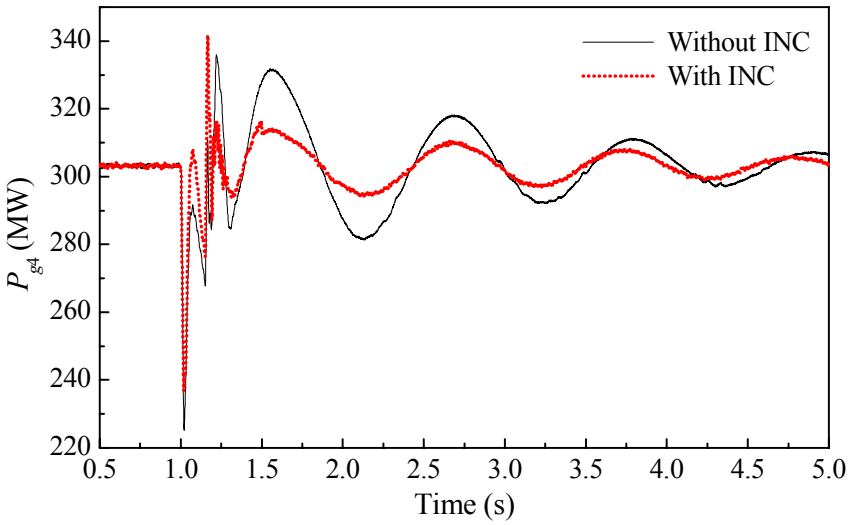

Figure 9.18: Comparison of the output active power of the wind farm with and without the INC (STATCOM in voltage control mode with reactive power limitation in the case of no INC).

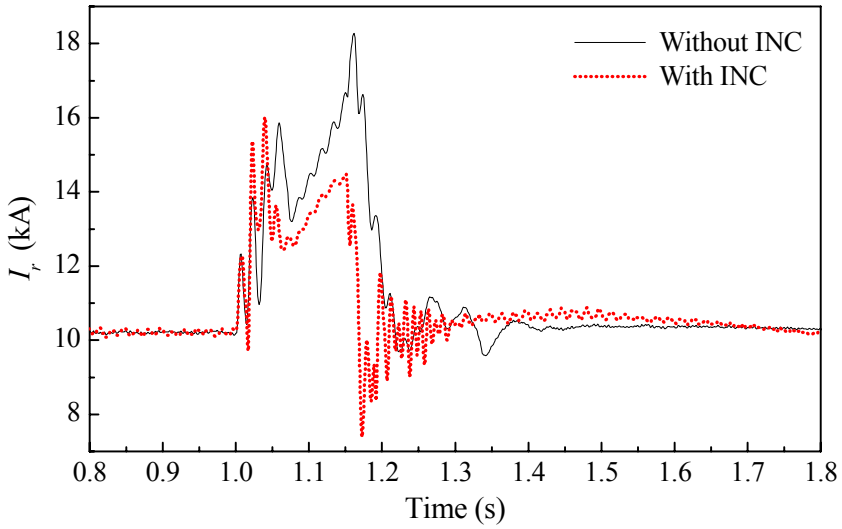

Figure 9.19: Comparison of the magnitude of rotor current with and without the INC (STATCOM in voltage control mode with reactive power limitation in the case of no INC).

A nonlinear optimal adaptive interface neurocontroller (INC), based on the heuristic dynamic programming (HDP) approach and radial basis function neural networks (RBFNNs), has been designed for the coordinated reactive power control between the wind farm and the STATCOM. Simulation studies have been carried out to examine the performance of the proposed INC during grid faults. Results have shown that the INC effectively reduces the level of voltage sags as well as the over-currents in the DFIG rotor circuit during grid faults and therefore significantly enhances the fault ride-through capability of the wind farm. Moreover, the INC acts as a coordinated external damping controller for the wind farm and the STATCOM and therefore improves the post-fault power oscillation damping of the power system.

The control strategies developed so far in this thesis are local noncoordinated or coordinated controllers. Each of them is designed to optimize certain local operating performance of the power system, but has no information of the overall system performance. However, power systems are large-scale, nonlinear, nonstationary, multivariable, complex systems distributed over large geographic areas. System-wide disturbances are a challenging problem. When severe disturbances or contingencies occur, these local controllers may not be able to guarantee stability [21]. To solve such problems, wide-area coordinating damping control is becoming an important issue. The following chapter will investigate this issue for a power system with wind power generation and FACTS devices.

CHAPTER 10

DHP-BASED NONLINEAR OPTIMAL WIDE-AREA COORDINATING CONTROL OF A POWER SYSTEM WITH A LARGE WIND FARM AND MULTIPLE FACTS DEVICES

To improve system-wide dynamic performance and stability of power systems, various wide-area coordinating control (WACC) strategies have been proposed by other researchers. However, all of these WACC strategies have some obvious limits, as discussed in Chapter 2. Some of them are developed based on linear optimization and control techniques and therefore are not sufficient to handle the nonlinearity and complexity of the practical power system; some of them are developed based on conventional nonlinear optimization and control techniques which might be too complicated to implement and may not be sufficient to handle the uncertainty of the practical power system.

To solve these problems, this chapter proposes a novel nonlinear optimal wide-area coordinating neurocontrol (WACNC) [143], [144], based on wide-area measurements, for a power system with power system stabilizers, a large wind farm, and multiple FACTS devices. An optimal wide-area monitor (OWAM), which is a radial basis function neural network (RBFNN), is designed to identify the input-output dynamics of the nonlinear power system. Its parameters are optimized through particle swarm optimization (PSO). Based on the OWAM, the WACNC is then designed by using an adaptive critic design (ACD) method and RBFNNs, while considering the effect of signal transmission delays. The WACNC operates at a global level to coordinate the actions of local power system controllers. Each local controller communicates with the WACNC, receives remote control signals from the WACNC to enhance its dynamic performance,

and therefore helps improve system-wide dynamic and transient performance. The proposed control is verified by simulation studies on a multimachine power system in PSCAD/EMTDC.

In ACDs (see Section 1.5 in Chapter 1), the use of derivatives of an optimization criterion, instead of the optimization criterion itself, is the most important information to have in order to find an optimal solution [30]. In heuristic dynamic programming (HDP) used in Chapter 9, the critic network is trained to approximate the cost-to-go function J (i.e., the optimization criterion) rather than its derivatives directly; the derivatives of J are obtained indirectly by backpropagation through the critic network. Therefore, there is a potential problem of being too coarse in HDP. On the other hand, the HDP is the simplest form of ACDs and therefore, easiest to implement, compared to the other ACD methods.

In this chapter, an advanced ACD method, called dual heuristic programming (DHP), is used to design the WACNC. DHP has an important advantage over HDP because its critic network is trained to approximate directly the derivatives of J. For instance, in the area of model-based control, as in the case of this chapter, an accurate model network and well-defined utility function exist. To adapt the action network, only the derivatives of J are required, rather than the cost-to-go function J itself. However, an approximation of these derivatives is already a direct output of the DHP critic network. It has been shown in [30] that the quality of such a direct approximation is always better than that of any indirect approximation for given sizes of the neural network and the training data.

10.1 Power System Model

The 4-machine 12-bus power system in [115] was proposed as a platform for studying FACTS device applications and integration of wind power, and was extended in [137] to include a large wind farm, a static synchronous compensator (STATCOM), and a

static synchronous series compensator (SSSC), as shown in Figure 10.1. The parameters of the original 4-machine 12-bus power system in [115] are presented in Appendix B.3.

In this study the STATCOM is placed at bus 4 in the load area (Area 3), for steady-state and transient voltage support, and not at the grid-connection point (bus 12) of the wind farm as in Chapter 9. This relieves the under-voltage problems in Area 3 [115]. In addition, an SSSC is placed at the bus 7 end of line 7-8 to regulate its power flow. This arrangement can relieve the possible transmission congestion on line 1-6 caused by some contingencies in Area 3 [137], [115]. Both synchronous generators G2 and G3 are equipped with power system stabilizers (PSSs) to improve damping of the local generator rotor oscillation modes. The synchronous generator (with PSS), wind farm, SSSC, and STATCOM controllers are each designed at the local level using standard linear control techniques and local signals, but are coordinated by the WACNC at a global level to achieve the system-wide performance goals.

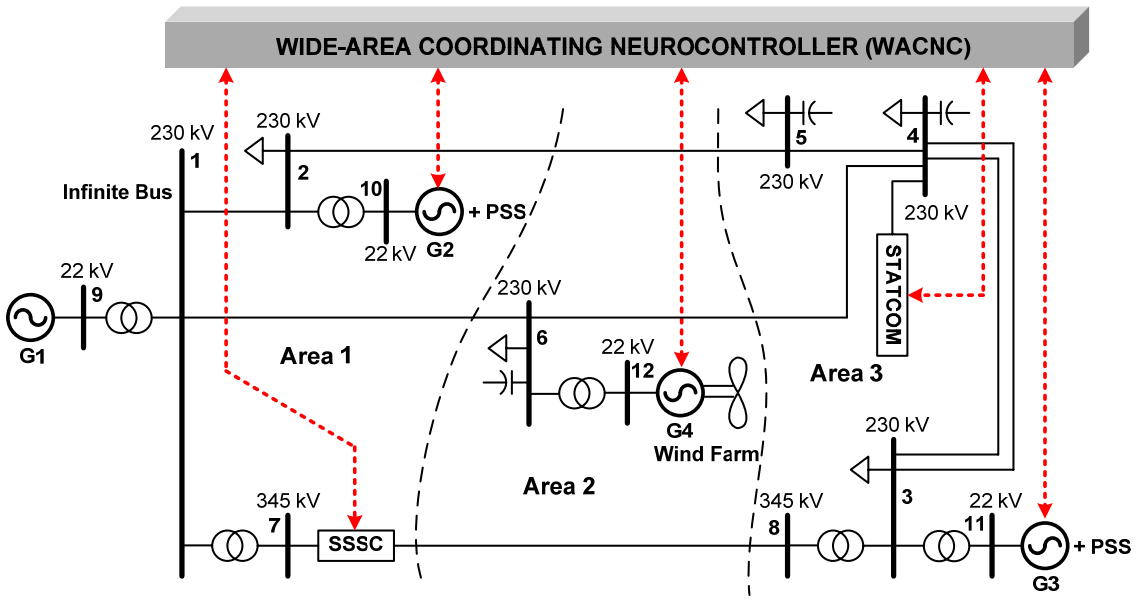

Figure 10.1: Single-line diagram of the 4-machine 12-bus power system with a large wind farm, a STATCOM, and an SSSC coordinated by a WACNC.

G1 is modeled as a three-phase infinite source, while the other two synchronous generators (G2 and G3) are modeled in detail, with the governor/turbine and automatic voltage regulator (AVR)/exciter (with PSS) dynamics taken into account (see Appendix B.3). The function of each PSS is to improve the damping of its generator rotor oscillations by controlling its generator's excitation using auxiliary stabilizing signal(s), e.g., the deviation of generator rotor speed [108]. The block diagram of the PSS is shown in Figure B.6 of Appendix B.

The wind farm consists of over one hundred individual wind turbines. Each wind turbine is equipped with a DFIG, as explained in Chapter 9. In this application, the wind farm is represented by an aggregated model, namely, one equivalent DFIG driven by a single equivalent wind turbine [144], as shown in Figure 1.3. The parameters of this equivalent DFIG wind turbine are presented in Appendix E.3 Control of the DFIG is achieved by control of the rotor side converter (RSC) and grid side converter (GSC), as shown in Figure 6.8 and Figure 9.2, respectively. The detailed control schemes of the RSC and the GSC are described in Section 6.2 and the controller parameters are provides in Tables G.3 and G.4 of Appendix G, respectively.

The STATCOM and the SSSC are each modeled as a GTO PWM converter with a dc-link capacitor. The schematic diagram of the STATCOM and its control scheme are shown in Figure 10.2. The parameters of the STATCOM controllers are given in Table G.6 of Appendix G. The objective of the STATCOM is to regulate the voltage at the point of common coupling (PCC) (bus 4 in Figure 10.1) rapidly over the desired range and keep the dc-link voltage constant. The voltage command V_4^* is the summation of two terms, the fixed set-point value V_{40} and the remote control signal ΔV_4 from the WACNC. The objective of using the supplementary control signal, ΔV_4, is to enhance the dynamic performance, such as the damping performance, of the local STATCOM controllers.

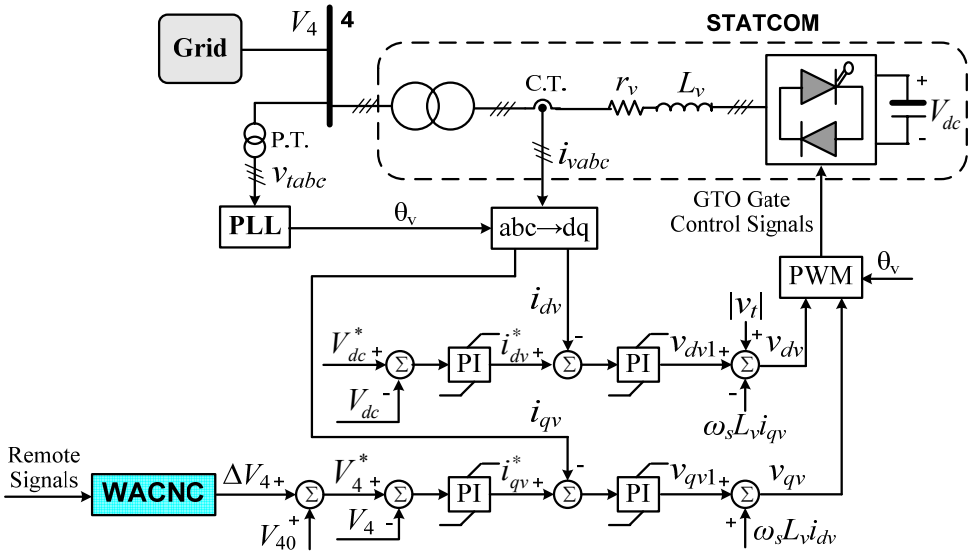

Figure 10.2: Schematic diagram of the STATCOM and its control scheme.

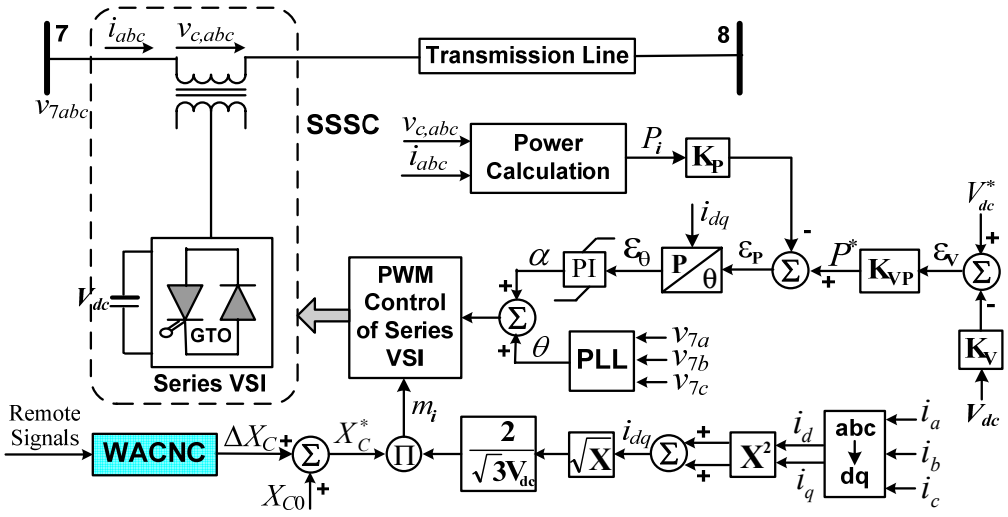

Figure 10.3: Schematic diagram of the SSSC and its control scheme.

The schematic diagram of the SSSC and its control scheme are shown in Figure 10.3. The main objective of the SSSC control is to inject a controllable capacitive or inductive reactance to line 7-8 that is independent of the line current, as well as keeping the dc-link voltage of the inverter constant at steady state. The total commanded value of the compensating reactance X_C^* at the input of the SSSC local control consists of two

terms, a fixed set-point value X_{C0} and a supplementary control signal ΔX_C from the WACNC. This external control signal provides a supplementary damping during transient power swings. The parameters of the SSSC local controller are provided in Table G.1 of Appendix G.

10.2 Design of the Wide-Area Coordinating Neurocontrol

Figure 10.4 shows the schematic diagram of the proposed WACNC which coordinates different local controllers of the synchronous generators, wind farm, STATCOM, and SSSC. The WACNC operates at the control center of the power system. It receives the GPS-synchronized remote signals from different devices over wide areas in the power system, including signals from G2 (speed deviation $\Delta\omega_2$), G3 (speed deviation $\Delta\omega_3$), wind farm G4 (output active power deviation ΔP_{g4} and voltage deviation ΔV_6 at bus 6), SSSC (active power deviation ΔP_{78} of line 7-8), and STATCOM (active power deviation ΔP_{54} of line 5-4 that is connected to the STATCOM bus 4). These remote signals contain the important dynamic/transient information of the local devices and the power network. ΔV_6 is used because of its direct coupling with the wind farm reactive power. In this design, it is simply assumed that the remote signals, $\Delta\omega_2$, $\Delta\omega_3$, ΔV_6, ΔP_{g4}, ΔP_{78}, ΔP_{54}, are transmitted to the control center from each local device with the same time delay of τ_1 ($\tau_1>0$). These delayed remote signals are fed into the WACNC to generate a set of global optimal control signals, ΔV_{T2}, ΔV_{T3}, ΔQ_s, ΔQ_g, ΔV_4, ΔX_C. They are then used as the auxiliary input signals to coordinate the actions of local controllers. Again, it is assumed that these remote control signals are transmitted from the control center to each local controller with a time delay of τ_2 ($\tau_2>0$). Therefore, the total time delay of the global control signals from the WACNC being available to each local controller is $\tau=\tau_1+\tau_2$ (assuming $\tau_1=\tau_2$ in this work). When a disturbance occurs, the coordination by the WACNC ensures that the power system returns back to the desired operating point as fast as possible after the disturbance.

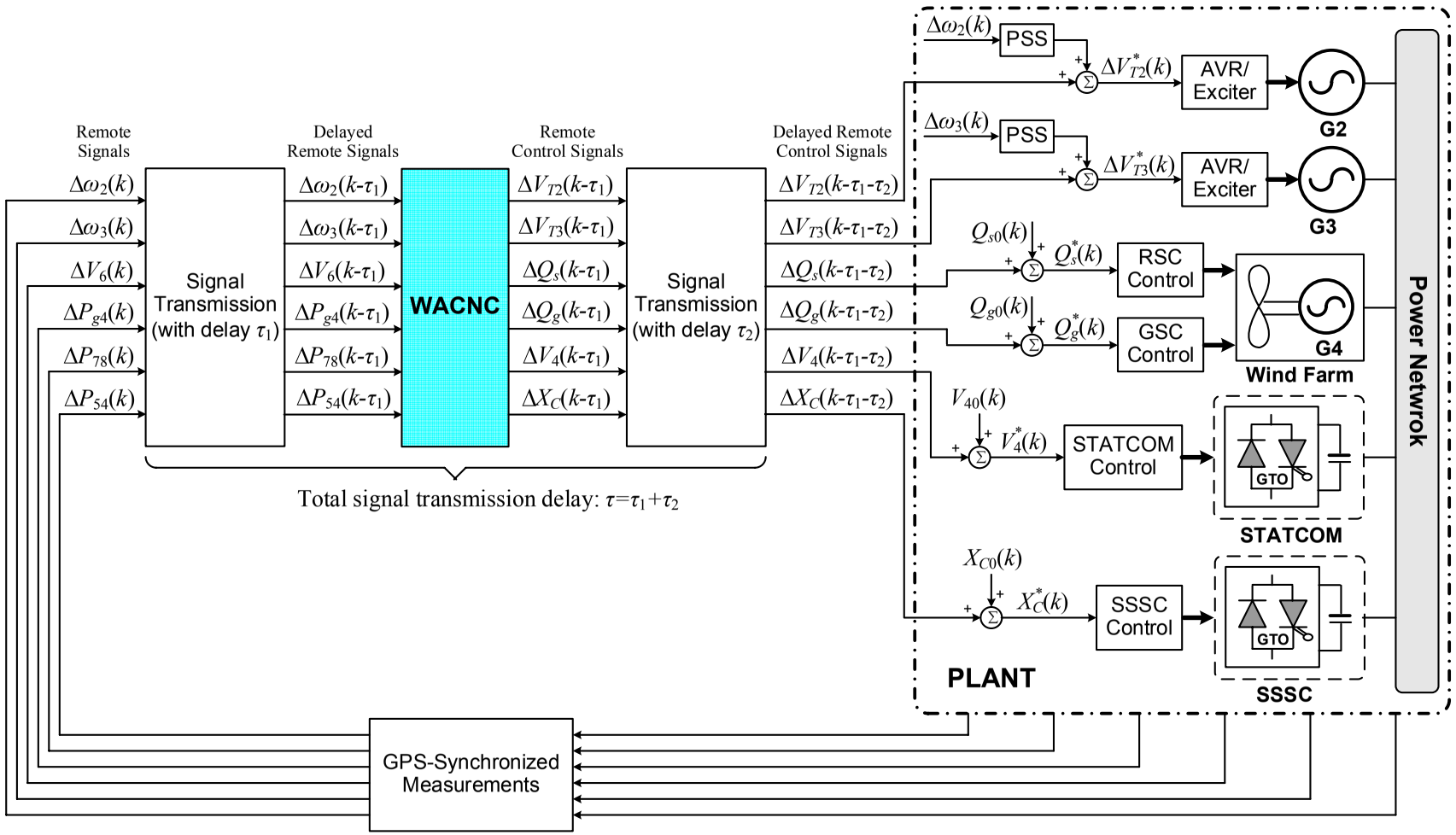

Figure 10.4: Schematic diagram of the synchronous generator, wind farm, STATCOM, and SSSC local controllers coordinated by the WACNC considering wide-area signal transmission delays.

At the local level, each local device is controlled by its local controllers. These local controllers use both local signals and auxiliary remote control signals from the WACNC to achieve local as well as global dynamic and transient performance improvement of the power system. For instance, for the reactive power control of the wind farm RSC, the command Q_s^* is the summation of two terms, Q_{s0} and ΔQ_s. The fixed set-point value Q_{s0} is determined by the local reactive power demand while taking into account the limit of the RSC rating. The supplementary command ΔQ_s is a remote signal generated by the WACNC, which enhances the dynamic performance of the local controller.

The transfer functions between (ΔV_{T2}, ΔV_{T3}, ΔQ_s, ΔQ_g, ΔV_4, ΔX_C) and ($\Delta\omega_2$, $\Delta\omega_3$, ΔV_6, ΔP_{g4}, ΔP_{78}, ΔP_{54}) are complicated, nonlinear, and depend on the network topology. To avoid having to derive such analytical functions, an adaptive critic design (ACD) approach – DHP, and RBFNNs are used to design the WACNC. In this design, the sampling rate for the WACNC implementation is chosen as 50 Hz in order to meet the phasor measurement unit (PMU) requirements for delivering the synchronized signals. Design of the WACNC should take into account the dynamics of local controllers. Therefore, the plant to be controlled includes the power network, the local devices and their controllers, as shown in the dash-dot-line block in Figure 10.4.

In Figure 10.4, because of the signal transmission delays τ_1 and τ_2, if the signals ($\Delta\omega_2$, $\Delta\omega_3$, ΔV_6, ΔP_{g4}, ΔP_{78}, ΔP_{54}) are measured from the local devices (inside the plant) and start to transmit to the WACNC at the time step k, then the corresponding input signals used by the WACNC are measured at the time step $k–\tau_1$ from the local devices, and the global control signals (ΔV_{T2}, ΔV_{T3}, ΔQ_s, ΔQ_g, ΔV_4, ΔX_C) used to coordinate the local controllers are generated by the WACNC using the input signals ($\Delta\omega_2$, $\Delta\omega_3$, ΔV_6, ΔP_{g4}, ΔP_{78}, ΔP_{54}) measured at the time step $k–\tau_1–\tau_2$ from the local devices.

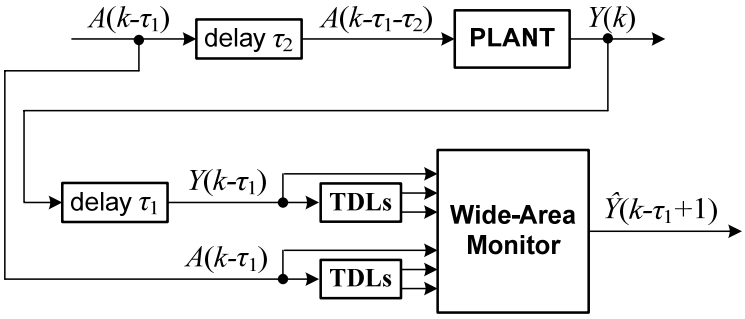

Figure 10.5: Structure of the wide-area monitor.

10.2.1 Design of the Optimal Wide-Area Monitor

A wide-area monitor is an essential part for designing the WACNC because it provides a dynamic plant model for training the critic and action networks. The wide-area monitor is a three-layer RBFNN (Figure 3.2). The plant inputs $A = [\Delta V_{T2}, \Delta V_{T3}, \Delta Q_s, \Delta Q_g, \Delta V_4, \Delta X_C]$ and outputs $Y = [\Delta\omega_2, \Delta\omega_3, \Delta V_6, \Delta P_{g4}, \Delta P_{78}, \Delta P_{54}]$ at time instants $k-\tau_1$, $k-\tau_1-1$, and $k-\tau_1-2$ are fed into the wide-area monitor to estimate the plant outputs $\hat{Y} = [\Delta\hat{\omega}_2, \Delta\hat{\omega}_3, \Delta\hat{V}_6, \Delta\hat{P}_{g4}, \Delta\hat{P}_{78}, \Delta\hat{P}_{54}]$ at time $k-\tau_1+1$, as shown in Figure 10.5.

The wide-area monitor is firstly pretrained offline using a suitably selected training data set from two sets of training: *forced training* and *natural training* (see Section 3.3.1). The forced training and natural training are carried out at several different operating points to form the training data set, given by:

$$\underline{Z} = \{\underline{A}, \underline{Y}\} = \left\{ \bigcup_{i=1}^{m} \underline{Z}_{Fi}, \bigcup_{i=1}^{m} \bigcup_{j=1}^{n} \underline{Z}_{Nij} \right\} \tag{10.1}$$

where $\underline{Z}$ is the entire training data set selected from m operating points; $\underline{A}$ and $\underline{Y}$ are the input and output data sets of the plant, respectively; $\underline{Z}_{Fi}$ is the subset collected from the forced training at the operating point i; $\underline{Z}_{Nij}$ is the subset collected from the natural training caused by the j^{th} natural disturbance event at the operating point i. The selected training data set ensures that the wide-area monitor can track the system dynamics over a wide operating range.

The performance of RBFNNs relies on a set of parameters, including the number of RBF units, the RBF centers, widths, and the output weights. Given the number of RBF units, the locations of RBF centers are determined by a *k*-means clustering algorithm [91] using the data from the training data set $\underline{Z}$. After locating the RBF centers, a good method to determine the RBF widths is the *p*-nearest neighbors heuristic [92] as described by (3.3). In this design, *p* is chosen the same as the number of RBF units *h* in the hidden layer. After determining the RBF centers and widths, the output weights of the RBFNN are then calculated by singular value decomposition (SVD) method [28].

However, the widths given by (3.3) are still nonoptimal. In [110], the authors have shown that the RBF widths can be optimized to achieve an optimal RBFNN with fewer RBF units and better performance. This section presents a method to design an OWAM by using PSO.

Suppose an initial width $\beta_i = \beta_{i,ini}$ of the i^{th} RBF unit has been calculated using (3.3), then the optimal width $\beta_{i,opt}$ can be defined by a set of equations, given by

$$\beta_{i,opt} = s_{i,opt} \cdot \beta_{i,ini} \qquad i = 1, 2, \cdots, h \tag{10.2}$$

where $s_{i,opt} \in R$ is the optimal scaling factor for β_i. Now the problem becomes using PSO to find out the set of optimal scaling factors $s_{opt} = \{s_{i,opt}\}$ in the problem space. In PSO implementation, the range of the scaling factors (i.e., the searching space of the PSO) should be appropriately determined in order to quickly locate the optimal solution. In this application, the scaling factors are within a small range of [0, 10] since (3.3) has already provided a set of good initial widths in (10.2).

Locating the set of optimal scaling factors s_{opt} is achieved by optimizing the following MSE in dB over the training data set:

$$MSE = 10\log\left(\sum_{j=1}^{N_T} \| Y(j) - \hat{Y}(j) \|^2 / N_T\right) \tag{10.3}$$

where N_T and $Y(j)$ are the number of data samples and the *j*th output data sample of the plant in the training set $\underline{Z}$ described by (10.1), respectively; $\hat{Y}(j)$ is the *j*th output sample

from the wide-area monitor. In this work, the training data set $\underline{Z}$ is selected from five different operating points [i.e., m = 5 in (10.1)]. At each operating point, the forced training and two different natural training events [i.e., n = 2 in (10.1)] are applied with 1000 data samples selected from each forced training and 300 data samples selected from each natural training event. Therefore, the total number of data samples in the training set is N_T = 8000. The MSE in (10.3) is employed as the performance measure function for PSO implementation.

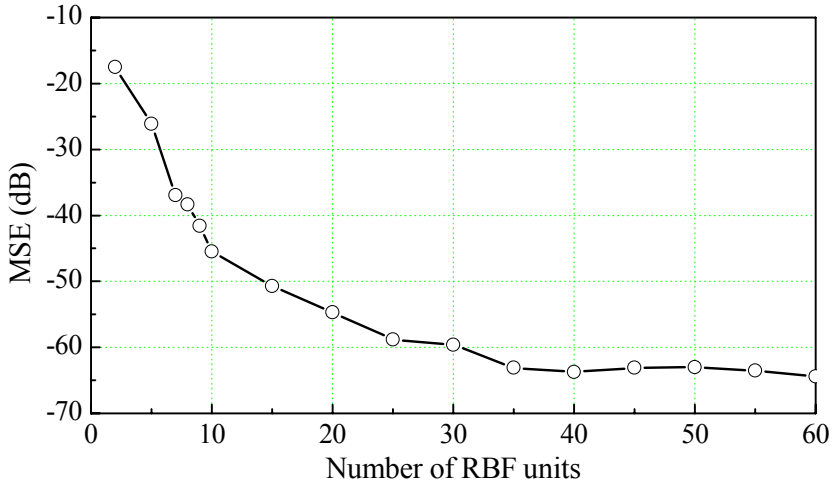

Figure 10.6: Performance of the wide-area monitor with the optimized width.

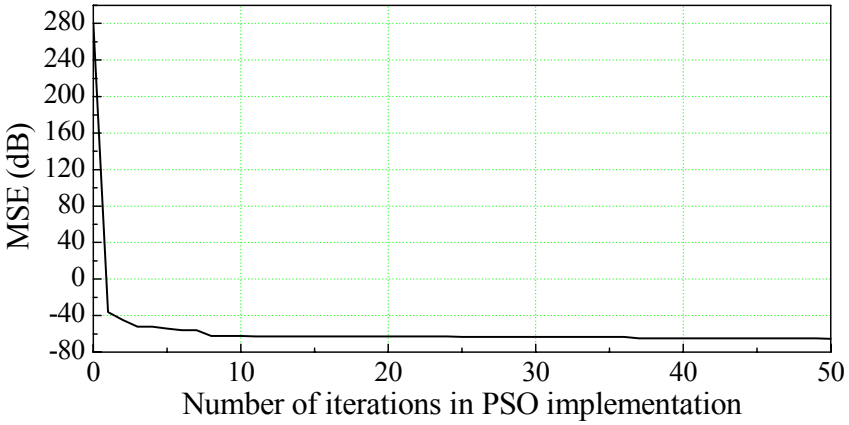

Figure 10.7: Performance of the wide-area monitor with 35 RBF units during RBF width optimization procedure.

The MSEs over the selected training data set are plotted in Figure 10.6 to show the performance of the wide-area monitor with the optimized widths but different numbers of RBF units. The minimum MSE is around -64 dB that can be achieved by using 35 or more RBF units, and any further increase over 35 does not improve the MSE significantly. Therefore, the optimal number of RBF units is chosen as 35 for the wide-area monitor.

Figure 10.7 shows the MSE as a function of the number of iterations in PSO during the RBF width optimization procedure for the wide-area monitor with 35 RBF units. The MSE at iteration no. 0, which denotes the RBFNN with initial widths from equation (3.3), is 280 dB. After 10 iterations, the MSE decreases to about -63 dB. These results indicate that the performance of the wide-area monitor is significantly improved by the proposed method. Further optimization using PSO with more than 10 iterations only slightly improves the MSE. Therefore, the optimal RBF widths can be found by PSO within only 10 iterations. Table 10.1 shows the initial and optimal RBF widths of the wide-area monitor with 35 RBF units.

The final OWAM therefore has 35 RBF units, the RBF centers determined by the *k*-means clustering algorithm, the optimized RBF widths found by PSO, and the output weights calculated by SVD method. It is now used for further implementation of the DHP.

10.2.2 Design of the Critic Network

The critic network is a three-layer RBFNN. The inputs to the critic network are the estimated plant outputs, $\hat{Y}$ (from the OWAM) and their two time-delayed values. The outputs of the critic network are the derivative, $\lambda = \partial J/\partial \hat{Y}$, of the function J in (1.1) with respect to the estimated plant outputs $\hat{Y}$, as shown in Figure 10.8. The critic network learns to minimize the following error measure over time [30]:

$$\|E_C\| = \sum_k E_C^T(k-\tau_1)E_C(k-\tau_1) \tag{10.4}$$

where

$$E_C(k-\tau_1)=\frac{\partial J[\hat{Y}(k-\tau_1)]}{\partial \hat{Y}(k-\tau_1)}-\gamma\frac{\partial J[\hat{Y}(k-\tau_1+1)]}{\partial Y(k-\tau_1)}-\frac{\partial U(k-\tau_1)}{\partial Y(k-\tau_1)} \tag{10.5}$$

The utility function is defined as

$$U(k-\tau_1)=\frac{1}{2}\sum_{i=1}^{6} w_i[Y_i^2(k-\tau_1)+0.5Y_i^2(k-\tau_1-1)+0.1Y_i^2(k-\tau_1-2)] \tag{10.6}$$

where Y is the vector of the plant outputs, and w_i is a weighting factor for Y_i. In DHP, application of the chain rule for derivatives yields

$$\frac{\partial J[\hat{Y}(k-\tau_1+1)]}{\partial Y(k-\tau_1)}=\lambda(k-\tau_1+1)\left[\frac{\partial \hat{Y}(k-\tau_1+1)}{\partial Y(k-\tau_1)}+\frac{\partial \hat{Y}(k-\tau_1+1)}{\partial A(k-\tau_1)}\frac{\partial A(k-\tau_1)}{\partial Y(k-\tau_1)}\right] \tag{10.7}$$

$$\frac{\partial U(k-\tau_1)}{\partial Y(k-\tau_1)}=\frac{\partial U(k-\tau_1)}{\partial Y(k-\tau_1)}+\frac{\partial U(k-\tau_1)}{\partial A(k-\tau_1)}\frac{\partial A(k-\tau_1)}{\partial Y(k-\tau_1)} \tag{10.8}$$

where $\lambda(k–\tau_1+1) = \partial J[\hat{Y}(k–\tau_1+1)]/\partial \hat{Y}(k–\tau_1+1)$.

Table 10.1: Initial and optimal RBF widths of the wide-area monitor with 35 RBF units

RBF unit No.	Initial width	Optimal width	RBF unit No.	Initial width	Optimal width	RBF unit No.	Initial width	Optimal width
1	1.4109	3.9226	13	1.4564	3.8342	25	1.3684	2.0294
2	1.3524	2.8657	14	1.4508	2.8008	26	1.4318	2.4646
3	1.3421	0.4513	15	1.3681	0.1368	27	1.5737	2.1201
4	1.3984	2.6842	16	1.4014	2.2703	28	1.4313	9.9075
5	2.9427	9.0170	17	1.4162	1.9557	29	1.3294	0.6490
6	1.3294	2.1773	18	1.6869	5.9304	30	1.4252	2.9524
7	1.7226	4.3782	19	1.3893	0.6893	31	1.6795	0.4665
8	1.3739	0.1374	20	1.4326	4.5073	32	2.0821	5.9215
9	1.3427	1.0385	21	1.3885	2.1598	33	2.5695	8.0537
10	1.3640	2.7715	22	1.3291	2.9626	34	2.9839	7.9225
11	2.4710	1.5335	23	1.4068	0.9873	35	3.0409	1.9695
12	1.3905	4.0342	24	1.3652	2.5910			

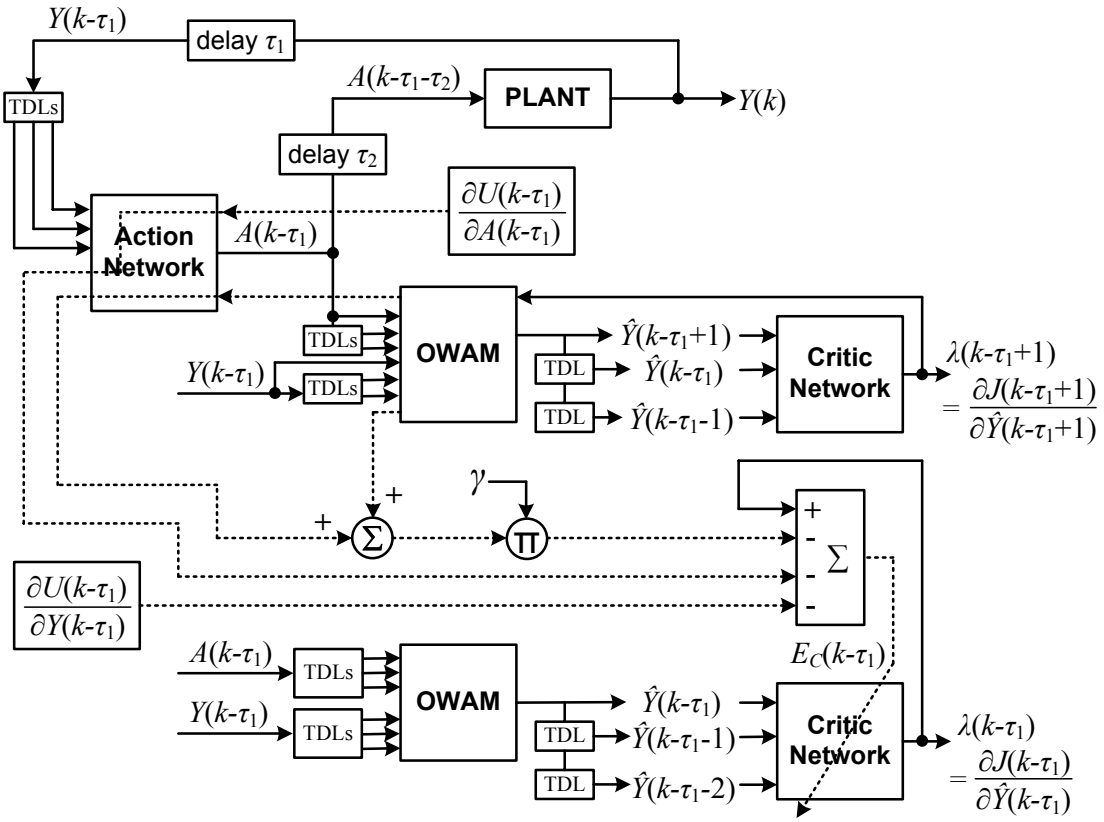

Figure 10.8: Adaptation of the critic network in DHP.

Generally, two critic networks are required in DHP to estimate $\partial J/\partial \hat{Y}$ arising from the present state $\hat{Y}(k-\tau_1)$ and the future state $\hat{Y}(k-\tau_1+1)$. The adaptation of the critic network in DHP takes into account all relevant pathways of backpropagation described by (10.5), (10.7), and (10.8), as shown in Figure 10.8. On the right-hand side of (10.5), the first term $\frac{\partial J[\hat{Y}(k-\tau_1)]}{\partial \hat{Y}(k-\tau_1)}$ is the output $\lambda(k-\tau_1)$ of the critic network at the time step $k-\tau_1$; the second term $\frac{\partial J[\hat{Y}(k-\tau_1+1)]}{\partial Y(k-\tau_1)}$ is obtained by propagating the output $\lambda(k-\tau_1+1)$ of the critic network at the time step $k-\tau_1+1$ back through both model and actions networks; the third term $\frac{\partial U(k-\tau_1)}{\partial Y(k-\tau_1)}$ is obtained by $\frac{\partial U(k-\tau_1)}{\partial Y(k-\tau_1)}$ itself as well as by propagating

$\frac{\partial U(k-\tau_1)}{\partial A(k-\tau_1)}$ back through the action network. The output weights of the critic network are then updated by

$$\Delta W_C(k-\tau_1) = -\eta_C E_C^T(k-\tau_1)\frac{\partial^2 J[\hat{Y}(k-\tau_1)]}{\partial \hat{Y}(k-\tau_1)\partial W_C(k-\tau_1)} \tag{10.9}$$

where $\eta_C = 0.05$ is a positive learning gain.

10.2.3 Design of the Action Network

As shown in Figure 10.9, the inputs to the action network are the plant outputs, Y, at time k–τ_1–1, k–τ_1–2, and k–τ_1–3. The outputs of the action network are the plant inputs, A, at time k–τ_1. The adaptation of the action network, is achieved by propagating $\lambda(k$–τ_1+1) back through the OWAM to the action network [30]. The objective of such adaptation is to find out the optimal control trajectory A^* in order to minimize the cost-to-go function J over time, given by

$$A^*(k-\tau_1) = \arg\min_u[J(k-\tau_1)] = \arg\min_u[U(k-\tau_1) + \gamma J(k-\tau_1+1)] \tag{10.10}$$

which is equivalent to achieving the following objective

$$\frac{\partial U(k-\tau_1)}{\partial A(k-\tau_1)} + \gamma\frac{\partial J(k-\tau_1+1)}{\partial A(k-\tau_1)} = 0, \quad \forall k \tag{10.11}$$

The output weights of the action network are then updated by

$$\Delta W_A(k-\tau_1) = -\eta_A\left[\frac{\partial U(k-\tau_1)}{\partial A(k-\tau_1)} + \gamma\frac{\partial J(k-\tau_1+1)}{\partial A(k-\tau_1)}\right]^T\frac{\partial A(k-\tau_1)}{\partial W_A(k-\tau_1)} \tag{10.12}$$

where $\eta_A = 0.05$ is a positive learning gain.

10.2.4 Overall Training Procedure

The training procedure to implement the DHP algorithm consists of two training stages: one for the OWAM and the other for the critic/action networks. The training of OWAM has been discussed in Section 10.2.1.

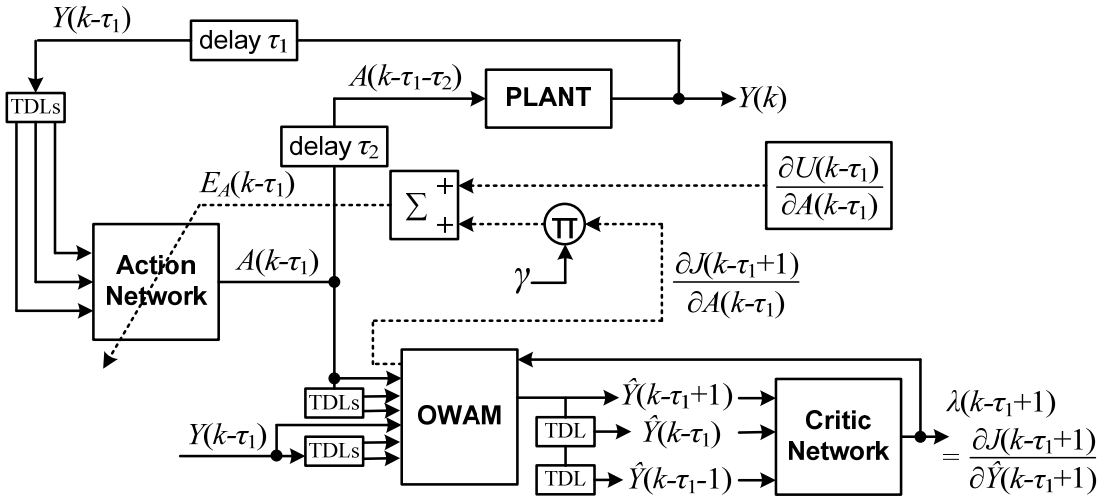

Figure 10.9: Adaptation of the action network in DHP.

The training stage of the critic/action networks contains two separate training cycles: one for the critic and the other for the action [30], [40], [145]. The critic network is firstly pretrained by the procedure in Figure 10.8 to approximate the deriviatives of the cost-to-go function J. During the critic's pretraining, the wind speed is varied over a certain range (e.g., ±2 m/s around the mean wind speed) using the wind model in [142] to simulate the real operation of the wind farm.

Once the critic's pretraining is over, its weights are fixed; the action network is then applied to control the plant in Figure 10.4 and is trained by the procedure in Figure 10.9 for N_A cycles. Then the action's weights are fixed, and the critic network is trained further for N_C cycles. This process of training the critic/action networks is repeated one after the other until an accepted performance is achieved. Once the critic and action networks' weights have converged, the action network with the fixed weights is used to control the plant during the real-time operation.

10.3 Simulation Results

In this section, simulation studies are carried out to show the dynamic performance enhancement of the power system in Figure 10.1 with the WACNC, while including the effect of signal transmission delays.

10.3.1 Case I: a Three-Phase Short Circuit without Line Tripping

The power system in Figure 10.1 is operated at a normal operating condition (OP-I) as specified in [137], where the active power generated by the wind farm is P_{g4} = 300 MW. Thereafter at t = 51 s, a three-phase short circuit is applied to the bus 7 end of line 7-8, which is a critical transmission line connecting Areas 1 and 3. The fault is cleared after 150 ms.

The dynamic performance of the power system, reinforced with the WACNC, is compared with the case without the WACNC. Figure 10.10 shows the responses of $\Delta\omega_2$, $\Delta\omega_3$, and ΔP_{g4} with and without the WACNC. The curves τ = 0, τ = 100 ms, and τ = 160 ms indicate the results by using the WACNC without any signal transmission delay, with 100 ms delay, and with 160 ms delay, respectively. This grid fault is not a severe disturbance. Therefore the local controllers are able to restore the system to the prefault normal operating condition without the coordination from the WACNC.

On the other hand, the WACNC improves the rotor oscillation damping of synchronous generators (G1 and G2) and power oscillation damping of the wind farm (G4). However, the performance of the WACNC depends on the period of the delay involved in the signal transmission. A larger delay will result in a further degradation of the WACNC performance. In this design, the WACNC improves the damping of ω_2, ω_3, and P_{g4} with the delay up to 160 ms, but cannot provide satisfactory coordinating control action for the system with a delay over 160 ms. These results show that the WACNC has the capability to improve the transient performance of all generation units in a power system with small signal transmission delays.

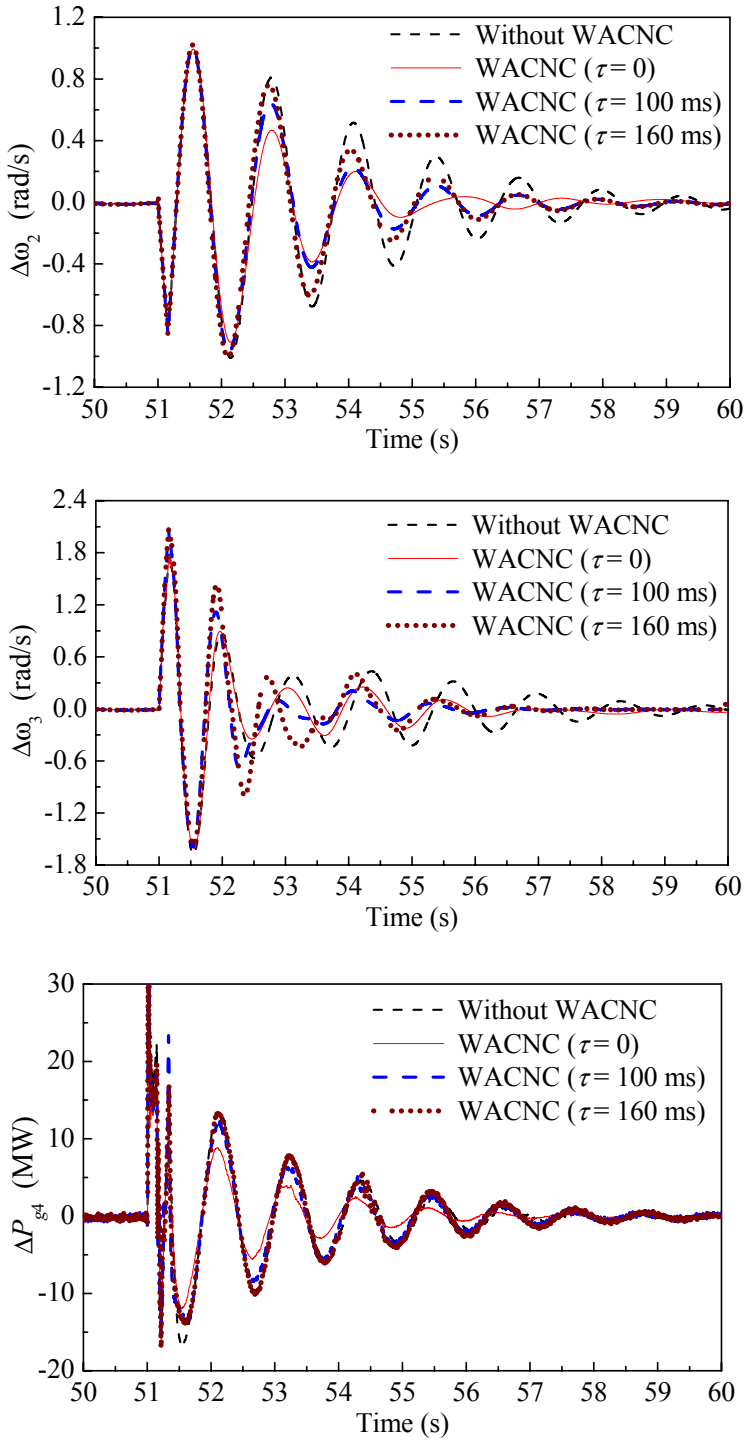

Figure 10.10: Comparison of power system dynamic performance with and without the WACNC for Case I.

10.3.2 Case II: a Three-Phase Short Circuit with Line Tripping

At the same operating condition OP-I, a three-phase short circuit is now applied to the bus 3 end of one of the parallel transmission lines 3-4 at t = 51 s. The fault is cleared after 150 ms by tripping the faulted line and the system changes to a different operating condition.

The dynamic responses of $\Delta\omega_2$, $\Delta\omega_3$, and ΔP_{g4} with and without the WACNC are compared in Figure 10.11. Compared to Case I, Case II is a more severe fault. The power oscillations of G2, G3, and G4 cannot be effectively damped by only using the local controllers. These results indicate that without the WACNC, the local controllers cannot restore the system to a normal operating condition after this severe disturbance. As a result, the power system will lose stability.

On the other hand, the WACNC significantly improves the damping of ω_2, ω_3, and P_{g4}, even with signal transmission delay up to 160 ms. However, any further increase of the delay over 160 ms will result in unsatisfactory coordinating control action from the WACNC, and the system may become unstable. It is well known that synchronous generators are the key components for power system stability. In addition, with the increased penetration of wind generation, the transient behavior of wind farms during grid disturbances begins to influence the stability of the associated power system. Figure 10.11 shows important results that the WACNC has the capability to improve the transient performance of all generation units in the power system, and therefore, the overall power system stability, without any compensation for the small delays involved in the signal transmission. These results are expected because the WACNC is designed at a global level to optimize the entire power system performance. This system-wide damping performance improvement and stability, however, could not be achieved by any single local controller.

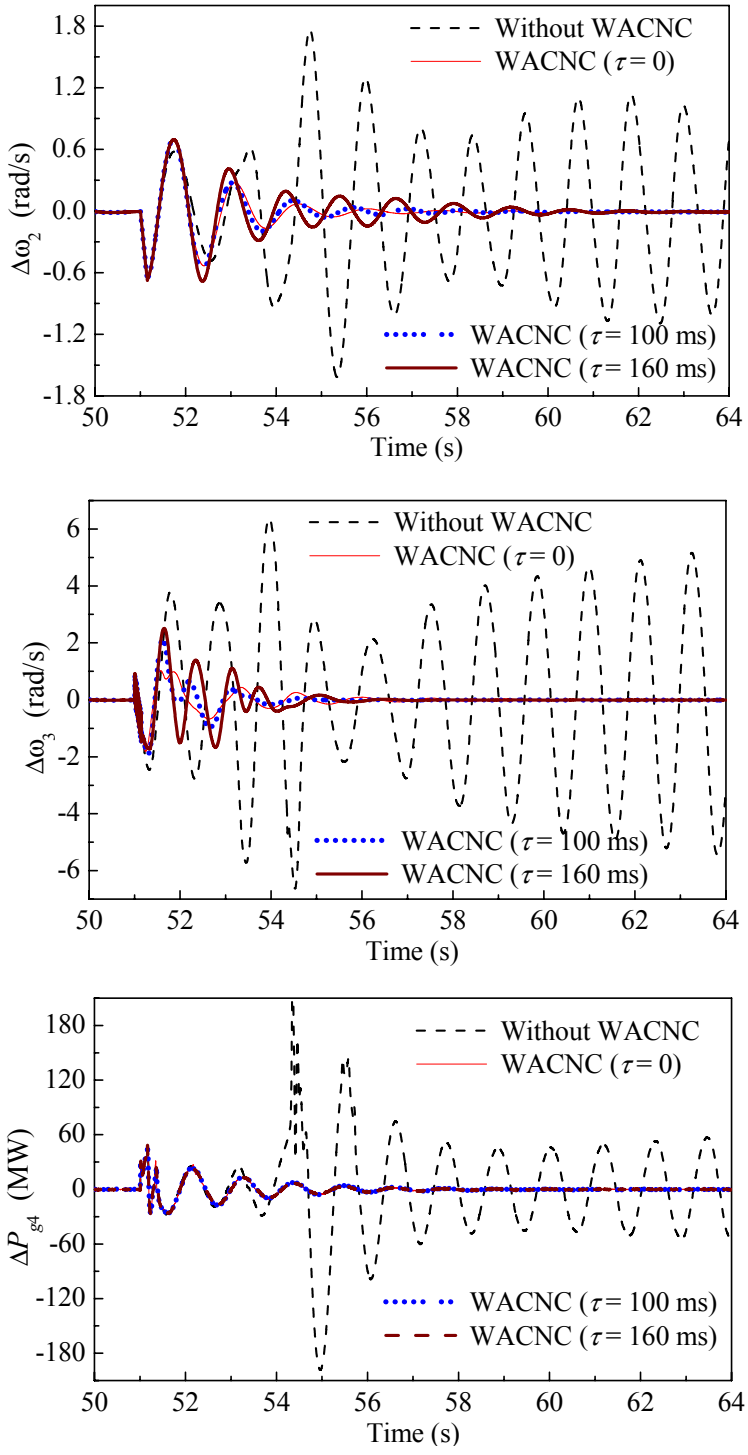

Figure 10.11: Comparison of power system dynamic performance with and without the WACNC for Case II.

Table 10.2: Dominant oscillation modes in ω_2 and ω_3: a 100 ms signal transmission delay is considered in the WACNC

Fault	Operating condition		Signal	Eigenvalues $\lambda = \sigma \pm j\omega$	Frequency (Hz)	Damping ratio (%)
Case I	OP-I	Without WACNC	ω_2	-0.539 ± j5.174	0.83	10.36
			ω_3	-0.874 ± j7.320	1.17	11.85
		With WACNC	ω_2	-0.660± j5.252	0.84	12.46
			ω_3	-1.025 ± j8.085	1.29	12.58
	OP-II	Without WACNC	ω_2	-0.732 ± j5.232	0.84	13.86
			ω_3	-0.683 ± j5.890	0.94	11.52
		With WACNC	ω_2	-0.854 ± j5.443	0.88	15.50
			ω_3	-0.786 ± j6.235	1.00	12.51
Case II	OP-I	Without WACNC	ω_2	-0.014 ± j5.267	0.84	0.27
			ω_3	-0.089 ± j5.702	0.90	1.57
		With WACNC	ω_2	-0.310 ± j4.910	0.78	6.30
			ω_3	-1.312 ± j8.698	0.92	14.91
	OP-II	Without WACNC	ω_2	-0.288 ± j5.227	0.83	5.51
			ω_3	-0.545 ± j6.107	0.98	8.89
		With WACNC	ω_2	-0.446 ± j5.647	0.90	7.87
			ω_3	-0.846 ± j5.933	0.95	14.12

10.3.3 Tests at a Different Operating Condition

The same 150 ms three-phase short circuit tests as for OP-I are now applied at another operating condition (OP-II), where the active power generated by the wind farm becomes P_{g4} = 350 MW. Applying Prony analysis [146] to the simulated waveforms, the eigenvalues, frequencies, and damping ratios of the dominant oscillation modes in ω_2 and ω_3 can be obtained, as shown in Table 10.2. In this investigation, a 100 ms signal transmission delay is considered in the WACNC design. At both operating conditions in

Case I, the WACNC improves the rotor oscillation damping of both synchronous generators. While at both operating conditions in Case II, the real parts of the eigenvalues are nearly zero and the resulting damping ratios are nearly zero without the WACNC. Therefore, the power system may lose stability after this severe disturbance. On the other hand, the WACNC is able to stabilize the system by coordinating the actions of the local controllers at a global level through its optimal control law. There results indicate that the WACNC increases the stability margin of the entire power system, and therefore more active power can be transmitted to the loads while maintaining the system stable during transient disturbances.

10.4 Chapter Summary

Wide-area coordinating control is becoming an important issue in the power industry. This chapter has proposed a novel wide-area measurements based optimal wide-area monitor (OWAM) and wide-area coordinating neurocontrol (WACNC), for a power system with power system stabilizers (PSSs), a large wind farm, and multiple FACTS devices. The OWAM, which identifies the input-output dynamics of the nonlinear power system, is a particle swarm optimization (PSO)-optimized radial basis function neural network (RBFNN). Based on the OWAM, the dual heuristic programming (DHP) method and RBFNNs have been employed to design the WACNC, while considering the delays involved in the wide-area signal transmission. The proposed WACNC operates at a global level to coordinate the actions of local power system controllers. Each local controller receives remote control signals from the WACNC to help improve system-wide dynamic and transient performance and stability.

Simulation studies have been carried out on a multimachine power system to evaluate the dynamic performance of the WACNC during transient events. The effect of different signal transmission delays has been investigated on the performance of the WACNC. Results have shown that the WACNC improved damping of all the generating

units in the power system and therefore the entire power system transient performance and stability, without the need to compensate for the small signal transmission delays.

CHAPTER 11

CONCLUSIONS, CONTRIBUTIONS, AND RECOMMENDATIONS

11.1 Conclusions

The objective of this work was to develop advanced intelligent control for power systems with wind power generation and flexible ac transmission system (FACTS) devices. The motivation of developing such advanced intelligent control was to improve the stability, reliability, dynamic and economical performance of wind energy generation systems, FACTS devices, and the power networks.

Worldwide continued growth of renewable and distributed energy penetration and the trend to maximally utilize the existing electricity infrastructure will bring new challenges to power system operation, control, stability, and reliability. These challenges require innovative solutions.

The controllability of a power system can be enhanced by using the power-electronics-based FACTS devices. Such devices, through their fast, flexible, and effective control capability, have been widely recognized as powerful controllers for voltage regulation, power flow control, power oscillation damping, and improving transient stability. Therefore, the use of FACTS devices allows more efficient utilization of existing electricity infrastructure. Among the family of FACTS devices, those based on the voltage source converter (VSC) concept, e.g., the static synchronous series compensator (SSSC) and the static synchronous compensator (STATCOM), are most attractive.

The SSSC is a series FACTS device typically used for power flow control. With a suitably designed external damping controller, the SSSC also has shown an excellent

performance in damping low-frequency power oscillations in a power network. In addition, if an SSSC is equipped with an energy storage system or is located as the series branch of a unified power flow controller (UPFC), it can be used to achieve independent active and reactive power flow control of the transmission line where it is connected. The conventional control schemes for the SSSC are based on the linear control techniques. These linear controllers are designed from a linearized system model with fixed parameters around a specific operating point. Final settings are made using field tests at one or two operating points. However, the FACTS devices and the power network are a large-scale nonlinear system with complex dynamics. In practical applications, such a system cannot be accurately modeled as a linear system with fixed and known parameters. Therefore, those linear controllers designed at a certain operating point may not able to provide an acceptable performance or stability over a wide system operating range or during a severe grid disturbance.

The control and operation of power systems rely on the availability and quality of sensor measurements. However, measurements are inevitably subjected to faults caused by sensor failure, broken or bad connections, bad communication, or malfunction of some hardware or software, etc. These faults, in turn, may result in the failure of power system controllers (e.g., FACTS controllers) and consequently severe contingencies in the power system. To prevent such contingencies, fault-tolerance is an essential requirement for power system control and operation.

State estimation is a commonly used technique to identify variables that are not accessible for direct measurements. This technique is based on the analysis of a system model and the redundancy of system state variables. By deriving closed-form solutions for the variables corresponding to the missing sensors, the missing data are explicitly represented by the remaining available data. However, for many systems, this model-based method converges slowly and the closed-form solutions can be unfeasible. Moreover, accurate system models are usually unavailable in real system applications.

An autoassociative neural network can capture correlations between the input data (i.e., sensor measurements) through an identity mapping. If some input data are missing, the correlations established by the network can be used to detect and restore the missing data. The application of such a method for offline or single missing sensor restoration has been reported by some authors; however, online missing sensor, especially multiple missing sensor detection and restoration for real-time fault-tolernat control is a challenging problem and has not yet been reported.

Worldwide concern about the environmental problems and a possible energy crisis has led to increasing interest in innovative technologies for clean and renewable energy generation and distribution. Among them wind power is the most rapidly growing renewable energy source. Therefore, how to provide efficient, reliable, and high-performance wind power generation and distribution has become a practical and important issue in the power industry. Much research effort has gone into modeling, control, operation, and grid integration of wind energy generation systems, as well as studying their impact on the dynamic performance and stability of the power system.

Most variable-speed wind turbine generators (WTGs) employ anemometers to measure wind speed that are required for maximum wind power generation and system protection. These mechanical sensors increase the equipment and maintenance costs and reduce the reliability of the WTG system. Recently, mechanical sensorless maximum power tracking controls, based on direct or indirect wind speed estimation or prediction, have been reported by some researchers. These sensorless control algorithms, however, have some obvious drawbacks: 1) requiring significant memory space, 2) requiring complex and time-consuming calculations, and/or 3) not accurate for real-time control. These drawbacks reduce WTG system performance.

The most commonly used techniques for controlling the wind turbines equipped with doubly fed induction generators (DFIGs) are linear PI/PID controllers, because of their simple structures. Unfortunately, tuning PI/PID controllers is tedious and it might

be difficult to tune the PI/PID gains optimally due to the nonlinearity and the high complexity of the system. Over the years, heuristic search based algorithms such as genetic algorithms (Gas), tabu search algorithm, and simulated annealing have been used for linear controller design. However, when the parameters being optimized are highly correlated, the performance of these heuristic search algorithms degrades.

One of the key issues related to the operation of the DFIG wind turbines is the grid fault ride-through capability. Because many WTGs are installed in remote, rural areas which usually have electrically weak power grids, voltage stability is a crucial issue for the WTGs to ride through grid faults. Therefore, the successful integration of WTGs will require local shunt FACTS devices, such as the STATCOM, to provide rapid and smooth steady-state and transient reactive compensation and voltage control. Further, it is necessary to coordinate the different control actions between the WTGs and the local shunt FACTS devices in order to achieve some optimal operating performance and economical benifits.

Power systems containing synchronous generators, WTGs, and FACTS devices are large-scale, stochastic, nonlinear and complex systems with dynamic characteristics over a wide range of operating conditions. In order to optimize the system-wide performance and stability of the power system, real-time wide-area coordinating control (WACC) is becoming an important issue in the power industry. With the increased availability of advanced computer, communication and measurement technologies, the development of WACC is becoming feasible. Various approaches have been addressed in the literature for coordinating the control action of different devices in power systems. The first category of the coordinating control schemes is based on the linear design. Because such designs are based on small disturbance analysis that requires linearization of the system involved, they cannot properly capture complex dynamics of the system, especially during critical disturbances. To overcome the shortcomings of the linear design methods, nonlinear control and optimization techniques have been employed to design the

coordinating controllers. The design of conventional nonlinear controllers requires an accurate system model and some knowledge of the system parameters. Compared to the linear controllers, they can provide good control capability over a wider operating range. However, the nonlinear controllers generally have sophisticated structures, complex control laws, and therefore, require much control effort and might be difficult for real-time implementation.

An unavoidable problem for designing a WACC is the delay involved between the instant of measurement and that of the signal being available to the controller. As the delay might be comparable to the time periods of some critical oscillating modes, it should be considered in the design of the WACC to ensure satisfactory control performance. In addition, designing the WACC needs knowledge of the entire power system dynamics to be available to the designers. Due to the large-scale, nonlinear, stochastic, and complex nature of power systems, the traditional mathematical tools and control techniques are not sufficient or too complicated to design such a WACC. Moreover, the existing designs of WACC are focused on the conventional power systems with power system stabilizers (PSSs) and/or FACTS devices. However, the coordinating control for the power systems with renewable energy sources, i.e., wind power, has not yet been reported.

To fully utilize the controllability of the SSSC FACTS device, a nonlinear indirect adaptive external neurocontroller (INDAEC) has been developed in this work for the external damping control of an SSSC. This INDAEC consists of two separate radial basis function neural networks (RBFNNs), one for the RBF neuroidentifier (RBFNI) and the other for the RBF neurocontroller (RBFNC). The RBFNI is trained to provide the dynamic model of the plant at all times. This dynamic plant model is then used for training the RBFNC. The RBFNC in turn generates the control signals as the plant inputs to drive the plant outputs to the desired values. The proposed INDAEC needs no mathematical model of the SSSC or the power network. The dynamic damping

performance of the SSSC with the INDAEC has been evaluated and compared with that without an external controller and with the conventional external linear controller (CONVEC) in a single machine infinite bus (SMIB) power system as well as a multimachine power system. Results have shown that the INDAEC significantly improved the damping of the SSSC and therefore the dynamic performance and stability of the power system over a wide system operating range.

To prevent power system contingencies caused by missing sensor measurements and to enhance power system reliability, maintainability and survivability, an online missing sensor restoration (MSR) algorithm has been developed in this work. It employs an autoassociative neural network as an auto-encoder to capture the correlations between its input data (through training), which are redundant time-varying sensor measurements. A well-trained auto-encoder is able to evaluate online the integrity of the sensor data. If any sensor measurements are detected to be missing, the MSR utilizes the particle swarm optimization (PSO) algorithm and the correlations established by the auto-encoder between the missing sensor data and the remaining healthy sensor data to quickly online restore the missing sensor measurements. The unique convergence of the MSR algorithm has been shown through the concepts of contractive and nonexpansive mapping. The use of the auto-encoder does not need an explicit plant model. In addition, the PSO algorithm provides a fast and efficient search for the missing sensor data, because of its attractive features including simple implementation, small computational load, and fast convergence. Therefore, the resulting MSR algorithm is suitable for online application.

Based on the MSR and the characteristics of the sensor data in power systems, a comprehensive online sensor evaluation and (missing sensor) restoration scheme (SERS) has been developed in this work for online evaluation and missing sensor restoration of the sensor data used by the SSSC controllers. The SERS utilizes several MSR blocks in a cascading structure and each MSR only monitors one crucial sensor measurement used by the SSSC controllers. This structure enables the SERS to detect which sensor

measurements are missing, and ensures that each MSR only searches in a 1-D space to quickly locate the optimal estimate of each missing measurement. The restored missing sensor readings are then combined with the healthy sensor readings together to provide a set of complete sensor data for the SSSC controllers.

Based on the SERS, a fault-tolerant indirect adaptive neurocontrol (FTIANC) strategy has been developed in this work for missing-sensor-fault-tolerant control of an SSSC with energy storage systems. This FTIANC consists of an SERS, an RBFNI, and an RBFNC. The RBFNI is trained to provide a dynamic predictive plant model for training the RBFNC. The RBFNC in turn provides the correct control action for the SSSC under the condition that all the required sensor data are available. The SERS provides a set of fault-tolerant complete current sensor data for the RBFNI and RBFNC. The resulting FTIANC is able to provide effective control for the SSSC when single and multiple crucial time-varying current sensor measurements are missing. Simulation studies have been carried out for an SSSC connected to an SMIB power system as well as the IEEE 10-machine 39-bus power system. The proposed FTIANC with and without missing sensor measurements has been compared with the conventional PI control scheme used by the SSSC without any missing sensor measurements. Results have shown that the FTIANC improved the dynamic performance, stability, and reliability of the SSSC and the power networks over a wide range of system operating conditions. The proposed fault-tolerant control is readily applicable to other plant models in power systems.

To demonstrate further the effectiveness of the SERS-based missing-sensor-fault-tolerant control for practical system applications, a missing-sensor-fault-tolerant control (MSFTC) strategy has been developed in this work for real-time control of an SSSC. The MSFTC consists of an SERS and a conventional internal and external SSSC control scheme (without any fault-tolerant design). The SERS works online to evaluate all the sensor measurements, including the three-phase voltage and current measurements and

the dc-link voltage measurement that are used by the SSSC controllers. If any of these sensor data are missing, it detects and restores all the missing sensor data. This provides a set of complete sensor measurements for the SSSC controllers, which in turn provide a fault-tolerant control for the SSSC. The MSFTC has been validated by a real-time implementation of an SSSC connected to the IEEE 10-machine 39-bus system using a Real Time Digital Simulator (RTDS) and TMS320C6701 DSP platform in the Real-Time Power and Intelligent Systems Laboratory at the Missouri University of Science and Technology. The SSSC and power network have been subjected to various grid disturbances and missing sensor faults. Results have shown that the SERS correctly restored the data from multiple missing sensors, and the resulting MSFTC provided fault-tolerant effective control for the SSSC and the power network during steady state, transient state of unbalanced and balanced grid faults, as well as a change of load conditions.

To solve the problems of using anemometers to measure wind speed for control and protection of WTG systems, this work has proposed a wind speed estimation based sensorless output maximum control for variable-speed WTG systems. A specific design of the proposed control has been presented for a DFIG wind turbine. A Gaussian radial basis function network (GRBFN) has been designed to approximate the nonlinear wind turbine aerodynamic characteristics. The wind turbine mechanical power is estimated from the measured generator electrical power while taking into account the power losses of the WTG and the dynamics of the WTG shaft system. Based on the nonlinear GRBFN mapping, the wind speed is estimated from the turbine mechanical power and speed. The optimal DFIG rotor speed command is then determined from the estimated wind speed. A DFIG speed controller has been suitably designed to achieve the maximum wind power generation as well as to sufficiently damp the low-frequency torsional oscillations of the WTG. Other control issues, such as the reactive power and voltage control, have been included in the DFIG control system for the successful grid integration of the WTG.

Simulation studies have been carried out on a 3.6 MW WTG system to verify the proposed sensorless control system. Results have shown that the wind speed is accurately estimated under both normal and transient operating conditions. The resulting WTG system delivered maximum electrical power to the grid with high efficiency and improved reliability without the need of mechanical anemometers. In addition, the proposed algorithm can be applied to other WTG systems. Its effectiveness has been further demonstrated by experimental studies on a small emulational WTG system.

A PSO-based approach has been proposed in this work to design the optimal parameters of the rotor side converter (RSC) PI controllers for the DFIG wind turbines. The RSC controllers are initially designed at a specific operating point with nonoptimal parameters. These parameters are then optimized by the proposed design approach, based on the minimization of the value of a time-domain performance measure function. A specific design has been presented to minimize the over-current in the rotor circuit of an equivalent DFIG wind turbine during grid faults. Simulation studies have been carried out in PSCAD/EMTDC and results have shown that the proposed design approach is efficient to find the optimal parameters of the RSC PI controllers. The resulting optimal RSC controllers improved the transient performance of the WTG system. The proposed design approach can be readily applied to design other controllers in power systems.

The application of a STATCOM to help achieve the uninterrupted operation of a DFIG wind turbine during grid faults has been investigated in this work. The STATCOM is placed at the bus [i.e., point of common coupling (PCC)] where the DFIG is connected to the power grid, for steady-state voltage regulation and transient voltage support. The control systems of the RSC and the grid side converter (GSC) of the DFIG and the STATCOM have been suitably designed and coordinated. An uninterrupted operation strategy of the WTG with the assistance of the GSC and the STATCOM for voltage control during grid faults has been presented. The necessity of using the STATCOM has been demonstrated by a real-time implementeation on a RTDS. During

the tests, the power system that contains a DFIG wind turbine and a STATCOM has been subjected to short-circuit grid faults. During the fault, the RSC was blocked and restarted when the fault was cleared and the PCC voltage was reestablished. Results have shown that with the STATCOM providing dynamic voltage support, the PCC voltage could be reestablished shortly after grid faults, and therefore, the WTG remained in service. However, without the STATCOM for voltage support, the PCC voltage could not be reestablished after the grid faults so that the WTG has to be tripped from the power network. The STATCOM improved the transient voltage stability and therefore enhanced the grid fault ride-through capability of the WTG system.

To achieve some optimal operating performance and economical benefits, a nonlinear optimal adaptive interface neurocontroller (INC) has been developed in this work for the coordinated reactive power control of a large wind farm and a STATCOM. The INC is based on the heuristic dynamic programming (HDP) method and RBFNNs. It uses the voltage deviation at the PCC of the wind farm and the STATCOM as well as the active power deviation of the wind farm as the input signals to produce two external control signals for the RSC and STATCOM reactive power controllers. By rapidly varying the amount of reactive power provided by the wind farm and the STATCOM during the grid faults, the proposed INC is able to reduce the level of voltage sags at the PCC and therefore control directly the transient imbalances between the electrical output power and the mechanical input power that are responsible for over-current in the DFIG rotor circuit. In addition, by using active power deviation as the input signal, which contains the important information of system oscillations, the INC also acts as a coordinated external damping controller for the wind farm and the STATCOM. It improved the post-fault power oscillation damping of the system. Simulation studies have been carried out on a multimachine power system to examine the performance of the proposed INC during grid faults. Results have shown that the INC significantly

enhanced the fault ride-through capability of the wind farm and improved the damping of the power system.

To improve the dynamic performance and stability of power systems globally, this work has also proposed a wide-area measurements based optimal wide-area monitor (OWAM) and wide-area coordinating neurocontrol (WACNC), for a power system with wind power generation and multiple FACTS devices. A wide-area monitor has been firstly designed by using an RBFNN, to identify the input-output dynamics of the nonlinear power system. The parameters of this wide-area monitor are then optimized by a PSO-based approach in terms of the performance and size of the RBFNN. The resulting OWAM is able to achieve the desired performance with the optimal number of RBF units, RBF centers, width, and output weights. Based on the OWAM, the dual heuristic programming (DHP) method and RBFNNs are then used to design the WACNC, while considering the delays involved in the wide-area signal transmission. The WACNC uses wide-area measurements and operates at a global level to coordinate the actions of the local synchronous generator, wind farm, and FACTS controllers. Each local controller communicates with the WACNC, and receives remote control signals from the WACNC as external input(s), to help improve system-wide dynamic and transient performance. Simulation studies have been carried out on a multimachine power system to evaluate the dynamic performance of the WACNC. The system has been subjected to different transient disturbances and different signal transmission delays in the wide-area measurements. Results have shown that the WACNC improved the damping of all the generating units in the power system and therefore the entire power system transient performance and stability, without the need to compensate for the small signal transmission delays. This system-wide dynamic performance improvement and stability, however, could not be achieved by any single local controller.

In conclusion, the proposed research was based on neural networks, adaptive critic designs, swarm intelligence, and intelligent control techniques. It significantly

improved the stability, reliability, economical and dynamic performance of WTGs, FACTS devices, and the power networks.

11.2 Contributions

The research performed in this work on the development of advance intelligent control to enhance the performance and reliability of the power systems with wind power generation and FACTS devices includes the following: 1) a RBFNN-based nonlinear indirect adaptive neurocontrol for external damping control of an SSSC (Chapter 3), 2) a missing-sensor-fault-tolerant indirect adaptive neurocontrol for an SSSC (Chapter 4), 3) a missing-sensor-fault tolerant control for an SSSC with real-time implementation (Chapter 5), 4) a wind speed estimation based sensorless output maximization control for a DFIG wind turbine (Chapter 6), 5) a PSO-based intelligent approach to design the optimal PI controllers for the RSC of the DFIG wind turbine (Chapter 7), 6) an uninterrupted operation strategy for the DFIG wind turbines with the assistance of a STATCOM for voltage control during grid faults (Chapter 8), 7) a HDP and RBFNN based nonlinear optimal adaptive coordinated reactive power control for a large wind farm and a STATCOM (Chapter 9), 8) a nonlinear optimal adaptive WACNC, based on the DHP method of adaptive critic designs (ACDs), PSO, and RBFNNs, for a power system with wind power generation and multiple FACTS devices while considering the effect of wide-area signal transmission delays (Chapter 10). Many original contributions have been made on control of FACTS devices, WTG systems, and the power networks. They are summarized as follows.

1) A comprehensive literature review on the existing techniques related to this work has been summarized in Chapter 2. The topics include control and operation of SSSC FACTS devices; modeling, control, and grid integration of DFIG wind turbines; local coordinating control of multiple devices and wide-area coordinating control of a

power system; missing sensor restoration and fault-tolerant control. Each of these techniques has some merits and disadvantages compared to other techniques.

2) A nonlinear INDAEC has been developed for the external control of an SSSC. This INDAEC consists of an RBFNI and an RBFNC. The RBFNI is trained to provide a dynamic plant model for training the RBFNC. This removes the need of a traditional mathematical model of the SSSC and the power network to design the controller. The resulting RBFNC provides a real-time external control for the SSSC. It significantly improves the damping of the SSSC and the dynamic performance and stability of the power system.

3) An online MSR algorithm has been developed by using an auto-encoder and PSO. The auto-encoder is trained to capture the correlations between the time-varying sensor measurements in power systems. If any sensor measurements are missing, these correlations are then used by the PSO algorithm to restore the missing data. The unique convergence of the MSR has been shown through the concepts of contractive and nonexpansive mapping. The proposed MSR algorithm is simple and fast, and therefore, is suitable for online application.

4) A comprehensive scheme (SERS) has been developed for online sensor evaluation and missing sensor restoration for the SSSC controllers. The SERS utilizes several MSR blocks in a cascading structure and the characteristics of the sensor data in power systems. It works online to evaluate all sets of sensor measurements used by the SSSC controllers, detects which sensor measurements are missing, and quickly locates the optimal estimate of each missing measurement.

5) A FTIANC has been developed for missing-sensor-fault-tolerant control of an SSSC with energy storage systems. This FTIANC consists of an SERS cascaded with a RBFNI and a RBFNC. The SERS provides a set of fault-tolerant complete three-phase current measurements for the RBFNI and RBFNC. They in turn are able to provide effective identification and control for the SSSC when single and multiple crucial time-

varying current sensor measurements are not available. The entire FTIANC significantly improves the dynamic performance, stability, and reliability of the SSSC and the power network.

6) A comprehensive MSFTC strategy has been developed for real-time control of an SSSC. It consists of an SERS and a conventional internal and external SSSC control scheme (without any fault-tolerant design). The SERS works online to evaluate the all the sensor data, including the three-phase voltage and current measurements and the dc-link voltage measurement, used by the SSSC controllers. If any of these sensor data are missing, the SERS detects and restores all the missing sensor data and therefore provides a set of complete sensor measurements for the SSSC controllers. The resulting MSFTC provides fault-tolerant effective control for the SSSC and the power network during various steady-state and transient operating conditions. The effectiveness of the MSFTC has been demonstrated by a real-time implementation of an SSSC connected to the IEEE 10-machine 39-bus system using the RTDS and TMS320C6701 DSP platform.

7) A GRBFN-based wind speed estimation algorithm has been proposed for wind power generation. A GRBFN has been designed to approximate the nonlinear inverse mapping of the wind turbine aerodynamic characteristics, in which the wind speed is mapped from the wind turbine mechanical power and shaft speed. The wind turbine mechanical power is estimated from the measured generator electrical power while taking into account the power losses of the WTG and the dynamics of the WTG shaft system. Based on the nonlinear GRBFN mapping, the wind speed is estimated from the turbine mechanical power and shaft speed. The proposed algorithm has been validated by simulation studies on a 3.6 MW DFIG wind turbine as well as by experimental studies on a small emulational WTG system.

8) Based on the proposed wind speed estimation algorithm, a sensorless output maximization control has been developed for variable-speed WTG systems. The proposed sensorless control has been demonstrated by a specific design for a 3.6 MW

DFIG wind turbine. The optimal DFIG rotor speed command is determined from the estimated wind speed. A DFIG speed controller has been suitably designed to achieve the maximum wind power generation as well as the damping of low-frequency torsional oscillations of the WTG system. In order for the successful grid integration of the WTG, the reactive power and voltage control have been included in the DFIG control system. The resulting WTG system delivers maximum electrical power to the grid with improved reliability.

9) A PSO-based approach has been proposed to design the optimal parameters of the RSC PI controllers for the DFIG wind turbines, based on a time-domain performance measure function. A specific design has been presented to minimize the over-current in the rotor circuit of an equivalent DFIG wind turbine during grid faults. This specific design has shown that the proposed approach is efficient to find the optimal parameters of the RSC PI controllers that improved the transient performance of the WTG system.

10) The application of a STATCOM to assist with the uninterrupted operation of a grid-connected DFIG wind turbine during grid faults has been investigated. The control schemes of the DFIG wind turbine and the STATCOM have been suitably designed and coordinated. The voltage stability of the power system and the fault ride through enhancement of the WTG with the assistance of the STATOCM has been demonstrated by a real-time implementation using a RTDS.

11) A nonlinear optimal adaptive INC, based on the HDP method and RBFNNs, has been developed for the coordinated reactive power control of a large wind farm and a STATCOM. This INC effectively reduces the level of voltage sags as well as the over-currents in the DFIG rotor circuit during grid faults. Therefore, it significantly enhances the fault ride-through capability of the wind farm. In addition, the INC acts as a coordinated external damping controller for the wind farm and the STATCOM. It improves the post-fault power oscillation damping of the power system.

12) A wide-area monitor, based on a three-layer RBFNN, has been developed to identify the input-output dynamics of a power system with wind power generation and multiple FACTS devices. A PSO-based approach has been proposed to optimize the parameters of the wide-area monitor. The resulting OWAM is able to achieve the desired performance with a set of optimal parameters, including the optimal number of RBF units, RBF centers, width, and output weights.

13) Based on the OWAM, a wide-area measurements based WACNC has been developed by using the DHP method and RBFNNs. This WACNC takes into account the effect of delays involved in the wide-area signal transmission. It operates at a global level to coordinate the actions of the local synchronous generator, wind farm, and FACTS controllers. Each local controller communicates with the WACNC, and receives remote control signals from the WACNC as external input(s), to help improve system-wide dynamic and transient performance. The entire control strategy (including the WACNC and local controllers) improves damping of all the generating units in the power system and therefore the entire power system transient performance and stability, without the need to compensate for the small signal transmission delays.

11.3 Recommendations

Some recommendations can be made for further studies in this research field. They are listed as follows.

1) A laboratory hardware implementation should be done to verify the performance of the nonlinear indirect adaptive external neurocontroller for the SSSC in an SMIB as well as a multimachine power system.

2) The SERS can be modified for online sensor evaluation and missing sensor restoration of other plants (devices and subsystems) in power systems. Consequently, the missing-sensor-fault-tolerant control can be designed to control other devices, such as synchronous generators, WTG, etc., in a power system. Moreover, the SERS can be

extended to design the wide-area missing-sensor-fault-tolerant coordinating control for multiple devices in a power system.

3) The parameters of many practical WTG systems are not fixed but vary with the operating and environmental conditions. The effect of parameter variations and uncertainties has not been considered in the GRBFN-based wind speed estimation algorithm. Therefore, further studies can be performed to improve the wind speed estimation algorithm by taking into account the effect of parameter variations and uncertainties of WTG systems. This will lead to a robust wind speed estimation for practical system applications.

4) The PSO-based controller design approach can be extended to design other power system controllers. Experimental implementations can be performed to verify the proposed approach to design practical power system controllers.

5) A coordinated control scheme can be developed to achieve an optimal reactive power control of the STATCOM and the DFIG GSC when the RSC has been blocked during grid faults. This will further enhance the fault ride-through capability of the DFIG wind turbines and help achieve certain economical benefits such as reducing the size of the STATCOM.

6) Further studies need to be performed to investigate the behavior of the INC when the RSC of the DFIG has been blocked during grid faults. A laboratory hardware implementation needs to be done to further verify the performance of the INC for a wind farm and a STATCOM in a multimachine power system.

7) The delay involved between the instant of measurement and that of the signal being available to the controller depends on the signal transmission hardware, distance, protocol of transmission, etc. These delays can typically be in the range of 0.01-1.0s. As large delays might be comparable to the time periods of some critical oscillating modes, it should be considered in the design of the WACC to ensure satisfactory control performance. An appropriate algorithm needs to be developed to compensate for large

signal transmission delays, e.g., the delays larger than 200 ms. This will make the WACNC applicable to many practical large-scale power systems with large delays in the wide-area signal transmission.

8) This work has focused on the power systems with only one type of renewable energy source, i.e., wind power. In the power industry, many other types of renewable energy sources, e.g., solar power and ocean power, are also receiving increasing interest. In addition, to achieve high levels of energy sustainability at a reasonable cost, dynamic energy storage devices and grid friendly appliances such as the plug-in pure or hybrid electric vehicles have been considered important to dynamically match the diurnal and seasonal intermittency of renewable resources. Therefore, a future research direction could be based on an extension of this work to the wide-area monitoring and coordinating control of power systems with different types of renewable energy sources, dynamic energy storage devices, and grid friendly appliances.

APPENDIX A

MODELING AND CONTROL OF A SYNCHRONOUS GENERATOR FOR SMIB POWER SYSTEMS IN PSCAD/EMTDC

In Chapters 3 and 4, the synchronous generator in the single machine infinite bus (SMIB) systems is modeled together with the AVR/exciter and governor/turbine dynamics taken into account. The generator is modeled based on synchronous machine two-axis equivalent circuits [90] and the parameters are listed in Table A.1, in which all the per-unit values are given on 160 MVA and 8.66 kV bases. The rotating shaft system of the turbine generator is modeled as one single lumped rotating mass.

Table A.1: Parameters of the synchronous generator in the SMIB power systems

Machine parameters	Actual value
MVA rating	160
Rated RMS line-to-line voltage (kV)	15.0
Inertia constant *H* (MWs/MVA)	2.37
Armature resistance (pu)	0.001096
Stator leakage reactance (pu)	0.15
D-axis unsaturated magnetizing reactance (pu)	1.55
Field resistance (pu)	0.000742
Field leakage reactance (pu)	0.101
D-axis damper resistance (pu)	0.0131
D-axis damper leakage reactance (pu)	0.055
Field-damp mutual leakage reactance (pu)	1.55
Q-axis magnetizing reactance (pu)	1.49
Q-axis damper resistance (pu)	0.054
Q-axis damper leakage reactance (pu)	0.036

The EXAC1A (IEEE alternator supplied rectifier excitation system) model in the PSCAD/EMTDC software library [90] is used for the AVR/exciter system, as shown in Figures A.1, where

V_C: Output of terminal voltage transducer and load compensation elements (pu),

V_{REF}: Voltage regulator reference (pu),

V_s: Power system stabilizer output (pu),

V_F: Excitation system stabilizer output (pu),

V_{AMAX}, V_{AMIN}: Maximum and minimum regulator internal output limits (pu),

K_A: Voltage regulator gain (pu),

T_A, T_B, T_C: Voltage regulator time constants (s),

V_{VEL}: Under-excitation limiter output (pu),

V_{OEL}: Over-excitation limiter output (pu),

V_{RMAX}, V_{RMIN}: Maximum and minimum regulator output limits (pu),

V_R: Voltage regulator output (pu),

V_{FE}: Signal proportional to exciter field current (pu),

T_E: Exciter time constant (s),

V_E: Exciter voltage back of commutating reactance (pu),

K_E: Exciter constant related to self-excited field (pu),

K_D: Demagnetizing factor, a function of exciter alternator reactance (pu),

K_F: Excitation control system stabilizer gain (pu),

V_X: Signal proportional to exciter saturation (pu),

$S_E(V_E)$: Exciter saturation function value at the corresponding exciter voltage V_E (pu),

K_C: Rectifier loading factor proportional to commutation reactance (pu),

I_{FD}: Synchronous machine field current (pu),

I_N: Normalized exciter load current (pu),

F_{EX}: Rectifier loading factor (pu),

E_{FD}: Exciter output voltage (pu).

The values of all the parameters in Figure A.1 are listed in Table A.2.

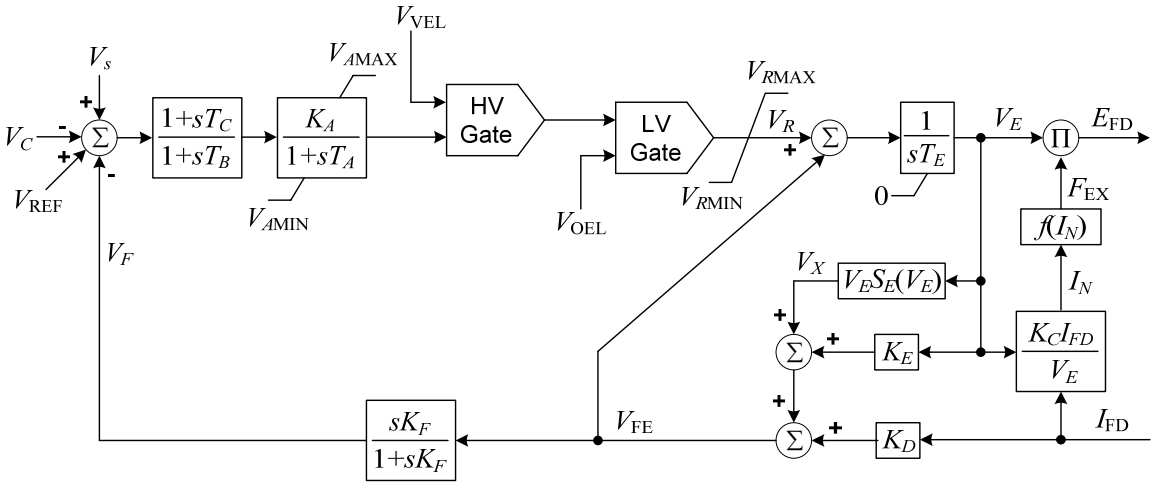

Figure A.1: Block diagram of the IEEE alternator supplied rectifier excitation system (EXAC1A model).

Table A.2: Parameters of the EXAC1A model

T_C (s)	0.0	V_{AMAX} (pu)	14.5	T_E (s)	0.8	K_C (pu)	0.2
T_B (s)	0.0	V_{AMIN} (pu)	-14.5	K_F (pu)	0.0	K_D (pu)	0.38
K_A (pu)	0.05	V_{RMAX} (pu)	6.03	T_F (s)	1.0	V_E (pu)	4.18
T_A (s)	0.1	V_{RMAX} (pu)	-5.43	K_E (pu)	1.0		

The H_TUR_1/H_GOV_1 (IEEE type hydro turbine-governor system) model in the PSCAD/EMTDC software library [90] is used for the governor/turbine system, as shown in Figures A.2, where

A_t: Turbine gain factor flow,

f_p: Penstock head loss coefficient (pu),

G: Gate position (pu),

q: Turbine flow before reduction by deflector and relief values (pu),

q_{nL}: No load water flow (pu),

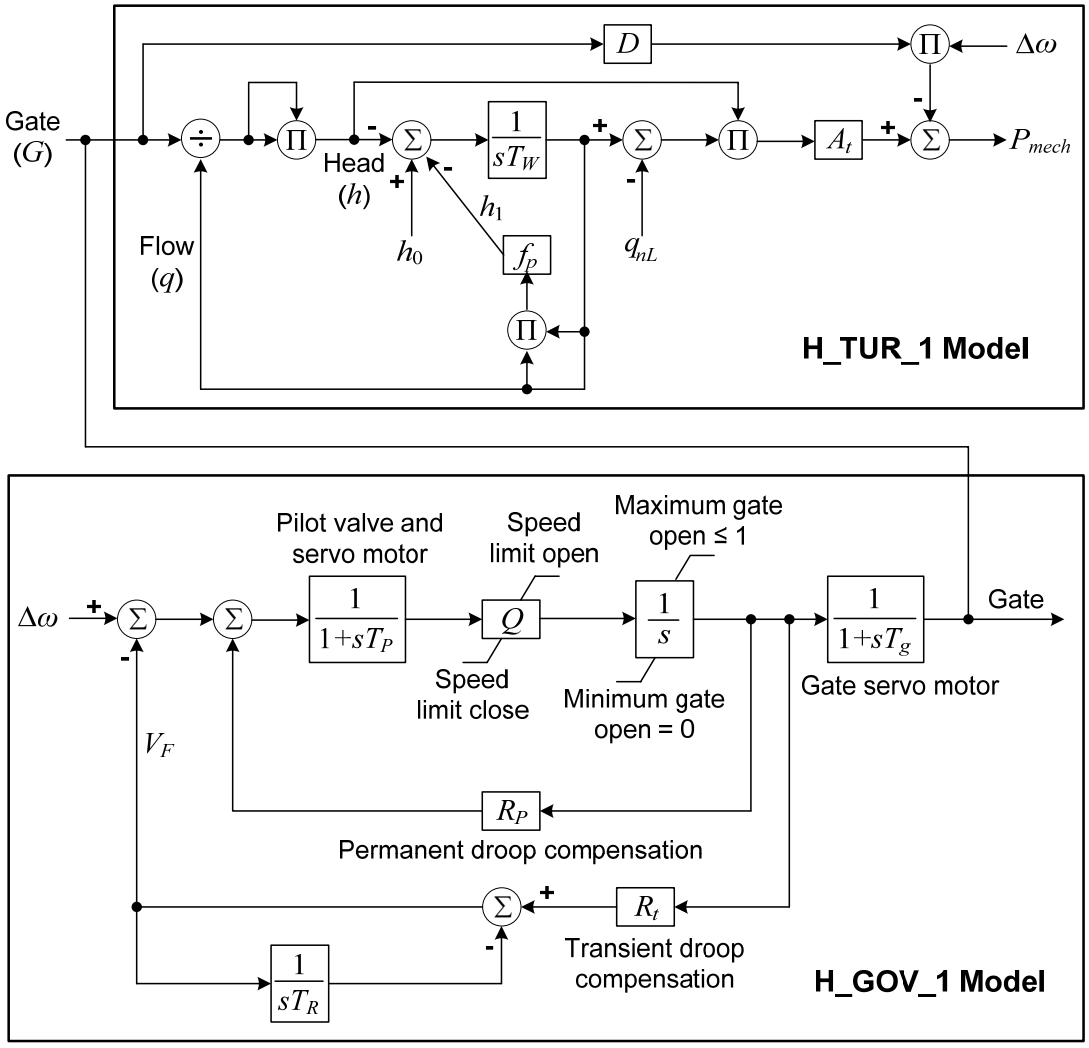

Figure A.2: Block diagrams of the hydro turbine model with a nonelastic water column and no surge tank (H_TUR_1 model) and mechanical-hydraulic governor system (H_GOV_1 model).

T_W: Water starting time (s),

D: Turbine damping constant (pu),

Q: Servo gain (pu),

R_P: Permanent droop (pu),

R_t: Temporary droop (pu),

T_g: Main servo time constant (s),

T_P: Pilot valve and servo motor time constant (s),

T_R: Reset or dashpot time constant (s),

$\Delta\omega$: Synchronous machine rotor speed deviation (pu),

P_{mech}: Turbine mechanical power (pu).

The values of all the parameters in Figure A.2 are listed in Table A.3.

Table A.3: Parameters of the H_TUR_1/ H_GOV_1 model

T_W (s)	2.0	f_p (pu)	0.02	D (pu)	0.5	T_P (s)	0.0
R_P (s)	0.4	T_R (s)	1.0	R_t (pu)	50.0	T_g (s)	1.0

APPENDIX B

MULTIMACHINE POWER SYSTEM DATA

Three different multimachine power systems are used in this thesis: a 3-machine 10-bus power system (Chapter 3), the IEEE 10-machine 39-bus New England power system (Chapters 4 and 5), and a 4-machine 12-bus benchmark power system (Chapters 9 and 10). Unless specified otherwise, all the simulation studies are carried out in PSCAD/EMTDC, which is a general-purpose time-domain simulation tool for studying the electromagnetic transient behavior of electric power systems. All the synchronous generators in the three multimachine power systems are modeled in detail, with the dynamics of the governor/turbine and automatic voltage regulator (AVR)/exciter taken into account. The transmission lines are modeled using a π-model, which takes into account the shunt admittance.

This Appendix provides the technical details and data of these three multimachine power systems. The rotating shaft system of each turbine generator is modeled as one single lumped rotating mass. Moreover, the saturation effects on the *d*-axis and *q*-axis are ignored for the synchronous generators.

B.1 3-Machine 10-Bus Equivalent Power System

Figure B.1 shows the single-line diagram of the original 3-machine 10-bus equivalent power system proposed in [95], [96]. This Appendix provides complete steady-state and dynamic data for this equivalent system.

B.1.1 Steady-State Data

Figure B.1 shows the system with some of the main data. Additional data (on a 100 MVA base) are:

- Transformer T1: 13.2/540 kV, X_l = 0.002 pu, no load and copper losses are zero.

- Transformer T2: 13.2/540 kV, X_l = 0.0045 pu, no load and copper losses are zero.
- Transformer T3: 13.2/530 kV, X_l = 0.00625 pu, no load and copper losses are zero.
- Transformer T4: 525/115 kV, X_l = 0.003 pu, no load and copper losses are zero, 500-550 kV tap range, 530 kV base case tap.
- Transformer T5: 115/13.8 kV, X_l = 0.001 pu, no load and copper losses are zero, 103.5-126.5 kV tap range, 112.1 kV base case tap.
- Transformer T6: 525/13.8 kV, X_l = 0.003 pu, no load and copper losses are zero, 500-550 kV tap range, 530 kV base case tap.
- Gen 1: slack bus, V = 0.98 pu.
- Gen 2: V = 0.964 pu, reactive power limits are -200 MVar and 725 MVar.
- Gen 2: V = 0.972 pu, reactive power limits are -200 MVar and 700 MVar.
- 500 kV transmission lines: Z = 0.0015 + j0.0288 pu, B/2 = 1.173 pu for each line.
- Shunt capacitor reactive power on Figure B.1 are at nominal voltage.

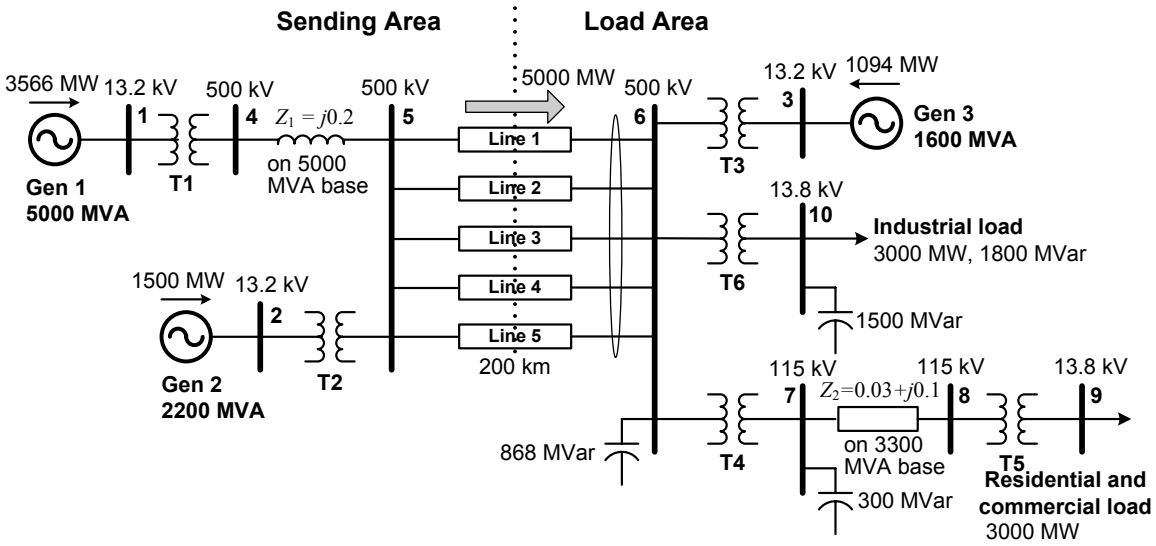

Figure B.1: Single-line diagram of the 3-machine 10-bus equivalent power system.

B.1.2 Dynamic Data

The generator Gen 1 is modeled as an infinite source, while the other two generators Gen 2 and Gen 3 are modeled in detail, with their conventional AVR/exciter and governor/turbine dynamics taken into account. The parameters of Gen 2 and Gen 3 are identical and based on Unit F18 in Appendix D of [97], as shown in Table B.1, in which the per-unit values for each generator are based on the corresponding machine MVA rating and rated phase voltage themselves. The AVR and exciter combination transfer function, as well as the turbine and governor combination transfer function are shown in Figure B.2 and Figure B.3, respectively [98]. The parameters in Figure B.2 and Figure B.3 are shown in Table B.2. The exciter saturation factor in Figure B.2 is given as

$$S_e = 0.6093 \exp(0.2165 V_{fd}) \tag{B.1}$$

Table B.1: Parameters of Gen 2 (2200 MVA) and Gen 3 (1600 MVA)

Rated kV	13.2	x_q (pu)	2.02	τ'_{d0} (s)	4.2
Rated PF	0.95	r_a (pu)	0.0046	τ''_q (s)	0.0225
H (MWs/MVA)	3.32	x_p (pu)	0.155	τ''_{q0} (s)	0.062
x''_d (pu)	0.215	r_2 (pu)	0.026	τ'_{q0} (s)	0.565
x'_d (pu)	0.28	x_2 (pu)	0.215	τ_a (s)	0.14
x_d (pu)	2.11	x_0 (pu)	0.15	r_F (Ω)	0.1094
x''_q (pu)	0.215	τ''_d (s)	0.0225		
x'_q (pu)	0.49	τ''_{d0} (s)	0.032		

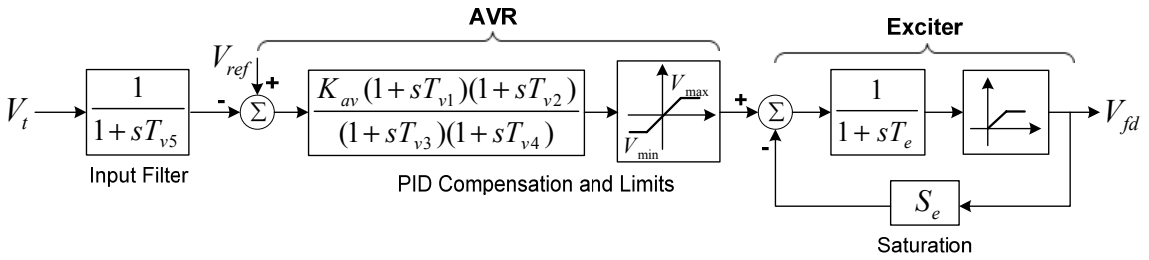

Figure B.2: Block diagram of the AVR and exciter combination transfer function.

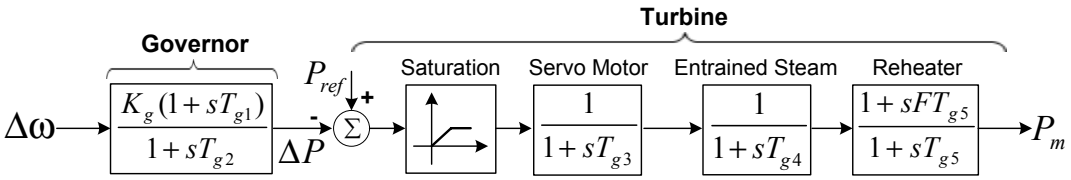

Figure B.3: Block diagram of the turbine and governor combination transfer function.

Table B.2: Parameters of the AVR/exciter and the governor/turbine transfer functions for Gen 2 and Gen 3

Time constants and gains	AVR/exciter		Time constants and gains	Governor/turbine	
	Gen 2	Gen 3		Gen 2	Gen 3
T_{v1} (s)	0.616	0.616	T_{g1} (s)	0.264	0.264
T_{v2} (s)	2.266	2.266	T_{g2} (s)	0.0264	0.0264
T_{v3} (s)	1.89	0.59	T_{g3} (s)	0.15	0.15
T_{v4} (s)	0.39	0.39	T_{g4} (s)	0.594	0.594
T_{v5} (s)	1.0235	1.0235	T_{g5} (s)	2.662	2.662
T_e (s)	0.04	0.2	K_g	0.05	0.04
K_{av}	3.76	3.564	F	0.322	0.322
V_{max} (pu)	19.59	19.59			
V_{min} (pu)	-14.51	-14.51			

B.2 IEEE 10-Machine 39-Bus Power System

Figure B.4 shows the single-line diagram of the IEEE 10-machine 39-bus New England power system [112], [113]. Generator 1 (G1) represents the aggregation of a large number of generators and is modeled as an infinite source, while other generators (G2-G10) are modeled together with their AVR/exciter and governor/turbine dynamics taken into account. Each generator of G2-G10 may be equipped with a power system stabilizer (PSS) to improve the damping of low-frequency rotor oscillations [108].

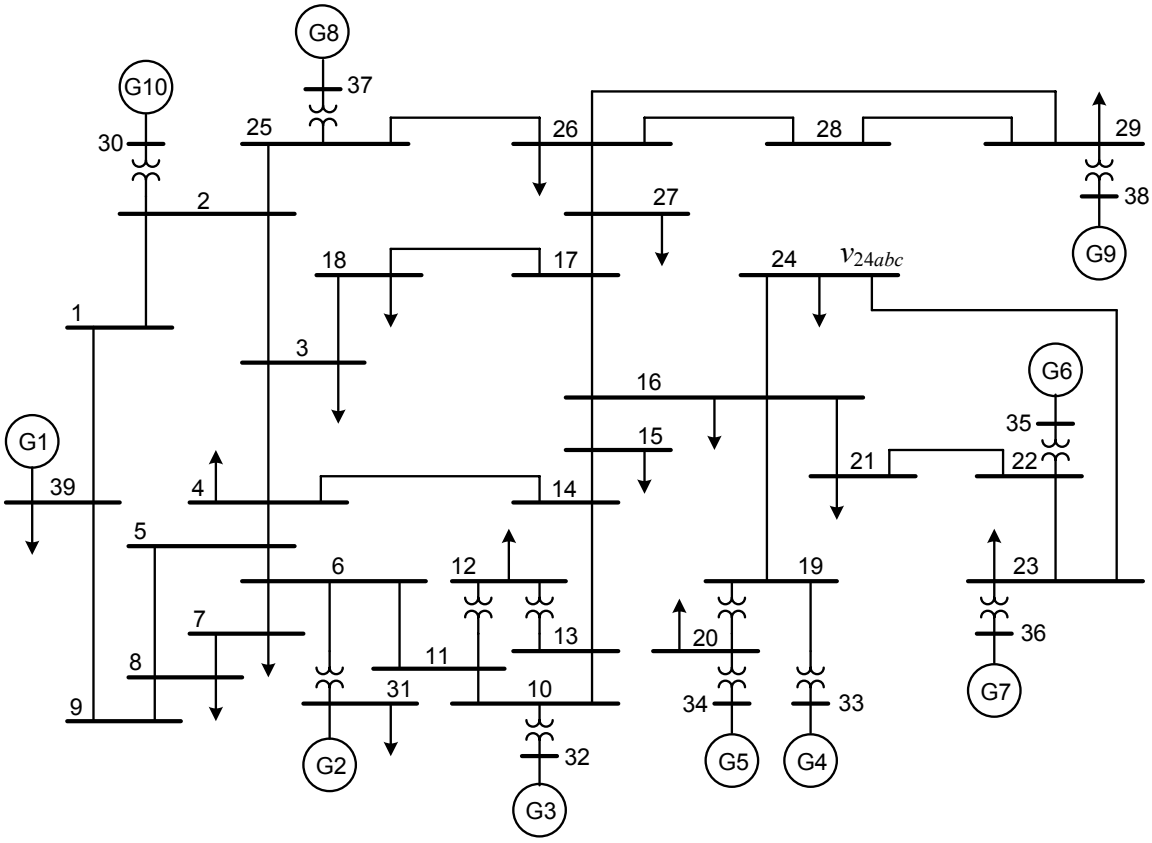

Figure B.4: Single-line diagram of the IEEE 10-machine 39-bus power system.

B.2.1 Steady-State Data

The transformer and line data for this multimachine power system are shown in Table B.3 and Table B.4, respectively. The rated voltage of all the transmission lines is 345 kV. Table B.5 shows the power and voltage setpoints in the base case of the system. All the per-unit values are given on a 100 MVA base.

Table B.3: Transformer data

From bus	To bus	R (pu)	X (pu)	B (pu)	Transformer tap	
					Magnitude	Angle
12	11	0.0016	0.0435	0.0000	1.006	0.00
12	13	0.0016	0.0435	0.0000	1.006	0.00

Table B.3: Transformer data (contd.)

From bus	To bus	*R* (pu)	*X* (pu)	*B* (pu)	Transformer tap	
					Magnitude	Angle
6	31	0.0000	0.0250	0.0000	1.070	0.00
10	32	0.0000	0.0200	0.0000	1.070	0.00
19	33	0.0007	0.0142	0.0000	1.070	0.00
20	34	0.0009	0.0180	0.0000	1.009	0.00
22	35	0.0000	0.0143	0.0000	1.025	0.00
23	36	0.0005	0.0272	0.0000	1.000	0.00
25	37	0.0006	0.0232	0.0000	1.025	0.00
2	30	0.0000	0.0181	0.0000	1.025	0.00
29	38	0.0008	0.0156	0.0000	1.025	0.00
19	20	0.0007	0.0138	0.0000	1.060	0.00

Table B.4: Line data

From bus	To bus	*R* (pu)	*X* (pu)	*B* (pu)
1	2	0.0035	0.0411	0.6987
1	39	0.0010	0.0250	0.7500
2	3	0.0013	0.0151	0.2572
2	25	0.0070	0.0086	0.1460
3	4	0.0013	0.0213	0.2214
3	18	0.0011	0.0133	0.2138
4	5	0.0008	0.0128	0.1342
4	14	0.0008	0.0129	0.1382
5	6	0.0002	0.0026	0.0434
5	8	0.0008	0.0112	0.1476
6	7	0.0006	0.0092	0.1130

Table B.4: Line data (contd.)

From bus	To bus	*R* (pu)	*X* (pu)	*B* (pu)
6	11	0.0007	0.0082	0.1389
7	8	0.0004	0.0046	0.0780
8	9	0.0023	0.0363	0.3804
9	39	0.0010	0.0250	1.2000
10	11	0.0004	0.0043	0.0729
10	13	0.0004	0.0043	0.0729
13	14	0.0009	0.0101	0.1723
14	15	0.0018	0.0217	0.3660
15	16	0.0009	0.0094	0.1710
16	17	0.0007	0.0089	0.1342
16	19	0.0016	0.0195	0.3040
16	21	0.0008	0.0135	0.2548
16	24	0.0003	0.0059	0.0680
17	18	0.0007	0.0082	0.1319
17	27	0.0013	0.0173	0.3216
21	22	0.0008	0.0140	0.2565
22	23	0.0006	0.0096	0.1846
23	24	0.0022	0.0350	0.3610
25	26	0.0032	0.0323	0.5130
26	27	0.0014	0.0147	0.2396
26	28	0.0043	0.0474	0.7802
26	29	0.0057	0.0625	1.0290
28	29	0.0014	0.0151	0.2490

Table B.5: Power and voltage setpoints

Bus No.	Type	Voltage (pu)	Load		Generator		
			MW	MVar	MW	MVar	Unit No.
1	PQ	-	0.0	0.0	0.0	0.0	-
2	PQ	-	0.0	0.0	0.0	0.0	-
3	PQ	-	322.0	2.4	0.0	0.0	-
4	PQ	-	500.0	184.0	0.0	0.0	-
5	PQ	-	0.0	0.0	0.0	0.0	-
6	PQ	-	0.0	0.0	0.0	0.0	-
7	PQ	-	233.8	84.0	0.0	0.0	-
8	PQ	-	522.0	176.0	0.0	0.0	-
9	PQ	-	0.0	0.0	0.0	0.0	-
10	PQ	-	0.0	0.0	0.0	0.0	-
11	PQ	-	0.0	0.0	0.0	0.0	-
12	PQ	-	7.5	88.0	0.0	0.0	-
13	PQ	-	0.0	0.0	0.0	0.0	-
14	PQ	-	0.0	0.0	0.0	0.0	-
15	PQ	-	320.0	153.0	0.0	0.0	-
16	PQ	-	329.0	32.3	0.0	0.0	-
17	PQ	-	0.0	0.0	0.0	0.0	-
18	PQ	-	158.0	30.0	0.0	0.0	-
19	PQ	-	0.0	0.0	0.0	0.0	-
20	PQ	-	628.0	103.0	0.0	0.0	-
21	PQ	-	274.0	115.0	0.0	0.0	-
22	PQ	-	0.0	0.0	0.0	0.0	-
23	PQ	-	247.5	84.6	0.0	0.0	-
24	PQ	-	308.6	-92.0	0.0	0.0	-
25	PQ	-	224.0	47.2	0.0	0.0	-
26	PQ	-	139.0	17.0	0.0	0.0	-

Table B.5: Power and voltage setpoints (contd.)

Bus No.	Type	Voltage (pu)	Load		Generator		
			MW	MVar	MW	MVar	Unit No.
27	PQ	-	281.0	75.5	0.0	0.0	-
28	PQ	-	206.0	27.6	0.0	0.0	-
29	PQ	-	283.5	26.9	0.0	0.0	-
30	PV	1.0475	0.0	0.0	250.0	-	G10
31	PV	0.9820	9.2	4.6	520.0	-	G2
32	PV	0.9831	0.0	0.0	650.0	-	G3
33	PV	0.9972	0.0	0.0	632.0	-	G4
34	PV	1.0123	0.0	0.0	508.0	-	G5
35	PV	1.0493	0.0	0.0	650.0	-	G6
36	PV	1.0635	0.0	0.0	560.0	-	G7
37	PV	1.0278	0.0	0.0	540.0	-	G8
38	PV	1.0265	0.0	0.0	830.0	-	G9
39	PV	1.0300	1104.0	250.0	1000.0	-	G1

B.2.2 Dynamic Data

The synchronous generators G2-G10 are modeled by a two-axis machine model in which the subtransient and transient dynamics are taken into account. The parameters for the two-axis model of each synchronous generator are shown in Table B.6. All values are given on 100 MVA and 22 kV bases. The AVR/exciter transfer function for each generator is shown in Figure B.5, while the turbine and governor combination transfer function is the same as that in Figure B.6. The parameters in Figure B.5 for each generator unit are shown in Table B.7. The parameters of the governor/turbine transfer functions of G2-G10 are identical and are listed in Table B.8. The block diagram of the PSS is shown in Figure B.6 and the parameters of the PSS transfer function for each generator unit is listed in Table B.9.

Table B.6: Generator data

Unit No.	2	3	4	5	6	7	8	9	10
MVA rating	612.0	765.0	700.0	612.0	800.0	660.0	660.0	1150.0	300.0
Rated voltage (kV)	22.0	22.0	22.0	22.0	22.0	22.0	22.0	22.0	22.0
H (MWs/MVA)	3.41	6.05	3.6	3.41	5.016	3.141	3.141	5.32	5.8
x_d'' (pu)	0.0338	0.0367	0.0333	0.0338	0.0393	0.0326	0.0326	0.0214	0.0747
x_d' (pu)	0.0421	0.0484	0.0403	0.0421	0.0524	0.0424	0.0424	0.0276	0.1063
x_d (pu)	0.2873	0.2444	0.2657	0.2873	0.2293	0.2788	0.2788	0.1429	0.7713
x_q'' (pu)	0.0338	0.0367	0.0333	0.0338	0.0393	0.0326	0.0326	0.0214	0.0747
x_q' (pu)	0.0754	0.061	0.0666	0.0754	0.1038	0.0724	0.0724	0.0417	0.1593
x_q (pu)	0.2765	0.2275	0.2586	0.2765	0.2248	0.2682	0.2682	0.1365	0.683
r_a (pu)	0.0003	0.0003	0.0003	0.0003	0.0003	0.0003	0.0003	0.0002	0.0007
x_p (pu)	0.0242	0.0301	0.0234	0.0242	0.0325	0.0235	0.0235	0.0167	0.0617
τ_{d0}'' (s)	0.0225	0.035	0.035	0.0225	0.053	0.03	0.03	0.043	0.033
τ_{d0}' (s)	3.826	6.7	5.8	3.826	5.318	3.8	3.8	7.61	3.797
τ_{q0}'' (s)	0.0225	0.07	0.054	0.0225	0.039	0.058	0.058	0.065	0.07
τ_{q0}' (s)	0.5084	0.41	1.2	0.5084	0.97	0.52	0.52	0.84	0.438

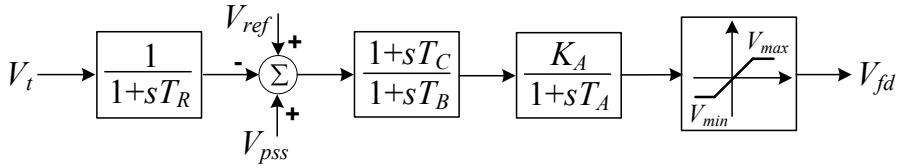

Figure B.5: Block diagram of the AVR/exciter transfer function.

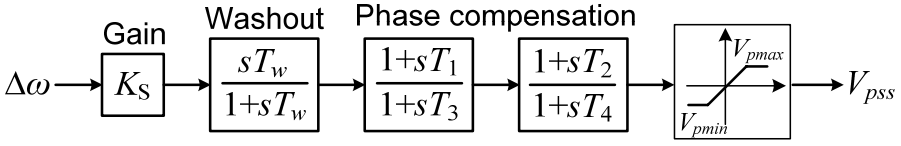

Figure B.6: Block diagram of the PSS.

Table B.7: Parameters of the AVR/exciter transfer functions

Unit No.	T_R (s)	K_A	T_A (s)	T_B (s)	T_C (s)	V_{ref} (pu)	V_{max} (pu)	V_{min} (pu)
2	0.01	200.0	0.015	10.0	1.0	0.9820	5.0	-5.0
3	0.01	200.0	0.015	10.0	1.0	0.9831	5.0	-5.0
4	0.01	200.0	0.015	10.0	1.0	0.9972	5.0	-5.0
5	0.01	200.0	0.015	10.0	1.0	1.0123	5.0	-5.0
6	0.01	200.0	0.015	10.0	1.0	1.0493	5.0	-5.0
7	0.01	200.0	0.015	10.0	1.0	1.0635	5.0	-5.0
8	0.01	200.0	0.015	10.0	1.0	1.0278	5.0	-5.0
9	0.01	200.0	0.015	10.0	1.0	1.0265	5.0	-5.0
10	0.01	200.0	0.015	10.0	1.0	1.0475	5.0	-5.0

Table B.8: Parameters of the turbine/governor transfer functions

Unit No.	T_{g1} (s)	T_{g2} (s)	T_{g3} (s)	T_{g4} (s)	T_{g5} (s)	K_g	F
2-10	0.264	0.0264	0.15	0.594	2.662	20.0	0.322

Table B.9: Parameters of the PSS transfer functions

Unit No.	K_S	T_w (s)	T_1 (s)	T_2 (s)	T_3 (s)	T_4 (s)	V_{pmax} (pu)	V_{pmin} (pu)
2	0.5	10.0	5.0	0.40	1.0	0.10	0.2	-0.2
3	0.5	10.0	3.0	0.20	2.0	0.20	0.2	-0.2
4	2.0	10.0	1.0	0.10	1.0	0.30	0.2	-0.2
5	1.0	10.0	1.5	0.20	1.0	0.10	0.2	-0.2
6	4.0	10.0	0.5	0.10	0.5	0.05	0.2	-0.2
7	7.5	10.0	0.2	0.02	0.5	0.10	0.2	-0.2
8	2.0	10.0	1.0	0.20	1.0	0.10	0.2	-0.2
9	2.0	10.0	1.0	0.50	2.0	0.10	0.2	-0.2
10	1.0	10.0	1.0	0.05	3.0	0.50	0.2	-0.2

B.3 4-Machine 12-Bus Power System

The 4-machine 12-bus benchmark power system [115] as shown in Figure B.7 was proposed as a platform for studying FACTS device applications. G1 represents the aggregation of a large number of generators and is modeled as an infinite source, while the other two synchronous generators (G2 and G3) are modeled in detail, with the exciter and turbine governor dynamics taken into account.

Table B.10 shows the specified voltage and the amount of active power generation at each generator bus, the load and shunt compensation at each load bus for the basic case. In the transient model, the loads are represented as fixed impedances. Table B.11 shows the line lengths for each of the 230- and 345-kV lines, as well as the series impedances and shunt reactances resulting from the above line geometries for an equivalent-π representation, corrected for long-line effects. Table B.12 shows the parameters of each transformer.

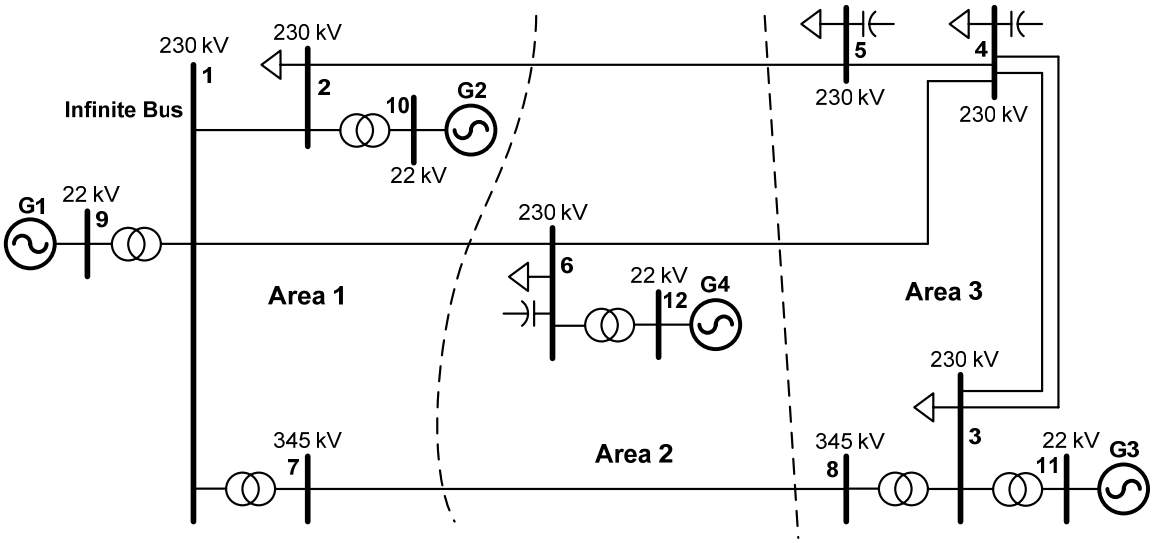

Figure B.7: Single-line diagram of the 4-machine 12-bus power system.

Table B.10: Bus data

Bus	Nominal Voltage (kV)	Specified Voltage (pu)	Load (MVA)	Shunt (MVar)	Generation (MW)
1	230				
2	230		280 + j200		
3	230		320 + j240		
4	230		320 + j240	160	
5	230		100+ j60	80	
6	230		440 + j300	180	
7	345				
8	345				
9	22	1.04			
10	22	1.02			500
11	22	1.01			200
12	22	1.02			300

Table B.11: Transmission Line data (on a 100 MVA base)

Line	Voltage (kV)	Length (km)	*R* (pu)	*X* (pu)	*B* (pu)	Rating (MVA)
1-2	230	100	0.01144	0.09111	0.18261	250
1-6	230	300	0.03356	0.26656	0.55477	250
2-5	230	300	0.03356	0.26656	0.55477	250
3-4(1)	230	100	0.01144	0.09111	0.18261	250
3-4(2)	230	100	0.01144	0.09111	0.18261	250
4-5	230	300	0.03356	0.26656	0.55477	250
4-6	230	300	0.03356	0.26656	0.55477	250
7-8	345	600	0.01595	0.17214	3.28530	500

Table B.12: Transformer data (on a 100 MVA base)

From-to	Voltage (kV)	X (pu)	Rating (MVA)
1-7	230/345	0.01	1000
1-9	230/22	0.01	1000
2-10	230/22	0.01	1000
3-8	230/345	0.01	1000
3-11	230/22	0.10	1000
6-12	230/22	0.02	500

Table B.13: Generator and exciter data (on a 100 MVA base)

Unit No.	G2	G3	G4
MVA rating	700	500	500
Rated voltage (kV)	22	22	22
H (MWs/MVA)	5.0	3.0	5.0
x_d'' (pu)	0.35	0.28	0.35
x_d' (pu)	0.4	0.3	0.4
x_d (pu)	1.5	1.4	1.5
x_q (pu)	1.2	1.35	1.2
r_a (pu)	0.0002	0.0002	0.0002
x_p (pu)	0.012	0.01	0.012
τ_{d0}'' (s)	0.002	0.002	0.002
τ_{d0}' (s)	5.0	6.0	5.0
K_a	20.0	20.0	20.0
T_a	0.05	0.05	0.05

The exciters of the synchronous generators (G2-G4) are simplified as first order transfer functions $K_a/(1+sT_a)$ rather than detailed representations. Table B.13 shows the parameters of synchronous generators and exciter transfer functions. The hydro turbine and governor models Hydro_Tur_1 and Hydro_Gov_1 in the standard PSCAD/EMTDC

library are used for G2 and G4, while the standard steam turbine and governor models Steam_Tur_1 and Steam_Gov_1 are used for G3 [90].

APPENDIX C

P-Q DECOUPLED LINEAR CONTROL OF AN SSSC

In terms of the instantaneous variables shown in Figure 4.2 (Chapter 4), the ac-side circuit equations of the SSSC can be written in per-unit form as follows:

$$\frac{d}{dt}\begin{bmatrix} i_a \\ i_b \\ i_c \end{bmatrix} = \begin{bmatrix} -\frac{r_{l3}\omega_s}{x_{l3}} & 0 & 0 \\ 0 & -\frac{r_{l3}\omega_s}{x_{l3}} & 0 \\ 0 & 0 & -\frac{r_{l3}\omega_s}{x_{l3}} \end{bmatrix} \begin{bmatrix} i_a \\ i_b \\ i_c \end{bmatrix} + \frac{\omega_s}{x_{l3}} \begin{bmatrix} v_{sa} + v_{ca} - v_{ra} \\ v_{sb} + v_{cb} - v_{rb} \\ v_{sc} + v_{cc} - v_{rc} \end{bmatrix} \tag{C.1}$$

Applying the synchronously rotating reference frame transformation [109], the following *d-q* vector representation can be obtained from (C.1) for modeling the ac-side of the SSSC:

$$\frac{d}{dt}\begin{bmatrix} i_d \\ i_q \end{bmatrix} = \begin{bmatrix} -\frac{r_{l3}\omega_s}{x_{l3}} & \omega \\ -\omega & -\frac{r_{l3}\omega_s}{x_{l3}} \end{bmatrix} \begin{bmatrix} i_d \\ i_q \end{bmatrix} + \frac{\omega_s}{x_{l3}} \begin{bmatrix} v_{sd} + v_{cd} - |v_r| \\ v_{sq} + v_{cq} \end{bmatrix} \tag{C.2}$$

Equation (C.2) can be rewritten as follows:

$$v_{cd} = \frac{x_{l3}}{\omega_s} y_1 - \frac{\omega x_{l3}}{\omega_s} i_q - v_{sd} + |v_r| \tag{C.3}$$

$$v_{cq} = \frac{x_{l3}}{\omega_s} y_2 + \frac{\omega x_{l3}}{\omega_s} i_d - v_{sq} \tag{C.4}$$

where

$$y_1 = \frac{d}{dt} i_d + \frac{r_{l3}\omega_s}{x_{l3}} i_d \tag{C.5}$$

$$y_2 = \frac{d}{dt} i_q + \frac{r_{l3}\omega_s}{x_{l3}} i_q \tag{C.6}$$

Equations (C.5) and (C.6) can be written into a matrix form as

$$\frac{d}{dt}\begin{bmatrix} i_d \\ i_q \end{bmatrix} = \begin{bmatrix} -\frac{r_{l3}\omega_s}{x_{l3}} & 0 \\ 0 & -\frac{r_{l3}\omega_s}{x_{l3}} \end{bmatrix}\begin{bmatrix} i_d \\ i_q \end{bmatrix} + \begin{bmatrix} y_1 \\ y_2 \end{bmatrix} \tag{C.7}$$

Equation (C.7) indicates that i_d and i_q respond to y_1 and y_2 respectively, through a first-order transfer function without cross-coupling. Therefore, it is possible to design the following feedback loops and PI controllers:

$$y_1 = \frac{\omega_s}{x_{l3}}\left(k_{p1} + \frac{k_{i1}}{s}\right)(i_d^* - i_d) \tag{C.8}$$

$$y_2 = \frac{\omega_s}{x_{l3}}\left(k_{p2} + \frac{k_{i2}}{s}\right)(i_q^* - i_q) \tag{C.9}$$

where i_d^* and i_q^* are the reference values of d-axis and q-axis current components, respectively. They are calculated as follows from the desired reference values of the transmitted real power P^* and reactive power Q^* at the receiving end of line 3.

$$P^* = \frac{3}{2}|v_r|\, i_d^* \tag{C.10}$$

$$Q^* = \frac{3}{2}|v_r|\, i_q^* \tag{C.11}$$

Substituting (C.8) and (C.9) into (C.3) and (C.4) yields the following P-Q decoupled power flow control scheme as shown in Figure 4.3:

$$v_{cd} = \left(k_{p1} + \frac{k_{i1}}{s}\right)(i_d^* - i_d) + v_{cd0} \tag{C.12}$$

$$v_{cq} = \left(k_{p2} + \frac{k_{i2}}{s}\right)(i_q^* - i_q) + v_{cq0} \tag{C.13}$$

where $v_{cd0} = -\frac{\omega x_{l3}}{\omega_s} i_q - v_{sd} + |v_r|$, and $v_{cq0} = \frac{\omega x_{l3}}{\omega_s} i_d - v_{sq}$.

APPENDIX D

MODELING AND CONTROL OF A DFIG WIND TURBINE IN PSCAD/EMTDC

D.1 Modeling of DFIG Wind Turbine

The DFIG wind turbine in Figure 1.3 is modeled in PSCAD/EMTDC, as shown in Figure D.1. It consists of a wind turbine, a doubly fed induction generator (DFIG) (with two six-pulse PWM IGBT converters connected back-to-back by a dc-link capacitor), and a mechanical shaft system connected between them. The wind turbine aerodynamic model described by equations (2.1)-(2.3) is represented by a user defined module "Wind Power Model" in PSCAD/EMTDC, as shown in Figure D.1. The generator is represented by a standard wound-rotor induction machine model in the PSCAD/EMTDC software library [90]. The IGBT converters are modeled in detail, in which the operation of individual IGBT switches is fully represented. The shaft system dynamics are represented by a two-mass model, as described by equations (2.6)-(2.8). They are represented by a Multimass model in the PSCAD/EMTDC software library [90].

The wind model is represented by a four-component model [135] defined by

$$v_w = v_{wM} + v_{wG} + v_{w\mathrm{R}} + v_{w\mathrm{N}} \tag{D.1}$$

where v_{wM} is the mean wind speed in m/s, v_{wG} is the gust wind component in m/s, v_{wR} is the ramp wind component in m/s, and v_{wN} is the noise wind component in m/s. The last three terms in (D.1) represent the turbulent wind speed components; among them v_{wG} and $v_{w\mathrm{R}}$ are deterministic turbulences while $v_{w\mathrm{N}}$ is the stochastic part to predict the occurrence of wind turbulence and the correlation of wind turbulence at different wind turbines in a wind farm. These four components provide reasonable flexibility for the study of one or a group of wind turbine generators (WTGs).

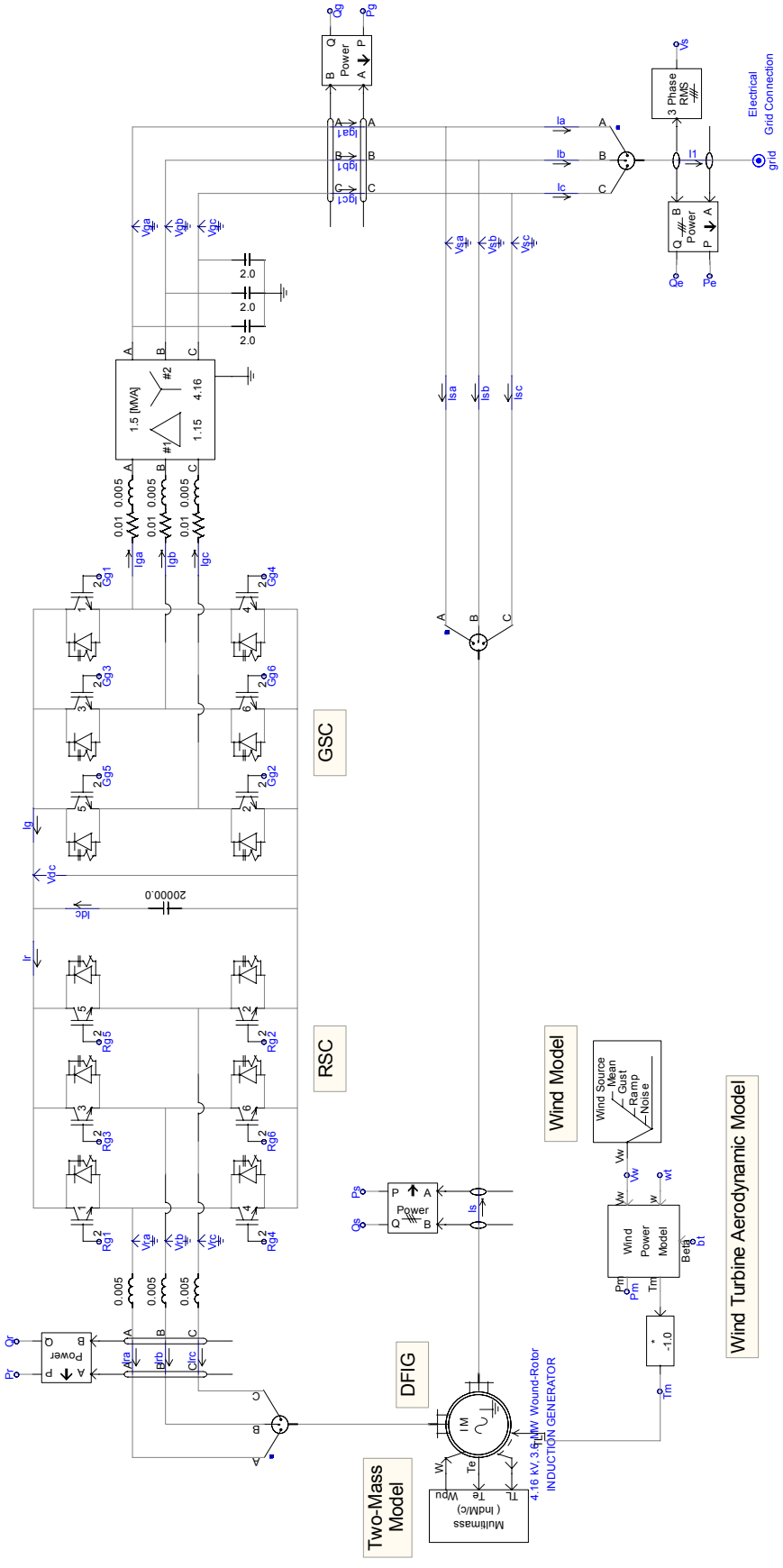

Figure D.1: PSCAD/EMTDC model for a DFIG wind turbine.

The mean wind speed is a constant. This component is always assumed to be present in studies where the WTG is in service.

The gust wind speed component is considered an essential component of wind speed for dynamic studies and is described by

$$v_{wG} = \begin{cases} 0 & t < t_{1G} \\ \dfrac{V_{G\max}}{2}\left[1 - \cos 2\pi\left(\dfrac{t - t_{1G}}{T_G}\right)\right] & t_{1G} < t < t_{1G} + T_G \\ 0 & t > t_{1G} + T_G \end{cases} \tag{D.2}$$

where V_{Gmax} is the gust peak in m/s, T_G is the gust period in s, and t_{1G} is the gust starting time in s.

The ramp wind speed component is described by

$$v_{wR} = \begin{cases} 0 & t < t_{1R} \\ V_{R\max}\left(1 - \dfrac{t - t_{2R}}{t_{1R} - t_{2R}}\right) & t_{1R} < t < t_{2R} \\ 0 & t > t_{2R} \end{cases} \tag{D.3}$$

where V_{Rmax} is the maximum ramp magnitude in m/s, t_{1R} is the ramp starting time in s, t_{2R} is the ramping stopping time in s and $t_{2R} > t_{1R}$. This component may be used to approximate a step change, by setting t_{2R} slightly larger than t_{1R}, or a slowly increasing wind speed to study ramp tracking.

The last wind speed component is the random noise component defined by

$$v_{wN} = 2\sum_{i=1}^{N}[S_V(\omega_i)\Delta\omega]^{1/2}\cos(\omega_i t + \varphi_i) \tag{D.4}$$

where N is the number of noise components, $\Delta\omega$ is the noise amplitude controlling parameter, $\omega_i = (i–0.5)\Delta\omega$, φ_i is a random variable with uniform probability density in the interval 0 to 2π, and the function $S_V(\omega_i)$ is the spectral density function [135] defined by

$$S_V(\omega_i) = \frac{2K_N F^2 \mid \omega_i \mid}{\pi^2[1 + (F\omega_i / \mu\pi)^2]^{4/3}} \tag{D.5}$$

where K_N is the surface drag coefficient, F is the turbulence scale, μ is the mean wind speed in m/s at some reference height.

D.2 Control of DFIG Wind Turbine

The DFIG wind turbine control system generally consists of two parts: the electrical control of the DFIG and the mechanical control of the wind turbine blade pitch angle, as shown in Figure 6.4. Control of the DFIG is achieved by control of the variable frequency converter (VFC), which includes control of the rotor side converter (RSC) and control of the grid side converter (GSC). The objective of the RSC is to govern both the stator-side active and reactive powers independently; while the objective of the GSC is to keep the dc-link voltage constant regardless of the magnitude and direction of the rotor power. The GSC control scheme can also be designed to regulate the reactive power or the stator terminal voltage of the DFIG.

D.2.1 Design of the RSC Controllers

The RSC control scheme consists of two cascaded control loops. The inner current control loop regulates independently the *d*-axis and *q*-axis rotor current components, i_{dr} and i_{qr}, according to some synchronously rotating reference frame. The stator-flux oriented reference frame [56] is the most commonly used one. The outer control loop regulates both the stator active power (or DFIG rotor speed) and reactive power (or DFIG terminal voltage) independently.

The mathematical model of the wound-rotor induction generator is represented by a set of equations (2.9)-(2.21). In the stator-flux oriented reference frame, the *d*-axis is aligned with the stator flux linkage vector λ_s, namely, $\lambda_{ds} = \lambda_s$ and $\lambda_{qs} = 0$. This gives the following relationships based on equations (2.9)-(2.16), (2.18) and (2.19)

$$i_{qs} = -L_m i_{qr} / L_s \tag{D.6}$$

$$i_{ds} = L_m (i_{ms} - i_{dr}) / L_s \tag{D.7}$$

$$P_s = -\frac{3}{2}\omega_s L_m^2 i_{ms} i_{qr} / L_s \tag{D.8}$$

$$Q_s = \frac{3}{2}\omega_s L_m^2 i_{ms}(i_{ms} - i_{dr}) / L_s \tag{D.9}$$

$$v_{dr} = r_r i_{dr} + \sigma L_r \frac{d}{dt} i_{dr} - s\omega_s \sigma L_r i_{qr} \tag{D.10}$$

$$v_{qr} = r_r i_{qr} + \sigma L_r \frac{d}{dt} i_{qr} + s\omega_s \left(\sigma L_r i_{dr} + L_m^2 i_{ms} / L_s\right) \tag{D.11}$$

where

$$i_{ms} = \frac{v_{qs} - r_s i_{qs}}{\omega_s L_m} \tag{D.12}$$

$$\sigma = 1 - \frac{L_m^2}{L_s L_r} \tag{D.13}$$

Equations (D.8) and (D.9) indicate that P_s and Q_s can be controlled independently by regulating the rotor current components, i_{qr} and i_{dr}, respectively. Consequently, the reference values of i_{dr} and i_{qr} can be determined directly from Q_s and P_s regulation.

Let

$$v_{dr1} = r_r i_{dr} + \sigma L_r \frac{d}{dt} i_{dr} \tag{D.14}$$

$$v_{qr1} = r_r i_{qr} + \sigma L_r \frac{d}{dt} i_{qr} \tag{D.15}$$

represent parts of (D.10) and (D.11). Equations (D.14) and (D.15) indicate that i_{dr} and i_{qr} respond to v_{dr1} and v_{qr1} respectively, through a first-order transfer function without cross-coupling. Therefore, it is possible to design the following feedback loops and PI controllers for the inner current control loop.

$$v_{dr1} = \left(k_{pr} + \frac{k_{ir}}{s}\right)(i_{dr}^* - i_{dr}) \tag{D.16}$$

$$v_{qr1} = \left(k_{pr} + \frac{k_{ir}}{s}\right)(i_{qr}^* - i_{qr}) \tag{D.17}$$

Substituting (D.16) and (D.17) into (D.10) and (D.11), respectively, gives

$$v_{dr} = \left(k_{pr} + \frac{k_{ir}}{s} \right) (i_{dr}^{*} - i_{dr}) - s\omega_s \sigma L_r i_{qr} \tag{D.18}$$

$$v_{qr} = \left(k_{pr} + \frac{k_{ir}}{s} \right) (i_{qr}^{*} - i_{qr}) + s\omega_s \left(\sigma L_r i_{dr} + \frac{L_m^2}{L_s} i_{ms} \right) \tag{D.19}$$

The design of the outer loop speed controller has been discussed in Chapter 6. The overall vector control scheme of the RSC is shown in Figure 6.8. The corresponding PSCAD/EMTDC model of the RSC control scheme is shown in Figure D.2. Figure D.3 shows the PSCAD/EMTDC model for stator flux angle calculation in order to implement the stator-flux orientation.

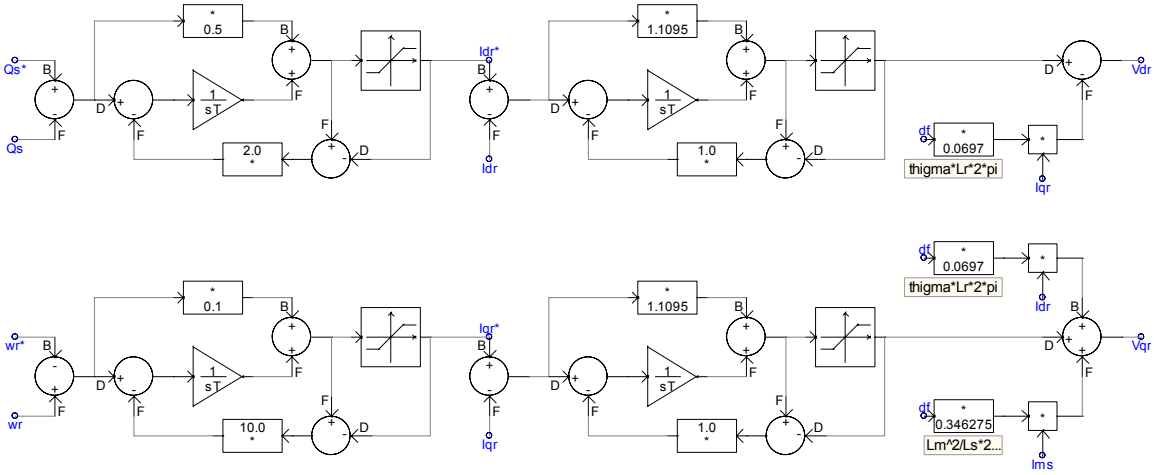

Figure D.2: PSCAD/EMTDC model for RSC PI controllers (with anti-windup design).

D.2.2 Design of the GSC Controllers

The GSC control scheme also consists of two cascaded control loops. The inner current control loop regulates independently the *d*-axis and *q*-axis GSC ac-side current components, i_{dg} and i_{qg}, in a synchronously rotating reference frame [109]. The outer control loop regulates the dc-link voltage and the reactive power exchanged between the GSC and the grid.

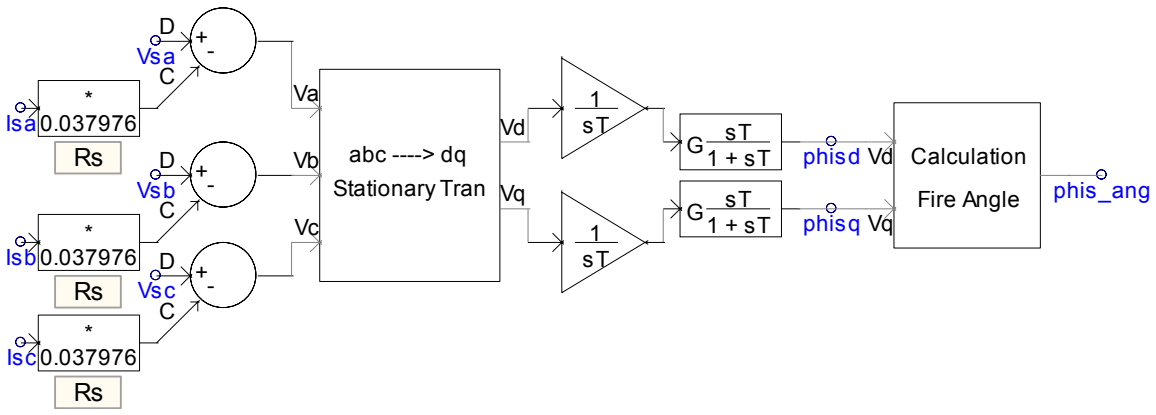

Figure D.3: PSCAD/EMTDC model for stator flux angle calculation.

In a synchronously rotating reference frame with the *d*-axis aligned to the grid voltage vector v_s ($v_s = v_{ds}$, $v_{qs} = 0$), the ac-side circuit equations of the GSC (Figure 1.3) can be written in per-unit form as:

$$v_{dg} = r_g i_{dg} + L_g \frac{d}{dt} i_{dg} - \omega_s L_g i_{qg} + v_s \tag{D.20}$$

$$v_{qg} = r_g i_{qg} + L_g \frac{d}{dt} i_{qg} + \omega_s L_g i_{dg} \tag{D.21}$$

Following the same procedure as in (D.14)-(D.19), v_{dg} and v_{qg} can be obtained by the following feedback loops and PI controllers

$$v_{dg} = \left(k_{pg} + \frac{k_{ig}}{s} \right) (i_{dg}^* - i_{dg}) - \omega_s L_g i_{qg} + v_s \tag{D.22}$$

$$v_{qg} = \left(k_{pg} + \frac{k_{ig}}{s} \right) (i_{qg}^* - i_{qg}) + \omega_s L_g i_{dg} \tag{D.23}$$

where the reference values i_{dg}^* and i_{qg}^* are obtained from the outer control loop.

Neglecting harmonics due to switching and the losses in the GSC, the filtering inductor and the transformer (Figure 1.3), the power balance equation is given by

$$P_r - P_g = v_{dc} i_{dc} = C v_{dc} \frac{d}{dt} v_{dc} \tag{D.24}$$

Let

$$v_{dc} = v_{dc0} + \Delta v_{dc} \tag{D.25}$$

where v_{dc0} (= v_{dc}^*) is the dc component of v_{dc}, Δv_{dc} is the ripple component of v_{dc}. Substituting (D.25) into (D.24) yields

$$P_r - P_g = C v_{dc0} \frac{d}{dt} v_{dc} + C \Delta v_{dc} \frac{d}{dt} v_{dc} \tag{D.26}$$

Since $\Delta v_{dc} \ll v_{dc0}$, (D.26) can be written as

$$P_r - P_g \approx C v_{dc0} \frac{d}{dt} v_{dc} \tag{D.27}$$

Therefore, the transfer function from P_g to v_{dc} is given by

$$\frac{v_{dc}(s)}{P_g(s)} = \frac{1}{C v_{dc0} s} \tag{D.28}$$

Since

$$P_g = \frac{3}{2} v_{ds} i_{dg} = \frac{3}{2} v_s i_{dg} \tag{D.29}$$

(D.28) becomes

$$\frac{v_{dc}(s)}{i_{dg}(s)} = \frac{3}{2} \frac{v_s}{C v_{dc0} s} \tag{D.30}$$

Therefore, it is possible to design a feedback loop and PI controller to generate the reference value of i_{dg} as follows

$$i_{dg}^* = \left(k_{pv} + \frac{k_{iv}}{s} \right) (v_{dc}^* - v_{dc}) \tag{D.31}$$

The reactive power exchanged between the GSC and the grid is given by

$$Q_g = -\frac{3}{2} v_{ds} i_{qg} = -\frac{3}{2} v_s i_{qg} \tag{D.32}$$

Therefore, the reference value of i_{dg} can be determined directly from the reactive power regulation.

The overall vector control scheme of the GSC is shown in Figure 6.9. The corresponding PSCAD/EMTDC model of the GSC control scheme is shown in Figure D.4.

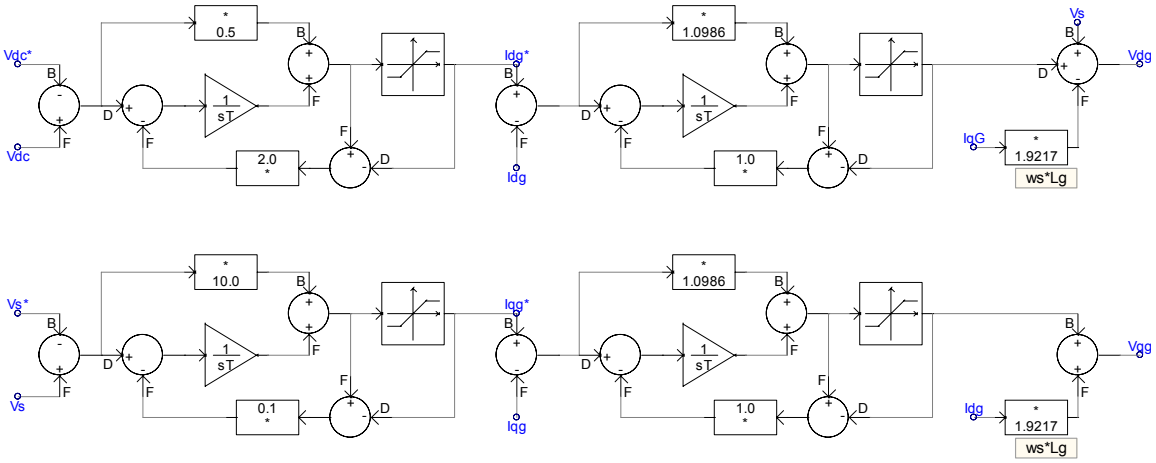

Figure D.4: PSCAD/EMTDC model for GSC PI controllers (with anti-windup design).

D.2.3 Design of the Wind Turbine Pitch Angle Controller

The PSCAD/EMTDC model of the wind turbine pitch angle controller (Figure 6.10) is shown in Figure D.5. The pitch angle controller is only activated during strong wind conditions. In such conditions, the blade pitch angle is controlled to reduce the mechanical power that the wind turbine extracts from the wind as well as to prevent over-speeding of the WTG. Therefore, the input signals of the pitch angle controller are the total output active power P_e and rotor speed ω_r of the generator. These two signals are compared with their corresponding reference values. The resulting deviation signals are passed through two PI controllers and their outputs are added together to form the reference value of the turbine blade pitch angle, which is then compared with the actual pitch angle. The error signals between the pitch angle and its reference is corrected by the pitch servo, which is represented by a first-order servo model [2] as shown in Figure D.5.

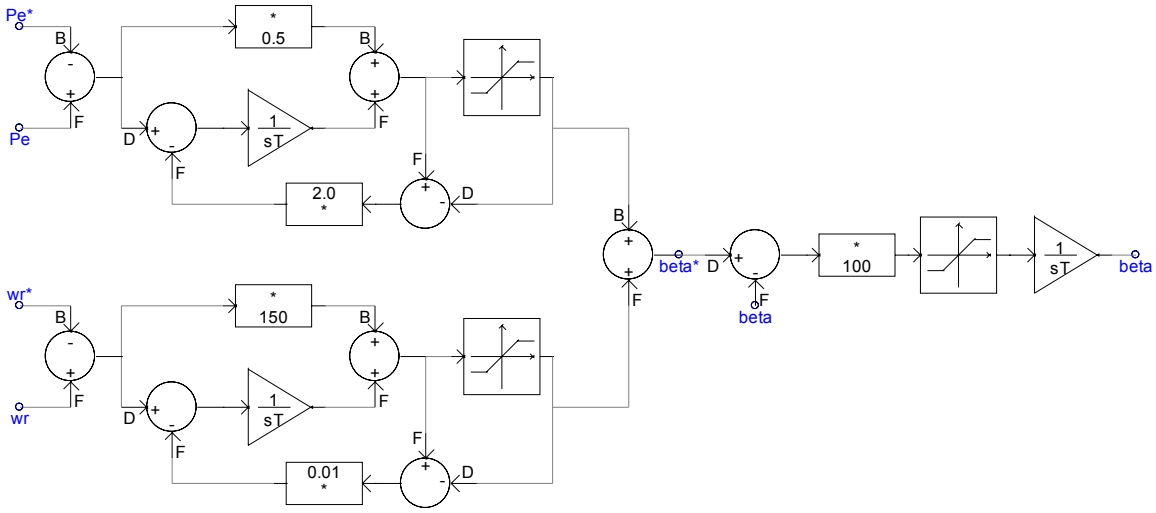

Figure D.5: PSCAD/EMTDC model for wind turbine pitch angle controller.

APPENDIX E

DFIG WIND TURBINE SYSTEM PARAMETERS

This Appendix provides the parameters of the DFIG wind turbine or equivalent DFIG wind turbine systems used in this thesis. These wind turbine generator systems include: a 3.6 MW DFIG wind turbine system [55], [121] in Chapters 6 and 8, an emulational wind turbine generator system used in Chapter 6 for experimental studies, an equivalent 400 MW DFIG wind farm system in Chapters 7, 9 and 10. The definition of base values in the per-unit system appears in Appendix H.

E.1 3.6 MW DFIG Wind Turbine System Parameters

Wind turbine: rated capacity = 3.6 MW, number of blades = 3, rotor diameter = 104 m, swept area = 8495 m^2, rotor speed (variable) = 8.5-15.3 rpm, cut-in wind speed = 3.5 m/s, cut-out wind speed = 27 m/s.

Mechanical shaft system (base power = 3.6 MW, base electrical angular frequency = 376.911 rad/s, base mechanical angular frequency for the generator shaft = 188.45 rad/s, and base mechanical angular frequency for the turbine shaft = $188.45N_g/N_t$ rad/s, where N_g/N_t is the gear ratio of the gear box in Figure 2.4): H_t = 4.29 s, H_g = 0.9 s, $D_t = D_g = 0$, D_{tg} = 1.5 pu, K_{tg} = 296.7 pu.

Wound rotor induction generator: rated power = 3.6 MW, rated stator voltage = 4.16 kV, number of poles p = 4, power factor pf = -0.9 ~ +0.9, r_s = 0.0079 pu, r_r = 0.025 pu, r_m = 66.57 pu, L_{ls} = 0.07937 pu, L_{lr} = 0.40 pu, L_m = 4.4 pu, base frequency f = 60 Hz. The per-unit values are given on 3.6 MW and 2.4 kV (i.e., the rated stator phase voltage) bases.

Other components in Figure 1.3: filter: r_g = 0.01 ohm, L_g = 5 mH, C_g = 2 μF, L_f = 5 mH; dc-link capacitor: C = 20 mF; step-up transformer: MVA rating = 1.5 MVA, turn ratio = 1.15/4.16 kV, no-load losses P_{nT} = 0.15%, copper losses P_{cT} = 1%.

Rotor and grid side converters of the DFIG: IGBT transistors: V_{CE} = 2.2 V, r_{CE} = 0.8 mΩ, E_{on} = 250 mJ, E_{off} = 300 mJ, I_{Tn} = 800 A, f_{sw} = 2 kHz; diodes: V_F = 1.7 V, r_F = 0.7 mΩ, E_{rr} = 150 mJ.

E.2 Experimental System Parameters for an Emulational Wind Turbine Generator System

DC motor: rated power = 10 Hp, rated armature voltage V_a = 125 V, armature resistance R_a = 0.2857 ohm, field resistance R_f = 47.6 ohm.

Induction generator: rated power = 7.5 Hp, number of poles = 4, rated stator voltage = 230 V, rated stator current = 19.6 A, R_s = 0.148 ohm, R_r = 0.134 ohm, L_m = 0.043 H, L_{ls} = 1.1 mH, L_{lr} = 1.6 mH.

The inertia constant of the system: H = 1 s.

E.3 Equivalent 400 MW Wind Farm System Parameters

Equivalent wind turbine to represent a wind farm: rated capacity = 400 MW, cut-in wind speed = 3.5 m/s, cut-out wind speed = 27 m/s, rated wind speed = 14 m/s, number of blades = 3, rotor diameter = 104 m, swept area = 8495 m^2, rotor speed (variable) = 8.5-15.3 rpm.

Equivalent wound-rotor induction generator: rated power = 400 MW, rated stator voltage = 22 kV, r_s = 0.0079 pu, r_r = 0.025 pu, L_{ls} = 0.07937 pu, L_{lr} = 0.40 pu, L_m = 4.4 pu. The per-unit values are given based on 400 MW and 12.7 kV (i.e., the rated stator phase voltage) bases.

APPENDIX F

MODELING AND CONTROL OF A STATCOM

The STATCOM used in Chapters 8-10 consists of a voltage source converter (VSC) that is connected in shunt to a bus through a coupling transform, as shown in Figure 8.1, Figure 9.3 and Figure 10.2, respectively. The objective of the STATCOM is to provide fast and smooth voltage regulation at the point of common coupling (PCC). In this work, the VSC is modeled as a six-pulse GTO PWM converter with a dc-link capacitor, as shown in Figure F.1. The operation of each individual switch (with a snubber circuit) in the VSC is fully represented, with a switching frequency of 900 Hz. The three inductances are used as low-pass filters to eliminate the high-frequency harmonics in the VSC ac-side currents.

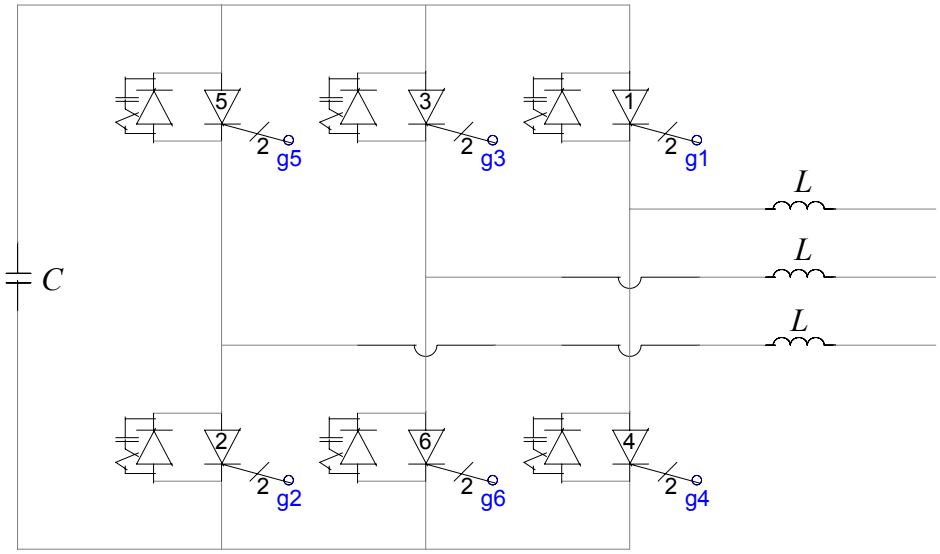

Figure F.1: A six-pulse GTO PWM VSC model in PSCAD/EMTDC.

Figure F.2 shows the simplified equivalent circuit of the STATCOM. It contains a dc-link capacitor, a VSC, and series inductances in the three lines connecting to the

system bus. These inductances account for the leakage inductances of the power transformer T2 as shown in Figure 8.1, as well as the inductances used for filtering the STATCOM ac-side currents. The circuit also includes resistance in shunt with the capacitor to represent the switching losses in the inverter, and resistance in series with the ac lines to represent the VSC and transformer conduction losses. The VSC block in the circuit is now treated as an ideal, lossless power transformer.

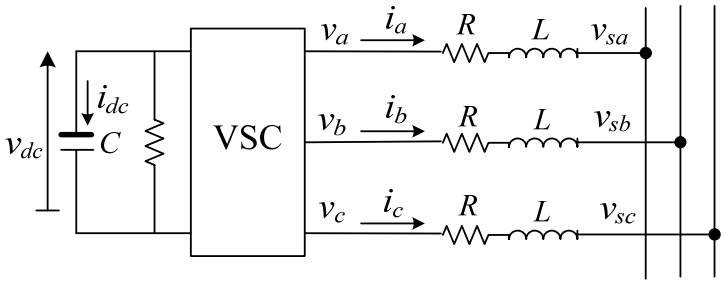

Figure F.2: Equivalent circuit of the STATCOM.

Assuming balanced conditions, the ac-side circuit equations in Figure F.2 can be written in a synchronously rotating reference frame using the *d-q* transformation [109] as:

$$\frac{di_d}{dt} = -\frac{R}{L} i_d + \omega_s i_q + \frac{1}{L} v_d - \frac{1}{L} v_{sd} \tag{F.1}$$

$$\frac{di_q}{dt} = -\frac{R}{L} i_q - \omega_s i_d + \frac{1}{L} v_q - \frac{1}{L} v_{sq} \tag{F.2}$$

where (i_d, i_q), (v_d, v_q), and (v_{sd}, v_{sq}) are the *d-q* components of (i_a, i_b, i_c), (v_a, v_b, v_c), and (v_{sa}, v_{sb}, v_{sc}), respectively.

Neglecting the harmonics due to switching and the losses in the VSC and the transformer, the power balance between the ac and dc sides of the VSC is given by

$$\frac{3}{2}(v_{sd} i_d + v_{sq} i_q) = v_{dc} i_{dc} = C v_{dc} \frac{dv_{dc}}{dt} \tag{F.3}$$

With correct alignment of the reference frame, the v_{sq} term is zero, and hence, the following equation can be written to relate the dc-link voltage to the *d*-axis current i_d and voltage v_{sd}:

$$\frac{dv_{dc}}{dt} = \frac{3v_{sd}i_d}{2Cv_{dc}} \tag{F.4}$$

The reactive power Q_C that the STATCOM exchanged with the system is given by

$$Q_C = 3v_{sd}i_q/2 \tag{F.5}$$

The dynamics of the VSC can be described by a set of first-order ordinary differential equations (ODEs) (F.1), (F.2) and (F.4). Since (F.4) is a nonlinear equation of the dc-link voltage, this set of ODEs represents a nonlinear model to be controlled. (F.4) and (F.5) indicate that the dc-link voltage and the voltage/reactive power at the PCC can be regulated by the *d*-axis current i_d and the *q*-axis current i_q, respectively; while (F.1) and (F.2) indicate that the *d*-*q* current components, i_d and i_q, respond to v_d and v_q respectively, through a first-order transfer function (with cross-coupling). Based on (F.1), (F.2), (F.4) and (F.5), linear PI control schemes can be developed to control the STATCOM, as shown in Figure 8.2, Figure 9.3 and Figure 10.2.

APPENDIX G

LINEAR CONTROLLER PARAMETERS

In this thesis, most linear controllers are PI-type controllers. The parameters of all the linear controllers are determined by a standard linear control design method, e.g., pole-zero placement or bode design, at a certain operating point. In this Appendix, the parameters of all the linear controllers as well as the operating conditions at which they are designed are provided.

The transfer function of a PI controller is given as:

$$G(s) = k_p + \frac{k_i}{s} \tag{G.1}$$

where k_p and k_i are the proportional and integral gains of the PI controller, respectively. The anti-windup design as shown in Figure 6.7 is applied to all the PI controllers.

G.1 Parameters of the SSSC Linear Controllers

A conventional internal (Figure 2.2) and external (Figure 2.1) linear control scheme is used to control the SSSC in Chapters 3, 5 and 10. The parameters of this linear control scheme in each of the three chapters are given in Table G.1.

Table G.1: Parameters of the SSSC linear controllers

		Internal control			External control				
Parameters		K_{VP}	K_P	K_I	K_w	K_P	T_C (s)	T_w (s)	T_P (s)
Chapter 3	Figure 3.1	50	5.0	100	3.0	0.5	1.0	0.1	0.1
	Figure 3.11	100	10	10	45	2.0	1.0	0.1	0.1
Chapter 5 (Figure 5.1)		100	120	100	-	2.0	2.0	-	10
Chapter 10 (Figure 10.3)		100	2.0	10	-	10	0.5	-	10

In Table G.1, the linear controllers in Figure 3.1 are designed at a specific operating point OP-I defined in Section 3.4.1, while the linear controllers in Figure 3.11 are designed at a specific operating point OP-III defined in Section 3.5; the linear controllers in Figure 5.1 are designed at the operating point described in Appendix B.2; and the linear controllers in Figure 10.3 are designed at the operating point described in Appendix B.3.

A PQ-decoupled linear control scheme is developed to regulate the SSSC connected to an SMIB power system in Chapter 4, as shown in Figure 4.3. In this control scheme, two PI controllers are designed to regulate independently the active and reactive power of the transmission line to which the SSSC is connected. The procedure to design these two PI controllers is discussed in Appendix C and their parameters are given in Table G.2. The operating point at which these two PI controllers are designed is OP-I defined in Section 4.4.1.

Table G.2: SSSC PI controller parameters in Figure 4.3

k_{p1}	K_{i1}	k_{p2}	K_{i2}
0.1	0.5	0.15	0.5

G.2 Parameters of the DFIG Wind Turbine PI Controllers

Control of a DFIG wind turbine consists of electrical control of the generator and mechanical blade pitch angle control of the wind turbine. Control of the generator is achieved by controlling the variable-frequency converter, which consists of controlling the rotor side converter (RSC) (Figure 6.8) and controlling the grid side converter (GSC) (Figure 6.9 and Figure 9.2). The procedure to design these controllers is discussed in Chapter 6 and Appendix D. The PI gains of the RSC and GSC controllers are listed in Table G.3 and Table G.4, respectively; while the parameters of the turbine blade pitch

angle controller are listed in Table G. 5. These controllers are designed at nominal operating conditions, where the DFIG wind turbines operate at the nominal terminal voltage and generate the nominal active power with the shaft rotational speed of 1.2 pu (i.e, 2160 rpm for a 4-pole DFIG). Moreover, the parameters RSC controllers in Chapter 7 are optimized by a particle swarm optimization-based approach, as listed in Table G.3.

Table G.3: Parameters of the RSC PI controllers

PI controller	i_{dr}		i_{qr}		ω_r		Q_s	
PI gains	k_p	k_i	k_p	k_i	k_p	k_i	k_p	k_i
Chapter 6	1.11	12.02	1.11	12.02	0.1	10	0.5	25.77
Chapter 7	3.05	17.86	4.87	4.76	18.23	26.32	0.001	1.0
Chapter 8	2.774	30.04	2.774	30.04	0.1	10	0.5	25.77
Chapter 9	1.96	9.08	1.96	9.08	10	20	0.01	0.5
Chapter 10	1.96	9.08	1.96	9.08	10	20	0.01	0.5

Table G.4: Parameters of the GSC PI controllers

PI controller	i_{dg}		i_{qg}		v_{dc}		V_s/Q_g	
PI gains	k_p	k_i	k_p	k_i	k_p	k_i	k_p	k_i
Chapter 6	1.10	161.29	1.10	161.29	0.5	5.0	10	2.0
Chapter 7	1.33	0.25	1.33	0.25	50	100	0.01	2.0
Chapter 8	1.10	161.29	1.10	161.29	0.5	1.0	0.01	20.0
Chapter 9	1.33	0.25	1.33	0.25	5	100	0.01	2.0
Chapter 10	1.33	0.25	1.33	0.25	5	100	0.01	2.0

Table G.5: Parameters of the pitch angle controller in Figure 6.10

ω_r		P_e		T (s)	$(d\beta/dt)_{max}$ (degree/s)	$(d\beta/dt)_{min}$ (degree/s)	β_{max} (degree)	β_{min} (degree)
k_p	k_i	k_p	k_i					
150	50	0.5	2.5	1.0	10	-10	27.0	0

G.3 Parameters of the STATCOM PI Controllers

The control systems of the STATCOMs used in Chapters 8-10 are shown in Figure 8.1, Figure 9.3 and Figure 10.2, respectively. The values of the PI controller parameters in these three figures are listed in Table G.6. In Table G.6, the PI controllers in Figure 8.2 are designed at the operating point where the DFIG wind turbine generates the nominal active power with the nominal terminal voltage and shaft rotational speed of 1.2 pu (i.e, 2160 rpm for a 4-pole DFIG); the PI controllers in Figure 9.3 are designed at the operating point described in Appendix B.2; and the linear controllers in Figure 10.2 are designed at the operating point described in Appendix B.3.

Table G.6: Parameters of the STATCOM PI controllers

PI controller	i_{dv}		i_{qv}		V_{dc}		$V_t/V_6/V_4$		Q_C	
PI gains	k_p	k_i	k_p	k_i	k_p	k_i	k_p	k_i	k_p	k_i
Figure 8.2	1.088	0.0063	1.088	0.0063	5.0	0.01	0.1	0.01		
Figure 9.3	2.602	0.016	2.602	0.016	20	0.01	30	0.1	1.0	0.01
Figure 10.2	2.602	0.016	2.602	0.016	20	0.01	30	0.1		

APPENDIX H

PER-UNIT SYSTEM

The per-unit model [147] of a system is derived by normalizing the system variables using base values, i.e., $\text{pu value} = \dfrac{\text{actual value}}{\text{base value}}$. In the *abc* reference frames, let the rms values of the rated phase voltage and current be the three-phase base voltage V_{B3} and current I_{B3}, respectively, then the base power is given as

$$P_B = 3V_{B3}I_{B3} \tag{H.1}$$

Selecting the base voltage and current in *dq* reference frames denoted by V_B and current I_B to be equal to the peak values of the rated phase voltage and current in *abc* reference frames yields

$$V_B = \sqrt{2}V_{B3} \tag{H.2}$$

$$I_B = \sqrt{2}I_{B3} \tag{H.3}$$

Hence, the base power is defined as

$$P_B = 3V_{B3}I_{B3} = \frac{3}{2}V_B I_B \tag{H.4}$$

The base impedance in Ω is defined as

$$Z_B = \frac{V_B}{I_B} = \frac{V_{B3}}{I_{B3}} \tag{H.5}$$

Let ω_B be the base angular frequency in rad/s (e.g., $\omega_B = 120\pi$ rad/s = 376.991 rad/s for a 60 Hz system), then the base rotational speed ω_{rB} of a p pole induction machine is given as:

$$\omega_{rB} = \frac{2}{p}\omega_B \tag{H.6}$$

and the base electromagnetic torque T_{eB} is given as:

$$T_{eB} = \frac{P_B}{\omega_{rB}} = \frac{p}{2}\frac{P_B}{\omega_B} \tag{H.7}$$

The actual value of the electromagnetic torque T_e in N·m is

$$T_e = \frac{3}{2}\frac{p}{2}\frac{1}{\omega_B}(\lambda_{ds}i_{qs} - \lambda_{qs}i_{ds}) = \frac{3}{2}\frac{p}{2}\frac{1}{\omega_B}(\lambda_{qr}i_{dr} - \lambda_{dr}i_{qr}) = \frac{3}{2}\frac{p}{2}L_m(i_{qs}i_{dr} - i_{ds}i_{qr}) \tag{H.8}$$

Therefore, the per-unit electromagnetic torque T_{eN} in pu is obtained as

$$\begin{aligned} T_{eN} &= \frac{T_e}{T_{eB}} = \frac{3}{2P_B}(\lambda_{ds}i_{qs} - \lambda_{qs}i_{ds}) = \frac{1}{V_B I_B}(\lambda_{ds}i_{qs} - \lambda_{qs}i_{ds}) = \left(\frac{\lambda_{ds}}{V_B}\right)\left(\frac{i_{qs}}{I_B}\right) - \left(\frac{\lambda_{qs}}{V_B}\right)\left(\frac{i_{ds}}{I_B}\right) \\ &= \lambda_{dsN}i_{qsN} - \lambda_{qsN}i_{dsN} = \lambda_{qrN}i_{drN} - \lambda_{drN}i_{qrN} = L_{mN}(i_{qsN}i_{drN} - i_{dsN}i_{qrN}) \end{aligned} \tag{H.9}$$

where subscript N in each variable denotes the per-unit value, and

$$\lambda_{dsN} = \frac{\lambda_{ds}}{V_B} \tag{H.10}$$

$$\lambda_{qsN} = \frac{\lambda_{qs}}{V_B} \tag{H.11}$$

where λ_{dsN} and λ_{dsN} are the d-axis and q-axis stator flux linkages in pu.

According to Figure 2.4, the base rotational shaft speed ω_{tB} of the wind turbine is given as:

$$\omega_{tB} = \frac{N_g}{N_t}\omega_{rB} = \frac{2}{p}\frac{N_g}{N_t}\omega_B \tag{H.12}$$

and the base mechanical torque T_{mB} of the wind turbine is given as:

$$T_{mB} = \frac{P_B}{\omega_{tB}} = \frac{N_t}{N_g}T_{eB} = \frac{p}{2}\frac{N_t}{N_g}\frac{P_B}{\omega_B} \tag{H.13}$$

Therefore, the per-unit mechanical torque T_{mN} in pu is obtained as

$$T_{mN} = \frac{T_m}{T_{mB}} = \frac{P_m/\omega_t}{P_B/\omega_{tB}} = \frac{P_{mN}}{\omega_{tN}} = \frac{2}{p}\frac{N_g}{N_t}\frac{P_m}{P_B}\frac{\omega_B}{\omega_t} \tag{H.14}$$

If the shaft system of a DFIG wind turbine is modeled as a single lumped-mass system, then the electromechanical dynamic equation (referred to the generator side) is given by

$$J_m \frac{d\omega_m}{dt} = \frac{N_g}{N_t} T_m - T_e - B_m \omega_m \tag{H.15}$$

where J_m is the moment of inertia in kg·m^2 of the lumped mass (including the turbine, generator, gearbox, and the shaft), B_m is the friction coefficient in N·m/rad/s of the lumped mass, ω_m is the mechanical shaft speed in rad/s of the lumped mass, and $\frac{N_g}{N_t} T_m$ is the equivalent mechanical torque in N·m converted to the generator side. Normalizing (H.15) using the base electromagnetic torque T_{eB} yields the following equation in the per-unit system:

$$\frac{J_m \frac{d\omega_m}{dt}}{T_{eB}} = \frac{\frac{N_g}{N_t} T_m - T_e - B_m \omega_m}{T_{eB}} \tag{H.16}$$

Substituting (H.6), (H.7) and (H.13) into equation (H.16), (H.16) can be rewritten as:

$$2H_m \frac{d\omega_{mN}}{dt} = T_{mN} - T_{eN} - D_m \omega_{mN} \tag{H.17}$$

where H_m is the inertia constant in seconds of the lumped system, defined by

$$H_m = \frac{1}{2} \frac{J_m \omega_B^2}{P_B (p/2)^2} \tag{H.18}$$

and D_m is the damping coefficient in pu of the lumped system, defined by

$$D_m = \frac{B_m \omega_B^2}{P_B (p/2)^2} \tag{H.19}$$

Following the procedure in (H.15)-(H.19), the per-unit electromechanical dynamic equations for the two-mass system can be obtained, as described by equations (2.6)-(2.8).

REFERENCES

[1] W. Qiao and R. G. Harley, "Power quality and dynamic performance improvement of wind farms using a STATCOM," in *Proc. 38th IEEE Power Electronics Specialists Conference*, June 17-21, 2007, pp. 1832-1838.

[2] V. Akhmatov, "Analysis of dynamic behavior of electric power systems with large amount of wind power," Ph.D. dissertation, Technical University of Denmark, Kgs. Lyngby, Denmark, Apr. 2003.

[3] R. Datta and V. T. Ranganathan, "Variable-speed wind power generation using doubly fed wound rotor induction – a comparison with alternative schemes,' *IEEE Trans. Energy Conversion*, vol. 17, no. 3, pp. 414-421, Sept. 2002.

[4] M. V. A. Nunes, J. A. Pecas Lopes, H. H. Zurn, U. H. Bezerra, and R. G. Almeida, "Influence of the variable-speed wind generators in transient stability margin of the conventional generators integrated in electrical grids," *IEEE Trans. Energy Conversion*, vol. 19, no. 4, pp. 692-701, Dec. 2004.

[5] J. Morren and S. W. H. de Haan, "Ridethrough of wind turbines with doubly-fed induction generator during voltage dip," *IEEE Trans. Energy Conversion*, vol. 20, no. 2, pp. 435-441, Jun. 2005.

[6] L. Angquist, B. Lundin, and J. Samuelsson, "Power oscillation damping using controlled reactive power compensation – a comparison between series and shunt approaches," *IEEE Trans. Power Systems*, vol. 8, no. 2, pp. 687-700, May 1993.

[7] N. G. Hingorani and L. Gyugyi, *Understanding FACTS: Concepts and Technology of Flexible AC Transmission Systems*, IEEE, New York, 2000.

[8] G. Reed, R. Pape, and M. Takeda, "Advantages of voltage sourced converter (VSC) based design concepts for FACTS and HVDC-link applications," in *Proc. IEEE PES 2003 General Meeting*, July 13-17, 2003, vol. 3, pp. 1816-1821.

[9] C. Schauder and H. Mehta, "Vector analysis and control of advanced static VAR compensators," *IEE Proceedings – Generation, Transmission and Distribution*, vol. 140, no. 4, pp. 299-306, Jul. 1993.

[10] P. Rao, M. L. Crow, and Z. Yang, "STATCOM control for power system voltage control applications," *IEEE Trans. Power Delivery*, vol. 15, no. 4, pp. 1311-1317, Oct. 2000.

[11] L. Gyugyi, C. D. Schauder, and K. K. Sen, "Static synchronous series compensator: a solid-state approach to the series compensation of transmission lines," *IEEE Trans. Power Delivery*, vol. 12, no. 1, pp. 406-417, Jan. 1997.

[12] B. T. Ooi, S.-Z. Dai, and X. Wang, "Solid-state series capacitive reactance compensators," *IEEE Trans. Power Delivery*, vol. 7, pp. 914-919, Apr. 1990.

[13] B. S. Rigby and R. G. Harley, "An improved control scheme for a series-capacitive reactance compensator based on a voltage-source inverter," *IEEE Trans. Industry Applications*, vol. 34, no. 2, pp. 355-363, Mar./Apr. 1998.

[14] B. S. Rigby, N. S. Chonco, and R. G. Harley, "Analysis of a power oscillation damping scheme using a voltage-source inverter," *IEEE Trans. Industry Applications*, vol. 38, no. 4, pp. 1105-1113, July/Aug. 2002.

[15] L. Zhang, M. L. Crow, Z. Yang, and S. Chen, "The steady state characteristics of an SSSC integrated with energy storage," in *Proc. IEEE PES 2001 Winter Meeting*, Jan. 28-Feb. 1, 2001, vol. 3, pp. 1311-1316.

[16] I. Cadirci and M. Ermis, "Double-output induction generator operating at subsynchronous and supersynchronous speeds: steady-state performance optimisation and wind-energy recovery," *IEE Proceedings – Electric Power Applications*, vol. 139, no. 5, pp. 429-442, Sept. 1996.

[17] R. Pena, J. C. Clare, and G. M. Asher, "Doubly fed induction generator using back-to-back PWM converters and its application to variable-speed wind-energy generation," *IEE Proceedings – Electric Power Applications*, vol. 143, no. 3, pp. 231-241, May 1996.

[18] M. Bruntt, J. Havsager, and H. Knudsen, "Incorporation of wind power in the East Danish power system," in *Proc. IEEE Power Tech*, Aug. 29-Sept. 2, 1999, pp. 202-205.

[19] A. Mullane, G. Lightbody, and R. Yacamini, "Wind-turbine fault ride-through enhancement," *IEEE Trans. Power Systems*, vol. 20, no. 4, pp. 1929-1937, Nov. 2005.

[20] S. W. Steven, "Wind parks as power plants," in *Proc. IEEE PES 2006 General Meeting*, June 18-22, 2006.

[21] F. Okou, L. A. Dessaint, and O. Akhrif, "Power system stability enhancement using a wide-area signals based hierarchical controller," *IEEE Trans. Power Systems*, vol. 20, no. 3, pp. 1465-1477, Aug. 2005.

[22] B. Fardanesh, "Future trends in power system control," *IEEE Computer Applications in Power*, vol. 15, no. 3, pp. 24-31, July 2002.

[23] I. Kamwa, R. Grondin, and Y. Hebert, "Wide-area measurement based stabilizing control of large power systems – a decentralized/hierarchical approach," *IEEE Trans. Power Systems*, vol. 16, no. 1, pp. 136-1531, Feb. 2001.

[24] H. Ni, G. T. Heydt, and L. Mili, "Power system stability agents using robust wide area control," *IEEE Trans. Power Systems*, vol. 17, no. 4, pp. 1123-1131, Nov. 2002.

[25] R. J. Patton, "Fault-tolerant control: the 1997 situation," in P*roc. IFAC Symposium on Fault Detection, Supervision, Safety for Technical Processes*, Aug. 1997, pp. 1033-1055.

[26] K. S. Narendra and K. Parthasarathy, "Identification and control of dynamical systems using neural networks," *IEEE Trans. Neural Networks*, vol. 1, no. 1, pp. 4-26, Mar. 1990.

[27] L. Ljung, *System Identification: Theory for the Users (2nd Edition)*, Upper Saddle River, NJ, USA: Prentice Hall PTR, 1999.

[28] S. S. Haykin, *Neural Networks: A Comprehensive Foundation (2nd Edition)*, Upper Saddle River, NJ, USA: Prentice Hall, 1998.

[29] P. J. Werbos, "Approximate dynamic programming for real-time control and neural modeling," in *Handbook of Intelligent Control*, D. White and D. Sofge, Eds., New York: Van Nostrand Reinhold, 1992, pp. 493-526.

[30] D. V. Prokhorov and D. C. Wunsch, "Adaptive critic designs," *IEEE Trans. Neural Networks*, vol. 8, no. 5, pp. 997-1007, Sept. 1997.

[31] D. A. White and M. I. Jordan, "Optimal control: a foundation for intelligent control," in *Handbook of Intelligent Control*, D. White and D. Sofge, Eds., New York: Van Nostrand Reinhold, 1992, pp. 185-214.

[32] J. Kennedy and R. C. Eberhart, "Particle swarm optimization," in *Proc. of the IEEE International Conference on Neural Network*s, Nov. 27-Dec. 1, 1995, vol. 4, pp. 1942-1948.

[33] Y. Shi and R. C. Eberhart, "A modified particle swarm optimizer," in *Proc. of the IEEE International Conference on Evolutionary Computation*, May 4-9, 1998, pp. 69-73.

[34] M. Clerc and J. Kennedy, "The particle swarm – explosion, stability, and convergence in a multidimensional complex space," *IEEE Trans. Evolutionary Computation*, vol. 6, no. 1, pp. 58-73, Feb. 2002.

[35] R. Hassan, B. Cohanim, O. de Weck, and G. Venter, "A comparison of particle swarm optimization and the genetic algorithm," in *Proc. 46th AIAA/ASME/ASCE/AHS/ASC Structures, Structural Dynamics and Materials Conference*, Austin, TX, USA, Apr. 18-21, 2005.

[36] B. A. Renz, *et al*, "AEP unified power flow controller performance," *IEEE Trans. Power Delivery*, vol. 14, no. 4, pp. 1374-1381, Oct. 1999.

[37] L. Y. Dong, L. Zhang, and M. L. Crow, "A new control strategy for the unified power flow controller," in *Proc. IEEE PES 2002 Winter Meeting*, Jan. 27-31, 2002, vol. 1, pp. 562-566.

[38] T. Makombe and N. Jenkins, "Investigation of a unified power flow controller," *IEE Proceedings on Generation, Transmission and Distribution*, vol. 146, no. 4, pp. 400-408, July 1999.

[39] F. J. Swift and H. F. Wang, "Application of the controllable series compensator in damping power system oscillations," *IEE Proc. Generation, Transmission and Distribution*, vol. 143, no. 4, pp. 359-364, July 1996.

[40] J-W Park, R. G. Harley, and G. K. Venayagamoorthy, "New external neuro-controller for series capacitive reactance compensator in a power network," *IEEE Trans. Power Systems*, vol. 19, no. 3, pp. 1462-1472, Aug. 2004.

[41] W. Qiao and R. G. Harley, "Indirect adaptive external neuro-control for a series capacitive reactance compensator based on a voltage source PWM converter in damping power oscillations," *IEEE Trans. Industrial Electronics*, vol. 54, no. 1, pp. 77-85, 2007.

[42] W. Qiao and R. G. Harley, "Indirect adaptive internal neuro-control for a static synchronous series compensator (SSSC) connected to a power system," in *Proc. 31st Annual Conference of the IEEE Industrial Electronics Society*, Nov. 6-10, 2005, pp. 50-55.

[43] E. Swidenbank, S. Mcloone, D. Flynn, G. W. Irwin, and B. W. Hogg, "Neural network nased control for synchronous generators," *IEEE Trans. Energy Conversion*, vol. 14, no. 4, pp. 1673-1679, Dec. 1999.

[44] J-W Park, R. G. Harley, and G. K. Venayagamoorthy, "Indirect adaptive control for synchronous generator: comparison of MLP/RBF neural networks approach with Lyapunov stability analysis," *IEEE Trans. Neural Networks*, vol. 15, no. 2, pp.460-464, Mar. 2004.

[45] J-W. Park, R. G. Harley, and G. K. Venayagamoorthy, "Adaptive-critic-based optimal neurocontrol for synchronous generator in power system using MLP/RBF neural networks," *IEEE Trans. Industry Applications*, vol. 39, no. 5, pp. 1529-1540, Sept./Oct. 2003.

[46] S. K. Salman and A. L. J. Teo, "Windmill modeling consideration and factors influencing the stability of a grid-connected wind power-based embedded generator," *IEEE Trans. Power Systems*, vol. 18, no. 2, pp. 793-802, May 2003.

[47] Y. Lei, A. Mullane, G. Lightbody, and R. Yacamini, "Modeling of the wind turbine with a doubly fed induction generator for grid integration studies," *IEEE Trans. Energy Conversion*, vol. 21, no. 1, pp. 257-264, Mar. 2006.

[48] T. Petru and T. Thiringer, "Modeling of wind turbines for power system studies," *IEEE. Trans. Power Systems*, vol. 17, no. 4, pp. 144-151, Nov. 2002.

[49] J. G. Slootweg, S. W. H. de Hann, H. Polinder, and W. L. Kling, "General model for representing variable speed wind turbines in power system dynamic simulations," *IEEE. Trans. Power Systems*, vol. 18, no. 1, pp. 1132-1139, Feb. 2003.

[50] A. Tapia, G. Tapia, J. X. Ostolaza, and J. R. Saenz, "Modeling and control of a wind turbine driven doubly fed induction generator," *IEEE Trans. Energy Conversion*, vol. 18, no. 2, pp. 194-204, Jun. 2003.

[51] P. Ledesma and J. Usaola, "Doubly fed induction generator model for transient stability analysis," *IEEE Trans. Energy Conversion*, vol. 20, no. 2, pp. 388-397, June 2005.

[52] J. B. Ekanayake, L. Holdsworth, X. G. Wu, and N. Jenkins, "Dynamic modeling of doubly fed induction generator wind turbines," *IEEE Trans. Power Systems*, vol. 18, no. 2, pp. 803-809, May 2003.

[53] T. Tang and L. Xu, "A flexible active reactive power control strategy for a variable speed constant frequency generating system," *IEEE Trans. Power Electronics*, vol. 10, no. 4, pp. 472-477, Jul. 1995.

[54] R. Cardenas, R. Pena, J. Clare, G. Asher, and J. Proboste, "MARS observers for sensorless control of doubly-fed induction generators," *IEEE Trans. Power Electronics*, vol. 23, no. 3, pp. 1075- 1084, May 2008.

[55] N. W. Miller, W. W. Price, and J. J. Sanchez-Gasca, "Dynamic modeling of GE 1.5 and 3.6 wind turbine-generators," GE-Power Systems Energy Consulting, General Electric International, Inc., Schenectady, NY, USA, Oct. 27, 2003.

[56] D. W. Novotny and T. A. Lipo, *Vector Control and Dynamics of AC Drives*, Oxford University Press, 2000.

[57] H. Li, K. L. Shi, and P. G. McLaren, "Neural-network-based sensorless maximum wind energy capture with compensated power coefficient," *IEEE Tran. Industry Applications*, vol. 41, no. 6, pp. 1548-1556, Nov./Dec. 2005.

[58] S. Bhowmik, R. Spee, and J. H. R. Enslin, "Performance optimization for doubly fed wind power generation systems," *IEEE Trans. Industry Applications*, vol. 35, no. 4, pp. 949-958, Jul./Aug. 1999.

[59] K. Tan and S. Islam, "Optimal control strategies in energy conversion of PMSG wind turbine system without mechanical sensors," *IEEE Trans. Energy Conversion*, vol. 19, no. 2, pp. 392-399, Jun. 2004.

[60] M. G. Simoes, B. K. Bose, and R. J. Spiegel, "Fuzzy logic based intelligent control of a variable speed cage machine wind generation system," *IEEE Trans. Power Electronics*, vol. 12, no. 1, pp. 87-95, Jan. 1997.

[61] Y. L. Abdel-Magid, M. A. Abido, S. Al-Baiyat, and A. H. Mantawy, "Simultaneous stabilization of multimachine power systems via genetic algorithms," *IEEE Trans. Power Systems*, vol. 14, no. 4, pp. 1428-1439, Nov. 1999.

[62] M. A. Abido, "A novel approach to conventional power system stabilizer design using tabu search," *Int. Journal Electrical Power and Energy Systems*, vol. 21, no. 6, pp. 443-454, Aug. 1999.

[63] M. A. Abido, "Robust design of multimachine power system stabilizers using simulated annealing," *IEEE Trans. Energy Conversion*, vol. 15, no. 3, pp. 297-304, Sept. 2000.

[64] D. B. Fogel, *Evolutionary Computation: Toward a New Philosophy of Machine Intelligence*, New York: IEEE Press, 2000.

[65] J. Yao, H Li, Y. Liao, and Z. Chen, "An improved control strategy of limiting the dc-link voltage fluctuation for a doubly fed induction wind generator," *IEEE Trans. Power Electronics*, vol. 23, no. 3, pp. 1205-1213, May 2008.

[66] Z.-L. Gaing, "A particle swarm optimization approach for optimum design of PID controller in AVR system," *IEEE Trans. Energy Conversion*, vol. 19, no. 2, pp. 384-391, June 2004.

[67] R. G. de Almeida, J. A. Pecas Lopes, and J. A. L. Barreiros, "Improving power system dynamic behavior through doubly fed induction machines controlled by static converter using fuzzy control," *IEEE Trans. Power Systems*, vol. 19, no. 4, pp. 1942-1950, Nov. 2004.

[68] M. El Moursi, G. Joos, and C. Abbey, "A secondary voltage control strategy for transmission level interconnection of wind generation," *IEEE Trans. Power Electronics*, vol. 23, no. 3, pp. 1178-1190, May 2008.

[69] J. Hochheimer, "Wind generation integration & operation – technical challenges/issues," in *Proc. IEEE PES General Meeting 2006*, Montreal, Canada, June 18-22, 2006.

[70] Z. Saad-Saoud, M. L. Lisboa, J. B. Ekanayake, N. Jenkins, and G. Strbac, "Application of STATCOMs to wind farms," *IEE Proceedings – Generation, Transmission and Distribution*, vol. 145, no. 5, pp. 511-516, Sept. 1998.

[71] M. Molinas, J. A. Suul, and T. Underland, "Low voltage ride through of wind farms with cage generators: STATCOM versus SVC," *IEEE Trans. Power Electronics*, vol.23, no. 3, pp. 1104-1117, May 2008.

[72] M. Begovic, D. Novosel, D. Karlsson, C. Henville, and G. Michel, "Wide-area protection and emergency control," *Proceedings of the IEEE*, vol. 93, no. 5, pp. 876-891, May 2005.

[73] J. J. Sanchez-Gasca, "Coordinated control of two FACTS devices for damping interarea oscillations," *IEEE Trans. Power Systems*, vol. 12, no. 2, pp. 428-434, May 1998.

[74] P. Pourbeik and M. J. Gibbard, "Simultaneous coordination of power system stabilizers and FACTS device stabilizers in a multimachine power system for enhancing dynamic performance," *IEEE Trans. Power Systems*, vol. 13, no. 2, pp. 473-479, May 1998.

[75] G. H. Golub and C. F. Van Loan, *Matrix Computations*, 3rd ed., Baltimore: Johns Hopkins University Press, 1996.

[76] G. J. Li, T. T. Lie, G. B. Shrestha, and K. L. Lo, "Real-time coordinated optimal facts controllers," *Electrical Power System Research*, vol. 52, pp. 273-286, 1999.

[77] G. J. Li, T. T. Lie, G. B. Shrestha, and K. L. Lo, "Implementation of coordinated multiple facts controller for damping oscillations," *Electrical Power and Energy Systems*, vol. 22, pp. 79-92, 2000.

[78] Y. Wang, Y. L. Tan, and G. Guo, "Robust nonlinear co-ordinated excitation and TCSC control for power systems," *IEE Proc. Generation, Transmission and Distribution*, vol. 149, no. 3, pp. 367-372, May 2002.

[79] L. Cong and Y. Wang, "Co-ordinated control of generator excitation and STATCOM for rotor angle stability and voltage regulation enhancement of power systems," *IEE Proc. Generation, Transmission and Distribution*, vol. 149, no. 6, pp. 659-666, Nov. 2002.

[80] H. Chen, Y. Wang, and R. Zhou, "Transient and voltage stability enhancement via co-ordinated excitation and UPFC control," *IEE Proc. Generation, Transmission and Distribution*, vol. 148, no. 3, pp. 201-208, May 2001.

[81] A. A. Hashmani, Y. Wang, and T. T. Lie, "Enhancement of power system transient stability using a nonlinear coordinated excitation and TCPS controller," *Electrical Power and Energy Systems*, vol. 24, pp. 201-214, 2002.

[82] Q. J. Liu, Y. Z. Sun, T. L. Shen, and Y. H. Song, "Adaptive nonlinear co-ordinated excitation and STATCOM controller based on Hamiltonian structure for multimachine-power-system stability enhancement," *IEE Proc. Control Theory Applications*, vol. 150, no. 3, pp. 285-294, May 2003.

[83] H. F. Wang, "Multiagent co-ordination for the secondary voltage control in power system contingencies," *IEE Proc. Generation, Transmission and Distribution*, vol. 148, no. 1, pp. 61-66, Jan. 2001.

[84] G. Glanzmann and G. Andersson, "Coordinated control of FACTS devices based on optimal power flow," in *Proc. the 37th Annual North American Power Symposium*, Oct. 23-25, 2005, pp. 141-148.

[85] B. Chaudhuri, R. Majumder, and B. C. Pal, "Wide-area measurement-based stabilizing control of power system considering signal transmission delay," *IEEE Trans. Power Systems*, vol. 19, no. 4, pp. 1971-1979, July 2004.

[86] O. Alsac, N. Vempati, B. Stott, and A. Monticelli, "Generalized state estimation," *IEEE Trans. Power Systems*, vol. 13, no. 3, pp. 1069-1075, Aug. 1998.

[87] M. A. El-Sharkawi and Robert J. Marks II, "Missing sensors restoration for system control and diagnostics," in *Proc. of the 4th IEEE International Symposium on Diagnostics for Electric Machines, Power Electronics and Drives*, Aug. 24-26, 2003, pp. 338-341.

[88] S. Narayanan, R. J. Marks II, J. L. Vian, J. J. Choi, M. A. El-Sharkawi,, and B. B. Thompson, "Set constraint discovery: missing sensor data restoration using auto-associative regression machines," in *Proc. of the 2002 International Joint Conference on Neural Networks*, May 12-17, 2002, vol. 3, pp. 2872-2877.

[89] H. Bouland and Y. Kamp, "Auto-Association by Multi-Layer Perceptrons and Singular Value Decomposition," *Biological Cybernetics*, 59(4-5): pp. 291-294, 1988.

[90] "*PSCAD User's Guide: Version 4*", Manitoba HVDC Research Centre Inc., 2003.

[91] K. Alsabti, S. Ranka, and V. Singh, "An efficient k-means clustering algorithm," in *Proc. First Workshop on High Performance Data Mining*, Mar. 1998.

[92] J. Moody and C. J. Darken, "Fast learning in networks of locally-tuned processing units," *Neural Computation*, vol. 1, pp. 281-294, 1989.

[93] W. Qiao and R. G. Harley, "An indirect adaptive external neuro-controller for series capacitive reactance compensator in damping power oscillations", in *Proc. 13th International Conference on Intelligent Systems Application to Power Systems*, Nov. 6-10, 2005, pp. 234-239.

[94] P. J. Werbos, "Backpropagation through time: what it does and how to do it," *Proceedings of the IEEE*, vol. 78, no. 10, pp. 1550-1560, Oct. 1990.

[95] C. W. Taylor, *Power System Voltage Stability*, New York: McGraw-Hill, 1994.

[96] C. W. Taylor, "Concept of undervoltage load shedding for voltage stability," *IEEE Trans. Power Delivery*, vol. 7, no.2, pp. 480-488, Apr. 1992.

[97] P. M. Anderson and A. A. Fouad, *Power System Control and Stability*, IEEE Press, New York, 1994.

[98] G. K. Venayagamoorthy and R. G. Harley, "A continually online trained neurocontroller for excitation and turbine control of a turbogenerator," *IEEE Trans. Energy Conversion*, vol. 16, no. 3, pp. 261-269, Sept. 2001.

[99] B. B. Thompson, R. J. Marks, and M. A. El-Sharkawi, "On the contractive nature of autoencoders: application to missing sensor restoration," in *Proc. 2003 International Joint Conference on Neural Networks*, July 20-24, 2003, pp. 3011-3016.

[100] W. Qiao, Z. Gao, and R. G. Harley, "Continuous on-line identification of nonlinear plants in power systems with missing sensor measurements," in *Proc. 2005 International Joint Conference on Neural Networks*, July 31-Aug. 4, 2005, pp. 1729-1734.

[101] W. Qiao, R. G. Harley, and G. K. Venayagamoorthy, "A fault-tolerant P-Q decoupled control scheme for static synchronous series compensator," in *Proc. IEEE PES 2006 Annual Meeting*, Montreal, QC, Canada, June 18-22, 2006.

[102] W. Qiao, R. G. Harley, and G. K. Vanayagamoorthy, "Fault-tolerant indirect adaptive neuro-control for a static synchronous series compensator in a power network with missing sensor measurements," *IEEE Trans. Neural Networks*, in press (available online).

[103] W. Qiao, R. G. Harley, and G. K. Venayagamoorthy, "Fault-tolerant optimal neurocontrol for a static synchronous series compensator connected to a power network," *IEEE Trans. Industry Applications*, vol. 44, no. 1, pp. 74-84, Jan./Feb. 2008.

[104] W. Qiao, Z. Gao, R. G. Harley, and G. K. Vanayagamoorthy, "Robust neuro-identification of nonlinear plants in electric power systems with missing sensor measurements," *IFAC Journal: Engineering Applications of Artificial Intelligence (Elsevier)*, vol. 12, no. 4, pp. 604-618, June 2008.

[105] M. A. Kramer, "Autoassociative neural networks," *Computers & Chemical Engineering*, vol. 16, no. 4, pp. 313-328, 1992.

[106] W. W. Hsieh, "Nonlinear principal component analysis by neural networks," *Tellus*, vol. 53A, pp. 599-615, 2001.

[107] W. A. Kirk and M. A. Khamsi, *An Introduction to Metric Spaces and Fixed Point Theory*, New York: John Wiley, 2001.

[108] P. Kundur, *Power System Stability and Control*. New York: McGraw-Hill, 1994.

[109] P. C. Krause, O. Wasynczuk, and S. D. Sudhoff, *Analysis of Electric Machinery and Drive Systems*, IEEE Press, 2002, pp. 111-125.

[110] W. Qiao and R. G. Harley, "Optimization of radial basis function widths using particle swarm optimization," in *Proc. 2006 IEEE Swarm Intelligence Symposium*, Indianapolis, Indiana, USA, May 12-14, 2006, pp. 55-60.

[111] D. Reichelt, E. Ecknauer, and H. Glavitsch, "Estimation of steady-state unbalanced system conditions combining conventional power flow and fault analysis software," *IEEE Trans. Power Systems*, vol. 11, no. 1, pp. 422-427, Feb. 1996.

[112] T. Athay, R. Podmore, and S. Virmani, "A practical method for direct analysis of transient stability," *IEEE Trans. Power Apparatus and Systems*, vol. PAS-98, no. 2, pp. 573-584, Mar./Apr. 1979.

[113] M. A. Pai, *Energy Function Analysis for Power System Stability*. Boston: Kluwer Academic Publishers, 1989.

[114] M. H. Haque, "Damping improvement by FACTS devices: a comparison between STATCOM and SSSC," *Electric Power Systems Research*, vol. 76, pp. 865-872, 2006.

[115] S. Jiang, U. D. Annakkage, and A. M. Gole, "A platform for validation of FACTS models," *IEEE Trans. Power Delivery*, vol. 21, no. 1, pp. 484-491, Jan. 2006.

[116] W. Qiao, G. K. Vanayagamoorthy, and R. G. Harley, "Missing-sensor-fault-tolerant control for SSSC FACTS device with real-time implementation," *IEEE Trans. Power Delivery*, under review.

[117] P. Forsyth, T. Maguire, and R. Kuffel, "Real time digital simulation for control and protection system testing," in *Proc. 35th Annual IEEE Power Electronics Specialists Conference*, June 20-25, 2004, pp. 329-335.

[118] "*RTDS Manual Set*," RTDS Technologies, Inc., 2005.

[119] "*OMNIBUS User's Manual*," Innovative Integration, California, USA, Feb. 2001.

[120] F. Blaabjerg, J. K. Pedersen, U. Jaeger, and P. Thoegersen, "Single current sensor technique in the DC link of three-phase PWM-VS inverters: a review and a novel solution," *IEEE Trans. Industry Applications*, vol. 33, no. 5, pp. 1241-1253, Sept./Oct., 1997.

[121] W. Qiao, W. Zhou, J. M. Aller, and R. G. Harley, "Wind speed estimation based sensorless output maximization control for a wind turbine driving a DFIG," *IEEE Trans. Power Electronics*, vol. 23, no. 3, pp. 1156-1169, May 2008.

[122] A. Petersson, "Analysis, modeling, and control of doubly-fed induction generators for wind turbines," Ph.D. dissertation, Chalmers University of Technology, Goteborg, Sweden, 2005.

[123] A. Grauers, "Design of direct-driven permanent-magnet generators for wind turbines," Ph.D. dissertation, Chalmers University of Technology, Goteborg, Sweden, Oct. 1996.

[124] *IEEE Standard Test Procedure for Polyphase Induction Motors and Generators*, IEEE Standard 112-2004, Nov. 2004.

[125] A. Grauers, "Efficiency of three wind energy generator systems," *IEEE Trans. Energy Conversion*, vol. 11, no. 3, pp. 650-657, Sept. 1996.

[126] B. Lu, T. G. Habetler, and R. G. Harley, "A survey of efficiency-estimation methods for in-service induction motors," *IEEE Trans. Industry Applications*, vol. 42, no. 4, pp. 924-933, Jul/Aug. 2006.

[127] F. Blaabjerg, U. Jaeger, S. Munk-Nielsen, and J. K. Pedersen, "Power losses in PWM-VSI inverter using NPT or PT IGBT devices," *IEEE Trans. Power Electronics*, vol. 10, no. 3, pp. 358-367, May 1995.

[128] F. Abrahamsen, F. Blaabjerg, J. K. Pedersen, and P. B. Thoegersen, "Efficiency-optimized control of medium-size induction motor drives," *IEEE Trans. Industry Applications*, vol. 37, no. 6, pp. 1761-1767, Nov./Dec. 2001.

[129] F. Abrahamsen, "Energy optimal control of induction motor drives," Ph.D. dissertation, Aalborg University, Aalborg, Denmark, Feb. 2000.

[130] J. Park and I. W. Sandberg,, "Universal approximation using radial-basis-function networks," *Neural Computation*, vol. 3, no. 3, pp. 246-257, 1991.

[131] G. Ellis, R. D. Lorenz, "Resonant load control method for industrial servo drives," in *Proc. IEEE Industry Applications Conference*, Oct. 8-12, 2000, pp. 1438-1445.

[132] N. J. Krikelis and S. K. Barkas, "Design of tracking systems subject to actuator saturation and integral wind-up," *International Journal of Control*, vol. 39, no. 4, pp. 667–682, 1984.

[133] M. V. Kothare, P. J. Campo, M. Morari, and C. N. Nett, "A unified framework for the study of anti-windup designs," *Automatica*, vol. 30, no. 12, pp. 1869–1883, 1994.

[134] T. Sun, Z. Chen, and F. Blaabjerg, "Flicker study on variable speed wind turbines with doubly fed induction generators," *IEEE Trans. Energy Conversion*, vol. 20, no. 4, pp. 896-905, Dec. 2005.

[135] P. M. Anderson and A. Bose, "Stability simulation of wind turbine systems," *IEEE Trans. Power Apparatus and Systems*, vol. PAS-102, no. 12, pp. 3791-3795, Dec. 1983.

[136] W. Qiao, G. K. Venayagamoorthy, and R. G. Harley, "Design of optimal PI controllers for doubly fed induction generators driven by wind turbines using particle swarm optimization," in *Proc. 2006 International Joint Conference on Neural Networks*, Vancouver, BC, Canada, July 16-21, 2006, pp. 1982-1986.

[137] W. Qiao, R. G. Harley, and G. K. Venayagamoorthy, "Effects of FACTS devices on a power system which includes a large wind farm," in *Proc. IEEE PES Power System Conference and Exposition 2006*, Oct. 27-Nov. 1, 2006, pp. 2070-207.

[138] W. Qiao and R. G. Harley, "Effect of grid-connected DFIG wind turbines on power system transient stability," *IEEE PES 2008 General Meeting*, Pittsburgh, PA, USA, July 20-24, 2008.

[139] W. Qiao, G. K. Venayagamoorthy, and R. G. Harley, "Real-time implementation of a STATCOM on a wind farm equipped with doubly fed induction generators," in *Proc. IEEE IAS 41th Annual Meeting*, Oct. 8-12, 2006, pp. 1073-1080.

[140] W. Qiao, R. G. Harley, and G. K. Vanayagamoorthy, "Coordinated reactive power control of a large wind farm and a STATCOM using heuristic dynamic programming," *IEEE Trans. Energy Conversion*, accepted for publication.

[141] V. K. Polisetty, S. R. Jetti, G. K. Vanayagamoorthy, and R. G. Harley, "Intelligent integration of a wind farm to an utility power network with improved

voltage stability," in *Proc. IEEE IAS 41th Annual Meeting*, Oct. 8-12, 2006, pp. 1128-1133.

[142] W. Qiao, R. G. Harley, and G. K. Venayagamoorthy, "Dynamic modeling of wind farms with fixed-speed wind turbine generators," in *Proc. IEEE PES 2007 General Meeting*, Tampa, FL, USA, June 24-28, 2007.

[143] W. Qiao, G. K. Venayagamoorthy, and R. G. Harley, "DHP-based wide-area coordinating control of a power system with a large wind farm and multiple FACTS devices," in *Proc. 2007 International Joint Conference on Neural Networks*, Orlando, Florida, USA, Aug. 12-17, 2007, pp. 2093-2098.

[144] W. Qiao, G. K. Venayagamoorthy, and R. G. Harley, "Optimal wide-area monitoring and nonlinear adaptive coordinating neurocontrol of a power system with wind power integration and multiple FACTS devices," *Neural Networks (Elsevier)*, vol. 21, no. 2-3, pp. 466-475, Mar.-Apr. 2008.

[145] G. K. Venayagamoorthy, R. G. Harley, and D. C. Wunsch, "Implementation of adaptive critic-based neurocontrollers for turbogenerators in a multimachine power system," *IEEE Trans. Neural Networks*, vol. 14, no. 5, pp. 1047-1064, Sept. 2003.

[146] J. F. Hauer, C. J. Demeure, and L. L. Scharf, "Initial results in Prony analysis of power system response signals," *IEEE Trans. Power Systems*, vol. 5, no. 1, pp. 80-89, Feb. 1990.

[147] R. Krishnan, *Electric Motor Drives: Modeling, Analysis, and Control*, Upper Saddle River, NJ: Prentice-Hall, 2001.

VITA

WEI QIAO

Wei Qiao was born in Anqing, China on April 21, 1975. He received the Bachelor of Engineering and Master of Engineering degrees in electrical engineering from Zhejiang University, China in 1997 and 2002, respectively, and the Master of Science degree in High Performance Computation for Engineered Systems from Singapore -MIT Alliance (SMA), Singapore in 2003.

From 1997 to 1999, he was an electrical engineer in China Petroleum & Chemical Corporation (Sinopec). Since August 2003, he has been with the Georgia Institute of Technology, Atlanta, GA, where he is currently completing a Ph.D. degree in electrical engineering. He worked as a Graduate Teaching Assistant in the School of Electrical and Computer Engineering from 2003 to 2005, and later as a Graduate Research Assistant in the Electric Power Group from 2005 to 2008. He is the first author of two book chapters, ten refereed journal papers (including seven IEEE Transactions papers), and over twenty refereed international conference proceeding papers. He is a student member of the IEEE and the IEEE Power Engineering Society's Georgia Tech Student Chapter.

He was the recipient of the first prize in the student paper and poster competition of the IEEE Power Engineering Society (PES) General Meeting, Montreal, QC, Canada, in June 2006. He received student travel grants from the IEEE Computational Intelligence Society (CIS) for the International Joint Conference on Neural Networks (IJCNN) in 2005 and 2006, from the IEEE PES for the General Meeting in 2006, 2007 and 2008, from the IEEE Power Electronics Society (PELS) for the 38th IEEE Power Electronics Specialists Conference (PESC) in 2007.

Wei Qiao will join the Department of Electrical Engineering at the University of Nebraska – Lincoln from August 2008 as a tenure-track Assistant Professor.